UNIVERSIDADE DA BEIRA INTERIOR
Engenharias

Gas Turbine Engines Ground Vortex Flows

Pedro Alexandre Rodrigues Manquinho

Tese para obtenção do Grau de Doutor em

Engenharia Aeronáutica

(3º ciclo de estudos)

Orientador: Prof. Doutor Jorge M. M. Barata

Covilhã, Abril de 2017

Dedicatory

This thesis is dedicated to my family, with particular attention to my mother who took me the first time to see a Public University when I was four or five years old, to my father who instilled in me a love for aviation, and to my lady who puts up with me for many years.

Acknowledgment

I would like to thank all who contributed to this work but I will thank all those who contributed to my academic growth, the Department of Aerospace Sciences, to all my teachers but of which I must mention two in particular, Professor Jorge M. M. Barata my supervisor and the person I have in great esteem as a human being and academic and Prof. André R. R. Silva who I watched growing as an academic and to the Aeronautics and Astronautics Research Center of the Associated Laboratory in Energy, Transports and Aeronautics (AeroG of LAETA) for making possible this work.

Resumo

Quando um motor de turbina de gás está operando perto do solo a baixas velocidades de aeronave, potências elevadas e exposto a um escoamento cruzado a formação de um “inlet ground vortex” pode surgir. Esta estrutura cria perdas significativas de pressões e distorções do escoamento e é admitida pelo motor. Como consequência, a eficiência do compressor e a força de propulsão são afetadas severamente e também pode ocorrer o fenómeno de “*surge*” do compressor. Os “inlet ground vortexes” são a causa de grandes danos causados por objetos estranhos (FOD) devido à ingestão de rochas, areia e outros detritos. A ingestão de objetos estranhos pode causar danos notáveis aos componentes do motor, bem como degradação do desempenho geral. No presente trabalho, os escoamentos para um motor de turbina de gás à escala real foram simulados para uma gama de distâncias ao solo, diâmetros de motor e razões de velocidade de admissão sob condições de vento cruzado. O objetivo deste estudo é compreender melhor os mecanismos do “inlet ground vortex” e fornecer novas informações para promover técnicas de prevenção desses vórtices. Este trabalho mostrou grandes regiões de baixa pressão em frente da admissão do motor para diferentes combinações de velocidade de admissão do motor / distância ao solo, que se estendem até ao chão especialmente onde o vórtice coalesce. Existem duas áreas sem vórtice em função de h/Di e U_i/U_∞. A primeira é a fronteira antecipada (“treshold”) entre as regiões vórtice / não vórtice, mas uma segunda foi detetada para valores elevados de U_i/U_∞ (U_i/U_∞> 50) que não foram mencionados em trabalhos anteriores. O mecanismo do “inlet ground vortex” é muito complexo e deve ser investigado mais a fundo e os trabalhos experimentais são desejáveis.

Palavras-chave

Vórtice de solo, Escoamento Cruzado.

Abstract

When an aero-engine is operating near the ground at low aircraft speeds, high thrust and exposed to a crosswind the formation of a potent inlet ground vortex can arise. This structure create significant pressures losses and flow distortions and is swallowed by the engine. As a consequence, fan efficiency and thrust are severely affected and compressor surge may also occur. Inlet ground vortices are the cause of major foreign object damage (FOD) due to the ingestion of rocks, sand and other debris. The ingestion of foreign objects can cause notable damage to engine components as well as overall performance degradation. In the present work the flow fields for a full-scale aero-engine have been simulated for a range of ground clearances, engine diameters and intake velocity ratios under crosswind conditions. The aim of this study is to better understand the ground vortex inlet mechanisms supplying new information to foster vortex avoidance techniques. This work has shown large low pressure regions in front of the engine face for different engine-velocity/ratio-clearance distance combinations that extend to the ground especially where the vortex coalesces. There are two areas of no vortex as a function of h/Di andU_i/U_∞ . The first is the anticipated frontier (threshold) between the regions vortex/no vortex, but a second one was detected for high values of U_i/U_∞ (U_i/U_∞ >50.00) that had not been mentioned in previous works. The inlet ground vortex mechanism is a very complex one which should be further investigated, and experimental works are desirable.

Keywords

Inlet Ground Vortex, Cross-Wind.

Index

DEDICATORY .... **III**

ACKNOWLEDGMENT .... **V**

RESUMO .... **VII**

PALAVRAS-CHAVE .... **IX**

ABSTRACT .... **XI**

KEYWORDS .... **XIII**

INDEX .... **XV**

LIST OF FIGURES .... **XIX**

LIST OF TABLES .... **XXVII**

NOMENCLATURE .... **XXIX**

CHAPTER 1 BACKGROUND AND MOTIVATION **1**

1.1 INTRODUCTION 1
1.2 CURRENT KNOWLEDGE 5
1.3 OBJECTIVES 7

CHAPTER 2 LITERATURE SURVEY **9**

2.1 INTRODUCTION 9
2.2 VORTICES BASICS 9
2.3 CORE VORTEX CHARACTERISTICS 11
2.4 CRITERIA FOR THE INLET VORTEX FORMATION 12
2.5 MECHANISMS OF GROUND VORTEX FORMATION 18
2.6 HEADWIND 19
2.6.1 No-wind 24
2.6.2 Crosswind 28
2.6.3 Crosswind with ambient vorticity 33
2.6.4 Tailwind and Reverse Thrust 33
2.7 VORTEX PREVENTION METHODS 37
2.8 GROUND BOUNDARY LAYER INDEPENDENCE 39
2.9 TRANSIENT EFFECTS 40

CHAPTER 3 MATHEMATICAL METHOD **41**

3.1 INTRODUCTION 41

3.2 GOVERNING DIFFERENTIAL EQUATIONS 41
3.3 FINITE-DIFFERENCE EQUATIONS 42
3.4 SOLUTION PROCEDURE 45
3.5 BOUNDARY CONDITIONS 45
3.6 GRID INDEPENDENCE 47
3.7 CONVERGENCE 47
3.8 SUMMARY 48

CHAPTER 4 RESULTS 51

4.1 INTRODUCTION 51
4.1.1 Test Cases 51
4.1.2 Graphical examples 51
4.2 TYPICAL FLOW PATTERNS 54
4.2.1 No Vortex 54
4.2.2 One Vortex 57
4.2.3 Two Vortices 59
4.2.4 Three Vortices 60
4.2.5 Four Vortices 62
4.3 SUMMARY 63

CHAPTER 5 DISCUSSION 65

5.1 INTRODUCTION 65
5.2 GROUND PRESSURE DISTRIBUTION 65
5.3 INLET GROUND VORTEX REGIMES 67

CHAPTER 6 CONCLUSIONS 73

REFERENCES 75

ANNEX A COMPLETE SET OF RESULTS 79

A.1. NO VORTEX 81

A.2. ONE VORTEX 103

A.3. TWO VORTICES 117

A.4. THREE VORTICES 125

A.5. FOUR VORTICES 137

ANNEX B PAPERS RESULTING FROM THE PRESENT WORK 139

List of Figures

Figure 1: Suction of debris and ground vortex visualization. 3

Figure 2: Effect of foreign objects damage (FOD) through ingestion. 4

Figure 3: Ground vortex on a military turbofan engine visible due to water condensation inside core 5

Figure 4: Velocity ratio against non-dimensional height of the intake, revealing a region of vortex formation. 6

Figure 5: Vortex line and vortex tube illustrations 10

Figure 6: Consequences of vortex stretching [21] 11

Figure 7: Idealization of the tangential velocity inside a tip vortex [22]. 11

Figure 8: Inlet vortex flow model [24] 12

Figure 9: Inlet capture surface above the ground [2]. 14

Figure 10: Correlation of velocity ratio and non-dimensional height combinations revealing a region of vortex formation and no-vortex formation. 15

Figure 11: Data showing the boundary between the vortex forming and non-vortex forming flow regimes. Where Vi/Vo = Ui/U∞ [29]. 16

Figure 12: Streamlines associated with twin inlets at 90° of yaw in an irrotational upstream flow [7] 18

Figure 13: Velocity profiles used in de Siervi et al. experiments [7]. 20

Figure 14: Deformation of the ambient vortex lines as they approach the intake for different upstream velocity gradients. 21

Figure 15: Spin of the inlet vortices for a) low, b) medium and c) high velocity ratios [21]... 23

Figure 16: Vortex filaments in head-wind. Modes at (a) high and (b) low speed velocity ratio [6]. 23

Figure 17: Reason explaining the sense of rotation of the counter rotating vortices at low velocity ratio [21] 24

Figure 18: Reason explaining the sense of rotation of the counter rotating vortices at high velocity ratio [21] 24

Figure 19: Vortex formation under no-wind conditions. 25

Figure 20: Flow modes observed under headwind conditions [6]. 26

Figure 21: Flow topology observed by Bissenger and Braun [31] under headwind conditions for (a) two trailing vortices (b) a complex vortex system involving a single ground and trailing vortex, plus vortices on the ground. 27

Figure 22: Formation of the intake vortex system for a twin inlet configuration [31] 28

Figure 23: Sense of rotation of the inlet vortex and the trailing vortex [7] 29

Figure 24: Flow field topology under crosswind conditions (a) two contra-rotating vortices and (b) a single trailing vortex, ground vortex system. 29

Figure 25: Separation line around the inlet seen from the top view [7]. 30

Figure 26: Side view display the flow field under crosswind settings with and without the sucked stream tube interacting with the ground [7]. 31

Figure 27: Flow for a twin inlet configuration (S denotes the symmetry plane, A is the intake-to-intake ground vortex and B the two trailing vortices) [7] 31

Figure 28: CFD simulations of the crosswind flow field topology for a non-dimensional height of 0.25 (h/Dl) and Mi = 0.58 at two different velocity ratios [34]. 33

Figure 29: Vortex formation in cross-wind with an upstream vertical vorticity [7]. 34

Figure 30: Reverse thrust operation introducing an effective tailwind to the intake 35

Figure 31: Ground vortex ingestion under reverse thrust operation. 35

Figure 32: Effect of wind direction and strength on the vortex location on the ground and its consequent ingestion location [5]. 35

Figure 33: Reverser targeting pattern configurations investigated [5]. 36

Figure 34: Blow-away jet system for inlet-vortex avoidance [12]. 37

Figure 35: System for inlet vortex attachment [14]. 37

Figure 36: Sprayer jet system. 38

Figure 37: Schematic of two different concepts that have been invented for ground vortex prevention 39

Figure 38: Vortex dissipater and gravel kit engine bleed air down and aft from 3 nozzles at the tip to break up the vortices in a Boeing 737-200.. 39

Figure 39: Effect of approaching boundary layer thickness on (a) the vortex strength and (b) fan face distortion, DC60 [39]. 40

Figure 40: Nodal configuration for the west face of a control volume [44]. 44

Figure 41: Nodal configuration for a control volume [44]. 44

Figure 42: a) Domain of the solution b) Representation of the intake with centered referential [48] 45

Figure 43: The near-wall nodes... 46

Figure 44: Dimensionless Vertical profile, at X/D=0.53, of the horizontal velocity component, W, at a Z=0.1 [49]. 47

Figure 45: Example of graphics used for monitoring the convergence............................ 48

Figure 46: Graphic with max number of vortices present for a value of r=0.9 m. 52

Figure 47: 3D Graphic of streamlines for set of values. 53

Figure 48: 3D graphic of iso-surfaces of pressure distribution...................................... 53

Figure 49: Graphic of pressure distribution in a plane parallel to the ground.................... 54

Figure 50: Graphic of velocity vectors in blue and streamlines in black parallel to the ground. 54

Figure 51: Graphic of velocity vectors in blue and streamlines in black parallel to the inlet plane 54

Figure 52: For $h/Di = 1.56$ and $Ui/U\infty = 9.09$: a) 3D stream traces; b) 3D pressure distribution; c) pressure distribution in the ground plane; d) plane X=0.95XTOT (ground plane); e) plane X=0.75XTOT; f) plane X=0.50XTOT; g) plane X=0.25XTOT; h) plane .X=0.05XTOT; i) plane Y=0.05YTOT; j) plane Y=0.50YTOT; k) planeY=0.95YTOT. 55

Figure 53: For $h/Di = 1.00$ and $Ui/U\infty = 36.36$: a) 3D stream traces; b) 3D pressure 58

Figure 54: For $h/Di = 0.82$ and $Ui/U\infty = 18.18$: a) 3D stream traces; b) 3D pressure 59

Figure 55: For $h/Di = 0.77$ and $Ui/U\infty = 72.73$: a) 3D stream traces; b) 3D pressure distribution; c) pressure distribution in the ground plane; d) plane Y=0.05YTOT; e) plane Y=0.50YTOT; f) plane Y=0.95YTOT. 61

Figure 56: For $h/Di = 0.86$ and $Ui/U\infty = 18.18$: a) 3D stream traces; b) 3D pressure distribution; c) pressure distribution in the ground plane; d) plane Y=0.50YTOT; e) plane Y=0.95YTOT... 62

Figure 57: For $h/Di = 1.17$ and $Ui/U\infty = 27.27$: a) 3D stream traces; b) 3D pressure distribution; c) pressure distribution in the ground plane; d) plane X=0.50XTOT; e) plane X=0.25XTOT; f) plane Y=0.05YTOT; g) plane Y=0.50YTOT; h) plane Y=0.95YTOT. 65

Figure 58: Number of vortex structures for r=1.5 m 68

Figure 59: Number of vortex structures for r=1.4 m 68

Figure 60: Number of vortex structures for r=1.3 m 69

Figure 61: Number of vortex structures for r=1.2 m 69

Figure 62: Number of vortex structures for r=1.1 m 69

Figure 63: Number of vortex structures for r=1.0 m 70

Figure 64: number of vortices present for a value of r=0.9 m...................................... 70

Figure 65: Number of vortex structures for r=0.8 m 70

Figure 66: Number of vortex structures for r=0.75 m 71

Figure 67: For $h/Di = 1.56$ and $Ui/U\infty = 9.09$: a) 3D stream traces; b) 3D pressure distribution; c) pressure distribution in the ground plane; d) plane X=0.95XTOT (ground plane); e) plane

X=0.75XTOT; f) plane X=0.50XTOT; g) plane X=0.25XTOT; h) plane .X=0.05XTOT; i) plane Y=0.05YTOT; j) plane Y=0.50YTOT; k) planeY=0.95YTOT. 82

Figure 68: For h/Di =1.44 and $Ui/U\infty$=9.09: a) 3D stream traces; b) 3D pressure distribution; c) pressure distribution in the ground plane; 83

Figure 69: For h/Di =1.06 and $Ui/U\infty$=9.09: a) 3D stream traces; b) 3D pressure distribution; c) pressure distribution in the ground plane; 84

Figure 70: For h/Di =1.62 and $Ui/U\infty$=9.09: a) 3D stream traces; b) 3D pressure distribution; c) pressure distribution in the ground plane; 85

Figure 71: For h/D_i=1.19 and $Ui/U\infty$=9.09: a) 3D stream traces; b) 3D pressure distribution; c) pressure distribution in the ground plane; 86

Figure 72: For h/Di =1.87 and $Ui/U\infty$=72.73: a) 3D stream traces; b) 3D pressure distribution; c) pressure distribution in the ground plane; d) plane X=0.95XTOT (ground plane); e) plane X=0.75XTOT; f) plane X=0.50XTOT; g) plane X=0.25XTOT; h) plane X=0.05XTOT; i) plane Y=0.05YTOT; j) plane Y=0.50YTOT; k) plane Y=0.95YTOT 88

Figure 73: For h/Di=1.53 and $Ui/U\infty$=72.73: a) 3D stream traces; b) 3D pressure 90

Figure 74: For h/Di=1.33 and $Ui/U\infty$=72.73: a) 3D stream traces; b) 3D pressure distribution; c) pressure distribution in the ground plane; d) plane X=0.70XTOT (ground plane); e) plane X=0.50XTOT; f) plane X=0.25XTOT; g) plane X=0.05XTOT; h) plane Y=0.05YTOT; i) plane Y=0.50YTOT; j) plane Y=0.95YTOT 92

Figure 75: For h/Di=0.63 and $Ui/U\infty$=72.73: a) 3D stream traces; b) 3D pressure 94

Figure 76: For h/Di =0.63 and $Ui/U\infty$=54.55: a) 3D stream traces; b) 3D pressure 96

Figure 77: For h/Di =0.63 and $Ui/U\infty$=36.36: a) 3D stream traces; b) 3D pressure 98

Figure 78: For h/Di =0.63 and $Ui/U\infty$=18.18: a) 3D stream traces; b) 3D pressure 100

Figure 79: For h/Di =0.63 and $Ui/U\infty$=9.09: a) 3D stream traces; b) 3D pressure...............102

Figure 80: For $h/Dih/D_i$ =1.00 and $Ui/U\infty$=63.64: a) 3D stream traces; b) 3D pressure 104

Figure 81: For h/Di=0.93 and $Ui/U\infty$=63.64: a) 3D stream traces; b) 3D pressure.............106

Figure 82: For h/D_i=0.82 and U_i/U_∞=63.64: a) 3D stream traces; b) 3D pressure 107

Figure 83: For h/D_i =0.75 and U_i/U_∞=63.64: a) 3D stream traces; b) 3D pressure 108

Figure 84: For h/D_i =0.68 and U_i/U_∞=63.64: a) 3D stream traces; b) 3D pressure 110

Figure 85: For h/D_i=1.00 and U_i/U_∞=72.73: a) 3D stream traces; b) 3D pressure 111

Figure 86: For h/D_i=1.00 and U_i/U_∞=36.36: a) 3D stream traces; b) 3D pressure 112

Figure 87: For h/D_i=1.00 and U_i/U_∞=9.09: a) 3D stream traces; b) 3D pressure 113

Figure 88: For h/D_i =1.87 and U_i/U_∞=45.45: a) 3D stream traces; b) 3D pressure 114

Figure 89: For h/D_i =1.60 and U_i/U_∞=45.45: a) 3D stream traces; b) 3D pressure 115

Figure 90: For h/D_i =1.33 and =45.45: a) 3D stream traces; b) 3D pressure 116

Figure 91: For h/D_i=1.4 and U_i/U_∞=45.45: a) 3D stream traces; b) 3D pressure 117

Figure 92: For h/D_i=1.17 and U_i/U_∞=18.18: a) 3D stream traces; b) 3D pressure 118

Figure 93: For h/D_i=0.93 and U_i/U_∞ =18.18: a) 3D stream traces; b) 3D pressure 119

Figure 94: For h/D_i =0.82 and U_i/U_∞ =18.18: a) 3D stream traces; b) 3D pressure 120

Figure 95: For h/D_i=0.75 and U_i/U_∞ =18.18: a) 3D stream traces; b) 3D pressure 121

Figure 96: For h/D_i =0.68 and U_i/U_∞ =18.18: a) 3D stream traces; b) 3D pressure 122

Figure 97: For h/D_i =1.08 and U_i/U_∞ =18.18: a) 3D stream traces; b) 3D pressure 123

Figure 98: For h/D_i=0.86 and U_i/U_∞=27.27: a) 3D stream traces; b) 3D pressure 126

Figure 99: For h/D_i=1.00 and U_i/U_∞=27.27: a) 3D stream traces; b) 3D pressure 127

Figure 100: For h/D_i =1.25 and U_i/U_∞=27.27: a) 3D stream traces; b) 3D pressure 128

Figure 101: For h/D_i =0.77 and U_i/U_∞=72.73: a) 3D stream traces; b) 3D pressure 131

Figure 102: For h/D_i=0.93 and U_i/U_∞=45.45: a) 3D stream traces; b) 3D pressure 132

Figure 103: For h/D_i =0.77 and U_i/U_∞=27.27: a) 3D stream traces; b) 3D pressure 133

Figure 104: For h/D_i =1.00 and U_i/U_∞=54.55: a) 3D stream traces; b) 3D pressure 134

Figure 105: For h/D_i=0.77 and U_i/U_∞=9.09: a) 3D stream traces; b) 3D pressure 135

Figure 106: For h/D_i=0.86 and U_i/U_∞=18.18: a) 3D stream traces; b) 3D pressure distribution; c) pressure distribution in the ground plane; d) plane Y=0.50YTOT; e) plane Y=0.95YTOT...137

Figure 107: For h/D_i=0.79 and U_i/U_∞=72.73: a) 3D stream traces; b) 3D pressure............138

List of Tables

Table 1: Turbulence model constants. 42

Table 2: Values tested. 51

Nomenclature

A_i = intake area

A_∞ = frequency of oscillation of the ground vortex

D_i = inner diameter of the intake

h = height of the engine axis above the ground

$\boldsymbol{k}$ = turbulent kinetic energy

L_q = intake stream tube length

$\dot{m}$ = mass flow

U_i = intake throat velocity

U_∞ = free stream velocity

V_∞ = tangential velocity

Γ = circulation

ζ = vorticity

ρ = density

μ = dynamic viscosity

ν = kinematic viscosity

ν_T = turbulent kinematic viscosity

ϕ = any dependent variable

Chapter 1 Background and motivation

1.1 Introduction

What is a vortex?

In fluid dynamics, a vortex is a region in a fluid in which the flow is rotating around an axis line. Vortices form in stirred fluids, and may be observed in almost all nature, having in account that chaos is the nature estate.

Vortices are a major component of turbulent flow. The distributions of velocity, vorticity, as well as the circulation are used to characterize vortices. In most vortices, the fluid flow velocity is greatest next to its axis and decreases in proportion to the distance from the axis.

In the absence of external forces, viscous friction within the fluid tends to organize the flow into a collection of irrotational vortices, possibly superimposed to larger-scale flows, including larger-scale vortices.

Once formed, *vortices* can move, stretch, twist, and interact in complex ways. A moving vortex carries with it some angular and linear momentum, energy, and mass.

Nowadays, civil airplanes engines are made to be silent and more effective. As a consequence of this ongoing evolution in turbofan configurations, intake diameters are larger than ever before to get a higher by-pass ratio.

The inlet is designed to give the appropriate amount of airflow required from the free-stream conditions to the conditions required at the entrance of the compressor with minimal pressure loss by the engine [1].

When the pressure losses and the flow distortions are very low, the performance of the engine is optimal, and that is the reason why the airflow has to be as uniform as possible when entering into the compressor. This airflow condition is necessary in all flight configurations including when the aircraft is maneuvering on ground tasks. The intake performance depends on the mass-flow delivered to the compressor. The internal mass-flow stays constant from the captured stream tube to the compressor face and assuming that the flow is incompressible due to low velocities, it will be given by $A_i U_i = A_\infty U_\infty$. Since the mass-flow is constant and the area ratio is related to the stream tube contraction ratio, the area ratio can be expressed as $\frac{A_\infty}{A_i} = \left(\frac{L_q}{D_i}\right)^2$. The capture ratio A_∞ / A_i is controlled by the engine, the engine mass-flow, the inlet diameter and the free-stream velocity.

In cross-wind configuration, the shape of the stream tube is modified near the lip. The cross-flow leads to an increase in the flow velocity near the lip depending on the strength of the cross-flow, high velocity origins in flow separation leading to a total pressure loss at the engine fan.

The formation of ground vortices depends on engine power, wind velocity and engine inlet height and size. Previous published work show that the phenomenon can only occur with the presence of a stagnation streamline between the ground and the intake which is dependent on the velocity ratio U_i / U_∞ and the non-dimensional height of the engine axis above the ground, h/D_i.

In static conditions, the inlet airflow demand increases, and the inlet capture surface increases in diameter and starts including the ground to bring the necessary airflow to the fan [2] [3]. Typically, the formation of ground vortices is characterized by low h/D_i and high U_i / U_∞ that corresponds to an engine operating close to the ground at a high inlet mass flow [4].

Four different types of conditions leading to the formation of inlet ground vortices have been identified.

A vortex can be generated without ambient wind and with a low ratio h/D_i <1. Due to the ground proximity, high levels of suction beneath the engine inlet leads into a strong flow underneath the inlet upstream towards the intake lip [5]. In these conditions, it is possible to visualize at the engine intake and at the ground two upward spiraling vortices. Under no-wind condition, it appears that the two vortices are counter-rotating, and the vorticity is induced by the boundary layer. Is a head-wind flow, when the air is sucked into the engine inlet, the flow field underneath the intake starts to roll up into two upright counter-rotating vortices and a fast flow into the opposite direction of the wind appears between them [6] [7]. For high velocity ratios (>20) the sense of rotation of the two vortices switches to the same as in the no-wind mechanism. With a 90° cross-wind two different kinds of vortices appear around the intake: an inlet vortex and a trailing vortex.

The ground vortex or inlet vortex can cause several operational problems. The engine surge may occur, severe inlet distortion that can cause vibrations in the fan and its blades damage, and also the ingestion of debris into the turbofan causing damage to it. Dust enters into the engine compressors eroding blades, degrading turbine cooling performance and so reducing the live span of the engine [8]. For conventional wing mounted engines, in particular, this increase has major consequences (Figure 1).

The ingested vortex is often invisible. However, in humid conditions, due to the high velocities within the vortex core, the local flow temperature can decrease below the dew point, promoting condensation of the humidity and the associated flow field is visualized.

Figure 1: Suction of debris and ground vortex visualization.

Understanding the formation of the ground vortex phenomenon is of utmost importance in the operational and economical points of view but its complex features of the flow are major obstacles to achieving it. Indeed, the ground vortex has a tree dimensional flow filed and has an unsteady nature. [8]

This ground vortex can be a major problem. With the advent of large passenger jets in the 1950s ground vortices were quickly identified as a problem because of its ability to ingest large objects into the engine [9] [10]. Low pressure in the vortex core can impart an impulsive force onto objects that are present on solid surfaces. Subsequently objects and also particles and dust (referred to as foreign objects) are lifted off the surface, entrained into the inlet flow field and carried into the engine by the induced velocity field of the intake. The ingested particles and debris can damage fan blades, erode compressor blades and seals and degrade turbine cooling performance [2].

The technological advancements of recent decades have made air travel more accessible than ever before. The consequent rising number of air travelers, coupled with increasing fuel prices, is now leading airlines to demand more fuel-efficient, low-maintenance jet engines. Engine manufacturers have responded with high-bypass turbofan engines characterized by larger-than-ever nacelle diameters for improved performance. However, this effective solution increases the risk of Foreign Object Damage (FOD) (Figure 2).

The likelihood of FOD is largely increased when a vortex is present. An inlet vortex has enough suction power to pick up objects such as sand, dirt and rocks when an aircraft is operating near the ground and especially over poorly-maintained tarmac or on dirt airstrips. If these are ingested by the engine, compressor blade erosion can occur, deteriorating engine performance and reducing service life.

Figure 2: Effect of foreign objects damage (FOD) through ingestion.

Additionally to FOD, the ground vortex can also provoke a severe distortion of the intake flow field [5]. Fan vibration is another hazard that has recently been identified as an additional major consequence of ground vortex ingestion [11].

This distorted flow field has a major impact on the aircraft performance, such as a reduction on the stall and surge margins and therefore compromising the safety of the aircraft. The non-uniform flow introduces momentum loss and large velocity gradients, which can significantly alter the local flow angle seen by the fan blade. As a consequence, local flow separation can occur which leads to large resonant forces potentially resulting in high cycle fatigue.

A jet engine operating near the ground in static or near static conditions, at high thrust, and subject to a crosswind, can experience a flow separation region on the windward inlet lip and the formation of a ground-to-inlet vortex, known as the inlet vortex. The operating conditions that cause these phenomena often coincide with engine power-up at the start of the take-off run. The inlet ground vortex, shown in Figure 3, has been investigated for over six decades, but the mechanisms by which it initiates and is sustained are still not very well understood, and acceptable inhibition techniques have yet to be established.

The impact of the inlet vortex and lip separation on engine performance is significant. Both create stagnation pressure losses resulting in reduced inlet recovery and flow distortions at the fan face. These distortions are associated with momentum loss and large velocity gradients as the non-uniform flow reaches the fan face. They can alter the local flow angle seen by the fan blades, decreasing fan efficiency and thrust, reducing compressor stall margins and consequently increasing the likelihood of compressor surge. Due to local flow separations on blade surfaces, inlet vortices and lip separation have been shown to induce fan vibration, generating large resonant forces leading to high cycle fatigue.

Figure 3: Ground vortex on a military turbofan engine visible due to water condensation inside core

1.2 Current Knowledge

It was previously identified that the key to the existence of inlet ground vortexes is the formation of a stagnation point on the ground ahead of the intake highlight plane [10].

In order for the abovementioned to exist, the capture stream tube must interact with the ground surface. This has been recognized to fundamentally depend on two key non-dimensional parameters.

The first of which is the non-dimensional height of the intake, h/D_i, typically defined in the literature using the centerline height of the intake, h, and the intake inner diameter, D_i.

The second dimensionless parameter is the velocity ratio, U_i / U_∞ , which characterizes the contraction ratio of the sucked stream tube and is a measure of the size of the stream tube upstream of the intake. This is derived from continuity considerations and is defined as being the intake velocity, U_i , divided by the free-stream velocity, U_∞ . In order for the stream tube of the intake to interact with the ground plane the height-to-diameter ratio, h/D_i, must be small and the contraction ratio, U_i / U_∞ , must be large.

Current design rules for the dodging of inlet ground vortex formation relies on the vortex/no-vortex map in which a number of previous researchers have correlated combinations of h/D_i and U_i / U_∞ for the threshold for its formation (Figure 4).

At present this represents the most advanced designs rules for engine installations and operations. However, this graphic gives no indication of what happens to the quantitative vortex characteristics as the engine operates in different regions of the vortex formation zone.

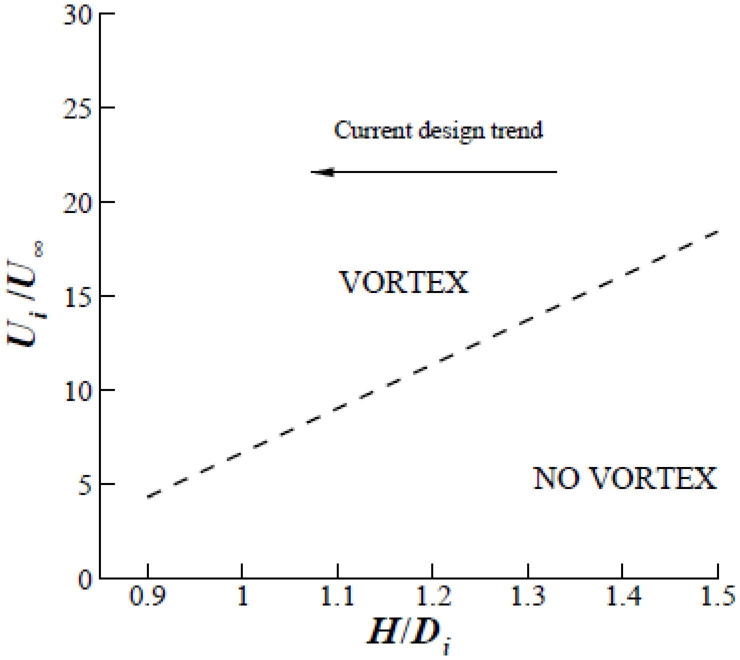

Figure 4: Velocity ratio against non-dimensional height of the intake, revealing a region of vortex formation.

In terms of alleviating the phenomenon a number of methods, past and present, have been attempted with a number of patents being documented [12] [13] [14] [13] [15] [16].

The majority of these actions concentrated in the elimination of the stagnation point on the ground plane which is documented as being an essential part to the formation of ground vortices.

Most measures use a jet of air, extracted from the compressor, impinging on the region of vortex creation on ground, in order to eliminate the FOD.

A prevention system of this form was even put into practice in the late 1950's, and early 1960's on the DC- 8 [2] [12]. However, after studying the unscheduled removal of engines due to FOD, the device was found to actually cause more problems by disturbing just as much debris as the vortex itself [2].

Despite a number of flow control methods being developed, the general consensus is that ground vortex formation is unavoidable.

With the current design trend of turbofans, intakes are operating further to the left in Figure 4 in which the formation envelope is considerably larger. As a consequence, ground vortex formation will occur over a wider range of operating conditions and will potentially be sustained for longer periods during the take-off phase. This significantly increases the number of vortex ingestion events that will occur over the lifespan of the engine. With limited quantitative information available particularly at different height-to-diameter ratios, it has become vitally important to further understand the severity of the ground vortex in different regions of the vortex zone of Figure 4.

1.3 Objectives

Barata et al. [17] [18] report Navier-Stokes calculations and predicted successfully the ground vortex phenomena using real operational conditions for the case of the engine Trent 9 and GE nx-1B64. The ground vortex formation in irrotational crosswind flow is analyzed in detail for this configuration, and the formation of the trailing vortex was associated to a very complex flow. Barata et al [19] extended the investigation to different values of inlet diameter, height of the engine axis above the ground and inlet velocity. The present work aims at providing quantitative information on the ground vortex formation and development over a wider range of operating conditions, and to identify all the regimes of inlet ground vortex formation as function of the velocity ratio U_i/U_∞ and height-to-diameter ratio h/d_i.

The specific objectives of this thesis are the following:

1. To improve the understanding of gas turbine engines inlet ground vortex formation;
2. To study the inlet ground vortex formation as a function of the characteristic non-dimensional parameters U_i/U_∞ and h/d_i and identify all the possible regimes;
3. To improve the understanding of gas turbine engines ground vortex behavior.

Chapter 2 Literature Survey

2.1 Introduction

A concise review of the published work on the inlet ground vortex formation is presented in this chapter.

The first part of this chapter discusses the criteria for inlet vortex formation based on the previous research. This is then followed by a discussion of the formation mechanisms that have been established to date, as well as the generation of inlet ground vortices under reverse thrust operation.

The review also includes CFD studies that have been published in the literature. The chapter concludes by discussing the methods for removing or reducing the impact of the inlet ground vortex.

Section 2.2 introduces the inlet ground vortex basics. Section 2.3 describes the core vortex characteristics. Then section 2.4 presents the requirements for vortex formation, and section 2.5 the mechanisms of the inlet of ground vortex formation. Section 2.6 highlights major inlet ground vortex prevention methods tried so far, and section 2.7 outlines the ground boundary layer independence. Finally, section 2.8 briefly addresses the formation transience.

2.2 Vortices basics

A vortex is a zone of focused vorticity. It is also defined by the motion of the fluid spinning speedily around a core. The speed and rate of revolution of the fluid are highest at the center, and decline gradually with distance from the core. The vorticity ζ is given by:

$$\varsigma = \nabla \times \vec{u} \tag{1}$$

And can be related to the angular velocity, ω, through the following relation:

$$\varsigma = 2 \times \omega \tag{2}$$

The rotation vector is constituted of three components ω_x, ω_y and ω_z which characterize correspondingly the rotation about the X axis, the Y axis and the Z axis:

$$\omega = \omega_x \hat{\imath} + \omega_y \hat{\jmath} + \omega_z \hat{k} \tag{3}$$

Using the average of angular velocities, the equation (1) for the vorticity ζ becomes:

$$\varsigma = 2 \times \omega = 2 \times \left\{ \left(\frac{\partial \omega}{\partial y} - \frac{\partial v}{\partial z} \right) \hat{\imath} + \left(\frac{\partial u}{\partial z} - \frac{\partial w}{\partial x} \right) \hat{\jmath} + \left(\frac{\partial v}{\partial x} - \frac{\partial u}{\partial y} \right) \hat{k} \right\} \tag{4}$$

The circulation Γ is the line integral around a closed curve C [20] and by using Stokes's law, the vorticity and the circulation are related with the relation:

$$\Gamma = \oint_C u.dl = \int_S \varsigma.nds \tag{5}$$

For a curved surface S, the circulation is the integral of the component of vorticity normal to the surface. In the presence of vorticity and circulation, the flow is considered as rotational.

The exact laws of motion that vortices follow were designated by Helmholtz. Figure 7 shows a vortex line of filament which is universally tangent to the vorticity vector. A group of vortex lines is often called a vortex tube.

The first part of the Helmholtz vortex law states that:

The vortex line represents a line which is tangent everywhere to the local vorticity vector. On each point of this line $\omega \times \vec{n} = 0$ that comes from the divergence theorem which specifies that the vorticity is divergence free [20].

The vortex tube is defined as a set of vortex lines passing through a surface in space [20].Because the two extremity surfaces S1 and S2 close the vortex tube and because the relation $\omega \times \vec{n} = 0$ must be satisfied along each vortex line, the circulation at the two end surfaces S1 and S2 are equal. So, the circulation along a vortex tube is constant,

$$\Gamma_1 = \Gamma_2. \tag{6}$$

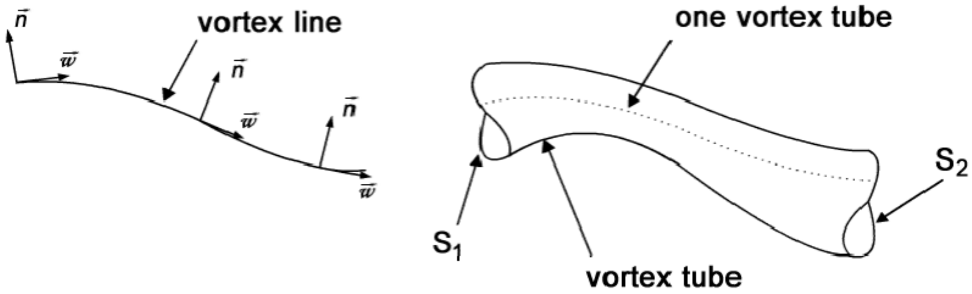

Figure 5: Vortex line and vortex tube illustrations

The second Helmholtz vortex law was confirmed by the Kelvin's theorem that states that the circulation of vortex lines is time independent. Hence:

$$\frac{D\Gamma}{Dt} = 0 \tag{7}$$

Vortex lines are compressed if they move through a cylindrical duct with a reducing area and they are stretched along their axis (Figure 6). Stretching the vortex results in diminishing the radius and therefore increasing the rotational speed to retain the kinetic momentum constant. Moreover, from the relation $\Gamma = \zeta \times S$ and because the circulation is constant, it has the consequence of reducing S and thereby increasing the vorticity.

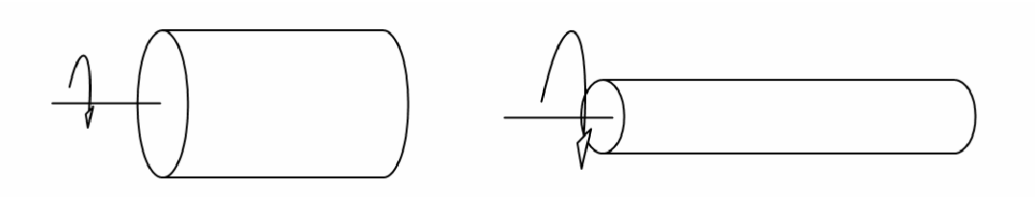

a) Solid body rotating at speed Ω_1 **b) After stretching $\Omega_2 > \Omega1$,**

Figure 6: Consequences of vortex stretching [21]

2.3 Core vortex characteristics

The size, defined by the radius r and the tangential velocity V_θ are two parameters that can be used to define a vortex. Figure 7 shows that V_θ varies along the vortex radius $r \times V_\theta$ equals to zero and r_c can be considered as the frontier between the pure rotational flow field which is named the inside part of the vortex and the external flow [22].

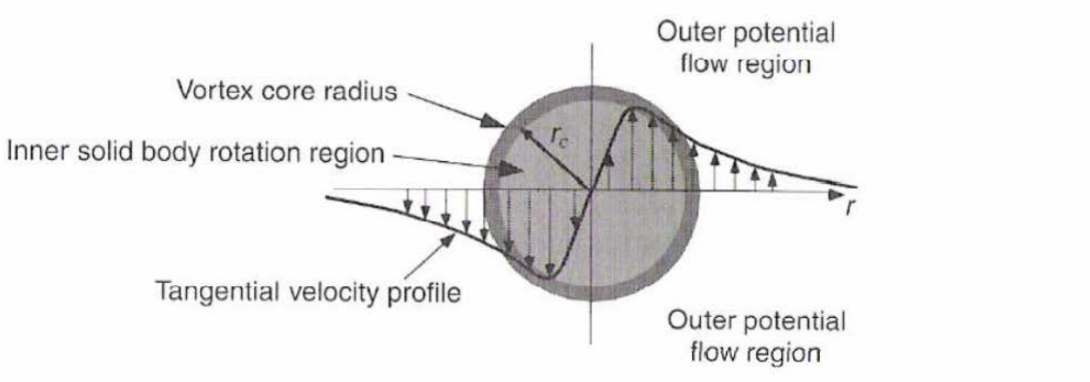

Figure 7: Idealization of the tangential velocity inside a tip vortex [22].

It should be noted that the swirl angle is also a pertinent feature of the flow that increases with the total pressure distortion [23].

The models used to describe some typical vortexes are the Burges vortex, the Lamb-Oseen vortex, the Rankine vortex or the Vatistas vortex (e.g. [24]).

2.4 Criteria for the Inlet Vortex Formation

The creation of inlet ground vortices is contingent on engine power, wind velocity and engine inlet height and size. Prior available works about inlet ground vortices determine that the phenomenon can only happen with the occurrence of a stagnation streamline between the ground and the intake which depends is at the mercy of on the velocity ratio U_i / U_∞ and the non-dimensional height h/D_i. This stagnation streamline characterizes the vortex line where $\omega \times \vec{n} = 0$ on each point.

The first author to propose the minimum requirements for an inlet vortex to exist was Klein [12], stating that a stagnation point must exist on the ground (or other fixed structure), where an omnidirectional airflow parallel to the surface converges in a manner similar to a sink.

So, there must be an updraft from the stagnation point to the inlet, and ambient vorticity must be present in the flow.

Figure 8 illustrates the model explained by Klein [12]. It shows that the flow coming from multiple directions convergences and forms a stagnation point on the ground. The inlet suction induces an updraft, which pulls this slower air around the stagnation point upwards, forming the vortex core. Klein [12] proposed that ambient vorticity was the principal source of vorticity in the vortex core flow, and without it the inlet vortex would not form.

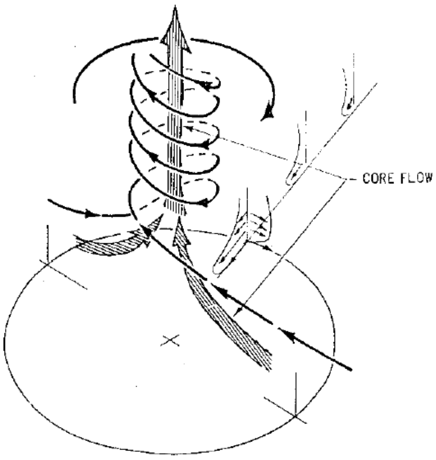

Figure 8: Inlet vortex flow model [24]

In the first available works on ground vortex formation, characteristics, and behavior, it was swiftly identified that an essential prerequisite for the inlet vortex formation is the presence of a stagnation point on the ground plane [10]. This performs as a pivotal point for the vorticity upstream to be focused and stretched into the intake. A requirement for this stagnation point to happen is that the sucked stream tube has sufficient contact with the ground surface. The capture stream tube himself is defined as being a stream tube of air which splits the airstream into an inner flow and an outer flow (Figure 9).

All flow inside the capture stream tube is consumed, while all air outside this frontier flows downstream. The quantitative characteristics of the sucked stream tube can be assessed from conservation of mass:

$$\rho_\infty A_\infty U_\infty = \rho_i A_i U_i$$

$$\frac{A_\infty}{A_i} = \frac{\rho_i}{\rho_\infty}\frac{U_i}{U_\infty} \tag{8}$$

For an incompressible flow the area ratio, A_∞/A_i, of the sucked stream tube is equal to the operational velocity ratio:

$$\frac{A_\infty}{A_i} = \frac{U_i}{U_\infty} \tag{9}$$

As described earlier, in stationary conditions, the inlet airflow demands growths. The diameter of the inlet capture surface increases towards the ground to allow the required airflow to the fan [2] as shown Figure 9. Air flowing into the engine from all directions produces a section on the ground surface underneath the engine in which there is no flow [3]. The streamlines coming from all directions encounter in one position where there is no velocity. This specific line is named the stagnation streamline. Figure 9 exemplifies this phenomenon.

Generally, the formation of inlet ground vortices is associated with low h/D_i and high U_i/U_∞ [3], that occur for an engine operating near to the ground at a high inlet mass flow.

Henceforth, the mechanism of ground vortex creation is strongly dependent of the elevation of the engine axis directly above the ground, the velocity ratio and the existence of an upstream velocity. In the published works on ground vortex formation, the velocity ratio, U_i/U_∞, is used to define the sucked stream tube size at far field in relation to the intake size. When the approaching velocity, U_∞ is low (i.e. U_i/U_∞ is large) the engine mass flow request growths and as a consequence the sucked stream tube size, A_∞, also growths to match this request.

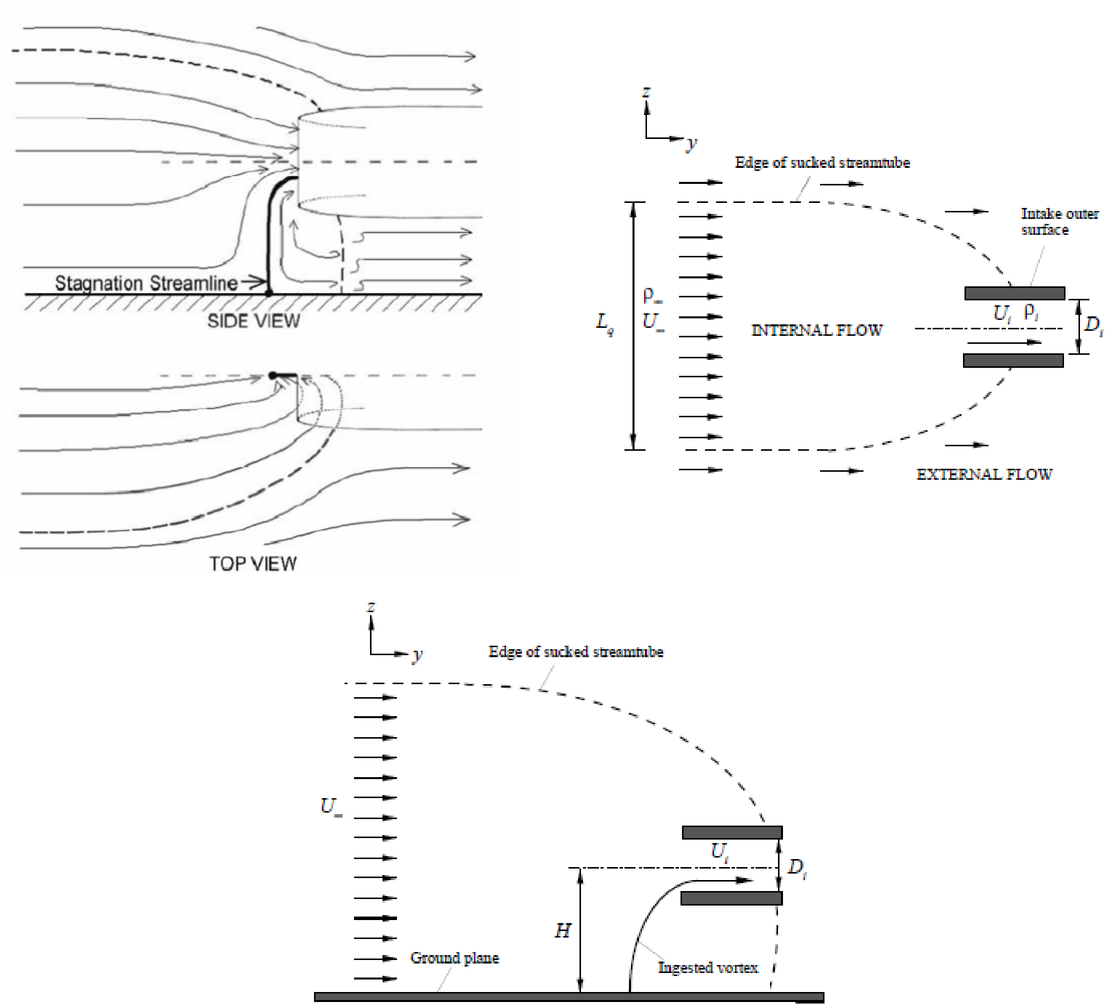

Figure 9: Inlet capture surface above the ground [2].

The primary parameters that dictate whether the capture stream tube interacts with the ground plane depends fundamentally on the height-to-diameter ratio, h/Di, of the intake (Figure 9) and the velocity ratio U_i / U_∞. High velocity ratios and low non-dimensional heights lead to a contact of the stream tube with the ground and consequently ground vortex creation. The dependency of these two parameters on the creation of ground vortices was clearly illustrated by Liu et al [25], in which pairs of h/Di and U_i / U_∞ values were associated for cases with and deprived of vortices.

Afterward, in an associated study, Shin et al [26] created a ground vortex formation map built around Liu et al. [25] results but also encompassed data from full scale engine visualizations and other investigators. The recognized threshold is represented in Figure 10, and Nakayama and Jones [27] also presented the corresponding analytical expression

(Equation 10). All the three datasets demonstrate an admirable agreement, but still they all seem to be founded on identical information.

$$\left(\frac{U_i}{U_\infty}\right)_{CRIT} = 24 \cdot \left(\frac{h}{D_i}\right) - 17 \tag{10}$$

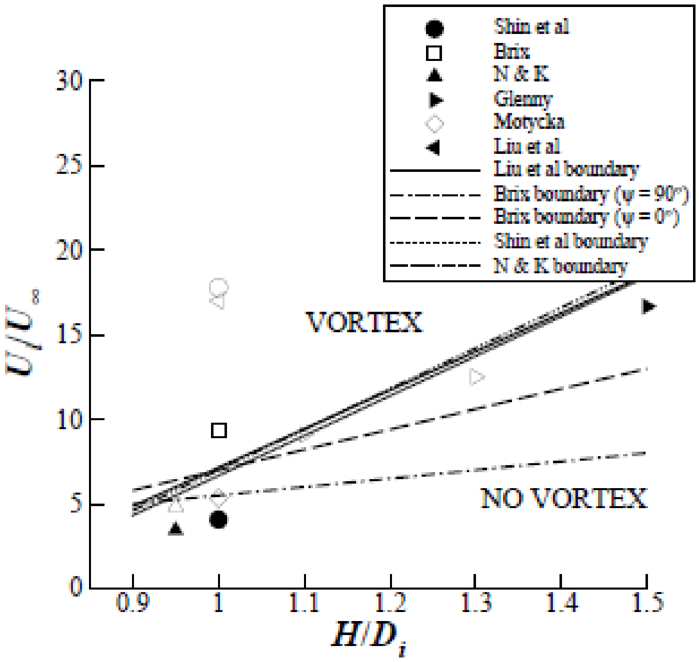

Figure 10: Correlation of velocity ratio and non-dimensional height combinations revealing a region of vortex formation and no-vortex formation.

The experimental information was collected by Jermy, M. and Ho. W. H [28] and plotted in Figure 11 that highlights the velocity ratios / heights combinations that correspond to the appearance or not of the inlet ground vortex.

Figure 11 shows that there is a good correlation of the intake ground vortex and the flow rate and the location of the intake. Nonetheless, additional limitations as external wind or external vorticity can have a part on the creation of ground vortices.

Nakayama and Jones [27] offered quantifiable total pressure quantities at two velocity ratios under headwind settings with both data points being included in Figure 10 and Figure 11. Their results challenged all the previous mentioned thresholds with data revealing that an inlet ground vortex can form at lower than before stated velocity ratios (Figure 10).

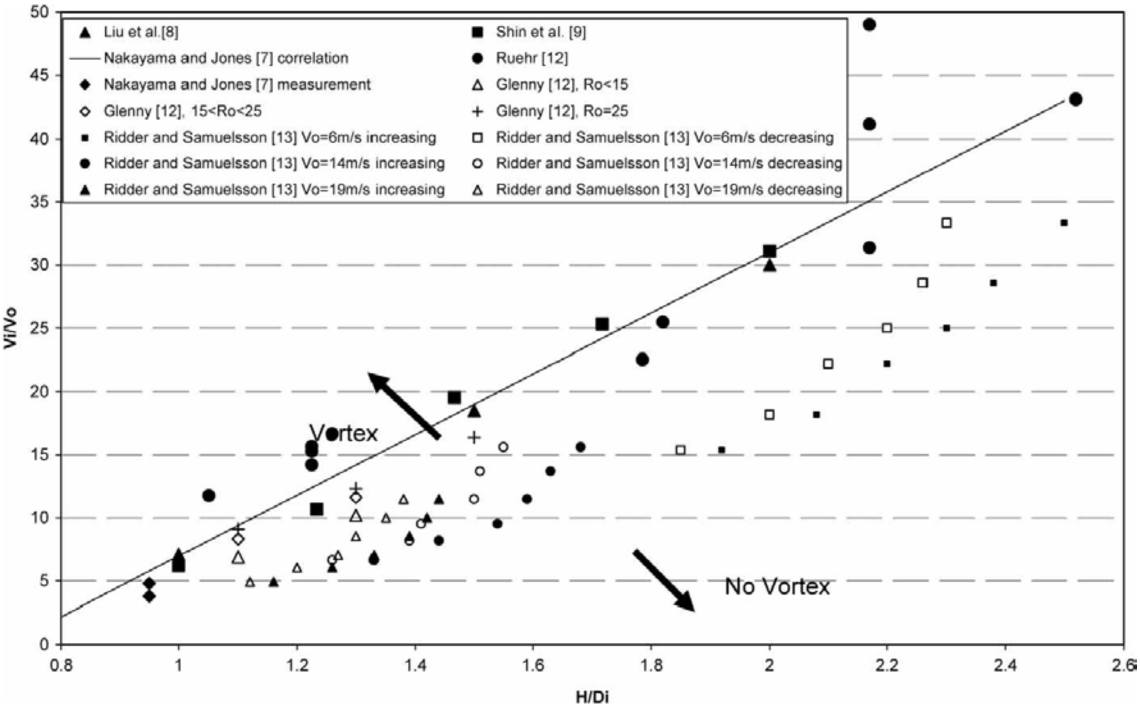

Figure 11: Data showing the boundary between the vortex forming and non-vortex forming flow regimes. Where Vi/Vo = U_i/U_∞ [29].

At this point it must be noted that both the formation norms recognized by Liu et al [25] and Shin et al [26] were created purely on crosswind configurations and were determined from visualizations only and as specified above the boundary offered by Nakayama and Jones looks to be built mostly on identical information.

More recently Brix et al [6] offered a vortex creation map with a standard being established for equally headwind and crosswind configurations. Mutually have been roughly take out and comprised in Figure 11. Brix et al. [6] present quantitative measurements in the intake tube by means of a rotating hot-wire. Though, it is unspecified whether this norm was created on visualizations or quantitative outcomes. Even so there is a substantial difference among the recognized boundary under crosswind conditions (ψ = 90◦) and the formerly declared vortex circumvention thresholds. This difference can be put down to the different approaches used to perceive a vortex, as well as hypothetically different operating settings (such as boundary layer thickness). Nevertheless, the lowest velocity ratio essential to create a vortex under headwind settings is higher in contrast to crosswind. No clarification was offered by the authors for this observation. Several possibilities could elucidate this finding such as different sucked stream tube features between head-wind and crosswind configurations, the crosswind vortex being significantly stronger and consequently easier to perceive, or that the instability is higher under headwind conditions, thus rendering its existence difficult to fix.

The computational study of Jermy and Ho [28] show the sensitivities of different upstream settings on the creation boundary under headwind settings. In this investigation different upstream velocity gradients and impending boundary layer thicknesses were studied. The authors found that '*no noticeable vortex*' formed when the upstream shear reduced under a certain threshold [28]. Prior research has revealed that vortices can form under inactive settings, in which there is no upstream shear or vorticity source at all. In terms of the impending boundary layer thickness, δ, results displayed that as δ got bigger the vortex creation threshold was reduced [28].

This leads to a significant argument in terms of the experimental sensitivities in the inlet ground vortex formation threshold. The velocity ratio defined by Jermy and Ho [28] and in all former works is based on the free-stream velocity, U_∞. Also, Equation 9 derived above fundamentally accepts a uniform velocity profile inside the sucked stream tube. If there is an approaching boundary layer present in the capture stream tube the velocity profile is hence obviously not uniform, and will subsequently take an effect on the sucked stream tube size. In order to ingest the equivalent mass flow, the ingested stream tube area must growth. As a consequence, the velocity ratio U_i / U_∞ at which the stream tube raises off the ground will be smaller [28]. Then, an area weighted average velocity should be used instead of U_∞ the definition of the velocity ratio. This would give an "*equivalent velocity ratio*" for any impending boundary layer thickness. One of the explanations for the inconsistencies in the inlet ground vortex threshold is attributed to this effect. Nevertheless, the size of the ingested stream tube is normally not identified, since it is difficult to determine the $\vec{U}_\infty$, and usually it is used the free-stream velocity, U_∞.

Taking into account that the ingested stream tube interacts with the ground (thus creating a stagnation point) all works confirm that there must be present a vorticity font for the vortex. In the initial studies, a frequently mentioned state was the presence of ambient vorticity in the arrangement of an impending ground boundary layer [24]. Nevertheless, studies of Siervi et al [7] and Brix et al [6] have discovered that vorticity can be present in the flow field even with no impending ambient vorticity font. The experiments were done by vertically lining up two inlet representations in a water tunnel and producing a crosswind flow, and visualization was done with hydrogen bubbles Figure 12.

Their annotations unveiled two captivating outcomes. Even lacking a ground, the ground vortex still shaped. Which means, that the vorticity created in the ground boundary layer is not essential for a ground vortex to be created.

This research was made in an irrotational flow field with no upstream vorticity sources. The circumstance that the ground vortex was detected in an upstream irrotational flow terminates Klein's third condition, meaning that a diverse source of vorticity is accountable for generating the ground vortex.

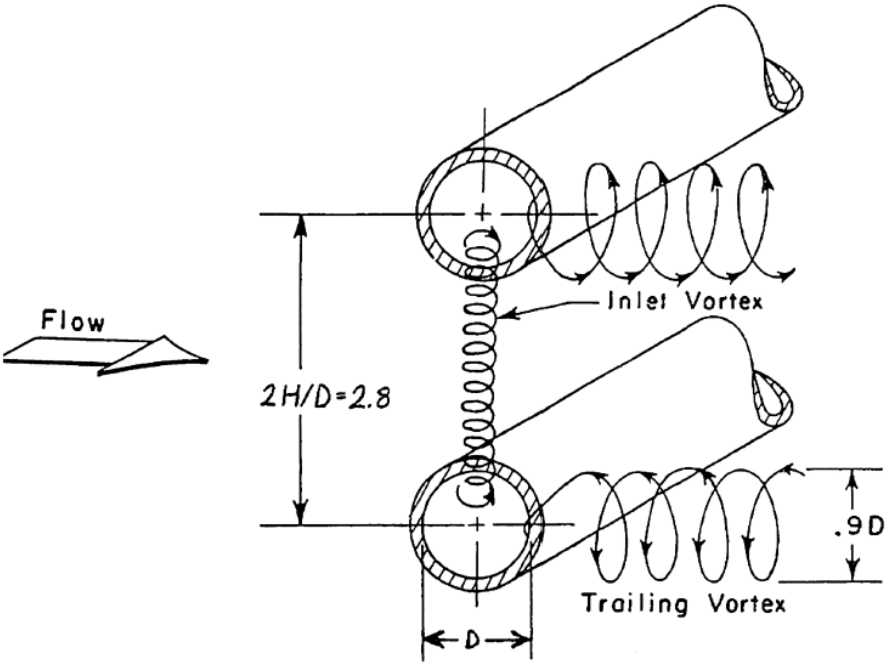

Figure 12: Streamlines associated with twin inlets at 90° of yaw in an irrotational upstream flow [7]

De Siervi et al. [7] anticipated that the vorticity in the core of the vortex was formed originally by the act of viscosity in the boundary layers on the exteriors of the inlet. After the vortex is shaped, nevertheless, there is no longer any vorticity convected into the core, and the vorticity required to sustain the vortex is fashioned by the extension of the vortex filaments in the core.

Hence the existence of a ground boundary layer or ambient vorticity is not essential for the development of an inlet ground vortex. However, would the impending air encompass vorticity, at that time an inlet ground vortex will form via a diverse mechanism, one that comprises of the augmentation of the vertical element of the present ambient vorticity as the vortex lines are convected into the inlet. This work was confirmed by Liu et al. [25] and Shin et al. [26], mutually supporting the above cited vortex creation mechanisms.

2.5 Mechanisms of Ground Vortex Formation

Investigation until now has identified two formation mechanisms. The first is pertinent to an intake under no-wind and headwind settings and the second recounts to an intake in crosswind conditions. The two are essentially different due to the dissimilar central vorticity fonts for the vortex. Accordingly, reasonably different interactive structures and features are detected through each individual mechanism which are defined below.

2.6 Headwind

The mechanism called headwind is pertinent to an intake with its axis parallel to the flow path. Many investigators have identified that it is the intensification of ambient vorticity that causes intense vortices to form. Sievri et al [7] demonstrated this concept after extensive water tunnel flow visualization experiments using the hydrogen bubble procedure. Different impending vorticity fonts and alignments were considered upstream of the intake counting a boundary layer, and clockwise and counter clockwise shear profiles (Figure 13). The results showed that the path, distortion and convection of the ambient vortex lines connected with the main vorticity controlled the rotation and quantity of vortices at the fan face. This was confirmed by means of potential flow model in which the main irrotational potential flow was overlaid linearly with a weak shear flow. Certain quantifiable lines were traced as they moved towards the intake and the distortion of the vortex lines, where found to agree with the investigational observations. The flow fields for the different boundary layer profiles are discussed next. The vortex lines are defined as actuality a line in the fluid whose tangent is all over parallel to the local vorticity vector. Henceforth for a boundary layer type profile seen in Figure 13a the vortex lines connected through this flow field, distant upstream of the intake, are parallel to the ground and perpendicular to the flow path. The vortex lines are convected by the mean flow and has they get near the intake they are stretched and distorted as showed in the figure by the influence of the induced intake flow field. The consequence is that two counter-rotating vortices are symmetrically positioned nearby the intake axis. The spin of the individually particular vortex is unswervingly determined by the rotation of the leg of the vortex line it is connected with. In the shear profiles the form is relatively dissimilar. A negative $\partial v/\partial x$ velocity gradient upstream (Figure 13b) the vortex lines are straight and vertical to the ground surface (Figure 14b). Once they get near the intake the high velocities connected by the intake flow field stretches the vortex filaments consequential one single ground vortex is consumed. The spin of the vortex is influenced by the equivalent spin of the main vortex lines upstream of the intake. Henceforth with a negative $\partial v/\partial x$ main velocity gradient upstream, the vortex spins in the intake tube that it has negative ω_y vorticity. The opposite occurs for the positive $\partial v/\partial x$ main velocity gradient upstream (Figure 14c) where the consumed vortex spins with positive ω_y. Also potential flow calculations were done to confirm the experimental explanations and to determine the performance of the upper legs of the consumed vortex lines. The results displayed that all the lower legs were focused on the stagnation point although the upper legs blown out over the top of the intake, with the presence of concentration being detected. The experimentations and concepts set by De Siervi remained contributory in the discernment on the essential instruments of vortex creation.

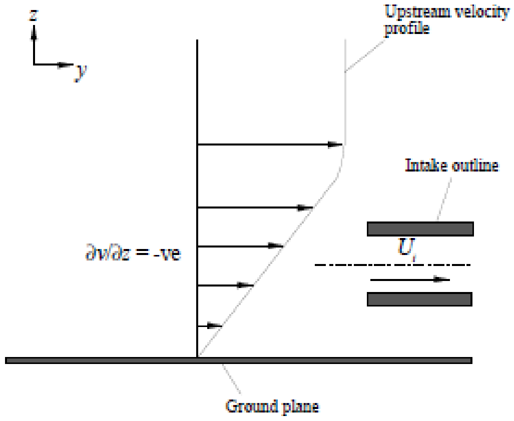

(a) $\partial v/\partial z = -ve$

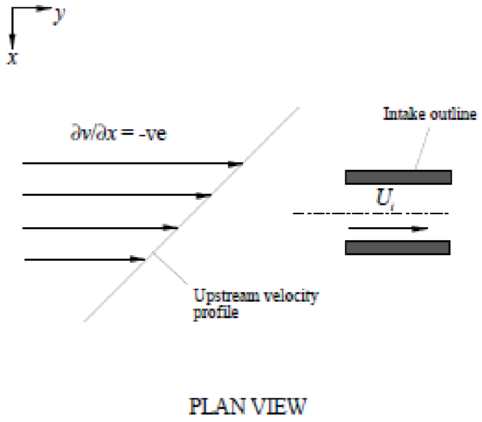

(b) $\partial v/\partial x = -ve$

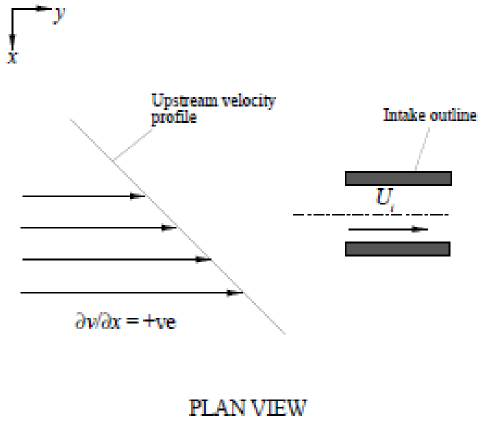

(c) $\partial v/\partial x = +ve$

Figure 13: Velocity profiles used in de Siervi et al. experiments [7].

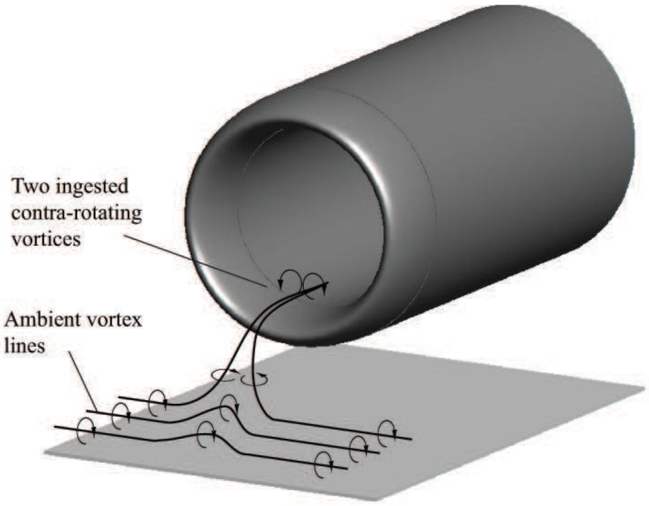

$\partial v/\partial z$ = +ve

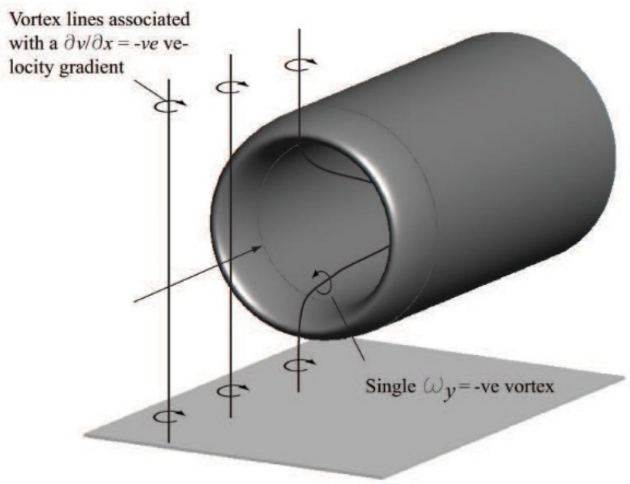

$\partial v/\partial x$ = −ve

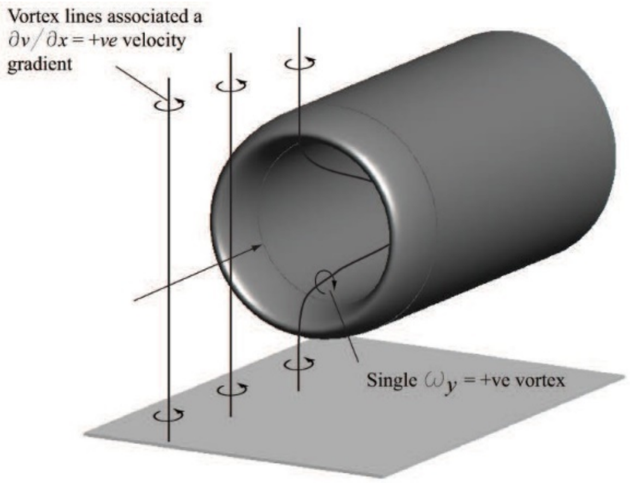

$\partial v/\partial x$ = +ve

Figure 14: Deformation of the ambient vortex lines as they approach the intake for different upstream velocity gradients.

Nevertheless, these works are mainly qualitative in their essence and none quantifiable data of the vortex is given. To assess the measure of the question distortion and vortex strength quantities are essential.

Following the De Siervi et al's [7] investigations, Shin et al [26] quantitatively confirm the potential flow calculations thru experimentations.

A negative $\partial v/\partial x$ velocity gradient upstream of the intake (Figure 13b) was presented and for a sole configuration hot-wire measurements were taken inside the intake. The results confirmed that the model in which the alignment and rotating sense of the ambient perpendicular vortex lines regulates the amount and spin of the vortex inside the intake. A first quantity of the vortex strength was specified for a h/D_i= 1.13 and U_i/U_∞ = 22:

$$\frac{\Gamma}{\omega_\infty A_\infty} \approx -2 \tag{11}$$

Nevertheless, it was only after the effort of Brix [6] that significant measurements of the ground vortex became available. Using two rotating hot-wires quantifiable information was obtained in the intake duct. The results were in agreement with the above remarks, with some new findings. Possibly the utmost of which was the development of two contra-rotating vortices under inactive settings $U_i/U_\infty = \infty$, which had not yet been described. Even though no quantifiable quantities were obtainable in such conditions the vortices were detected to spin in the contrary direction to those in headwind settings. It has also demonstrated quantitatively under headwind settings that if the velocity ratio surpasses a certain threshold the vortices spin in agreement with the inactive settings. So, with the very comprehensive and perceptive experimentations in 2000, Brix [6] confirmed the outcomes anticipated by De Sievri et al [7]. Once the air is sucked into the engine inlet, in a headwind flow, the flow field beneath the intake begins to roll up into two straight counter-rotating vortices (Figure 15a) and a fast flow into the contrary path of the wind appears among them [6]. Unexpectedly the sense of spin of the two vortices shifts as demonstrated in Figure 15c when the rate of the velocity ratio U_i/U_∞ is high enough (≅20). The sense of spin is precisely the equivalent to the no-wind settings. Figure 15b reveals the pattern amongst high and low ratios U_i/U_∞. In this case, two pairs of proportioned vortices spinning in the contrary sense occur together. Due to its very unstable characteristic this situation hardly ever appears. The two vortices try to cancel each other out and if they do not, one of the two pair of vortex is going to prevail but, the strength of the subjugated vortex is very weak.

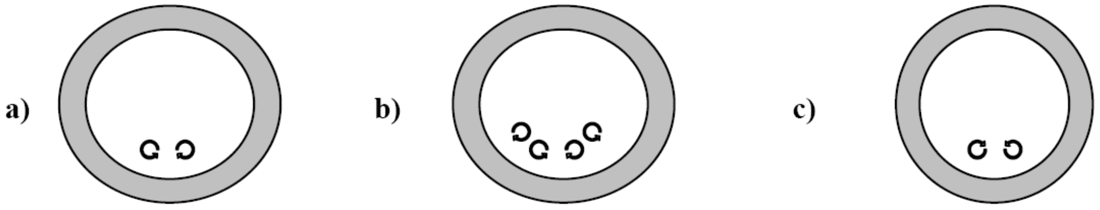

Low U_i/U_∞

Medium U_i/U_∞ (Transition phase)

High U_i/U_∞

Figure 15: Spin of the inlet vortices for a) low, b) medium and c) high velocity ratios [21].

The boundary layer effects are stronger on one side than the other identical as in the no-wind case contingent on the velocity ratio. Figure 16 shows the alignments of the font of vorticity depending on this velocity ratio.

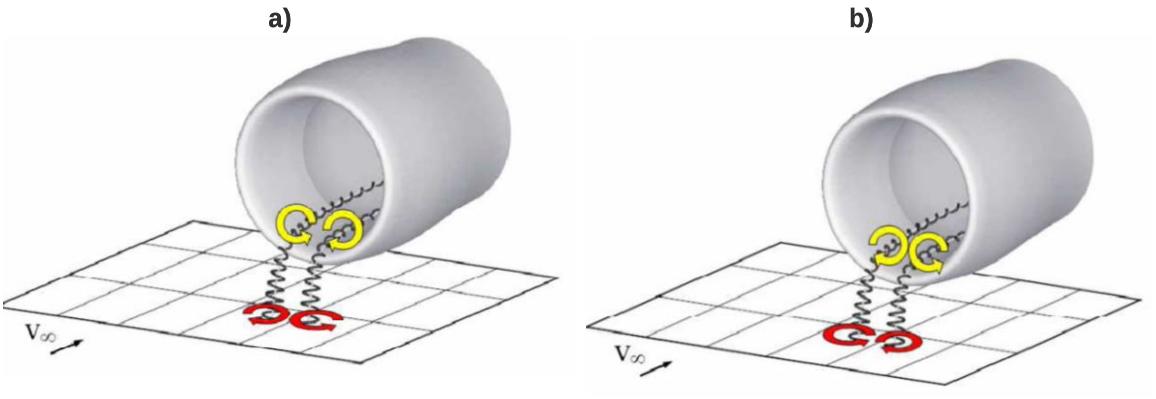

Figure 16: Vortex filaments in head-wind. Modes at (a) high and (b) low speed velocity ratio [6].

This alteration in the sense of spin occurs, because the upstream flow in the direction of the intake lip produces a boundary layer smaller when related to the flow beneath the engine streaming in the direction of the inlet at low velocity ratios U_i/U_∞ as shown in Figure 17.

The growth in the free-stream velocity decreases the magnitude of the upstream boundary layer and the flow in the direction of the intake lip is now in command, and at high velocities ratios the boundary sizes are flipped, as shown in Figure 13.

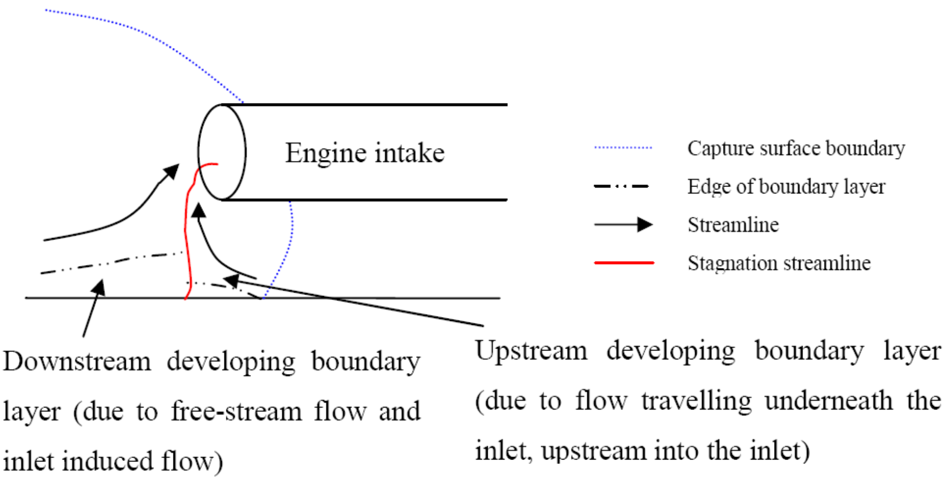

Figure 17: Reason explaining the sense of rotation of the counter rotating vortices at low velocity ratio [21]

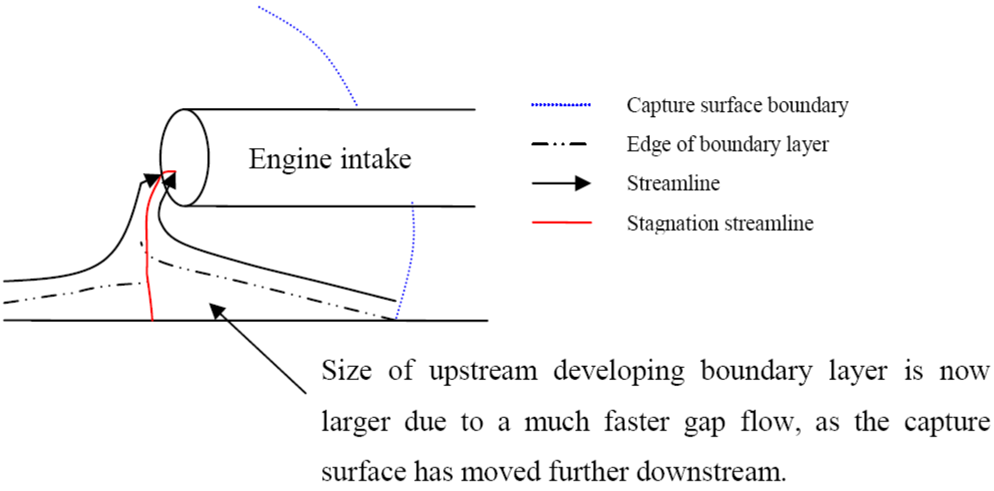

Figure 18: Reason explaining the sense of rotation of the counter rotating vortices at high velocity ratio [21]

2.6.1 No-wind

Because of the ground immediacy, high levels of suction under the engine inlet leads into a strong flow under the inlet upstream towards the intake lip [6]. A vortex can be created short of ambient wind and with a low ratio h/D_i ($h/D_i < 1$). It is probable to see on the engine intake and in the ground two rising spiraling vortices in these settings.

Under no-wind settings, it looks like the two vortices are counter-rotating (Figure 19). The vorticity is brought by the boundary layer. The air flowing below the engine upstream in the path of the inlet lip leads and is stronger than the flow downstream in the direction of the intake lip, causing the two counter rotating vortices.

The flow assembly changes when the ground vortex creation is subjugated by an impending induced boundary layer. The sense of the vorticity will be clockwise leading to reversing the sense of spin off the ground vortices as revealed in Figure 21. The intake vortex rotation sense is highly dependent on of the sense of rotation of the primary vorticity.

A peripheral flow field in the direction of the intake that originates from all directions in the vicinity is created by the engine under no-wind settings. The surface interacts with the induced velocities instantly adjacent to the ground producing vorticity. By definition this creation setting necessitates no ambient vorticity and this 'induced' vorticity is the cause for the vortex. Brix et al. [6] records that it is the flow behind and amid the intake and the ground that governs under no-wind settings. Figure 19 shows the stretching deforming of the vortex lines related with this leading flow.

This condition is identical to the headwind settings excluding the cause of vorticity is linked to flow impending from the opposite path and is a straight consequence of the intake induced flow field rather than the impending flow. As shown in

Figure 20a the vortices inside the intake tube spin in the reverse path to that under headwind settings. The vortices caused under no-wind settings can be viewed as a flow setting of the headwind settings because the creation settings are mostly identical in comparison to headwind settings.

No quantifiable quantities have been conveyed under such settings until now, since the work of Brix et al [6] is only built on flow visualization. Their findings have quantitatively verified by one of the most recent work by Murphy et al [30].

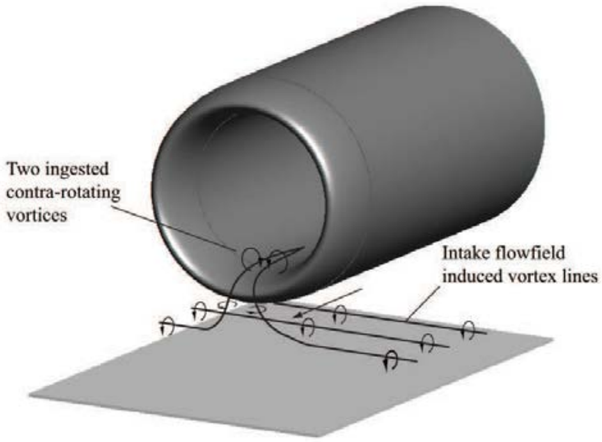

Figure 19: Vortex formation under no-wind conditions.

Two contra-rotating vortices were found to form in agreement with the flow settings offered in Figure 19, using Stereoscopic Particle Image Velocimetry (SPIV) the flow under quiescent conditions was quantitatively studied nevertheless, the flow field was detected to be highly unstable and frequently only a single main vortex was detected. The vortices created were observed to be weak but not insignificant under no-wind settings.

Brix et al. [6] also confirmed that even beneath headwind settings $U_i / U_\infty = \infty$, the vortices will spin in agreement with the no-wind settings inside the intake tube if the velocity ratio is big enough. This was revealed for a setting in which the intake height, h/D_i, was equal to 1 and the velocity ratio was U_i / U_∞ = 33. At a velocity ratio of 12 the vortices were found to spin in the predictable style for the headwind settings in accord with the flow setting offered in Figure 14a and

Figure 20c. In this spin change there were an intermediate stage in which the influence from the impending (Figure 14a) and induced vorticity causes (Figure 19) are about identical and the contrary (

Figure 20) leading to an uncertainty in the vortex pair. The precise velocity ratio at which this happened was not given in.

(a) No-wind mode **(b) Transition phase**

(c) Headwind mode

Figure 20: Flow modes observed under headwind conditions [6].

Hydrogen bubble visualization was executed inside a water tunnel but then with a significantly minor intake diameter, *Di*, of 16mm. A variety of intake formations were studied for a single inlet close to the ground and for two evenly placed inlets with no ground. At low velocity ratios used for the single intake arrangement, when no ground vortex was present two trailing vortices were ingested into the intake (Figure 21a). As the intake velocity and henceforward velocity ratio augmented a single ground vortex, a trailing vortex and a number of ground based stream wise vortices appeared. They found that all vortices were non-stationary and every so often the ground vortex would show up on the other side of the intake with an inverted sense of spin with the trailing vortex also inverting its location and spin sense. Frequently the arrangement was seen to break and then restructuring irregularly.

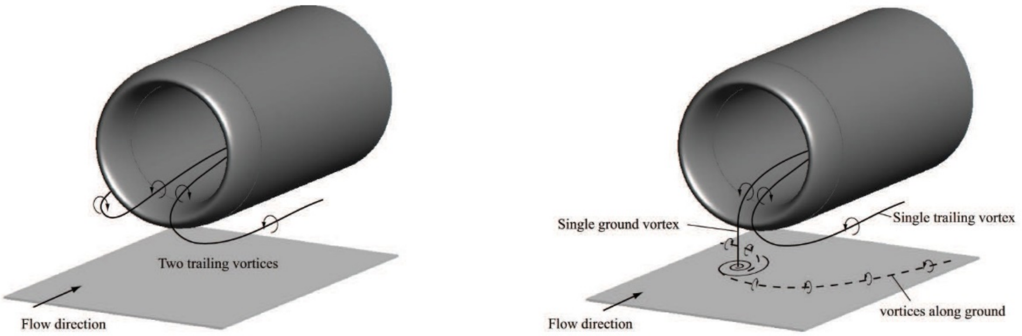

(a) Low velocity ratios **(b) High velocity ratios**

Figure 21: Flow topology observed by Bissenger and Braun [31] under headwind conditions for (a) two trailing vortices (b) a complex vortex system involving a single ground and trailing vortex, plus vortices on the ground.

No upstream velocity profile was prearranged in the tests. It is anticipated that the vortex lines connected with the boundary layer type contour would lead one would assume two contra-rotating vortices to be detected. This could be due to a little asymmetric flow field or small non-uniformities integral in the tunnel flow. In addition, the hydrogen bubble generator was placed just upstream of the intake and spanned across the test section which may have influenced the flow field. Still, the non-dimensional heights were considerably larger and ranged from 1.5 to 3 h/*Di*. Other works say that higher ground clearances have has consequence in a more unsteady behavior [3] [32].

For the two intakes one above the other with no ground plane configuration the existence of another intake introduces a symmetry plane that acts as an inviscid ground, henceforth the impact of the impending boundary layer vorticity cause can be studied. They observed amongst the two intakes an area of 'random motion' shaped at low velocity ratios (Figure 22a). As the velocity ratio amplified the 'random motion' stretched into the two intakes (Figure 22b) with an additional growth in the velocity ratio a vortex arrangement appeared which has an intake-to-intake vortex and a single trailing vortex from each respective inlet (Figure 22c). The authors consequently determined that the impending boundary layer has not vital for vortex creation. It is also clear that the existence of the hydrogen bubble generator has introduced a cause of vorticity which is realized by the existence of this 'random motion' region.

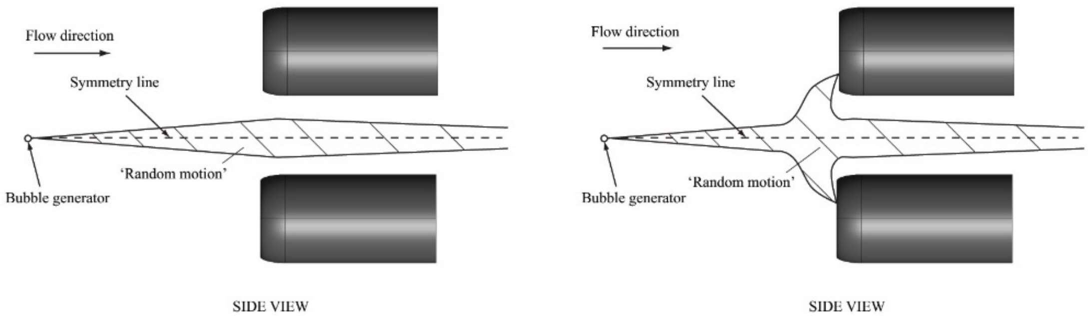

(a) Low velocity ratios **(b) Intermediate velocity ratios**

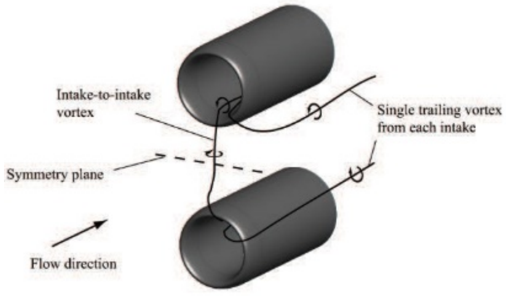

(c) High velocity ratios

Figure 22: Formation of the intake vortex system for a twin inlet configuration [31]

2.6.2 Crosswind

With a 90° crosswind and an irrotational flow field[1], two different kinds of vortices appear around the intake: an inlet vortex and a trailing vortex. From the downstream side of the inlet lip region a trailing vortex appears larger in size than the inlet ground vortex. The sense of rotation of these two vortices is represented in Figure 23. The experimentations under these settings were intended to test the concept of the intensification of ambient vortex lines upstream of the intake to non-zero yaw angles. A supplementary vortex creation

---

[1] By "irrotational flowfield" is meant that no boundary layer is considered.

mechanism applicable to intakes in significant crosswinds settings was found.

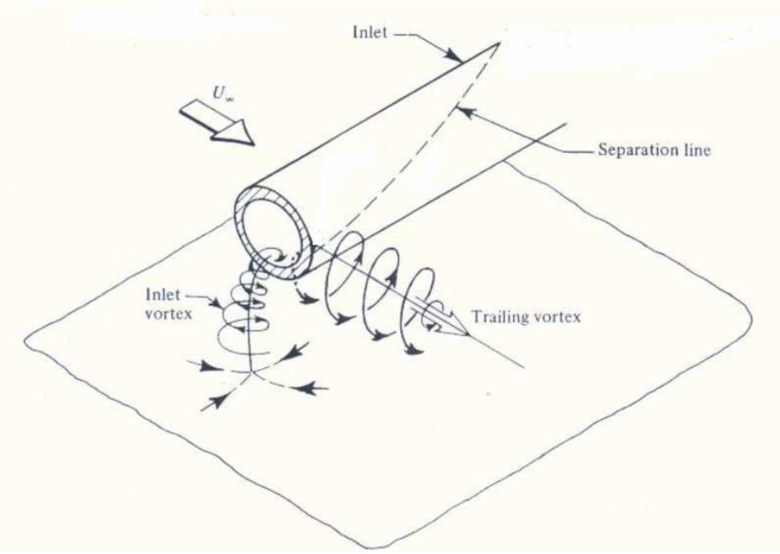

Figure 23: Sense of rotation of the inlet vortex and the trailing vortex [7]

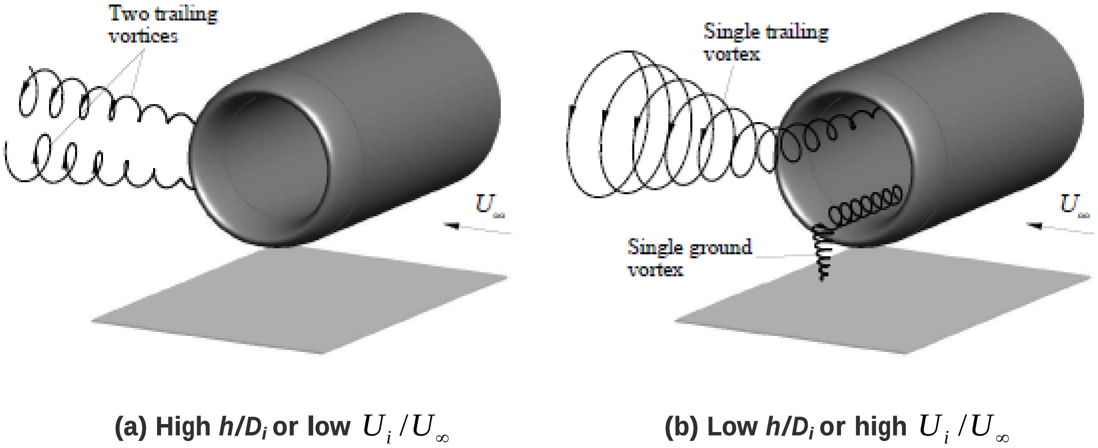

(a) High *h/D* or low U_i/U_∞

(b) Low *h/D* or high U_i/U_∞

Figure 24: Flow field topology under crosswind conditions (a) two contra-rotating vortices and (b) a single trailing vortex, ground vortex system.

It was expected that an alteration in the sense of spin of the ambient vortex lines would lead to an alteration in the spin of the vortex from the results under headwind settings (Figure 14). Nevertheless, a fairly different performance to that in headwind was detected for the crosswind situation. The ground vortex at all times had positive ω_y vorticity inside the intake tube from a left to right crossflow. Changing the upstream spin of the vortex lines consequently leading to no variation in the vortex spin, suggesting another thing was at work.

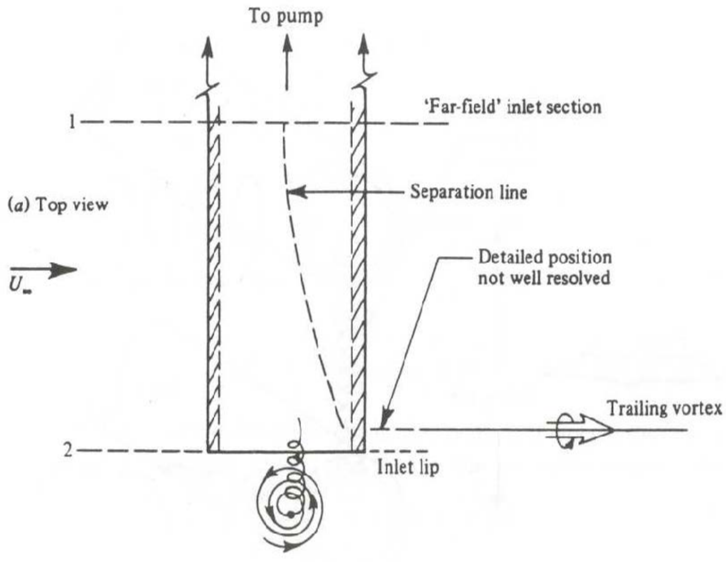

Figure 25: Separation line around the inlet seen from the top view [7].

This has driven additional experimentation for the case of an irrotational flow upstream of an intake at 90 degrees to the flow direction. The creation of a single ground vortex together with by a trailing vortex off the outer edge of the intake was revealed (Figure 24b). The outer diameter, *D* of the intake was observed to be the size of the trailing vortex. Due to a variation in the circulation about the intake the existence of the trailing vortex was assumed. Bearing in mind the variation in the circulation at different axial positions along the external surface of the intake this was reasoned. The flow around the intake is crudely two-dimensional some diameters after the lip, in which the local flow velocity is of the order of U_∞, henceforth the local circulation around the intake must scale with $U_\infty D$ [7]. Since around the intake nearby to the lip the induced intake flow field has a controlling effect [7] is anticipated at this location the circulation to be proportional to $U_\infty D$. It was argued due to the difference in circulation that is required to have trailing vorticity among the two axial positions. It was theorized that by De Siervi et al [7] the circulation of the ground vortex is roughly that of the trailing vortex which was later verified by Shin et al [27]. The vortex lines associated with the ground vortex and trailing vortex must join at infinity was on which this concept based.

Nevertheless, Brix et al [6] acquired measurements which indicate that the two vortices are not the same with the trailing vortex being weaker. At low velocity ratios two contra-rotating vortices trailed from the leeward edge of the intake and no ground vortex is detected, when the sucked stream tube has no ground interaction (Figure 24a and Figure 26a). With the increasing of the velocity ratio, the two trailing vortices displayed substantial sideways and up and down movement, with the lower vortex occasionally attaching to the ground [27]. The ground vortex and trailing vortex arrangement brusquely appeared as the velocity ratio was a little increased (Figure 24b and Figure 26b). All of this situations where detected by Brix et al. [6]

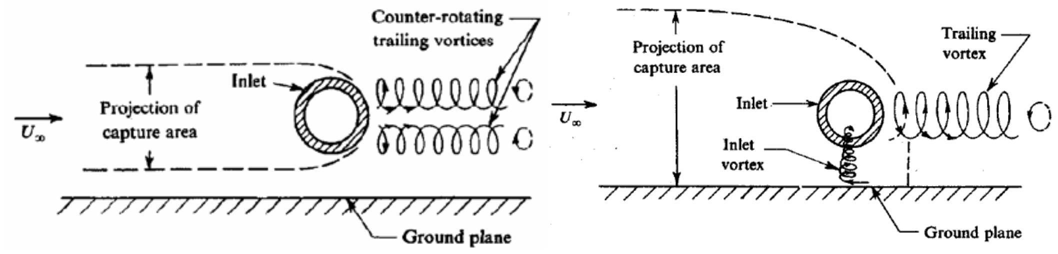

(a) High h/D_i or low U_i/U_∞ **(b) Low h/D_i or high U_i/U_∞**

Figure 26: Side view display the flow field under crosswind settings with and without the sucked stream tube interacting with the ground [7].

The flow field was additionally studied by investigating the influence of the ground boundary layer given that the direction of the upstream ambient vorticity had no influence on the vortex spin. De Siervi et al. [7] led experimentations with a twin inlet setting in which the ground is changed by an inviscid symmetry plane, that revealed the existence of one intake-to-intake vortex and a single trailing vortex form each intake (Figure 27). The core of the intake-to-intake vortex is a constant convection of vorticity away from the symmetry plane, and the only source of vorticity is that associated with the boundary layer over the intake surface. This is a most important finding since before it was supposed that the ground was playing the major role on the inlet ground vortex formation.

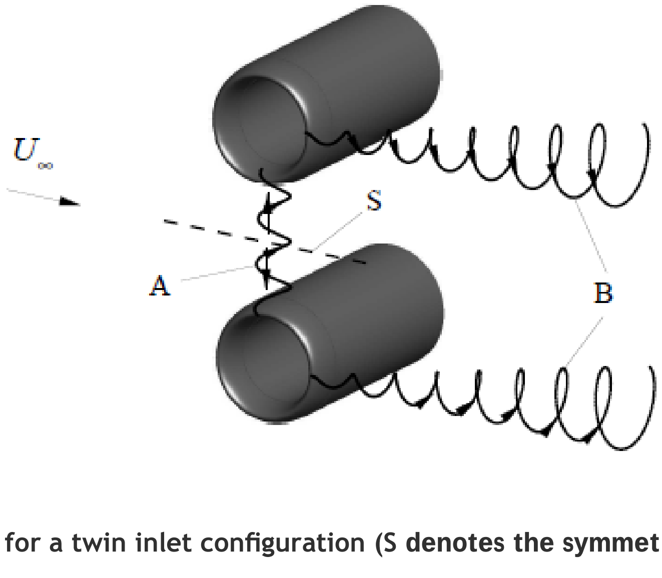

Figure 27: Flow for a twin inlet configuration (S denotes the symmetry plane, A is the intake-to-intake ground vortex and B the two trailing vortices) [7]

Flow visualizations exposed that vorticity is shed from the intake all through the transient and a vortex appears downstream of the inlets, reinforces and transfers upstream to a location among the intake after the stable state is reached. The time scale cited was approximately $10h/U_\infty$. It was noted that no additional convection of vorticity was detected into the core from the neighboring fluid after the transient. It was suggested that the creation of vorticity due to extending of the vortex filaments inside the core balanced the convection of vorticity away from the symmetry plane. Analogous opinions with respect to the trailing vortex were also provided by Shin et al. [27].

Nevertheless, it seems to be contradictions in the flow field as defined by De Siervi et al. [7] and Shin et al. [27]. In the first place stretching of vortex lines do not create it, but can only preserve previously existing vorticity. The vortex ought to disperse with time if there is no constant convection of vorticity into the core, which is not the case. It is clear, nevertheless, that the cause of vorticity organized by the vortex is coming from the detached flow over the intake external surface. Consequently, it is conceivable that vorticity is shed from the intake during the transient and journeys a minor distance downstream having into account the momentum conveyed by the free-stream flow. Somewhere in the downstream a stagnation area occurs which marks the edge of the sucked stream tube; then the intake induced velocity field convects the vorticity back upstream to be focused and stretched to create a ground vortex. There must be a constant convection of vorticity originating from the intake external surface and the ground that feeds the vortex during the steady state. In the twin inlet setting it is possible that vorticity shed from the inferior part of the intake is convected back upstream along the symmetry plane and goes in the core of the vortex. This is a more reliable description.

In relation to the trailing vortex, the illustrations presented in De Siervi et al [7] and in associated works [27] [33] portray the vortex originating off the leeward edge of the intake and drifting downstream through the sucked stream tube still a flow such as this appears to by improbable since a stagnation point is need at the edge of the capture surface. However, CFD simulations by Zantopp [34] exposes a to some extent different flow field more complex but seems to be more credible. One ground vortex is created between the intake and the ground for a non-dimensional height of 0.25 (h/Dl) and a velocity ratio U_i/U_∞ of 19.8, but there are two trailing vortices, one inside and one outside the sucked stream tube (Figure 28a). This vorticity originally journeys downstream and when the edge of the capture stream tube is grasped is convected back to the intake this inverse flow creates the core flow of the trailing vortex. Fresh vorticity created at the same time over the external intake surface originally journeys downstream and as it goes coils around the core of the vortex when it grasps the edge of the sucked stream tube it goes in to the core of the vortex and is reingested into the intake. The second vortex is linked with the flow that journeys over the exterior of the capture stream tube that also collects vorticity from the external intake surface as also from the ground downstream of the intake and it seems to be weaker than the ingested trailing vortex. A lower velocity ratio of 9.9 exposes one trailing vortex not consumed by the intake. Maybe the size of the sucked stream tube downstream of the intake is reduced hence constraining the creation of a fixed trailing vortex at this velocity ratio. Compared to the previous settings, in upstream irrotational flow, the ground vortex is part of a vortex arrangement. The creation of the circulation along the intake is right connected to the creation of the trailing vortex settings and thus to the ground vortex.

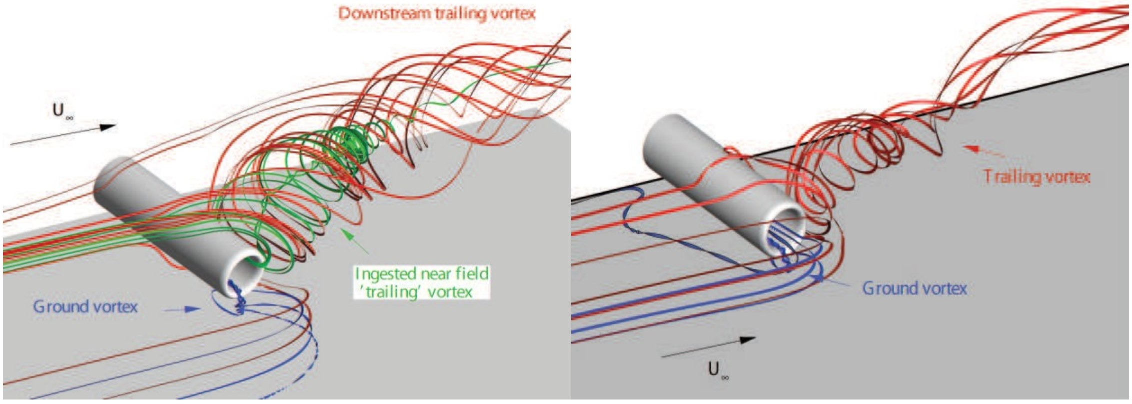

Figure 28: CFD simulations of the crosswind flow field topology for a non-dimensional height of 0.25 (h/Dl) and Mi = 0.58 at two different velocity ratios [34].

2.6.3 Crosswind with ambient vorticity

One clockwise vortex inside the intake is generated with an engine intake at a 90° yaw angle and clockwise far upstream ambient vorticity. A single clockwise vortex is found for the same arrangement but with a far upstream vorticity taking a counter-clockwise spin. The sense of spin of the vortex is therefore reverse to the ambient vorticity and this would not happen if the only source is the intensification of the ambient vorticity.

There are two vortices revealed at the intake in Figure 29. One is very strong near the trailing edge although the other is very weak and very close to the other. The existence of the two vortices with different strength is due to the fact that this setting is a mixture of the three previous settings defined before. Two symmetrical weak counter-rotating vortices have been seen in no-wind conditions. In head-wind similarly creates two vortices, the strength of these vortices should be bigger. In crosswind with irrotational flow, one strong vortex and one weak vortex are also created.

2.6.4 Tailwind and Reverse Thrust

Ground vortex creation can also happen with tailwind and under reverse thrust maneuver. Both conditions are comparable subsequently that engine airflow is sent back upstream in the direction of the intake effectively producing a tailwind (Figure 30). An example picture of an ingested vortex under reverse thrust operation is shown in Figure 31.

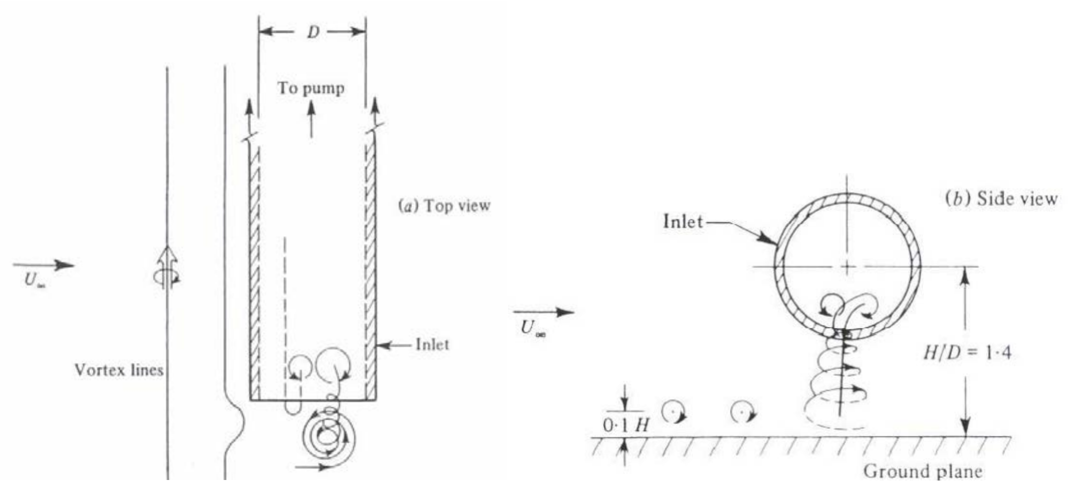

Figure 29: Vortex formation in cross-wind with an upstream vertical vorticity [7].

The vortex created is frequently ingested into the core of engine which is acknowledged to cause significantly bigger problems. Yet very little investigation has been directed under such settings. Motycka et al [5] studied this configuration, and together with Nakayama and Jones [28] are the only to present distortion measurements made by ground vortex ingestion at the fan face. The results of the potential flow calculations which comprised swirl effects can be summarized in the subsequent arguments:

1. Increasing the upstream ambient vorticity diminishes the velocity ratio at which the vortex dissipates;
2. Diminishing the ground clearance of the intake raises the array of wind speeds at which a vortex will be created;
3. The dissipating velocity essential to eliminate the stagnation point on the ground is autonomous of wind path excluding for yaw angles among 0 and 55◦;
4. The area of probable vortex creation on the ground rises as the non-dimensional height is bigger;
5. As the tailwind raises the standoff distance of the vortex base from the high-light plane rises. Therefore, the vortex ingestion position changes (Figure 32);
6. The vortex core diameter under 135◦ tailwind settings with U_i / U_∞ = 8.7 was found to be nearly 3.1% of the intake outer diameter and in addition, vortex core size was found to scale with the intake diameter.

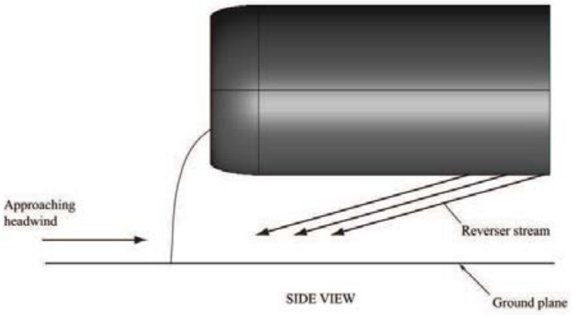

Figure 30: Reverse thrust operation introducing an effective tailwind to the intake

Figure 31: Ground vortex ingestion under reverse thrust operation.

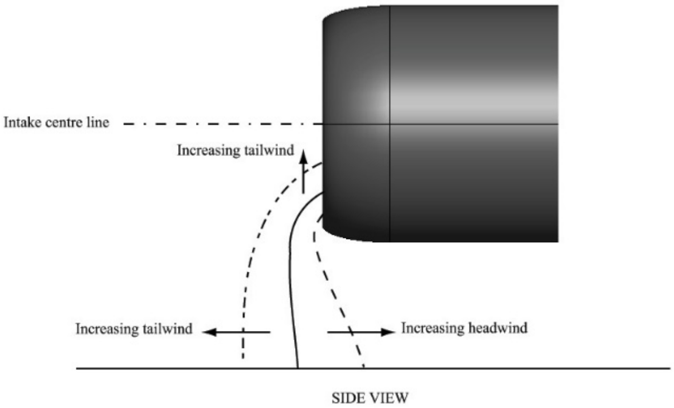

Figure 32: Effect of wind direction and strength on the vortex location on the ground and its consequent ingestion location [5].

Experimentations were conducted to assess the influence of reverser targeting, inlet height, headwind speed on ground vortex creation thru reverse thrust maneuver (Figure 33). The key assumptions from this investigation are emphasized in the subsequent:

- The mechanism for vortex creation under reverse thrust operation is similar to that in headwind because two loss cores are identified;
- Local total pressure retrieval inside the core of the vortex was characteristically detected to be about 0.85 (P/P_∞);
- In continuous reverser maneuver the headwind speed raises the distortion rises and gets to a maximum and then decreases subsequently (this was credited to a decrease in the contact amid the reverser and ambient air streams);
- Dropping engine power reduced inlet distortion at all airspeeds;
- Bigger ground clearances brought about a reduction in levels of distortion;
- The reverser jet configuration looked to affect the dissipating velocity ratio.

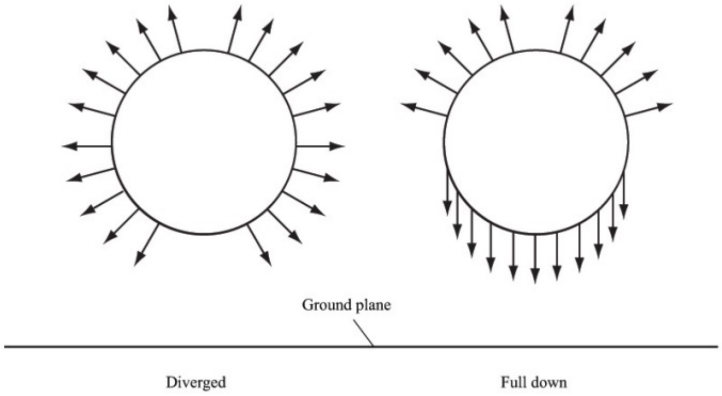

Figure 33: Reverser targeting pattern configurations investigated [5].

This is perhaps the only study in the public domain to include full scale measurements of ground vortex ingestion. The trials were done on the JT9D engine fixed on a B-52 flying test bed intended at defining the top distortion levels just previous to engine surge during reverse thrust maneuver. Results indicated that ground vortex ingestion was the primary cause of engine surges. As expected this is partially due to the high total pressure distortion made by the vortex and the fact of the ingestion of the vortex.

2.7 Vortex prevention methods

There have been many patents that try to avoid or eradicate the ground vortex. The first ground vortex inhibition scheme to be put into commercial service was the Blow-away Jet used on the DC-8 in the late 1950s and early 1960s, as illustrated in

Figure 34 [12]. This design was to blow high-pressure compressor-bled air in to the ground on the neighborhood of where the vortex stagnation point would be and with it trying to dissipate the vortex. However, it failed due to several factors and it causes the precise impairment it was projected to evade by thrusting up debris into the air and entrained in the airflow [35].

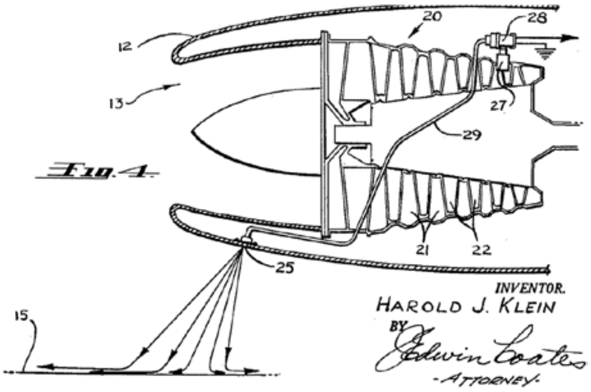

Figure 34: Blow-away jet system for inlet-vortex avoidance [12].

Another idea was that was patent is shown in Figure 35. It consists of extending a platform out in front and below the inlet thru ground man oeuvres to prevent a ground vortex creation and therefore cut the odds of FOD. Inlet ground vortices were still being created and finding a way into the inlet by working around the plate or attaching to itself. The plate did help avoid some degree of FOD, but not fan face distortion.

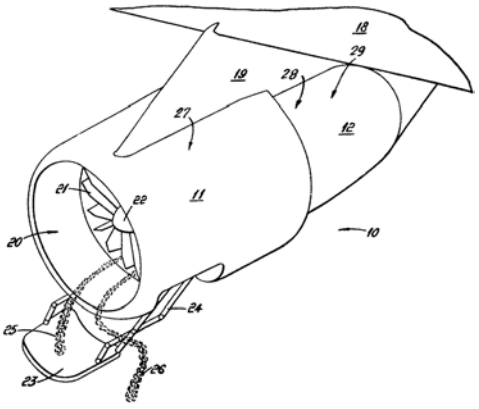

Figure 35: System for inlet vortex attachment [14].

With the aid of CFD active flow control devices were established that effectively deteriorate and then eradicate the vortex. A pulsed actuation system was developed by Smith [16] which comprises of two air-ejecting, angled nozzles mounted under the lip it makes available adequate turbulent mixing to avoid the creation of a clear vortex [36]. There are two major disadvantages with this system:

1. It is triggered after the vortex is present making it a vortex mitigation system;
2. There is substantial air flow impingement on the ground which will unavoidably raises the risk of FOD.

A sprayer jet system was advanced and verified using CFD by Shmilovich and Yadlin [37] (Figure 36) that is comprised of one spinning jet below the inlet lip. This technique was effective in alleviating the vortex but it also impinged on the ground henceforth FOD was a worry to.

Figure 36: Sprayer jet system.

Vanfleet [38] introduce the concept of a jet of air is focused at the back beneath the intake introducing an effective headwind (Figure 37). Johns [2] notes that this “vortaway” jet has had no commercial attention [2]. More recent works by Smith and Dorris [15] highpoints the difficulties in realizing such counter measures in practice.

An amount of ground vortex counter measures where explored by Brix et al [6] as well as vortex generators in the intake (Figure 38). Almost all systems are not being applied on aircraft due to their inadequate operational range and success. Up-to-date ground vortex inhibition approaches are all operational limiting the aircraft speed and engine thrust to safe vortex free settings.

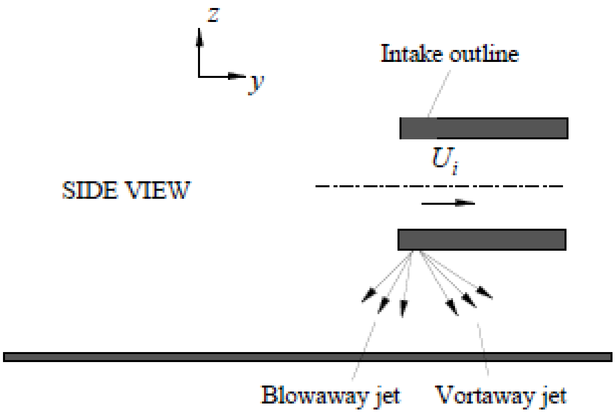

Figure 37: Schematic of two different concepts that have been invented for ground vortex prevention

Figure 38: Vortex dissipater and gravel kit engine bleed air down and aft from 3 nozzles at the tip to break up the vortices in a Boeing 737-200.

2.8 Ground boundary layer independence

The inlet vortex is not largely connected with the ground boundary layer or the ambient vorticity of the impending flow: Murphy and MacManus [39] provided new data to prove that. The impending boundary layer thickness has no substantial consequence on the features of ground vortices. This was confirmed by plotting curves of non-dimensionalized circulation around the vortex and fan-face pressure distortion parameter DC60 versus velocity ratio, for boundary layer thicknesses of $\delta * / Dl$ equal to 0.11 and 0.03 (Dl is the authors' notation for highlight diameter). The DC60 constant is defined as:

$$DC_{60} = \frac{P_i - P_{60}}{q_i} \tag{12}$$

Where Pi is the area-weighted average of stagnation pressure at the fan face measured by the PIV system, P60 is the area-weighted average of stagnation pressure at the worst 60-degree sector on the fan face, and q_i is the local dynamic pressure at the fan face. The results, shown in Figure 42, revealed negligible differences for the two cases, which had a fixed h/Dl = 0.25.

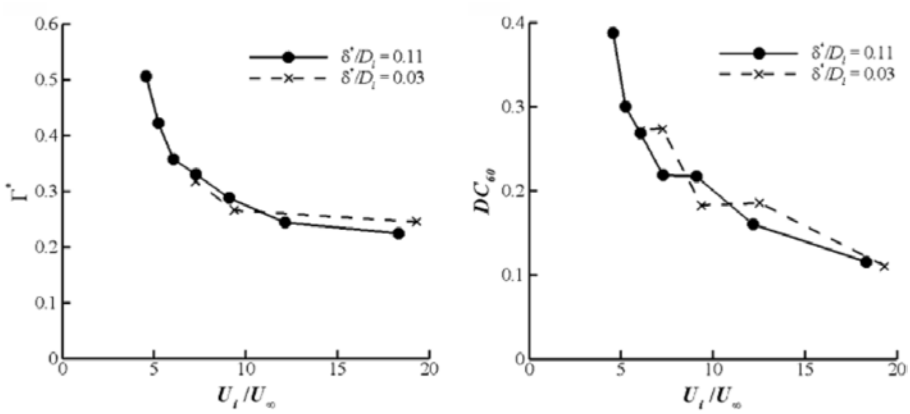

Figure 39: Effect of approaching boundary layer thickness on (a) the vortex strength and (b) fan face distortion, DC60 [39].

2.9 Transient Effects

The inlet ground vortex is probably a highly unstable process, with vortex twisting happening as it attaches himself to the ground. Nevertheless, the available studies that deal with this aspect are quite scarce. Brix et al. [6] and Secareanu et al. [39] mentioned the issue, but there has been insufficient research.

Chapter 3 Mathematical Method

3.1 Introduction

The mathematical model used to find a result of equations of Navier-Stokes that rules the fluid flow simulating an intake in cross-wind with irrotational flow is described in this chapter.

Section 3.2 presents the governing differential equations, and the turbulence model [40]. Section 3.3 and 3.4 are dedicated to the solution process and boundary conditions. The grid study is offered in section 3.5.

3.2 Governing Differential Equations

The time averaged partial differential equations ruling the steady, uniform-density isothermal three-dimensional flow may be inscribed in Cartesian coordinates as

$$\rho \overline{U}_j \frac{\partial \overline{U}_i}{\partial X_j} = -\frac{\partial \overline{P}}{\partial X_i} + \frac{\partial}{\partial X_j}\left(\mu \frac{\partial \overline{U}_i}{\partial X_j} - \rho \overline{u'_i u'_j} \right) \tag{13}$$

and the continuity equation as

$$\frac{\partial \overline{U}_i}{\partial X_i} = 0 \tag{14}$$

where the overbars signify averaged quantities. The turbulent diffusion fluxes are approached with the high Reynolds number version of the two-equation $k-\varepsilon$ model defined in detail by Launder and Spalding [40].

The Reynolds stresses may be stated as

$$\overline{u'_i u'_j} = -\upsilon_T \left(\frac{\partial \overline{U}_i}{\partial X_j} + \frac{\partial \overline{U}_j}{\partial X_i} \right) + \frac{2}{3} k \delta_{ij} \tag{15}$$

Where ν_T is the turbulence kinematic viscosity, which is consequential from the turbulence model and stated by

$$\upsilon_T = C_\mu \frac{k^2}{\varepsilon} \tag{16}$$

The values for k and ε are found by resolving the subsequent transport equations:

$$\overline{U}_j \frac{\partial k}{\partial X_j} = \frac{\partial}{\partial X_j}\left(\frac{\upsilon_T}{\sigma_k}\frac{\partial k}{\partial X_j}\right) - \overline{u'_i u'_j}\frac{\partial \overline{U}_i}{\partial X_j} - \varepsilon \tag{17}$$

$$\overline{U}_j \frac{\partial \varepsilon}{\partial X_j} = \frac{\partial}{\partial X_j}\left(\frac{\upsilon_T}{\sigma_\varepsilon}\frac{\partial \varepsilon}{\partial X_j}\right) - C_1 \frac{\varepsilon}{k}\overline{u'_i u'_j}\frac{\partial \overline{U}_i}{\partial X_j} - C_2 \frac{\varepsilon^2}{k} \tag{18}$$

Where C_1 and C_2 are supplementary dimensionless model constants, σ_k and σ_ε are the turbulent Prandtl numbers for kinetic energy and turbulent dissipation.

The turbulence model coefficients that are used are those specified by Launder and Spalding [41]:

C_μ	C_1	C_2	σ_k	σ_ε
0.09	1.44	1.92	1.0	1.3

Table 1: Turbulence model constants.

The ruling equations create a set of coupled partial differential equations that can be inscribed in the general form as

$$\frac{\partial U\phi}{\partial X} + \frac{\partial V\phi}{\partial Y} + \frac{\partial W\phi}{\partial Z} = \frac{\partial}{\partial X}\left(\Gamma_\phi \frac{\partial \phi}{\partial X}\right) + \frac{\partial}{\partial Y}\left(\Gamma_\phi \frac{\partial \phi}{\partial Y}\right) + \frac{\partial}{\partial Z}\left(\Gamma_\phi \frac{\partial \phi}{\partial Z}\right) + S_\phi \tag{19}$$

Where ϕ may stand for any of the velocities, turbulent kinetic energy, or dissipation, and Γ_ϕ and S_ϕ take on different values for each particular ϕ.

3.3 Finite-Difference Equations

The resolution of the ruling equations was attained using a finite-difference method that used discretized algebraic equations deduced from the exact differential equations that they represent. This discretization includes the integration of the transport equation over an elementary control volume around a central node with a scalar value ϕ_P [42], and as far as the convection terms are concerned, it needs the spatial average value of ϕ at each cell face. The hybrid scheme uses central differencing in obtaining those values when $Pe < 2$ and upwind differencing for $Pe \geq 2$. In the latter case, false diffusion is presented into the finite-difference equation [42]. Inaccurate resolution may then be attained in regions of the flow with velocity vectors tending to the numerical grid lines and large diffusive transport normal to flow path if fine grids are not used, and limit calculation of complex flows. The QUICK scheme (Quadratic Upstream Interpolation for Convective Kinematics) by Leonard [42] is free of fake diffusion and gives more exact results with grid spacing much larger than obligatory by the hybrid scheme. It is a higher-order differencing scheme that uses a three point upstream weighted quadratic interpolation for the cell phase values. To find the cell face value a quadratic function transitory over two connecting or surrounding nodes and one node on the upstream side must be used. QUICK is most suitable for steady flow or quasi-steady very convective elliptic flow. Due to the use of quadratic upstream-weighted interpolation to compute the cell values for each control volume, Figure 44 illustrates the west face of a control volume around a central node with a value ϕ_P. For this face, using a uniform grid for ease, the value of ϕ is expressed by

$$\phi_w = \frac{1}{2}(\phi_P + \phi_w) - \frac{1}{8}(\phi_P + \phi_w + \phi_{ww}) \tag{20}$$

The convective velocity component U_w is expected to have the path shown in Figure 43. If U_w were negative, then ϕ_E would be involved rather than ϕ_{ww}. The first term in the preceding equation is the central difference formula, and the second is the significant stabilizing upstream weighted normal curvature influence. Stating the values of ϕ at each cell face with the suitable interpolation formula and writing gradients also in terms of node values, the finite-difference equation conforming to Equation 20 may be inscribed in the universal form:

$$A_P^\phi \phi_P = \sum A_i^\phi \phi_i + S_U^\phi \tag{21}$$

where

$$A_P^\phi = \sum A_i^\phi + S_P^\phi \tag{22}$$

The summation occurs over the 12 nodes adjacent P (see Figure 44).

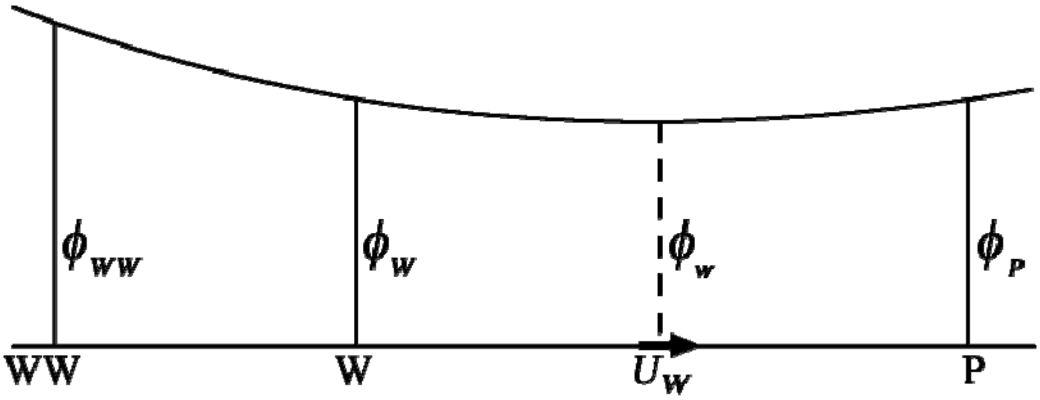

Figure 40: Nodal configuration for the west face of a control volume [44].

The set of equations for the whole field are resolved by the technique typically used with hybrid scheme design [45], but when via QUICK, the A_i^{ϕ} coefficients may become negative and stable results cannot be found.

In the current work, diagonal dominance of the coefficient matrix is guaranteed and improved by reorganizing the difference equation for the cell where the coefficients A_i^{ϕ} become negative. This reorganization comprises of subtracting $A_i^{\phi}\phi_P$ from both sides of Equation 21 removing the negative influence of A_i^{ϕ} and at the same time enhancing the diagonal dominance of the coefficient matrix [44] [46] [47]. The source term S_U^{ϕ} turn into

$$S_U^{\phi} = S_U^{\phi} - A_i^{\phi}\phi'_P \tag{23}$$

Where ϕ'_P is the newest obtainable value of ϕ at node P.

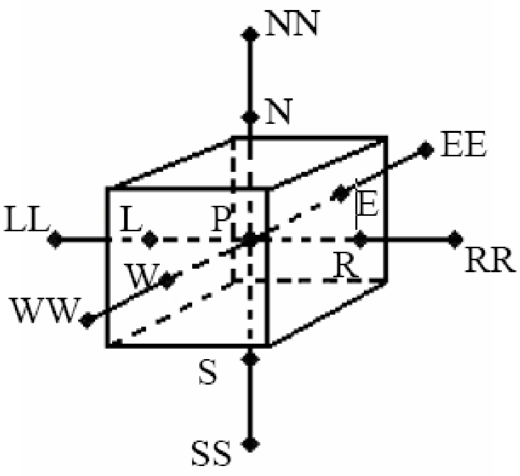

Figure 41: Nodal configuration for a control volume [44].

Then the QUICK scheme is used in calculating all variables.

3.4 Solution Procedure

The resolution process is founded on the SIMPLE algorithm extensively used and described in the literature [48].

It uses the staggered grid arrangement and a guess and correct procedure field such that the solution of the momentum equations satisfies continuity.

3.5 Boundary Conditions

The computational domain has six boundaries where dependent values are specified: an inlet plane, a symmetry plane, and two solid walls at the top and side of the channel.

On the symmetry plane, the normal velocity vanishes, and the normal derivate of the other variables are zero.

At the solid surfaces, the wall function method defined in detail by Launder and Spalding [41] is used to prescribe the boundary conditions for the velocity and turbulence quantities, assuming that the turbulence is in state of local equilibrium.

The domain of the solution is shown in Figure 42.

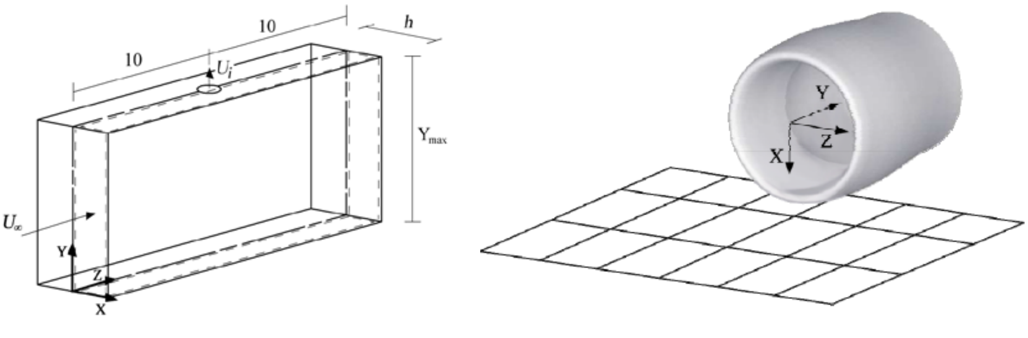

Figure 42: a) Domain of the solution b) Representation of the intake with centered referential [48]

Integrating two equations “*k*- ε” models over the near wall area and using the no-slip state harvests disappointing outcomes and that is a recognized circumstance. A method to go over this shortage is to put damping effects, making these models in to a Low-Reynolds-number arrangement. An alternative tactic is to use empirical laws which model the near-wall area to evade the incapacity of the “*k*- ε” model to forecast a logarithmic velocity outline near a wall the so-called wall functions. With them it is possible to determine wall settings such as pressure gradient, wall heat transfer and wall shear stress and the mean velocity parallel to the wall and turbulence amounts external the viscous sublayer in relation of the distance to it. Henceforward, there is no need to solve the viscous sublayer circumventing the requirement for a very fine mesh which economizes computer time and storage because the wall functions can be used to determinate near-wall boundary settings for the momentum and turbulence transport equations rather than the settings at the wall itself.

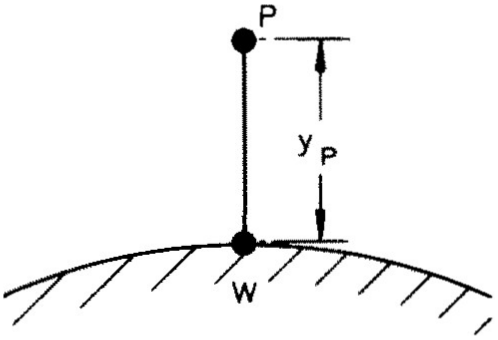

Figure 43: The near-wall nodes.

The first thing is that the point P is appropriately distant from W for $(k^{1/2}l/\nu)_p$ to be considerable larger than one so that the viscous effects are completely overcome by the turbulent. The fluxes of momentum and heat to the wall are theoretical found to follow the relations:

$$\frac{U_p}{(\tau/\rho)_w} C_\mu^{1/4} k_p^{1/2} = \frac{1}{\kappa} ln \left[E y_p \frac{(C_\mu^{1/2} k_p)^{1/2}}{\nu} \right] \tag{24}$$

$$\frac{(T_p - T_w) C_p \rho C_\mu^{1/4} k_p^{1/2}}{\dot{q}''_w} = \frac{\sigma_h}{\kappa} ln \left[\frac{E y_p (C_\mu^{1/2} k_p)^{1/2}}{\nu} \right] + \sigma_h \frac{\pi/4}{\sin \pi/4} \left(\frac{A}{k} \right)^{1/2} \left(\frac{\sigma_{h,l}}{\sigma_h} - 1 \right) \left(\frac{\sigma_h}{\sigma_{h,l}} \right)^{1/4} . \tag{25}$$

Them U_P is the time-average velocity of the fluid on point P along the wall, τ_w the shear stress on the wall in the path of the velocity U_P, T_P and T_w the time-average temperatures of the fluid at points P and W, $\dot{q}''_w$ the heat flux to the wall, y_p the distance of the point P from the wall, E a function of the wall roughness, about equal to 9.0 for a smooth wall, C_P the constant-pressure specific heat of the fluid, σ_h the effective Prandtl number of the fully turbulent fluid (frequently taken as being of the order of 1), $\sigma_{h,l}$ the Prandtl number of the solely laminar fluid and A is the Van Driest constant, equal to 26.0 for a smooth wall.

When calculating k_P, it is of course required to give a value for the average energy-dissipation ratio over the control volume this is to be assumed from the postulation that:

$$\int_{0}^{y_P} \epsilon \, dy = C_\mu \frac{k_P^{3/2}}{\kappa} In \left[\frac{E y_p (\sqrt{C_\mu^{1/2}} k_p)^{1/2}}{\nu} \right] \tag{26}$$

3.6 Grid independence

Grid independence tests were made with diverse mesh sizes. The horizontal velocity component, *W*, is used in Figure 44 to illustrate the grid independency of the computations. It shows the vertical profiles of the horizontal velocity component, W, at *X/D* = 0.53, and plane *Z/D* =0.035 with different grids. The grid spacing was non-uniform in all directions. The results were found to be independent of numerical influences with the grids 33 × 59 × 33 and 49 × 88 × 49.

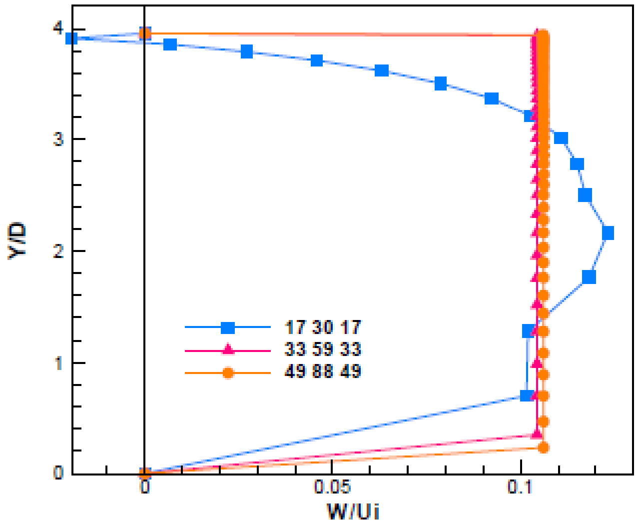

Figure 44: Dimensionless Vertical profile, at X/D=0.53, of the horizontal velocity component, W, at a Z=0.1 [49].

3.7 Convergence

Convergence was ensured by calculating the residuals of the equations, and in particular the sum of all the mass residuals (DSUM) of the continuity equation in the solution domain. Additionally, the values of the dependent variables were monitored at a location where difficulties were expected. Usually, at least more 1,000 iterations were performed after convergence was achieved to ensure that a large number of iterations remained with the residuals bellow the convergence criteria. The residuals and values of the variables at monitoring locations were registered along the iterative process and analyzed at the end, using a graph as illustrated in Figure 45.

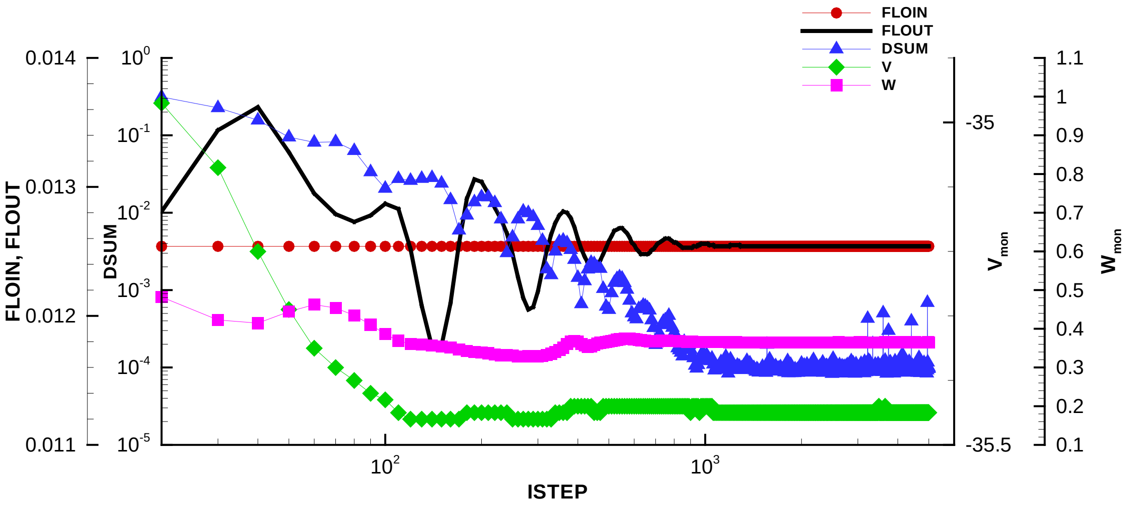

Figure 45: Example of graphics used for monitoring the convergence.

3.8 Summary

This chapter has summarized the mathematical model used to study turbulent flows.

A numerical solution for this kind of turbulent flow was found from the resolution of the set of discretized algebraic equations, representatives of momentum, mass, and the equations from the turbulent model “k” and “ε”.

The use of first-order hybrid difference handling for the convention terms can cause difficulties in permitting false diffusion errors to present grid independence realized in practical meshes and, thus, hiding the true performance of the turbulence model. In the current study the quadratic upstream interpolation QUICK method was used making possible a good numerical accuracy with much coarser grids.

A grid independence study was presented together with the details of controlling the convergence.

Chapter 4 Results

4.1 Introduction

The present work has the objective of improving the knowledge on the inlet ground vortex phenomena.

The numerical simulations were carried out for several different values inlet velocity, inlet diameter and height of the engine axis above the ground.

All of them were done for a setting of irrotational crosswind.

4.1.1 Test Cases

Most of the simulations are in the vortex region of Figure 10 and Figure 11, because this is the area where the newer engines are situated in terms of velocity U_i / U_∞ and non-dimensionalized height h/D_i ratios.

Table 2 displays all the values for which simulations were made in a total number of 572 combinations.

r (m)	D_i (m)	h (m)	U_i (m/s)	U_∞ (m/s)
1.5	3.0	2.8	160	2.2
1.4	2.8	2.6	140	
1.3	2.6	2.4	120	
1.2	2.4	2.3	100	
1.1	2.2	2.2	80	
1.0	2.0	2.1	60	
0.9	1.8	2.0	40	
0.8	1.6	1.9	20	
0.75	1.5			

Table 2: Values tested.

4.1.2 Graphical examples

Having in account the sheer number of figures that will be displayed and some unorthodox display settings, the next figures will serve as examples to explain better how to interpret them.

For Figure 46 to be correctly analyzed it should be taken in account that from left to right occurs the increasing of the value of h, from top to down the variation of U_i and U_∞ is always 2,2 m/s. This figure represents the results for a fixed value of r and if one wants to study its effect, and then several graphics for the different values of r should be used. Each set of color/symbol/number correspond to the maximum number of vortex structures identified, and the red line is approximately the threshold (boundary between the regions of no-vortex and vortex) assumed by the literature.

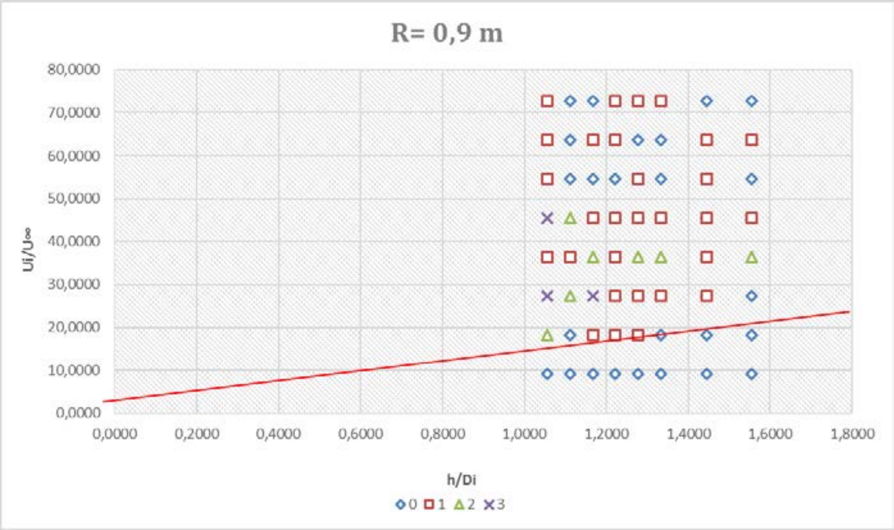

Figure 46: Graphic with max number of vortices present for a value of r=0.9 m.

In the case of Figure 47 and Figure 48 the black arrows represent U_i and U_∞, and the plane limited by green arrows is the ground. The first figure represents streamtraces for a set particles released in a plane of the solution domain, while the second one shows iso-surfaces of the static pressure.

Figure 49 shows isolines of the static pressure in a plane parallel to the ground. The two white arrows highlight the relative position of the inlet and the black one represents the crosswind velocity (U_∞) .

Figure 50 shows for the same plane of Figure 49 streamtraces produced by particles released at the crosswind entrance (black colored), together with velocity vectors (in blue color).

Finally, Figure 51 shows the same type of information of Figure 50, but in a plane parallel to inlet plane of the engine. The dashed line represents the relative position of the inlet (not in rigorous scale).

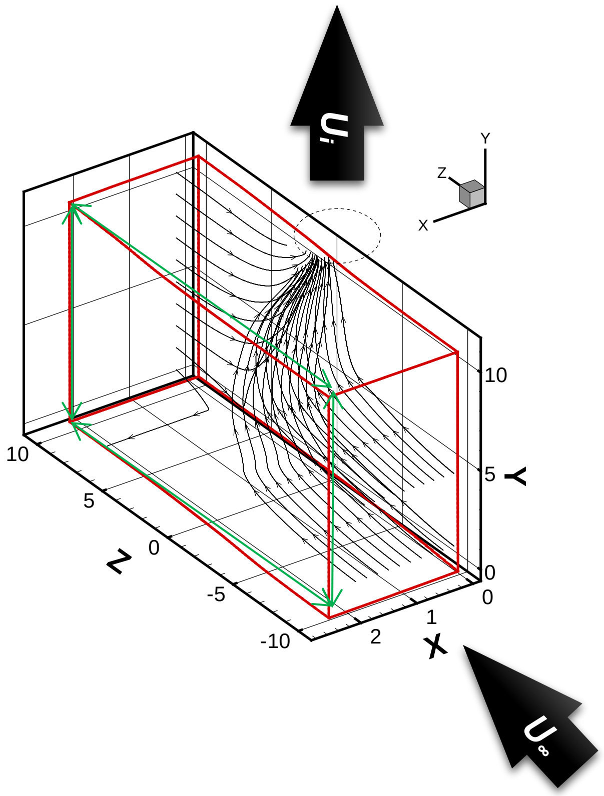

Figure 47: 3D Graphic of streamlines for set of values.

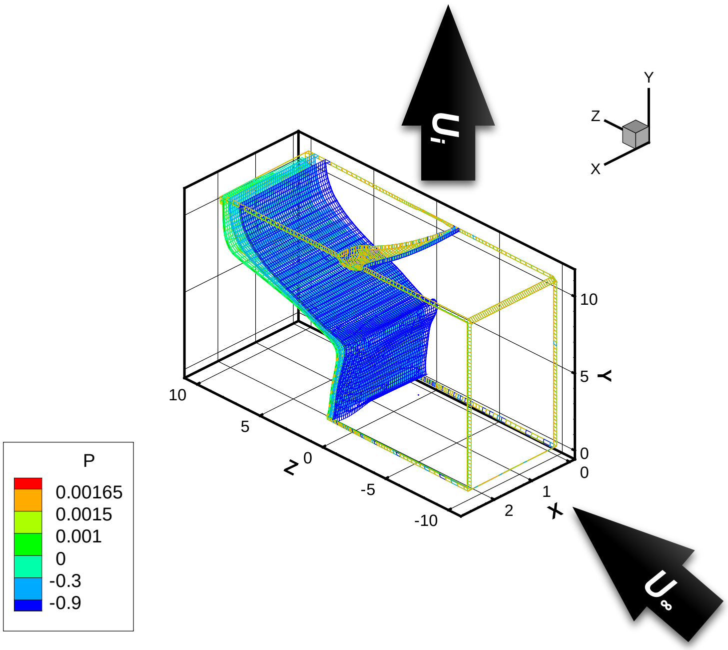

Figure 48: 3D graphic of iso-surfaces of pressure distribution.

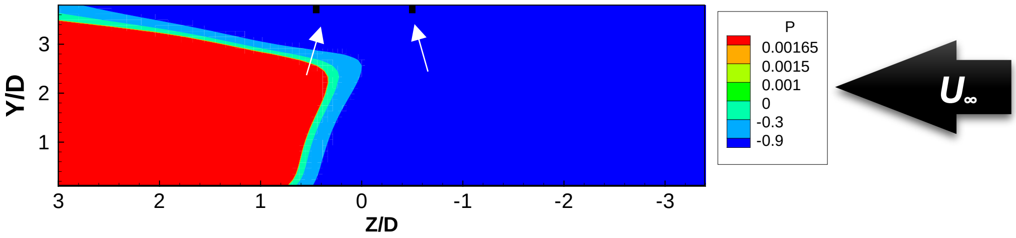

Figure 49: Graphic of pressure distribution in a plane parallel to the ground.

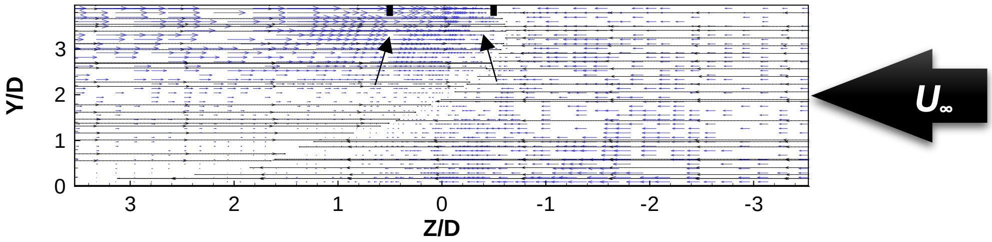

Figure 50: Graphic of velocity vectors in blue and streamlines in black parallel to the ground.

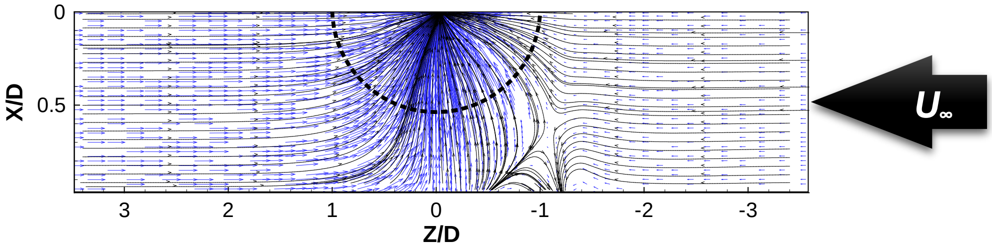

Figure 51: Graphic of velocity vectors in blue and streamlines in black parallel to the inlet plane

4.2 Typical Flow Patterns

4.2.1 No Vortex

Most of the cases of no inlet ground vortex structure are situated below the threshold red line. Nevertheless, some cases were found outside of that region.

Figure 52 shows the results for $h/D_i = 1.56$ and $U_i/U_\infty = 9.09$, that correspond to a case below the threshold line. Several slices parallel to the plane of the ground and to the plane of inlet are presented together with 3D streamtraces, 3D pressure distribution and ground pressure distribution. The results confirm the expected result of no vortex structure formation, and agree with the results available in the literature. The flow is essentially aligned with the crosswind, and only a small region near the inlet is affected by the suction. Nevertheless, no vortex structure can be identified, and neither the inlet nor the ground induce any relevant flow distortion.

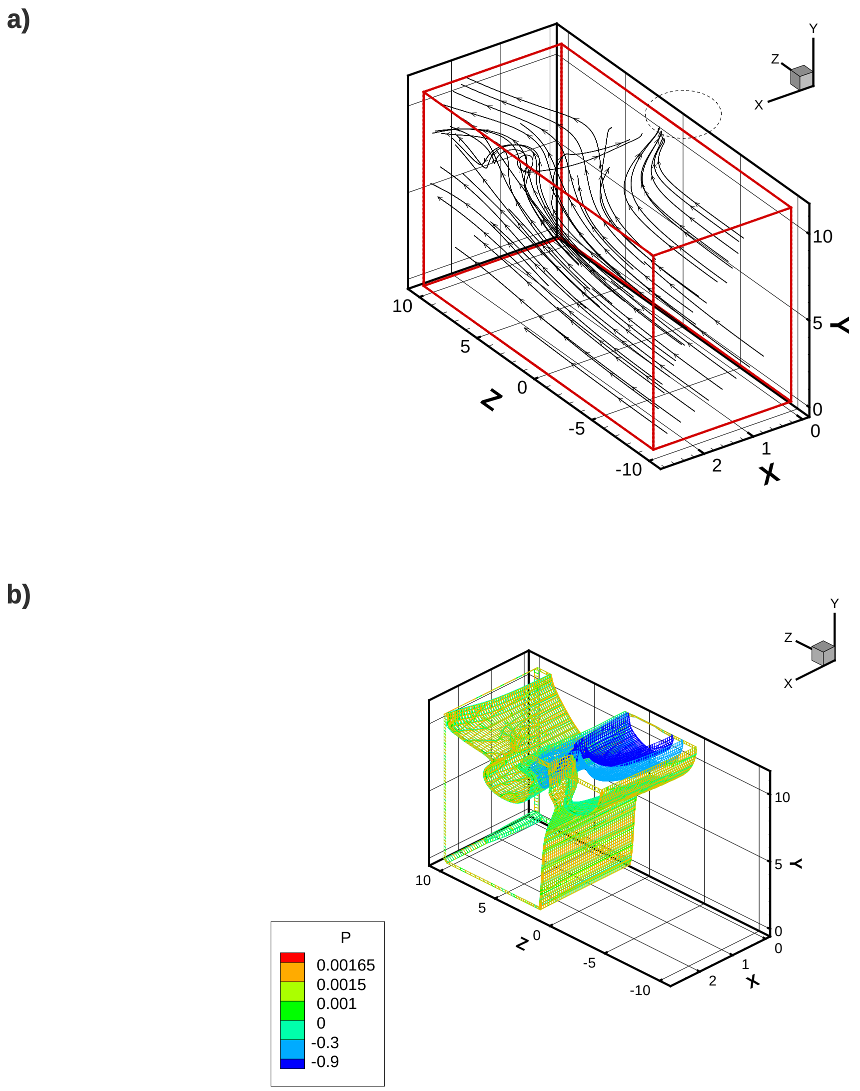

Figure 52: For $h/D_i = 1.56$ and $U_i/U_\infty = 9.09$: a) 3D stream traces; b) 3D pressure distribution; c) pressure distribution in the ground plane; d) plane X=0.95XTOT (ground plane); e) plane X=0.75XTOT; f) plane X=0.50XTOT; g) plane X=0.25XTOT; h) plane .X=0.05XTOT; i) plane Y=0.05YTOT; j) plane Y=0.50YTOT; k) planeY=0.95YTOT.

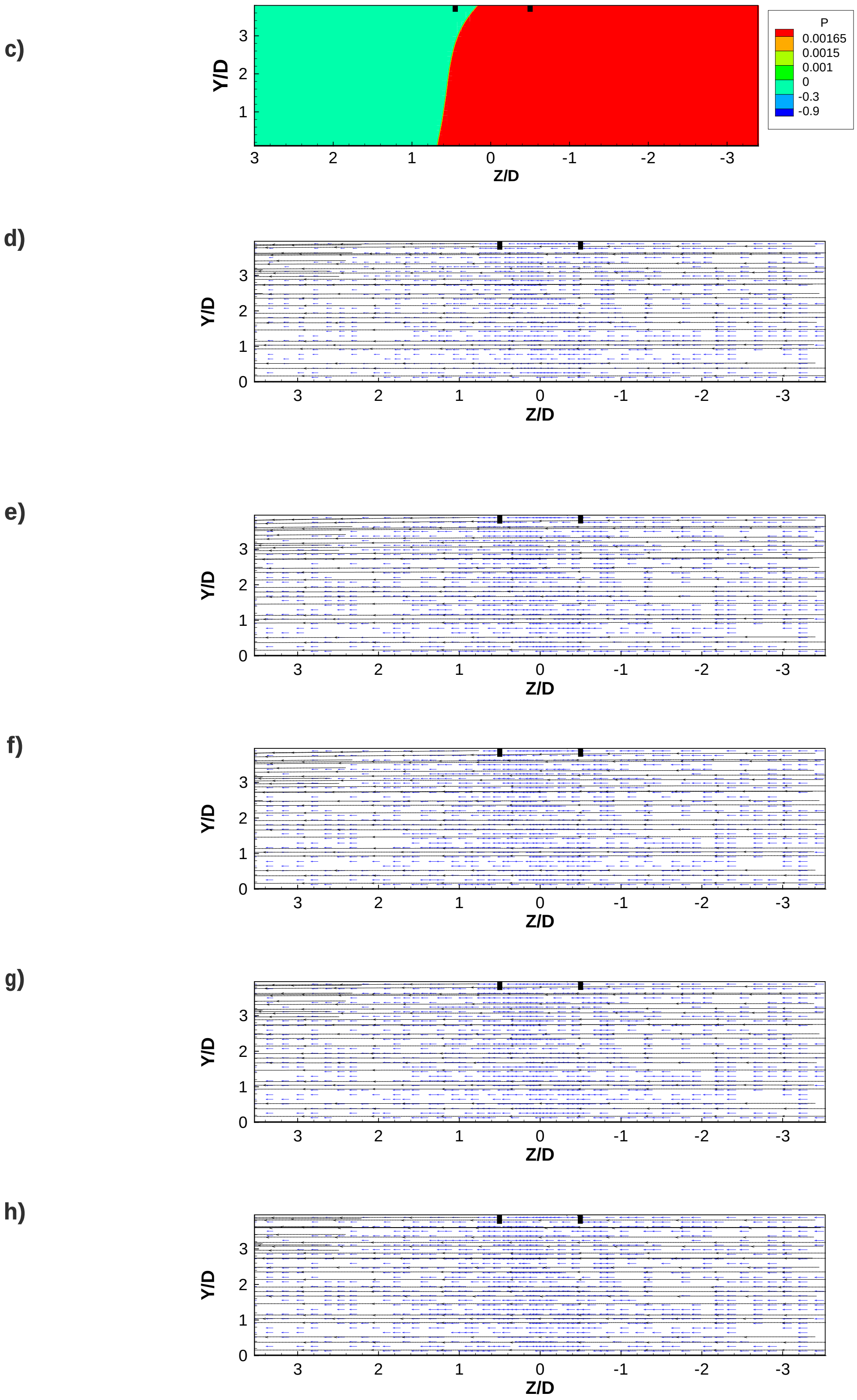

Figure 55 (cont’d)

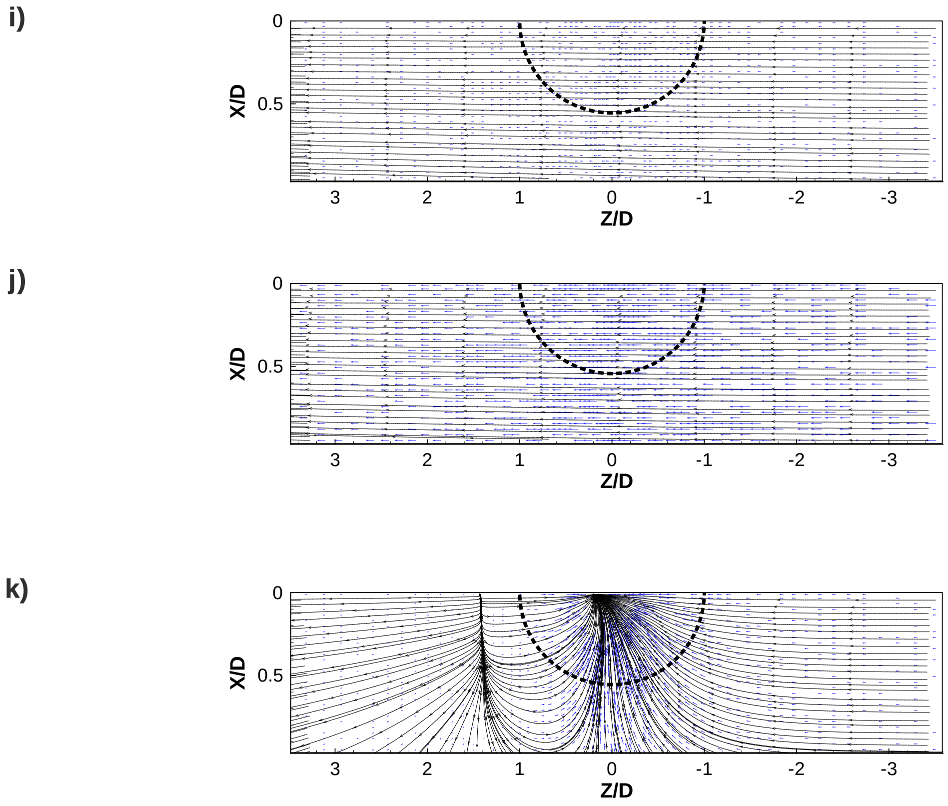

Figure 55 (cont’d)

4.2.2 One Vortex

This section presents an example of the flow with the presence of one inlet ground vortex structure.

The variation of h/D_i affects the position, spin direction and size of the vortical structure. Sometimes the second structure is located far away from the inlet and consists in a small vortex that is blown away downstream. The formation on the main inlet vortex starts upstream of the inlet with a counter clockwise spin and for relatively low U_i/U_∞ the vortex position reaches a more central one, and the spin direction changes from counter to clockwise and finally ends up downstream of the inlet. The suction zone is more intense in the downstream side were the pressure reaches the lowest values.

The interference of the crosswind with the inlet jet flow can be identified from Figure 53d and e with the center of the vortex clearly visible. This was obtained in a plane parallel to the ground at half and 25% of the height of the inlet axis above the ground, confirming that the inlet vortex is a result of the interaction between the crosswind and the inlet flow and does not result from any kind of transformation of the boundary layer vorticity that exists near the ground. In Figure 53f that corresponds to the plane of the inlet the axis of the ground vortex is almost parallel to the engine and close to lower inlet border, as expected.

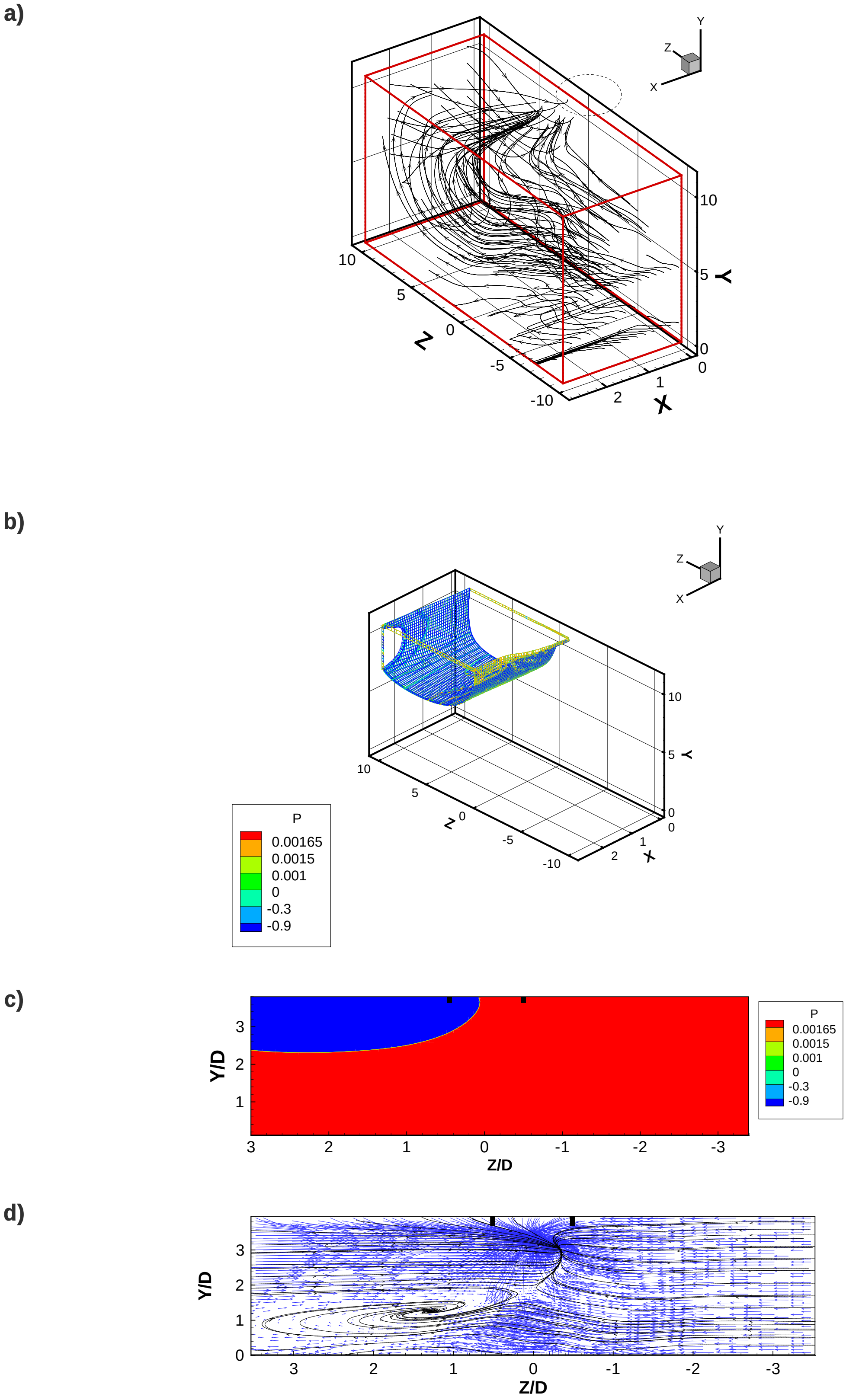

Figure 53: For $h/D_i = 1.00$ and $U_i/U_\infty = 36.36$: a) 3D stream traces; b) 3D pressure distribution; c) pressure distribution in the ground plane; d) plane X=0.50XTOT; e) plane X=0.25XTOT; g) plane Y=0.50YTOT.

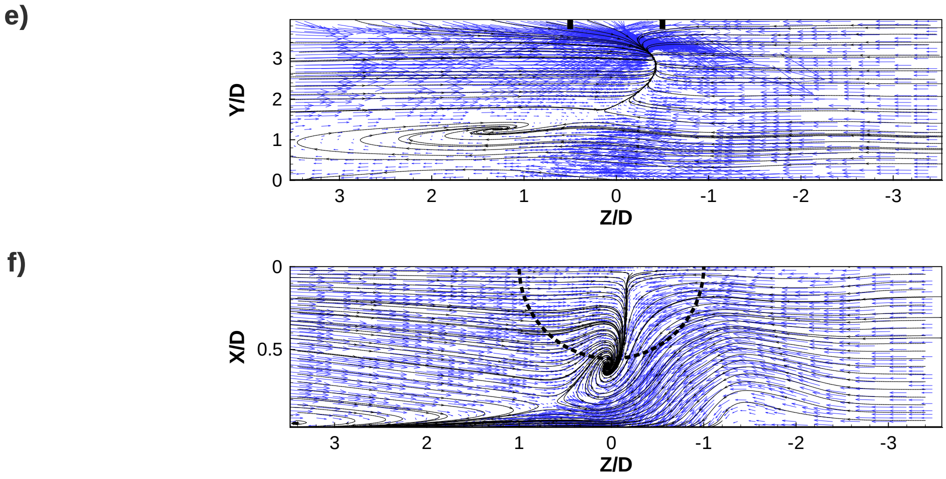

Figure 56 (cont’d).

4.2.3 Two Vortices

Figure 54 shows the results for $h/D_i = 0.82$ and $U_i/U_\infty = 18.18$, revealing a completely different flow pattern. The only suction zones that are detected exist very close the inlet as shown in Figure 54b. In the ground plane the static pressure is always positive (Figure 54c) revealing that the inlet flow is produces relatively close to the engine. Two vortex structures are detected with their axis perpendicular to the engine axis in a horizontal plane at 0.5D from it. These vortex structures already exist near the ground in front of the engine inlet at about 5D of distance (Figure 54e). These two structures are counter rotating, and while the first one enters the engine, the second one remains, and seems to transport fluid from the crosswind directly to the downstream side.

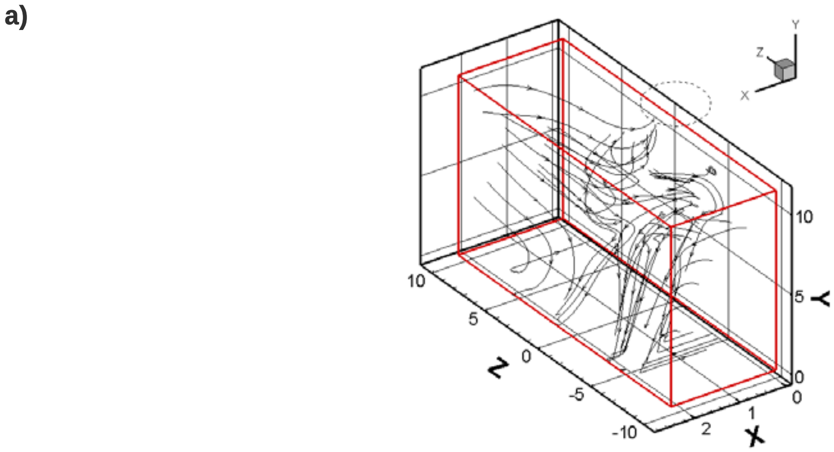

Figure 54: For $h/D_i = 0.82$ and $U_i/U_\infty = 18.18$: a) 3D stream traces; b) 3D pressure distribution; c) pressure distribution in the ground plane; d) plane X=0.50XTOT; e) plane Y=0.50YTOT.

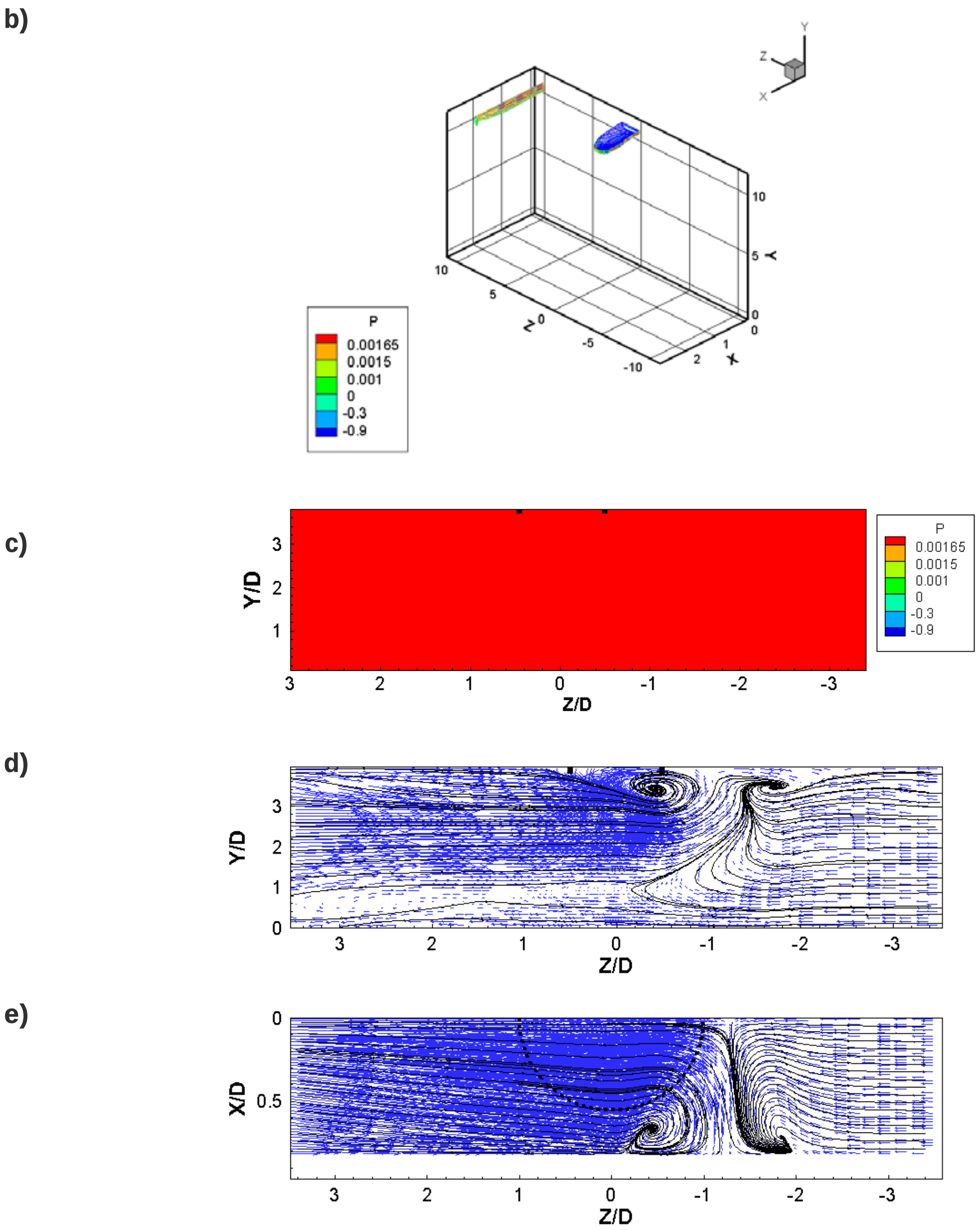

Fig. 54 (cont'd)

4.2.4 Three Vortices

In this section the three vortex flow configurations is analyzed. Preliminary results of this work were firstly shown in the literature by Barata et al. [19]. This setting seems to occur more often with lower values of h/D_i (h/D_i<1.00) and for various values of U_i/U_∞.

Figure 55 shows large vortices in farthest plane parallel to the inlet plane, then halfway through to the inlet only two vortices become visible, and then nearest to the inlet all vortices are ingested.

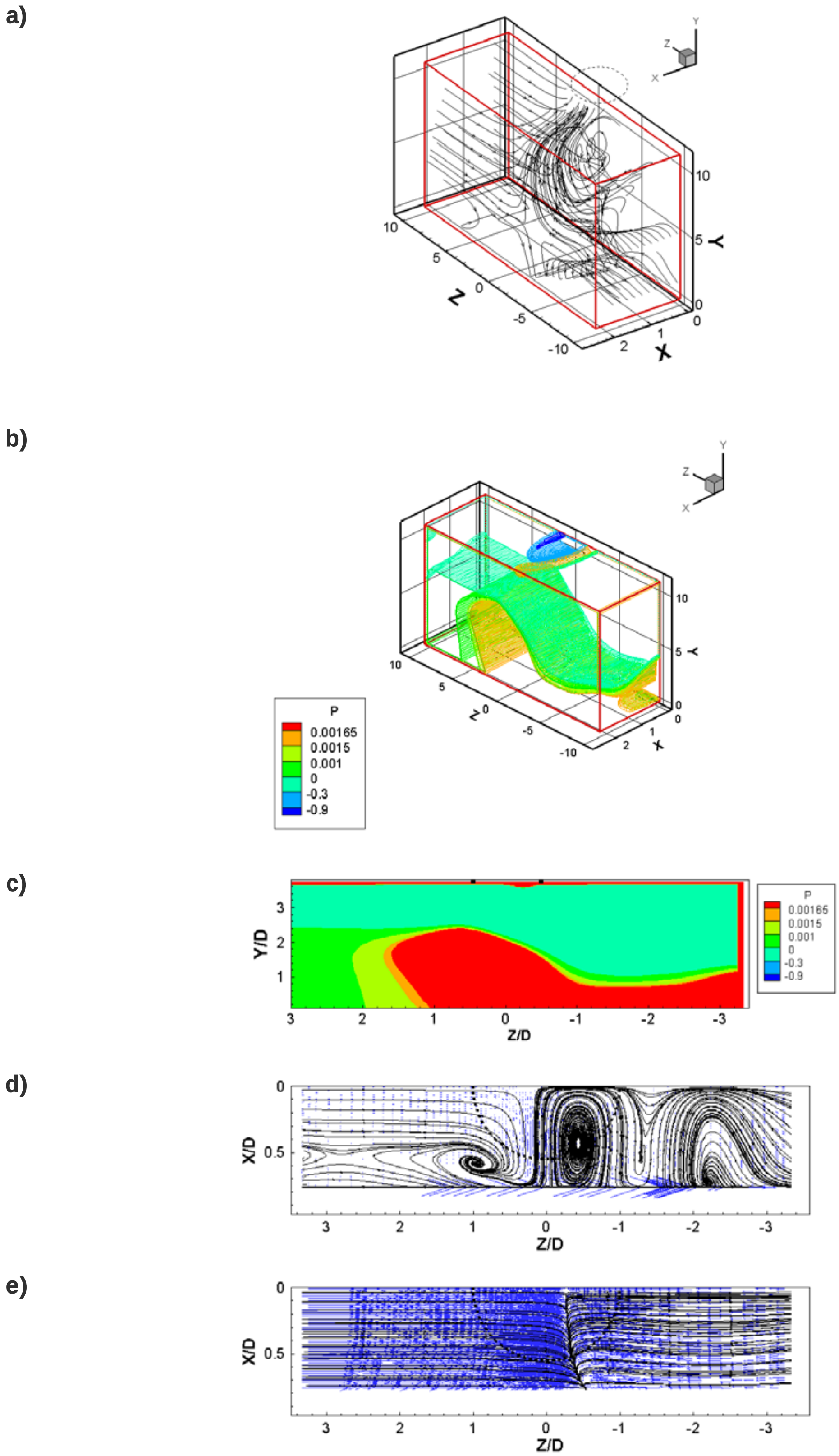

Figure 55: For $h/D_i = 0.77$ and $U_i/U_\infty = 72.73$: a) 3D stream traces; b) 3D pressure distribution; c) pressure distribution in the ground plane; d) plane Y=0.05YTOT; e) plane Y=0.50YTOT; f) plane Y=0.95YTOT.

f)

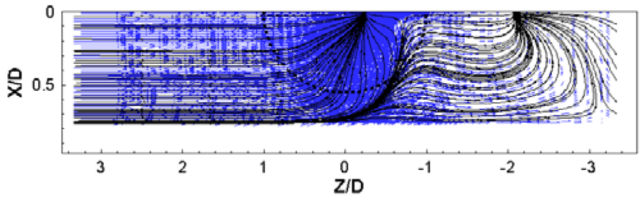

Figure 55 (cont'd)

4.2.5 Four Vortices

This mode has been described as a transition phase between two modes of counter rotating vortices one for high U_i/U_∞ and another for low U_i/U_∞.

Figure 56 shows the flow pattern for $h/D_i = 0.86$ and $U_i/U_\infty = 18.18$ with the four vortex structures present. This condition is characterized by a strong blockage of the crosswind that has only 0.36 D_i without the direct effect of the suction from the engine inlet. Far away from the inlet plane a single vortex is in formation (Figure 56e), but closer to the inlet in a plane parallel to it at 5D$_i$ the four structures can be identified. The central one is probably the responsible for the other since interacts with the crosswind and generates first two counter-rotating vortices side-by-side, and then a fourth one appears only in the crosswind side.

This flow pattern is extremely complex, and more investigation is required to determine all the mechanisms involved, and why it is generated for heights and velocity combinations that usually are expected to correspond to a different regime.

a)

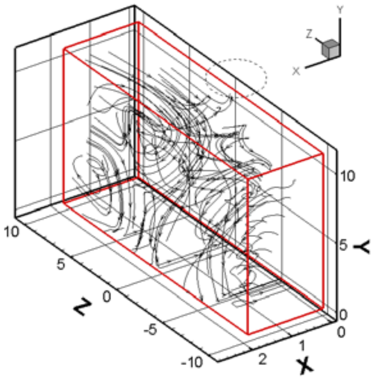

Figure 56: For $h/D_i = 0.86$ and $U_i/U_\infty = 18.18$: a) 3D stream traces; b) 3D pressure distribution; c) pressure distribution in the ground plane; d) plane Y=0.50YTOT; e) plane Y=0.95YTOT.

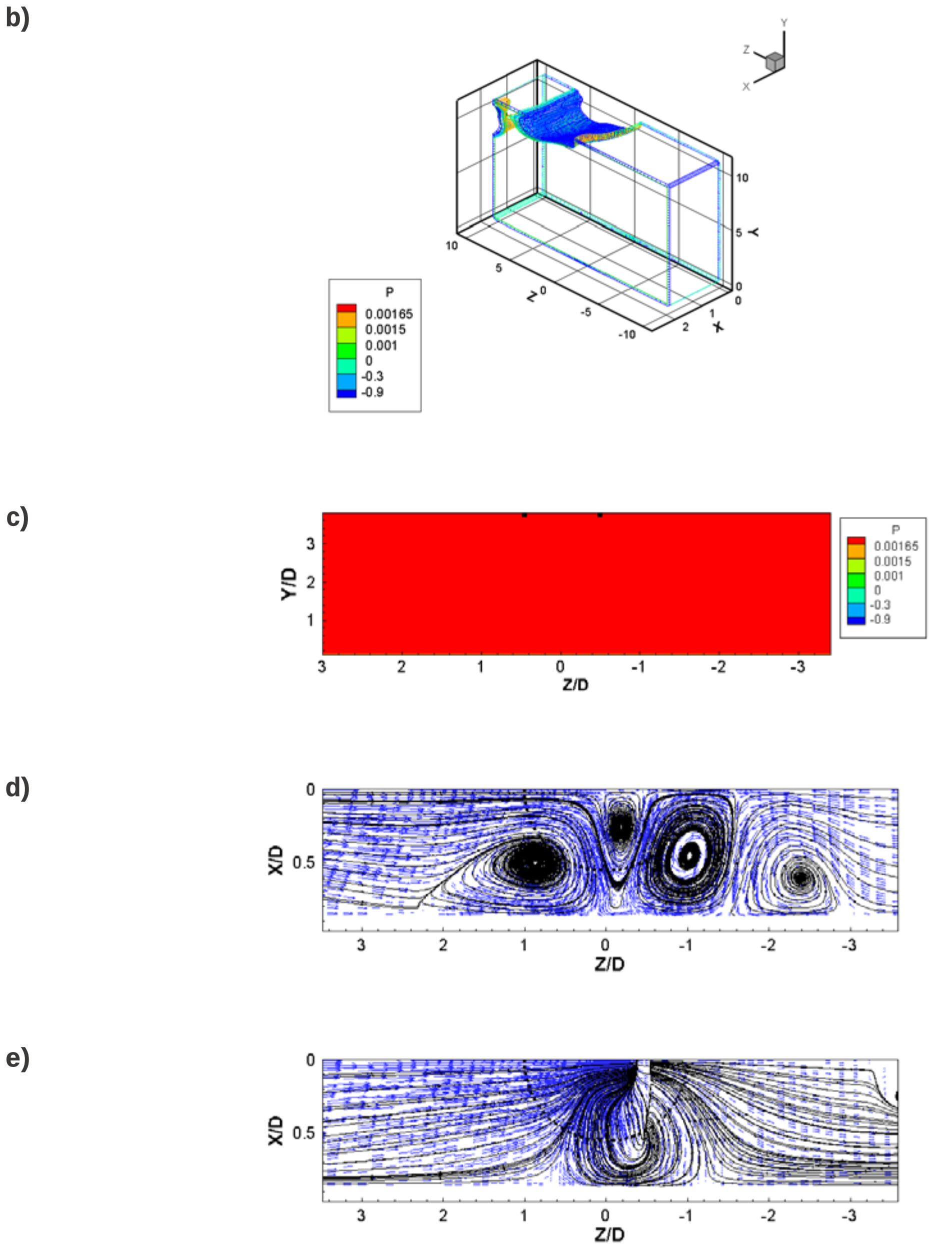

Figure 56 (cont'd).

4.3 Summary

This chapter has shown the typical flow patterns of the inlet ground vortex.

Selected configurations that produced no vortex or several vortex structures were analyzed in detail.

A complete set of the computations are presented in Annex A.

Chapter 5 Discussion

5.1 Introduction

This chapter discusses the main results of the present study under two headings. First the notable ground pressure distributions will be analyzed and related with the inlet ground vortex phenomena. Then the complete set of calculations that resulted from the present work is systematized in terms of the relevant adimensional parameters ($h/D_i = 0.86$ and U_i/U_∞).

5.2 Ground Pressure Distribution

The analysis of the ground pressure distribution in conjugation with the streamtraces is a good indication of the flow behavior. The existence of a large region of negative pressures (that can extend up to the ground plane) induces the most complex of the flows (Figure 57).

a)

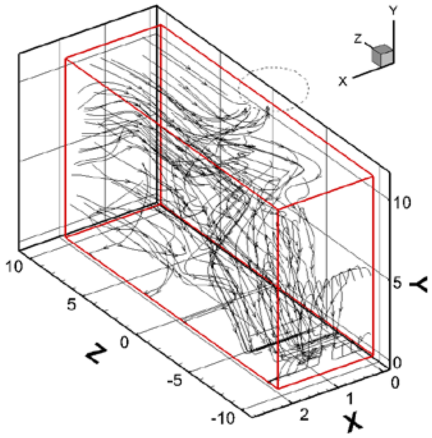

Figure 57: For $h/D_i = 1.17$ and $U_i/U_\infty = 27.27$: a) 3D stream traces; b) 3D pressure distribution; c) pressure distribution in the ground plane; d) plane X=0.50XTOT; e) plane X=0.25XTOT; f) plane Y=0.05YTOT; g) plane Y=0.50YTOT; h) plane Y=0.95YTOT.

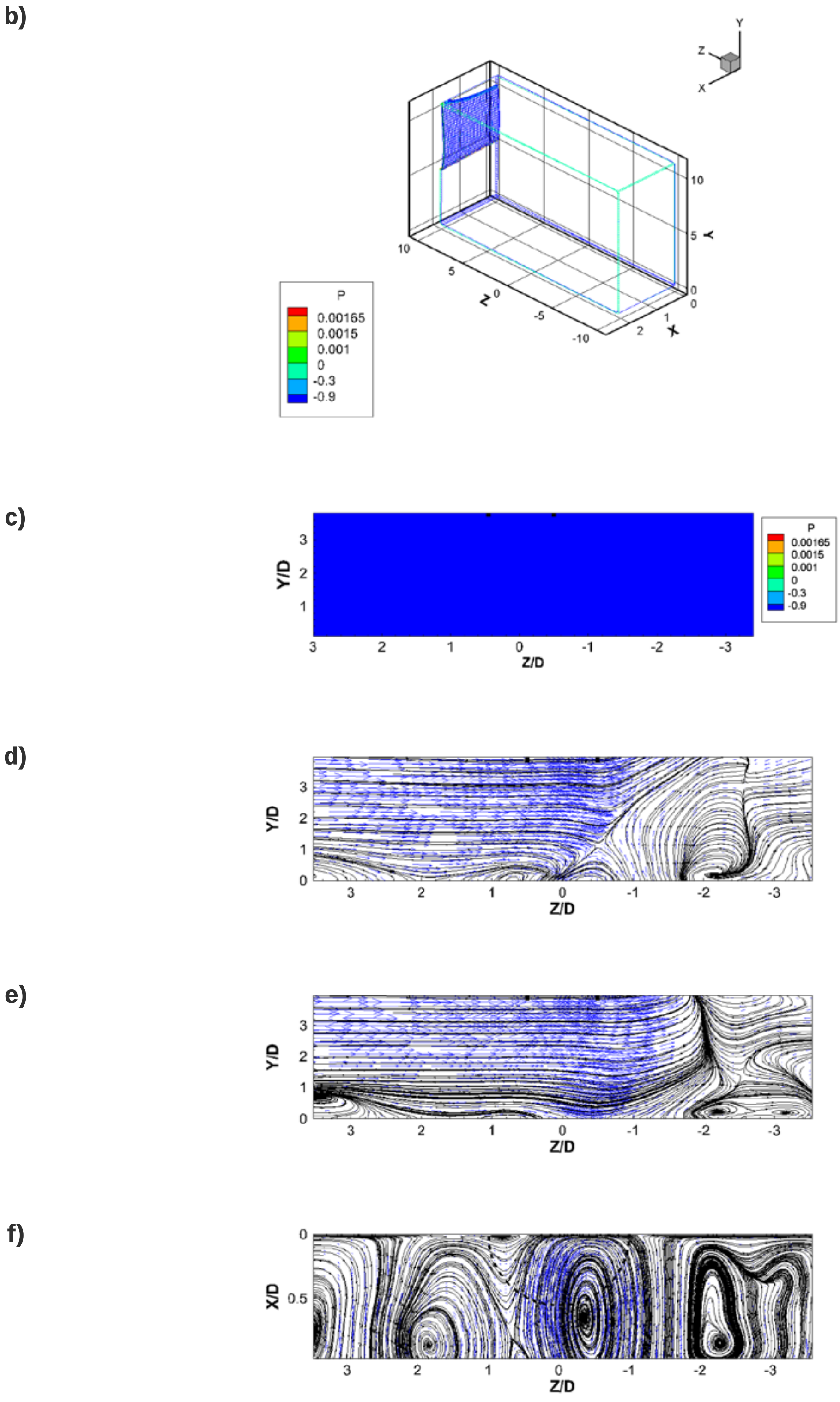

Figure 57 (cont'd).

g)

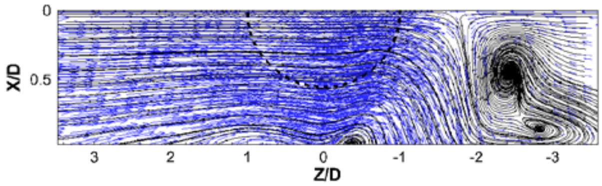

h)

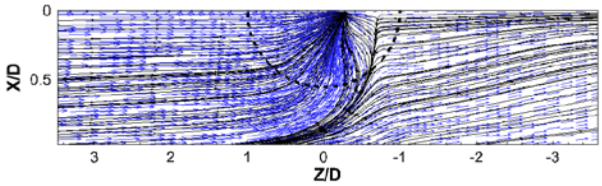

Figure 57 (cont'd).

Usually the larger the negative pressure region the more complex is the flow, and more ground vortex structures are formed. The flow is essentially tridimensional, and once the inlet ground vortex structure is formed due to the interaction with the crosswind at the engine inlet, then other secondary vortex structures appear. These structures are not directed to the engine inlet but are bended by the crossflow, and align with the crossflow, although at some position far from the inlet plane they can have their axis parallel to the engine. This happens in the present case at about 10Di from the inlet plane (Figure 57f).

5.3 Inlet ground vortex regimes

The next figures represent the number of vortex structures as a function of the velocity ratio h/D_i and U_i/U_∞ for all the 572 cases studied in the present work.

All these simulations where made for an irrotational crosswind of 2.2 m/s and different engine sizes (R from 0.75 to 1.5m).

As explained in Section 2.4 the red line represents the threshold reported in the literature between the vortex and no vortex formation as a function of the non-dimensional parameters h/D_i and U_i/U_∞.

Figure 58 to Figure 66 show that for high values of h/D_i or lower values of r (r<1.00) there are more simulations with no vortex and that the level of complexity of the flows is lower for all range of $\boldsymbol{U_i/U_\infty}$.

Figure 64 to Figure 66 exhibit two areas of greater concentration of no vortex $\boldsymbol{h/D_i}$ and U_i/U_∞ combinations. The first is the expected frontier between the regions above mentioned (vortex/no vortex) that is clearly in agreement with the threshold reported in the literature. This is quite evident from Figure 63, Figure 64, and Figure 65, but also a second zone exists for high values of U_i/U_∞ (>50.00) that is not mentioned in the literature.

The present study also revealed that some situation above the threshold line, which had been not considered before, can also correspond to situations of no vortex formation. For example Figure 58 for the lowest values of h/D_i and for all range of $\boldsymbol{U_i/U_\infty}$ six of the eight simulations corresponds to no vortex cases.

These graphics have been accepted to provide the threshold for the inlet ground vortex formation are useful for low velocity ratios $U_i/U_\infty$where a good agreement with the experiments and computations is observed. However, in the upper part (above the threshold line) it is not possible to ensure that there is always one inlet ground vortex formation. Additionally, when this is the case this chart is of no help to predict the number of vortex structures that will be produced or what is the nature of the flow pattern. This is an indication that other parameters may influence the flow for higher velocity ratios U_i/U_∞ which have not been considered so far and require further investigation.

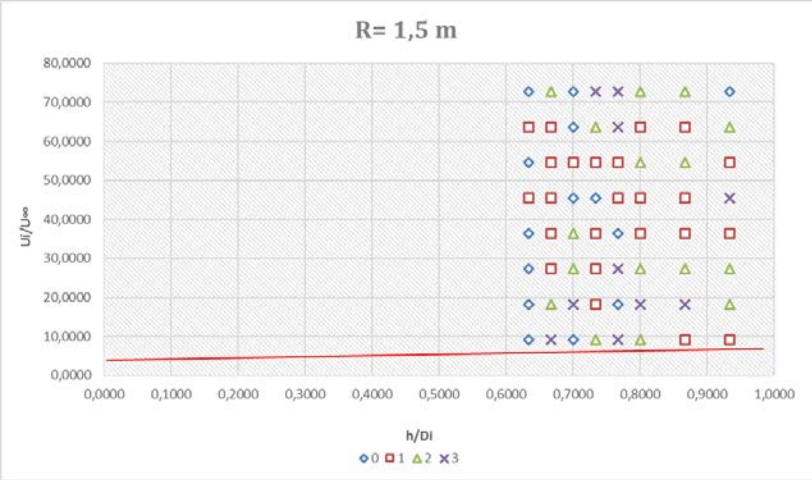

Figure 58: Number of vortex structures for r=1.5 m

Figure 59: Number of vortex structures for r=1.4 m

Figure 60: Number of vortex structures for r=1.3 m

Figure 61: Number of vortex structures for r=1.2 m

Figure 62: Number of vortex structures for r=1.1 m

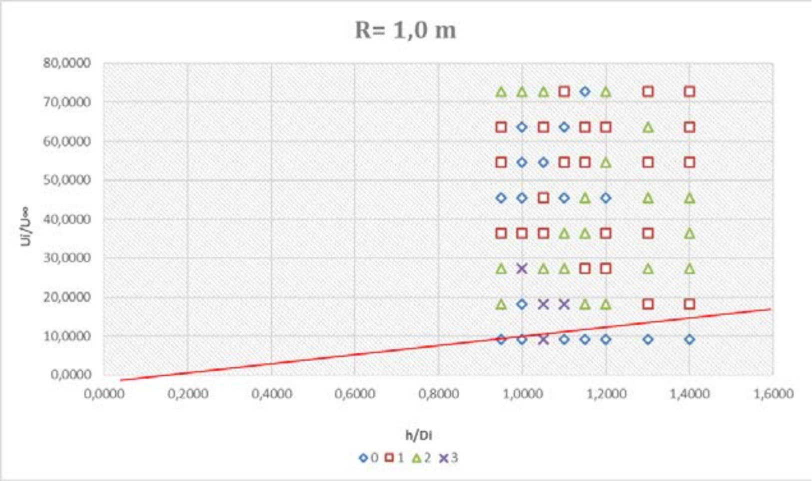

Figure 63: Number of vortex structures for r=1.0 m

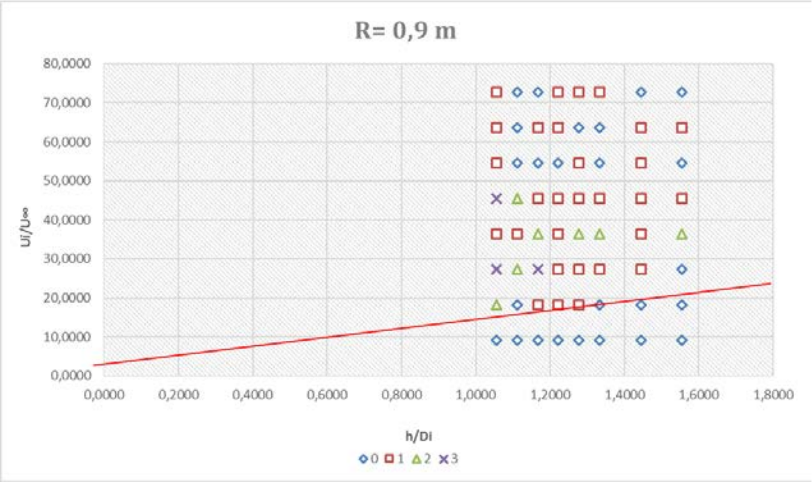

Figure 64: number of vortices present for a value of r=0.9 m

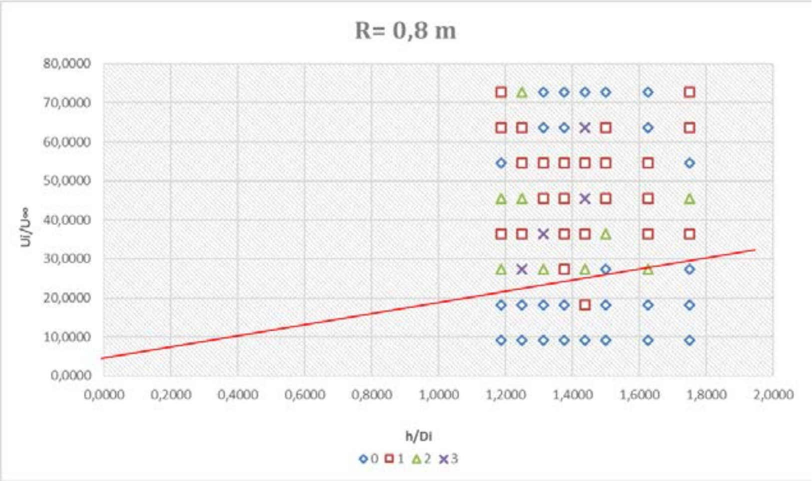

Figure 65: Number of vortex structures for r=0.8 m

Figure 66: Number of vortex structures for r=0.75 m

Chapter 6 Conclusions

The first thing we can conclude is that for high values of h/D_i or lower values of r (r<1.00) there are more simulations with no vortex and the level of complexity of the flows is lower for all range of U_i/U_∞.

There are two areas of no vortex as a function of h/D_i and U_i/U_∞. The first is the anticipated frontier (threshold) between the regions vortex/no vortex, but a second one was detected for high values of U_i/U_∞ (U_i/U_∞ >50.00) that had not been mentioned in previous works.

However, when the value of h/D_i declines in virtue of the growth of r (r≥1.00) this state changes then we can see a rise of the complexity of the flows and a decline in no vortex states.

This clearly indicates an influence of r not only h/D_i.

Also for the lowest value of h/D_i and for all range of U_i/U_∞ we can find simulations that are on no vortex state.

It could be identified the structure downstream of the intake that captures some of the free flow and forces it back to be ingested be inlet as exposed by Zantopp [32].

We have identified a structure upstream of the inlet that we cannot call a ground vortex because it rotates towards the ground that cause a deflection of the ingested flow and its increase in velocity and then it is capture and ingested. The conjugation of both has also been identified. This is probably due to the conjugation of high h/D_i and high U_i/U_∞ and the interaction of the flow with the inlet lip or with the sucked stream tube.

In all the cases the ingested flow is relatively undisturbed.

Has expected for high h/D_i or low U_i/U_∞ most of the flow ingested by the inlet comes from upstream and for low h/D_i or high U_i/U_∞ the ingested flow comes more evenly from both upstream and downstream. This is due to the difference in shape of the captured area.

For the case of one vortex the position, spin direction and size of the vortical structure changes with D_i and U_i/U_∞. The vortex formation starts in the upstream of the inlet with a counterclockwise spin and with the decreasing of U_i/U_∞ and D_i the vortex position passes to a more central one, the spin direction changes from contra to clockwise and finally ends up downstream of the inlet with a clockwise spin and similar size of the first on. With a further reduction of D_i the vortex tends to stay in a more central area and with a clockwise spin.

As expected, in the case of two vortices the majority are encountered in counter rotation in a more central position and some smaller ones in an upstream position.

This kind of setting has a larger occurrence for high values of r ($r \geq 1.00$) and are manly concentrated in a region near the border between the vortex/no vortex areas even for the cases of lower r ($r<1.00$) which may represent that this setting is manly a transition setting between the two regions. In the case of the lower r almost all occurred for a $U_i/U_\infty < 50.00$.

In relation to the three vortex mode this setting does seems to occur more often with lower values of h/D_i ($h/D_i<1.00$) and for various values of U_i/U_∞. This case may be considered a transition phase between two other settings.

The four vortex mode has been described as a transition phase among two modes of counter rotating vortices one for high U_i/U_∞ and another for low U_i/U_∞. All sets of this mode are for $30>U_i/U_\infty>18$ and have essentially the same flow pattern.

When ground pressure distribution it is completely negative vorticity is always present with a tendency to be the most complex of the flows.

With a large positive pressure and an abrupt switch to negative pressure also always presents vorticity. The same happens when the reverse occurs.

When the pressure is low but gradually rises in the direction of the crosswind then no vorticity is verified.

The inlet ground vortex mechanism is a very complex one which should be further investigated, and experimental works are desirable.

References

[1] K. Hünecke, Jet Engines: Fundamental of theory, design and operation, UK: Airlife publishing, 1997.

[2] C. Johns, "The Aircraft Engine Inlet Vortex Problem," em *AIAA's Aircraft Technology, Integrations and Operations*, Los Angles, California, 2002.

[3] M. Swainston, "Vortex Formation Near Intakes to Turbomachinery and Duct Systems," *Heat and Fluid Flow,* vol. Vol. 4, p. No. 2, 1974.

[4] A. Nakayama e J. Jones, "Correlation for Formation of Inlet Formation," *AIAA Journal,* vol. Vol. 37, p. No. 4: Technical Notes, 1998.

[5] D. Motycka e W. Walter, "An Experimental Investigation of Ground Vortex Formation During Reverse Thrust Operation," em *AIAA/SAE 11th Propulsion Conference AIAA Paper No. 75/1322*, 1975.

[6] S. Brix, G. Neuwerth e D. Jacob, "The Inlet-Vortex System of Jet Engines Operating Near the Ground," *AIAA Paper,* Vols. %1 de %22000-3998, 2000.

[7] F. De Siervi, H. Viguier, E. Greitzer e C. Tan, "Mechanisms of Inlet Vortex Formation," *J. Fluid Mech,* vol. Vol. 124, pp. pp. 173-207, 1982.

[8] Y. Yadlin, "Simulation of Vortex Flows for Airplanes in Ground operations," *AIAA Paper 2006-56,* 2006.

[9] D. Glenny, "Ingestion of debris into intakes by vortex action," Ministry of Technology, Aeronautical Research Council, , 1968.

[10] L. Rodert e F. Garrett., "Ingestion of foreign objects into turbine engines by vortices," National Advisory Committee for Aeronautics, 1953.

[11] L. Di Mare, G. Simpson e A. Sayma, "Fan forced response due to ground vortex ingestion," em *Proceedings of ASME Turbo Expo 2006: Power for Land, Sea and Air*, Barcelona, Spain, 2006.

[12] H. J. Klein, "Vortex inhibitor for aircraft jet engines". US Patent Patente 2,915,262, 1st December 1959.

[13] A. Shmilovich, " Active system for wide area suppression of engine vortex". US Patent Patente 6,763,651, 10th July 2004.

[14] P. O. Cox, J. William e R. R. Engines, "Pod for a Gas Turbine Engine". 28 Oct Patente 3,474,988, 28 Oct 1969.

[15] D. M. Smith e D. M. Dorris, "Aircraft engine apparatus with reduced inlet vortex". US Patente 6,129,309, 10th Oct 2000.

[16] J. P. Smith, "Protective Air Curtain for Aircraft Engine Inlet". U.S. Patent Patente

3,527,430, 8 Aug 1970.

[17] J. M. M. Barata, A. Maneta e A. Silva, "Numerical Study of a Gas Turbine Engine Ground Vortex," em *45th AIAA/ASME/SAE/ASEE Joint propulsion Conference & Exhibit*, Denver, 2009.

[18] J. M. M. Barata, P. Manquinho e A. Silva, "A Comparison of Different Gas Turbine Engines Ground Vortex Flows," em *AIAA 2010-7116, 46th AIAA/ASME/ SAE/ASEE Joint Propulsion Conference and Exhibit*, Nashville, Tennessee, 2010.

[19] J. M. M. Barata, P. Manquinho e A. Silva, "Identification of Gas Turbine Ground Vortex Formation Regimes," em *50th AIAAAerospace Sciences Meeting*, Nashville, 2012.

[20] S. Green, Fluid Vortices: Fluid Mechanics and its Applications, Kluwer Academic Publishers, 1995.

[21] L. Rehby, "Jet Engine Ground Vortex Studies," MSc Aerodynamics , Crandfield University, 2007.

[22] J. Leishman, Principles of Helicopter Aerodynamics, Cambridge University Press, 2000.

[23] J. Seddon e E. Goldsmith, Intake Aerodynamics, Blackwell science, 1985.

[24] G. Batchelor, An Introduction to Fluid Dynamics, Cambridge University Press, 1967.

[25] J. J. Colehour e B. Farquhar, "Inlet vortex," *Journal of Aircraft,* vol. 8(1), p. 39–43, 1971.

[26] W. Liu, E. Greitzer e C. Tan, " Surface static pressures in an inlet vortex flow field," *Journal of Engineering for Gas Turbines and Power,* vol. 107, p. 387–393, 1985.

[27] H. W. Shin, E. M. Greitzer, W. K. Cheng, C. S. Tan e C. L. Shippee, "Circulation measurements and vortical structure in an inlet vortex flow field," *Journal of Fluid Mechanics,* vol. 162, p. 463–487, 1986.

[28] A. Nakayama e J. Jones, "Correlation for Formation of Inlet Formation," *AIAA Journal,* vol. Vol. 37, p. No. 4: Technical Notes, 1998.

[29] M. Jermy e H. W. H., "Location of the vortex formation threshold at suction inlets near ground planes by computational fluid dynamics simulation," Department of Mechanical Engineering, University of Canterbury,, Christchurch, New Zealand,, 2008.

[30] J. Murphy, D. MacManus e M. Taylor., " A quantitative study of intake ground vortices," em *ISABE Paper ISABE-2007-1209*, Beijing, China, 2007.

[31] N. Bissenger e G. Braun, "On the inlet vortex system," National Aeronautics and Space Administration, 1974.

[32] D. Motycka, W. Walter e G. Muller, "An analytical and experimental study of inlet ground vortices," em *AIAA/SAE 9th Propulsion Conference*, 1973.

[33] I. A. Waitz, E. M. Greitzer e C. S. Tan, "Vortices in Aero-Propulsion Systems," em *Fluid Vortices, volume 30 of Fluid Mechanics and its Applications*, Kluwer Acedemic Publishers, 1995, p. 471–532.

[34] S. Zantopp, “Jet engine ground vortex studies,” Cranfield University, 2008.

[35] L. G. Trapp e R. d. M. Girardi, “Crosswind Effects on Engine Inlets: The Inlet Votex,” *Journal of Aircraft,* Vols. %1 de %2 Vol. 47, No. 2, pp. 577-590, 2010.

[36] A. Shmilovich e Y. Yadlin, “Flow Control Techniques for Transport Aircraft,” *AIAA Journal,* Vols. %1 de %2 Vol. 49, No. 3, 2011.

[37] A. Shmilovich e Y. Yadlin, “Engine Ground Vortex Control,” em *24th Applied Aerodynamics Conference*, San Francisco, California, 2006.

[38] C. R. Vanfleet e W. C. Ruehr, “Method and apparatus for limiting ingestion of debris into the inlet of a gas turbine engine.”. US Patente 4,070,827, 31st Jan 1978.

[39] J. P. Murphy e D. G. MacManus, “Inlet Ground Vortex Aerodynamics Under Headwind Conditions,” *Aerospace Science and Technology,* Vols. %1 de %2Vol. 15,, pp. 207-215, 2011.

[40] A. Secareanu, D. Moroianu, A. Karlsson e L. Fuchs, ““Experimental and Numerical Study of Ground Vortex Interaction in an Air-Intake,” *AIAA Paper,* Vols. %1 de %22005-1206,, 2005.

[41] B. E. Launder e D. B. Spalding, “The Numerical Computation of Turbulent Flows,” *Computer Methods in Applied Mechanics and Engineering,* Vols. %1 de %2Vol. 3, No. 2, pp. 269-289, 1974.

[42] B. P. Leonard, M. A. Leschziner e J. J. McGuirk, “Third-Order Finite-Difference Method for Steady Two-Dimensional Convection edited by C. Taylor et a,” em *1st International Conference on Numerical Methods in Laminar and Turbulent Flow*, London , 1978.

[43] B. P. Leonard, “A Stable and Accurate Convective Modelling Procedure Based on Quadratic Upstream Interpolation,” *Computer Methods in Applied Mechanics and Engineering,* Vols. %1 de %2Vol. 19, No.1, pp. 59-98, 1979.

[44] J. M. M. Barata, D. F. G. Durão e J. J. McGuirk, “Numerical Study of Single Impinging Jets Through a Crossflow,” *Journal Of Aircraft,* vol. Vol. 26, pp. 1002-1008, 1989.

[45] A. D. Gosman e W. M. Pun, “Calculation of Recirculating Flows,” *Imperial College,* vol. Ret. HTS/74/2, 1974.

[46] J. M. M. Barata, A. Cometti, A. Mendes e A. R. R. Silva, “Numerical Simulation of an Array of Droplets Through a Crossflow,” em *40th AIAA Aerospace Sciences Meeting and Exhibit AIAA paper 2002-0872*, Reno, Nevada, 2002.

[47] A. R. R. Silva, A. Mendes, A. Cometti e J. M. M. Barata, “Numerical Studies of biphasic tridimensional Flows",,” em *V Congresso de Métodos Numéricos en Ingenéria*, Madrid, Spain, 2002.

[48] S. V. Patankar e D. B. Spalding, “A Calculation Procedure for Heat, Mass and Momentum Transfer in Three- Dimensional Parabolic Flows,” *International Journal of Heat and Mass Transfer,* Vols. %1 de %2Vol. 15, No. 10, pp. 1787-1805, 1972.

[49] A. Maneta, “Numerical study of Ground vortex formation,” UBI, Covilhã, 2009.

[50] J. Mattingly, W. Heiser e D. Daley, Aircraft Engine Design, New York: AIAA Education Series, 1987.

[51] J. Mattingly, Elements of Gas Turbine Propulsion, Singapore: McGraw-Hill, 1996.

[52] G. B. (. A. I. t. F. D. C. U. Press, An Introduction to Fluid Dynamics, Cambridge University Press, 1967.

Annex A Complete Set of Results

A.1. No Vortex

a)

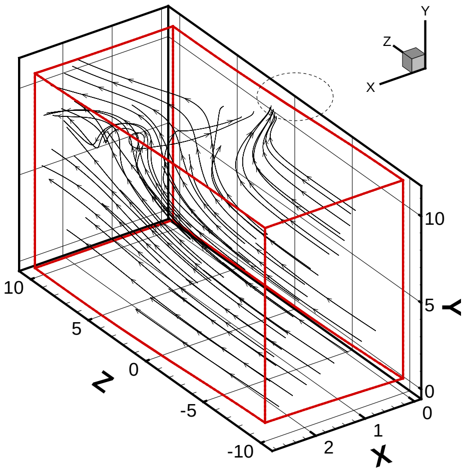

b)

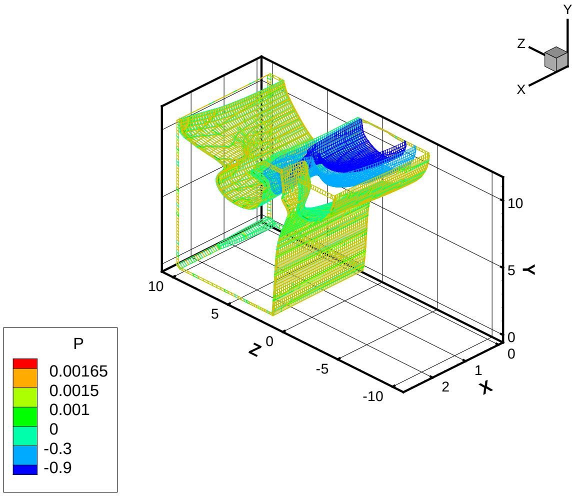

c)

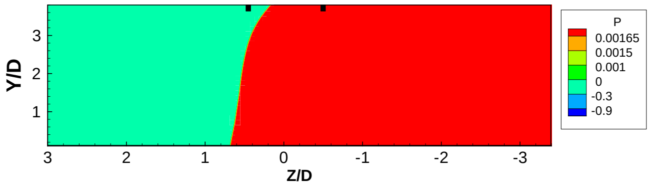

d)

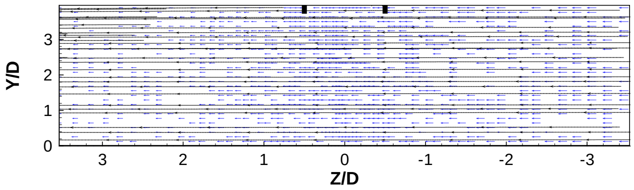

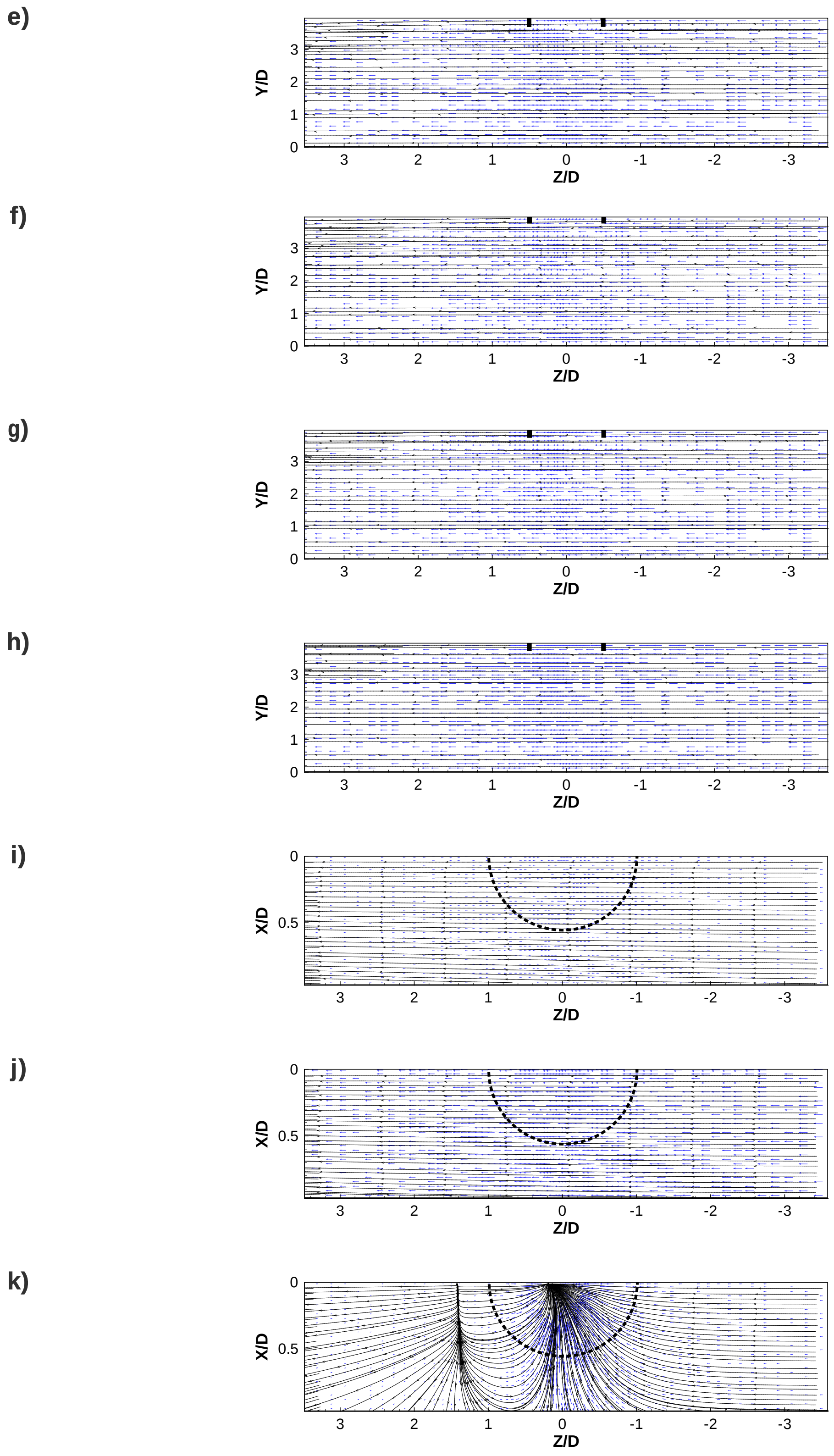

Figure 67: For $h/D_i = 1.56$ and $U_i/U_\infty = 9.09$: a) 3D stream traces; b) 3D pressure distribution; c) pressure distribution in the ground plane; d) plane X=0.95XTOT (ground plane); e) plane X=0.75XTOT; f) plane X=0.50XTOT; g) plane X=0.25XTOT; h) plane .X=0.05XTOT; i) plane Y=0.05YTOT; j) plane Y=0.50YTOT; k) planeY=0.95YTOT.

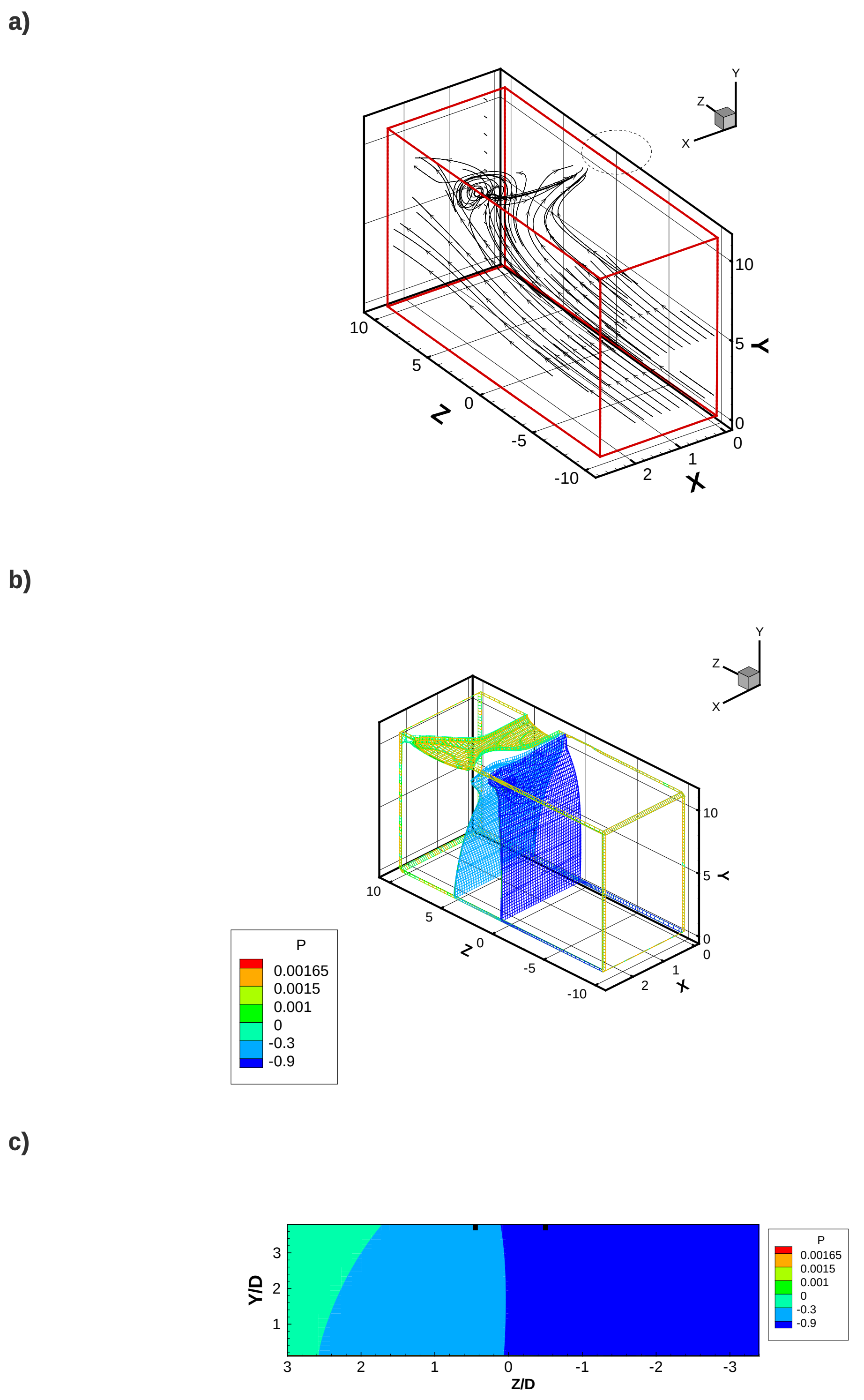

Figure 68: For h/D_i =1.44 and U_i/U_∞=9.09: a) 3D stream traces; b) 3D pressure distribution; c) pressure distribution in the ground plane;

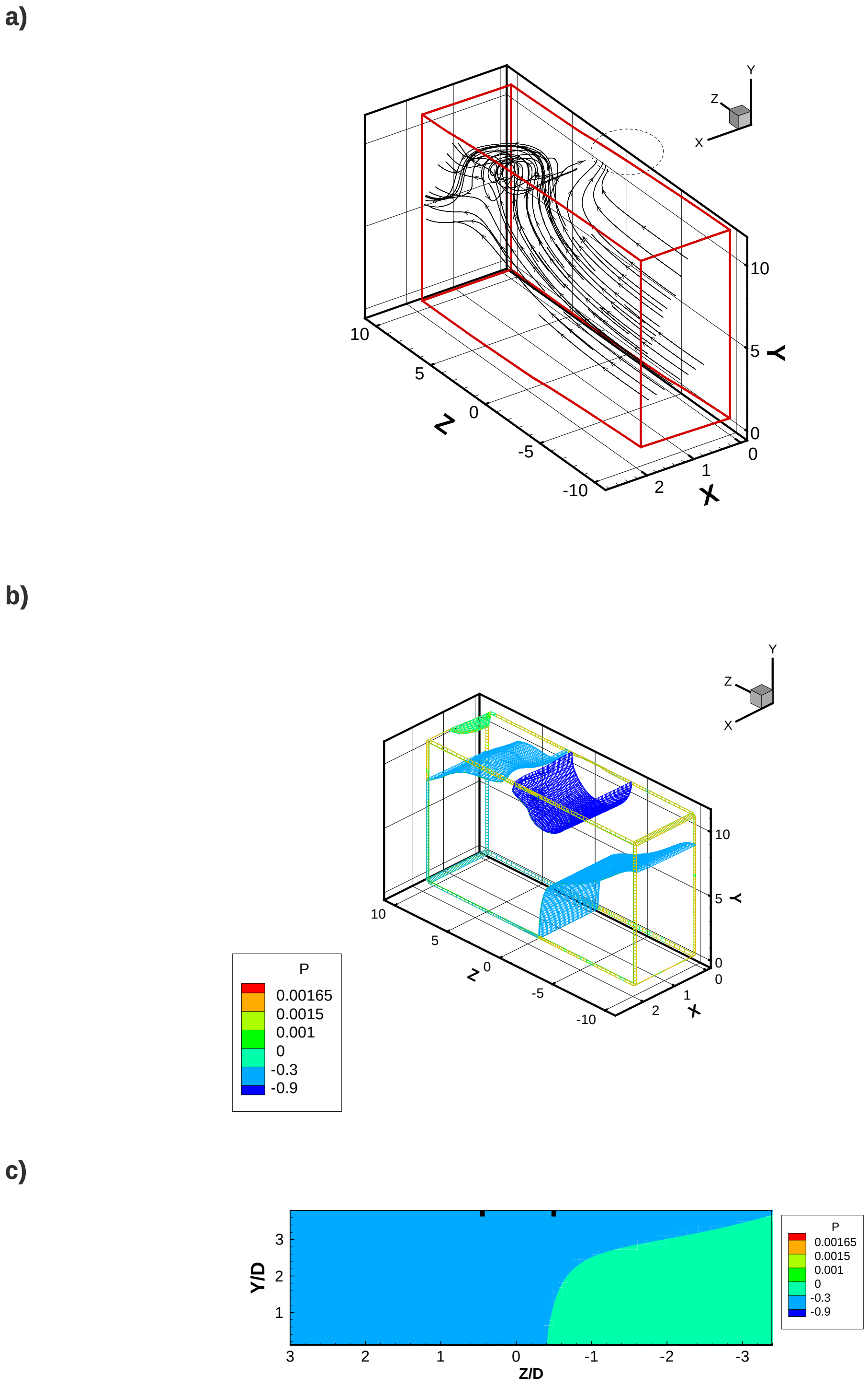

Figure 69: For h/D_i =1.06 and U_i/U_∞=9.09: a) 3D stream traces; b) 3D pressure distribution; c) pressure distribution in the ground plane;

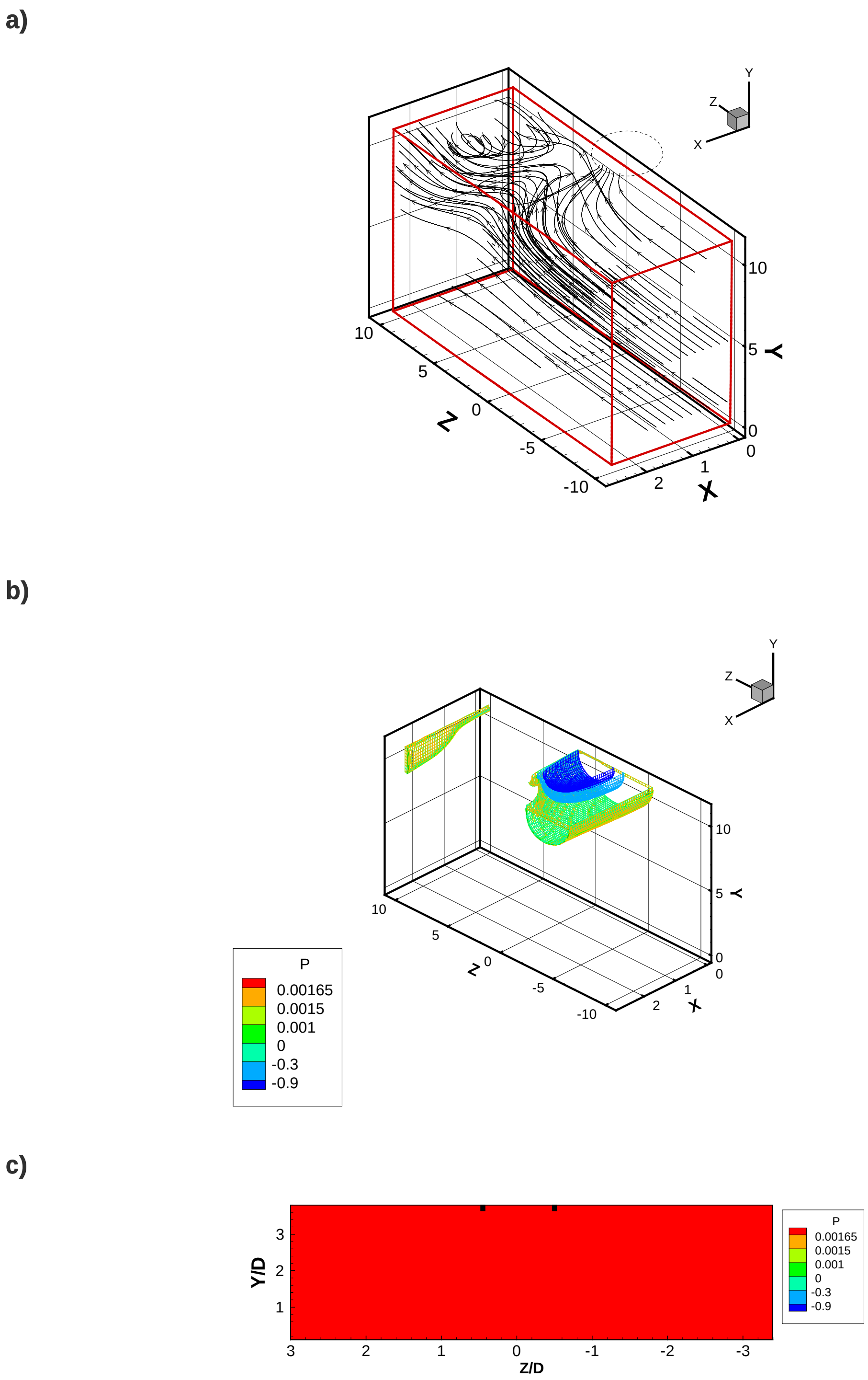

Figure 70: For h/D_i =1.62 and U_i/U_∞=9.09: a) 3D stream traces; b) 3D pressure distribution; c) pressure distribution in the ground plane;

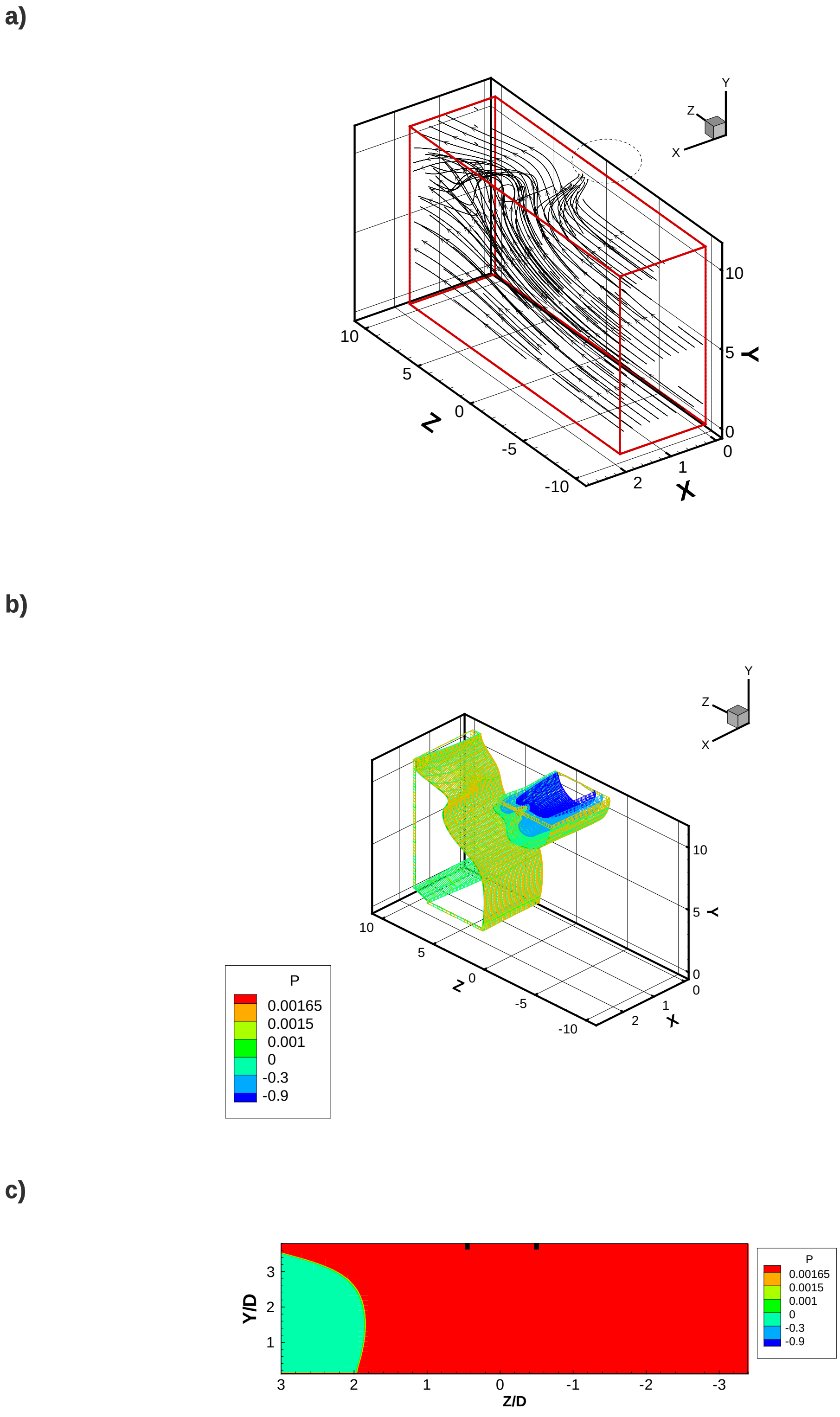

Figure 71: For h/D_i=1.19 and U_i/U_∞=9.09: a) 3D stream traces; b) 3D pressure distribution; c) pressure distribution in the ground plane;

a)

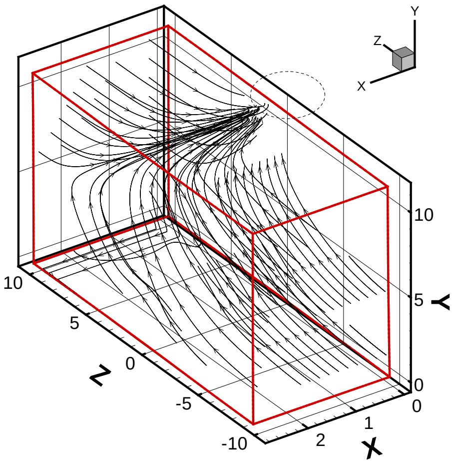

Y
Z
X
10
5
Y
0
0
1
2
X
10
5
Z
0
-5
-10

b)

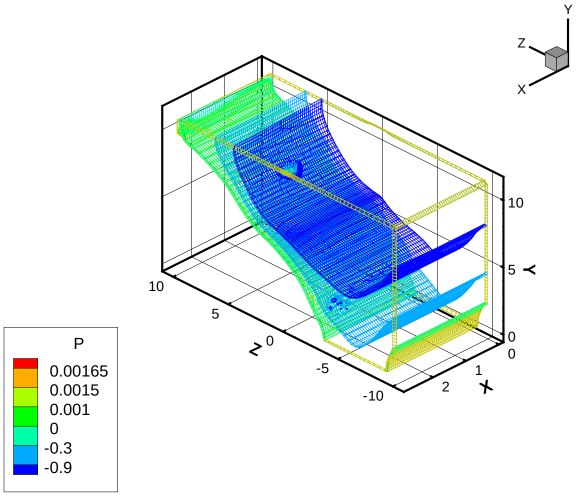

Y
Z
X
10
5
Y
0
0
1
2
X
10
5
Z
0
-5
-10
P
0.00165
0.0015
0.001
0
-0.3
-0.9

c)

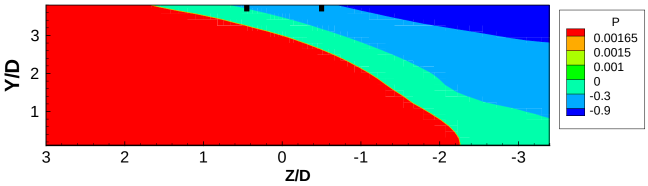

Y/D
3
2
1
3
2
1
0
-1
-2
-3
Z/D
P
0.00165
0.0015
0.001
0
-0.3
-0.9

d)

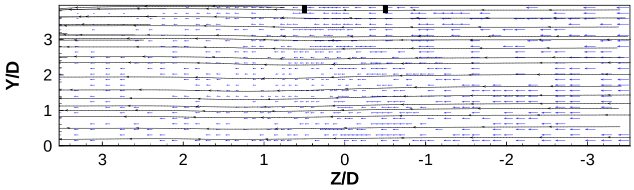

Y/D
3
2
1
0
3
2
1
0
-1
-2
-3
Z/D

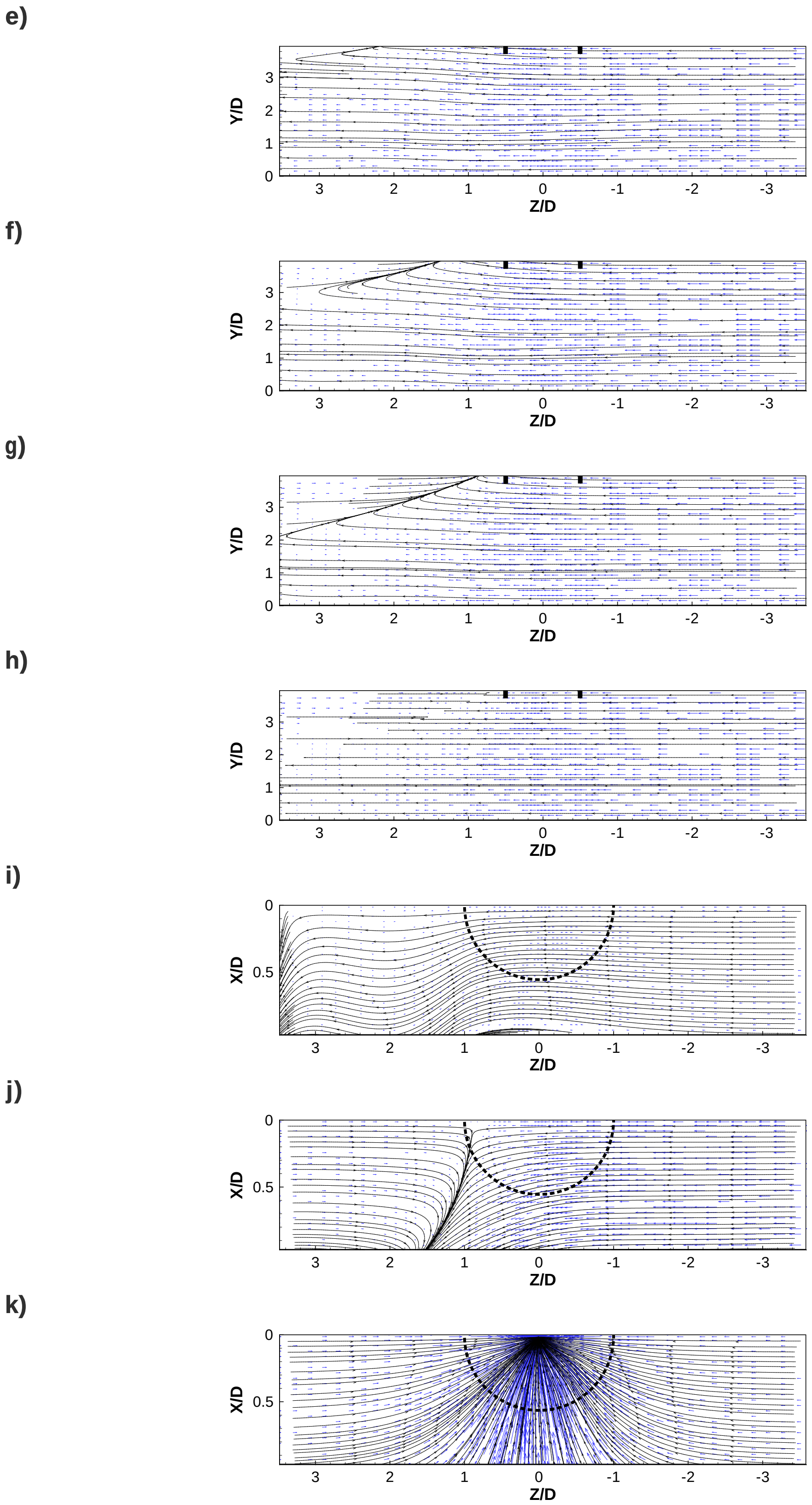

Figure 72: For h/D_i =1.87 and U_i/U_∞=72.73: a) 3D stream traces; b) 3D pressure distribution; c) pressure distribution in the ground plane; d) plane X=0.95XTOT (ground plane); e) plane X=0.75XTOT; f) plane X=0.50XTOT; g) plane X=0.25XTOT; h) plane X=0.05XTOT; i) plane Y=0.05YTOT; j) plane Y=0.50YTOT; k) plane Y=0.95YTOT

a)

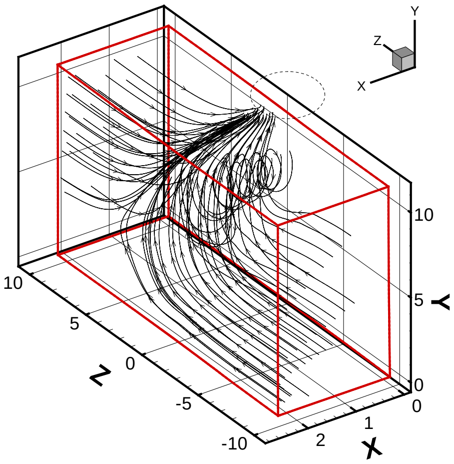
Y
Z
X
10
5
Y
0
0
1
2
X
10
5
0
Z
-5
-10

b)

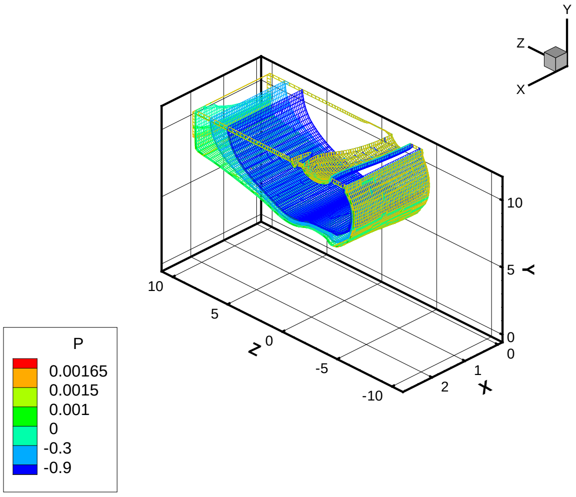
Y
Z
X
10
5
Y
0
0
1
2
X
10
5
0
Z
-5
-10
P
0.00165
0.0015
0.001
0
-0.3
-0.9

c)

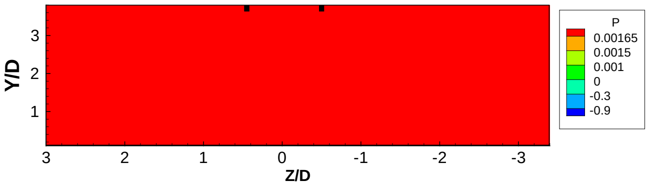
Y/D
3
2
1
3
2
1
0
-1
-2
-3
Z/D
P
0.00165
0.0015
0.001
0
-0.3
-0.9

d)

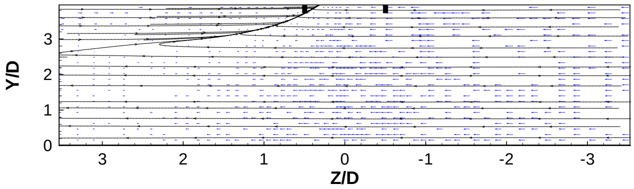
Y/D
3
2
1
0
3
2
1
0
-1
-2
-3
Z/D

e)

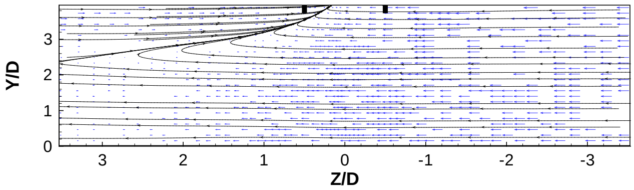
Y/D
3
2
1
0
3
2
1
0
-1
-2
-3
Z/D

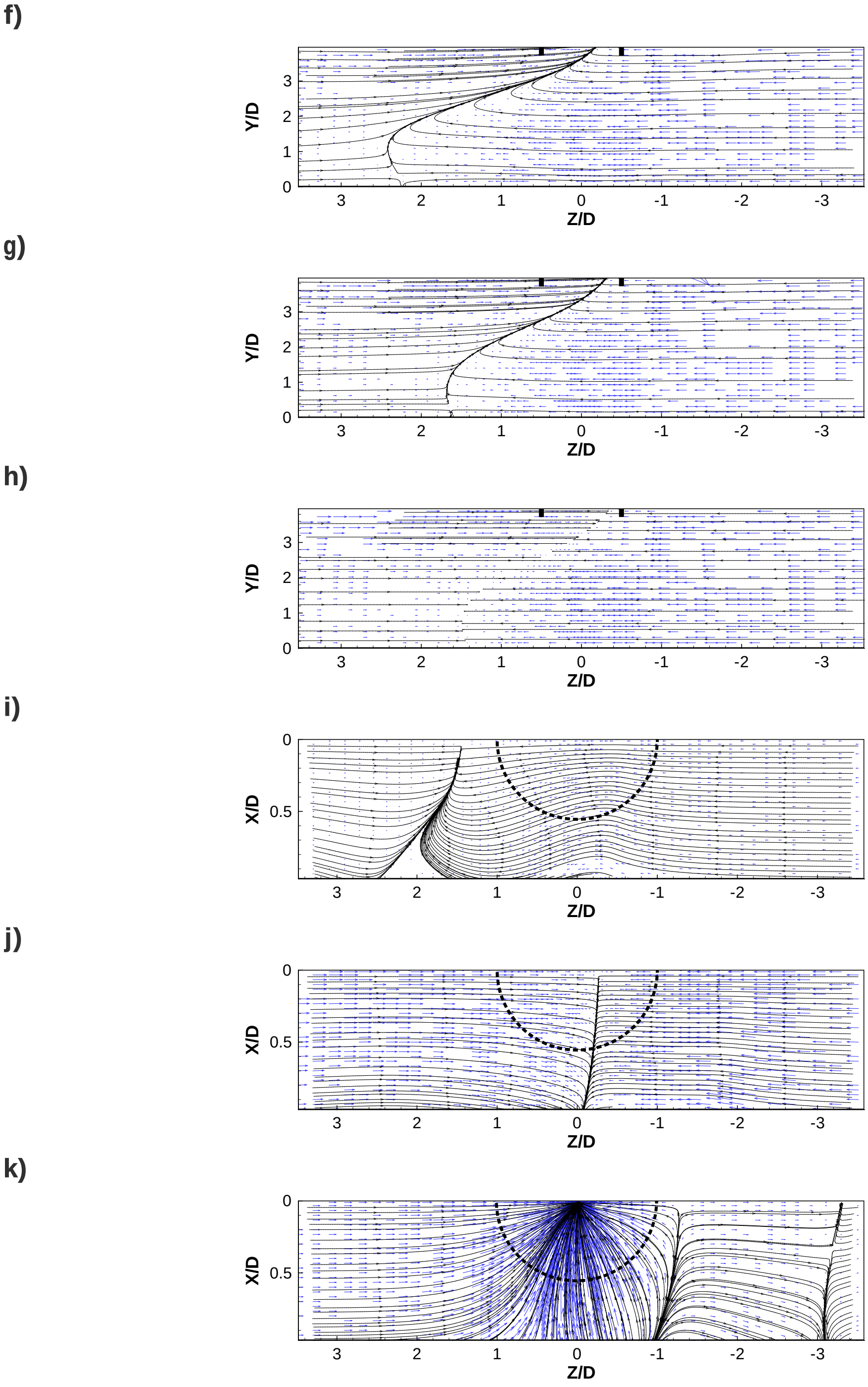

Figure 73: For h/D_i=1.53 and U_i/U_∞=72.73: a) 3D stream traces; b) 3D pressure distribution; c) pressure distribution in the ground plane; d) plane X=0.80XTOT (ground plane); e) plane X=0.75XTOT; f) plane X=0.50XTOT; g) plane X=0.25XTOT; h) plane X=0.05XTOT; i) plane Y=0.05YTOT; j) plane Y=0.50YTOT; k) plane Y=0.95YTOT

a)

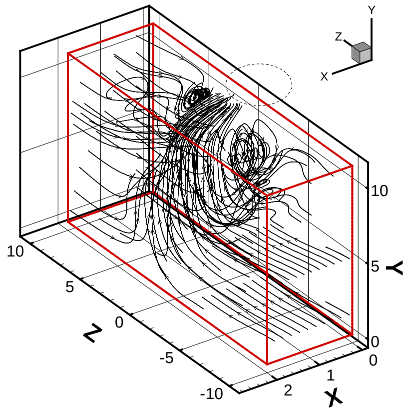

Y
Z
X
10
5
0
-5
-10
Z
10
5
0
Y
0
1
2
X

b)

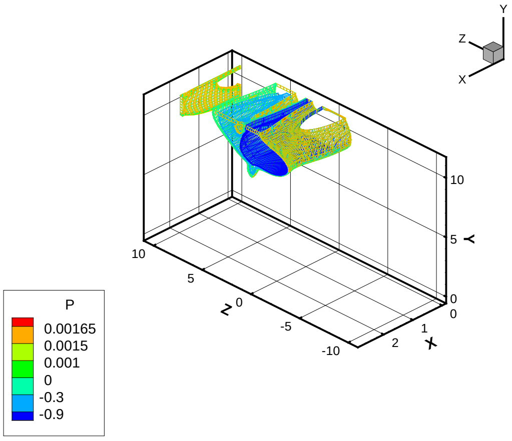

Y
Z
X
10
5
Y
0
0
1
2
X
10
5
Z 0
-5
-10
P
0.00165
0.0015
0.001
0
-0.3
-0.9

c)

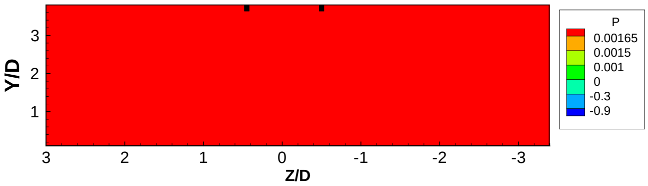

Y/D
3
2
1
3
2
1
0
-1
-2
-3
Z/D
P
0.00165
0.0015
0.001
0
-0.3
-0.9

d)

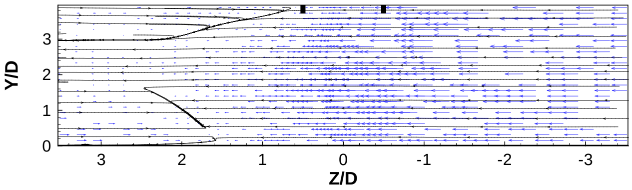

Y/D
3
2
1
0
3
2
1
0
-1
-2
-3
Z/D

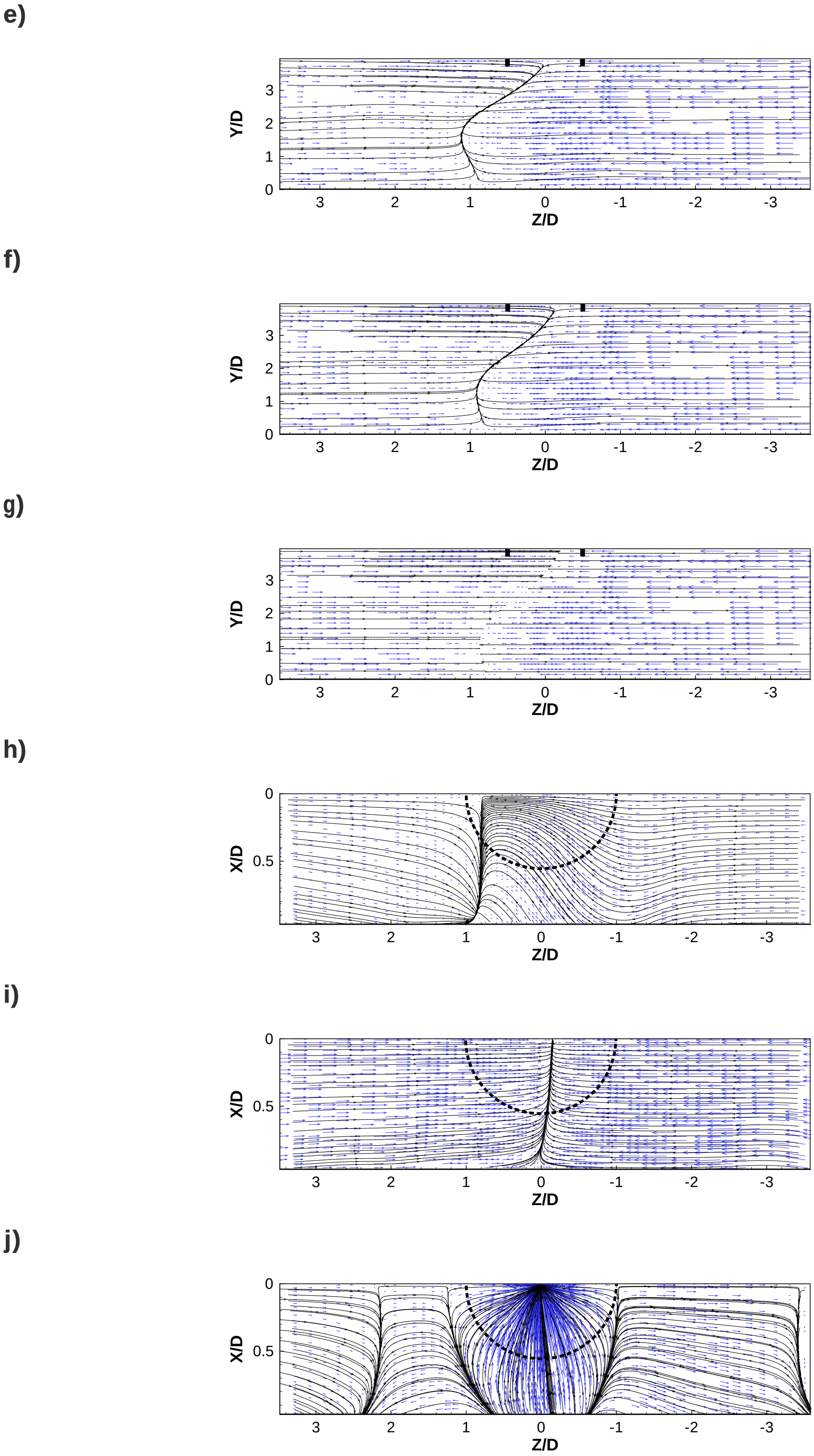

Figure 74: For h/D_i=1.33 and U_i/U_∞=72.73: a) 3D stream traces; b) 3D pressure distribution; c) pressure distribution in the ground plane; d) plane X=0.70XTOT (ground plane); e) plane X=0.50XTOT; f) plane X=0.25XTOT; g) plane X=0.05XTOT; h) plane Y=0.05YTOT; i) plane Y=0.50YTOT; j) plane Y=0.95YTOT

a)

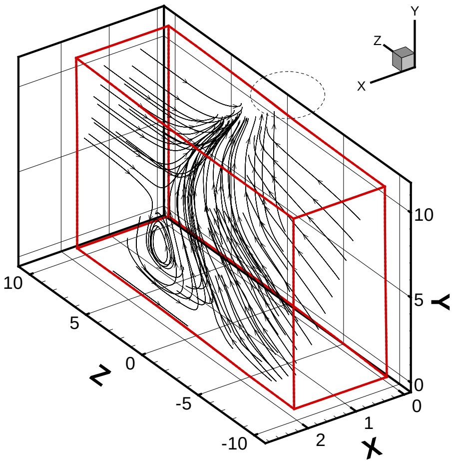
Y
Z
X
10
5
Y
0
0
1
2
X
10
5
0
-5
-10
Z

b)

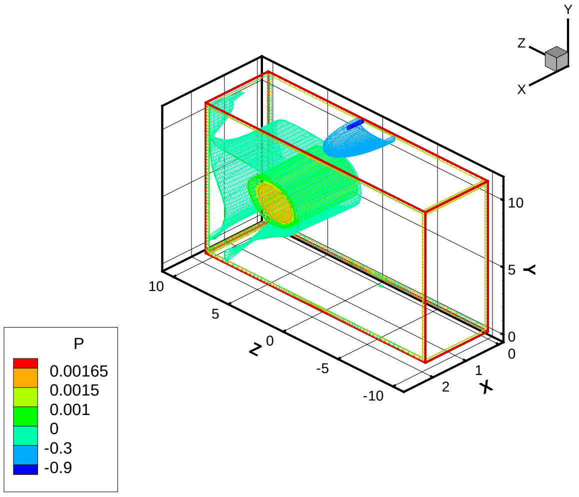
Y
Z
X
P
0.00165
0.0015
0.001
0
-0.3
-0.9
10
5
Y
0
0
1
2
X
10
5
Z
0
-5
-10

c)

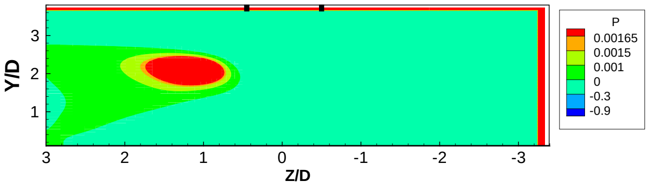
Y/D
3
2
1
3
2
1
0
-1
-2
-3
Z/D
P
0.00165
0.0015
0.001
0
-0.3
-0.9

d)

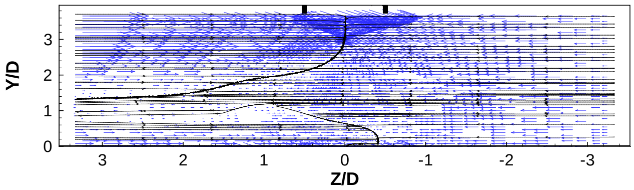
Y/D
3
2
1
0
3
2
1
0
-1
-2
-3
Z/D

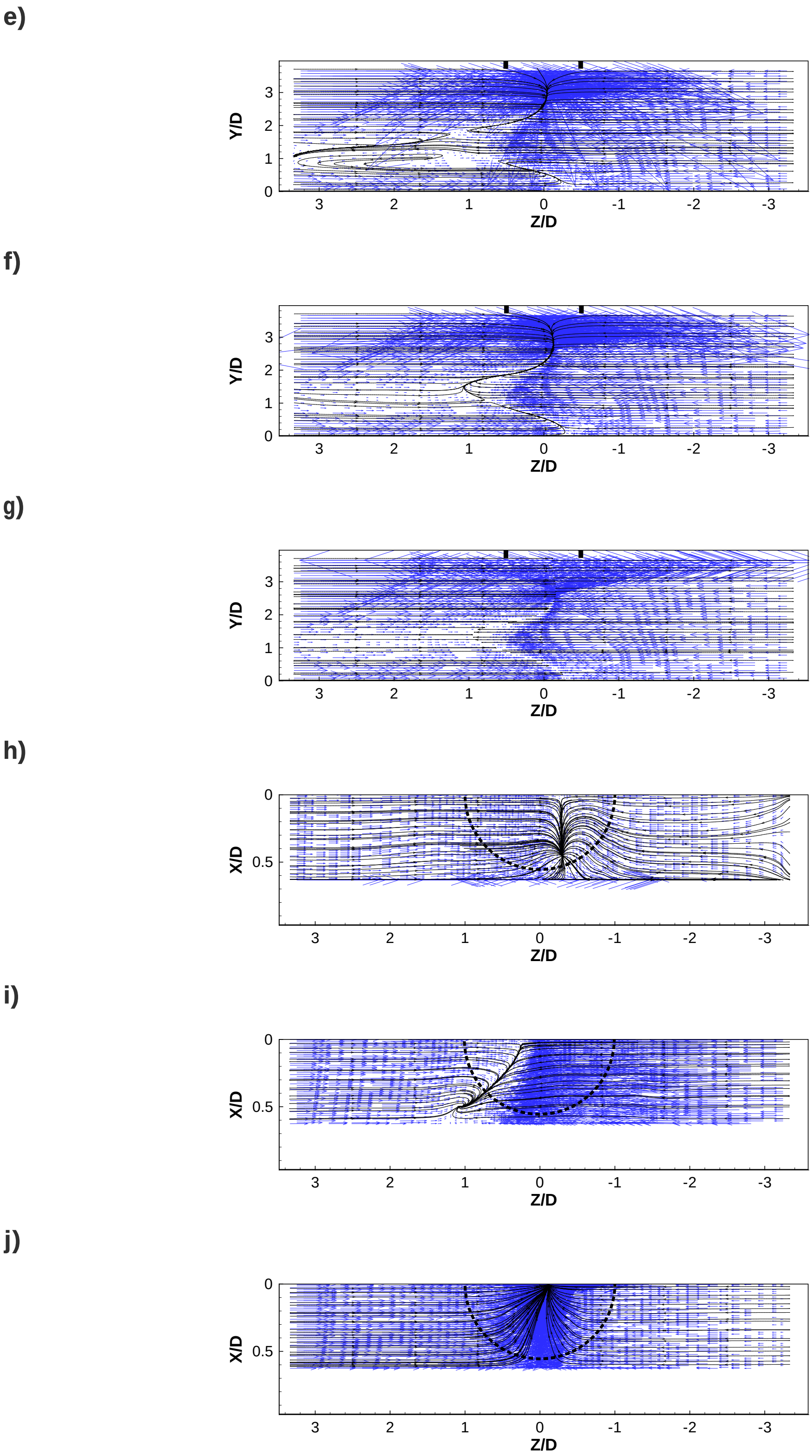

Figure 75: For h/D_i=0.63 and U_i/U_∞=72.73: a) 3D stream traces; b) 3D pressure distribution; c) pressure distribution in the ground plane; d) plane X=0.67XTOT(ground plane); e) plane X=0.50XTOT; f) plane X=0.25XTOT; g) plane X=0.05XTOT; h) plane Y=0.05YTOT; i) plane Y=0.50YTOT; j) plane Y=0.95YTOT

a)

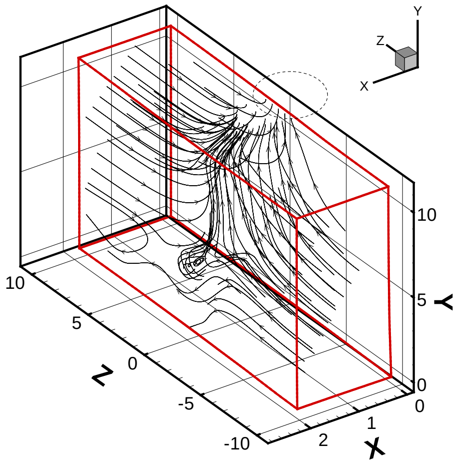
Y
Z
X
10
5
Y
0
0
1
2
X
10
5
Z
0
-5
-10

b)

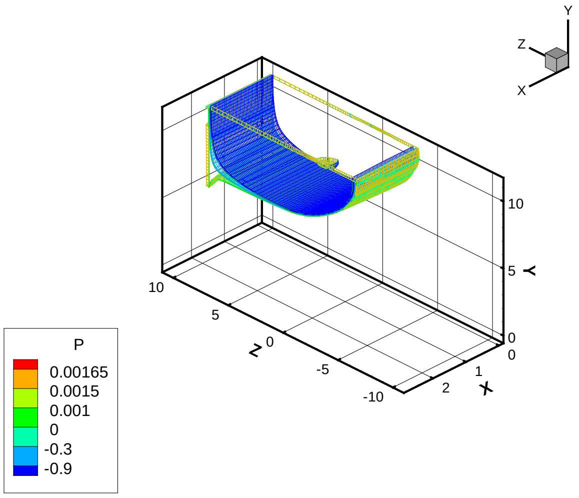
Y
Z
X
P
0.00165
0.0015
0.001
0
-0.3
-0.9
10
5
Y
0
0
1
2
X
10
5
Z
0
-5
-10

c)

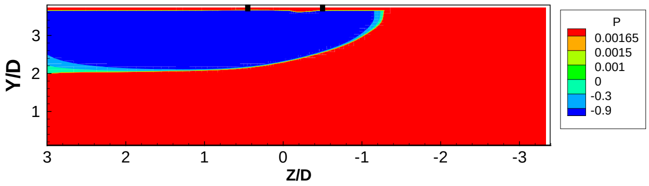
3
2
1
Y/D
3
2
1
0
-1
-2
-3
Z/D
P
0.00165
0.0015
0.001
0
-0.3
-0.9

d)

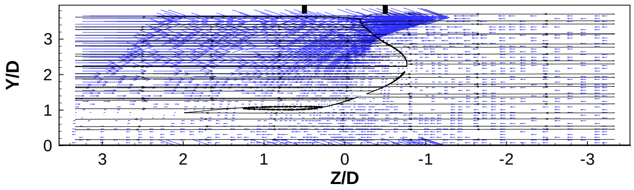
3
2
1
0
Y/D
3
2
1
0
-1
-2
-3
Z/D

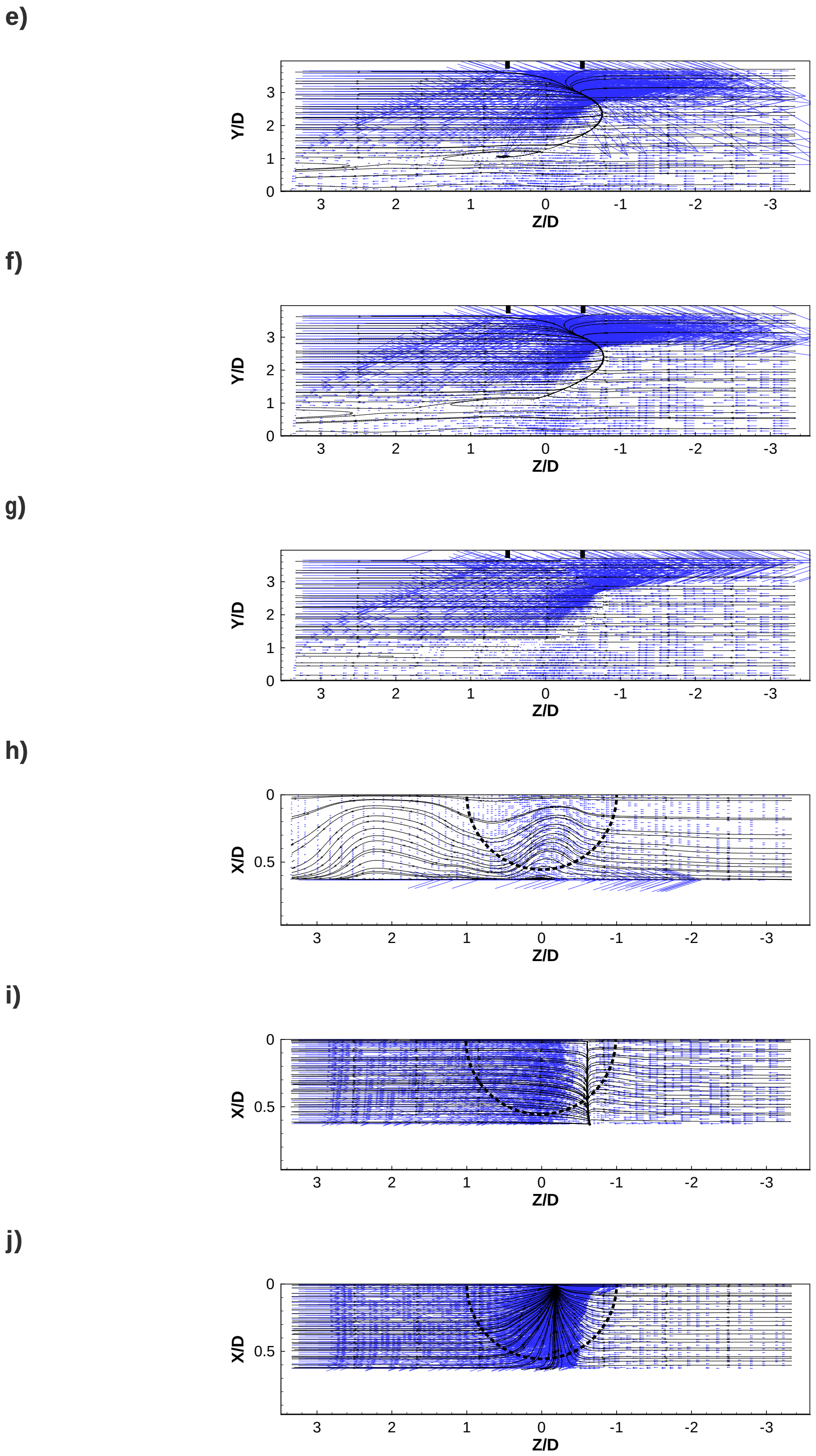

Figure 76: For h/D_i =0.63 and U_i/U_∞=54.55: a) 3D stream traces; b) 3D pressure distribution; c) pressure distribution in the ground plane; d) plane X=0.67XTOT(ground plane); e) plane X=0.50XTOT; f) plane X=0.25XTOT; g) plane X=0.05XTOT; h) plane Y=0.05YTOT; i) plane Y=0.50YTOT; j) plane Y=0.95YTOT

a)

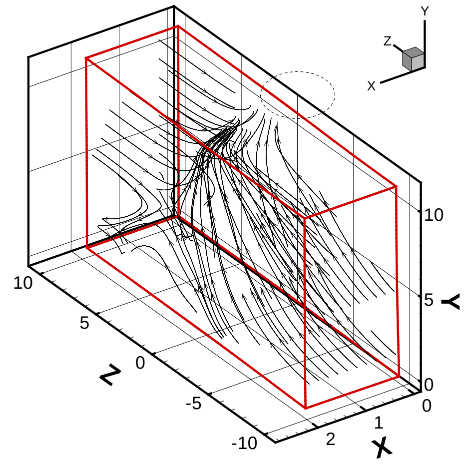

Y
Z
X
10
5
Y
0
0
1
2
X
10
5
Z
0
-5
-10

b)

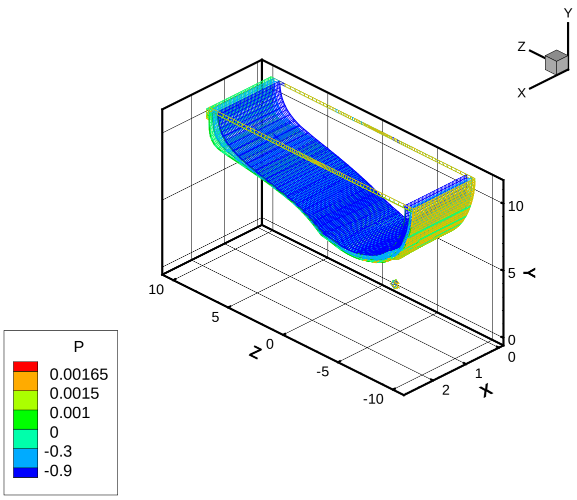

Y
Z
X
10
5
Y
0
0
1
2
X
10
5
Z
0
-5
-10
P
0.00165
0.0015
0.001
0
-0.3
-0.9

c)

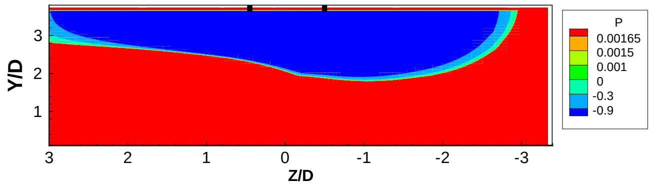

Y/D
3
2
1
3
2
1
0
-1
-2
-3
Z/D
P
0.00165
0.0015
0.001
0
-0.3
-0.9

d)

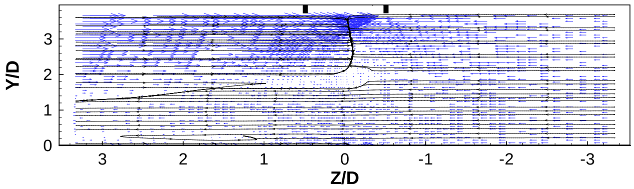

Y/D
3
2
1
0
3
2
1
0
-1
-2
-3
Z/D

e)

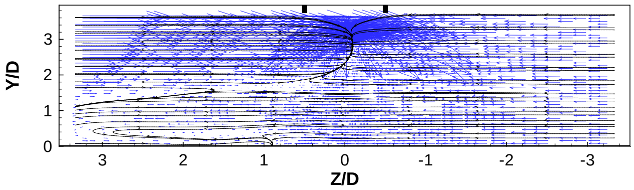

Y/D
3
2
1
0
3
2
1
0
-1
-2
-3
Z/D

f)

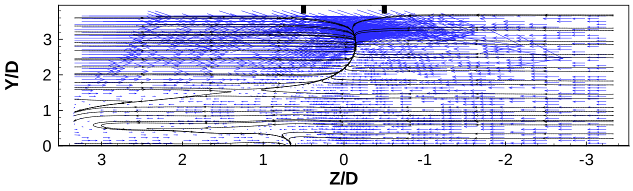

g)

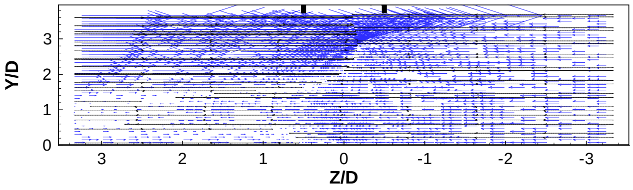

h)

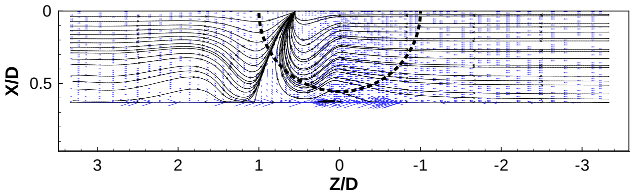

i)

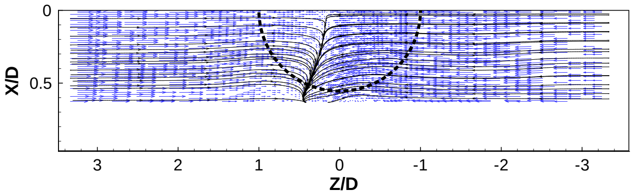

j)

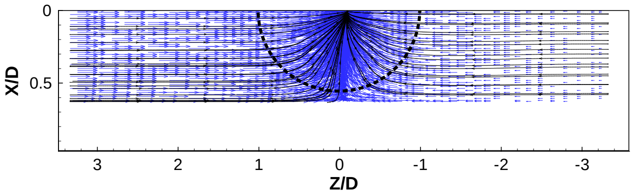

Figure 77: For h/D_i =0.63 and U_i/U_∞=36.36: a) 3D stream traces; b) 3D pressure distribution; c) pressure distribution in the ground plane; d) plane X=0.67XTOT(ground plane); e) plane X=0.50XTOT; f) plane X=0.25XTOT; g) plane X=0.05XTOT; h) plane Y=0.05YTOT; i) plane Y=0.50YTOT; j) plane Y=0.95YTOT

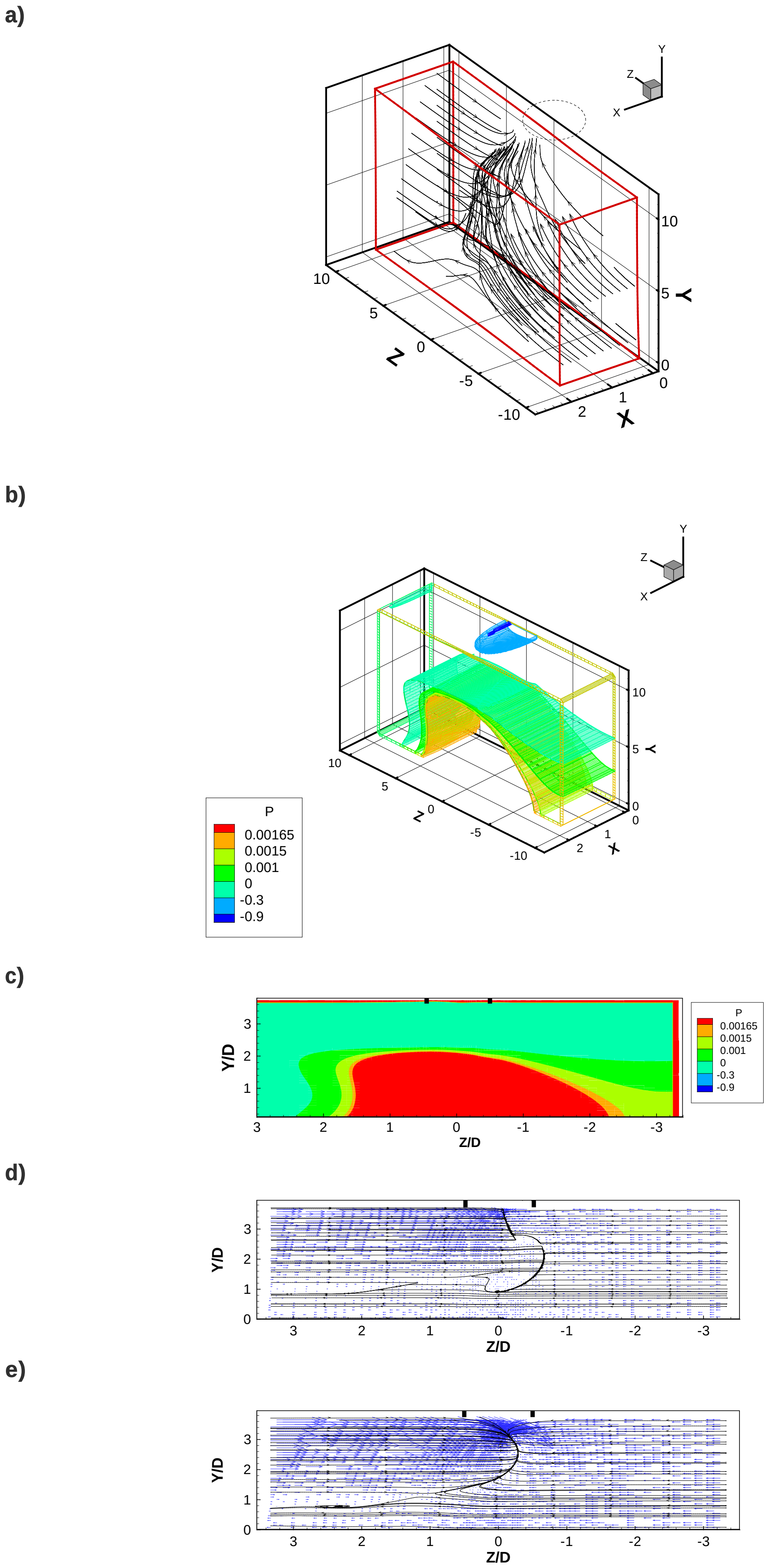
a)
Y
Z
X
10
5
Y
0
0
1
2
X
10
5
0
Z
-5
-10
b)
Y
Z
X
10
5
Y
0
0
1
2
X
10
5
Z
0
-5
-10
P
0.00165
0.0015
0.001
0
-0.3
-0.9
c)
Y/D
3
2
1
3
2
1
0
-1
-2
-3
Z/D
P
0.00165
0.0015
0.001
0
-0.3
-0.9
d)
Y/D
3
2
1
0
3
2
1
0
-1
-2
-3
Z/D
e)
Y/D
3
2
1
0
3
2
1
0
-1
-2
-3
Z/D

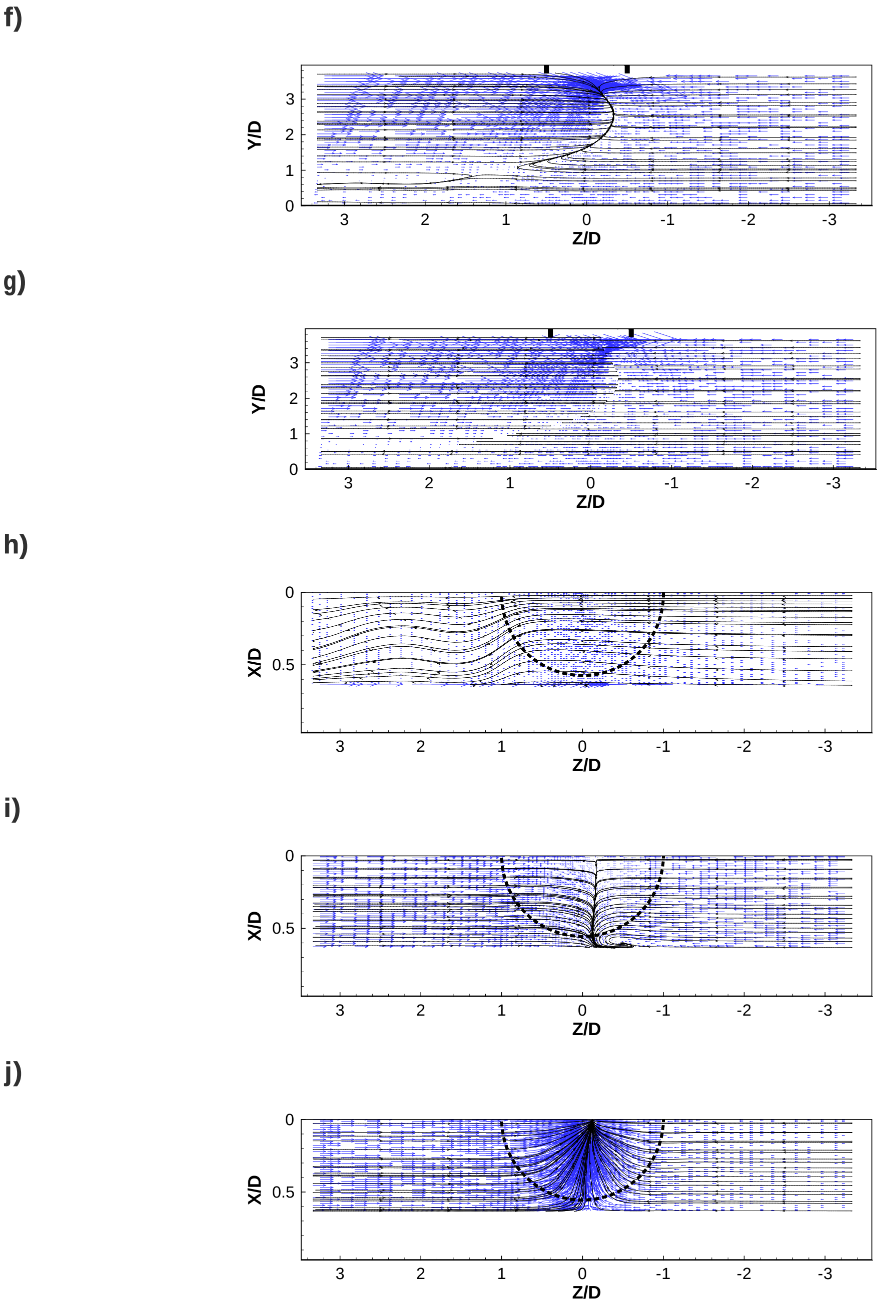

Figure 78: For h/D_i =0.63 and U_i/U_∞=18.18: a) 3D stream traces; b) 3D pressure distribution; c) pressure distribution in the ground plane; d) plane X=0.67XTOT(ground plane); e) plane X=0.50XTOT; f) plane X=0.25XTOT; g) plane X=0.05XTOT; h) plane Y=0.05YTOT; i) plane Y=0.50YTOT; j) plane Y=0.95YTOT

a)

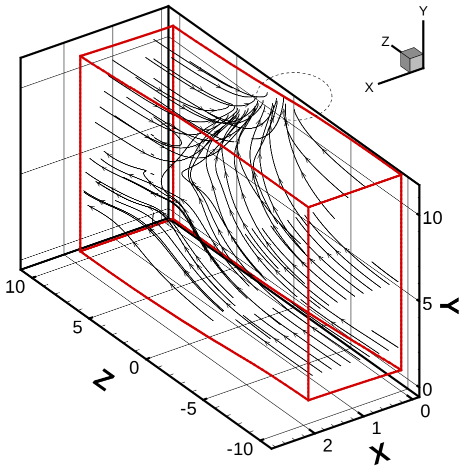

Y
Z
X
10
5
0
-5
-10
Z
0
1
2
X
0
5
10
Y

b)

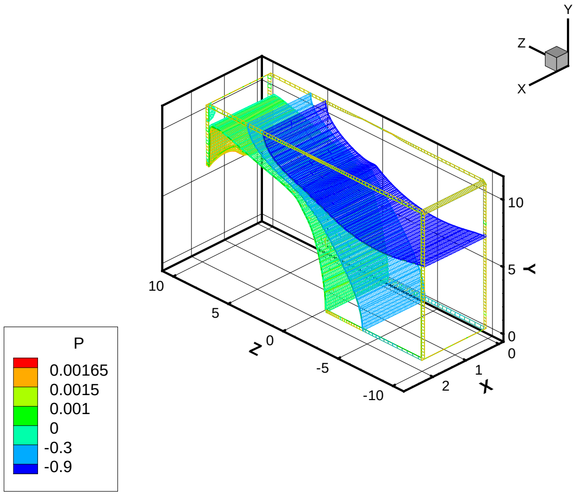

Y
Z
X
P
0.00165
0.0015
0.001
0
-0.3
-0.9
10
5
0
-5
-10
Z
0
1
2
X
0
5
10
Y

c)

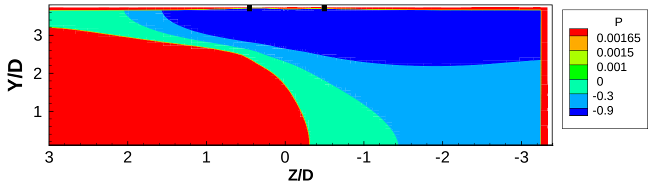

Y/D
1
2
3
3
2
1
0
-1
-2
-3
Z/D
P
0.00165
0.0015
0.001
0
-0.3
-0.9

d)

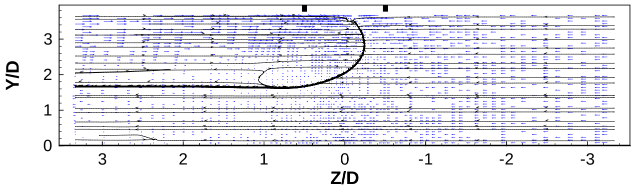

Y/D
0
1
2
3
3
2
1
0
-1
-2
-3
Z/D

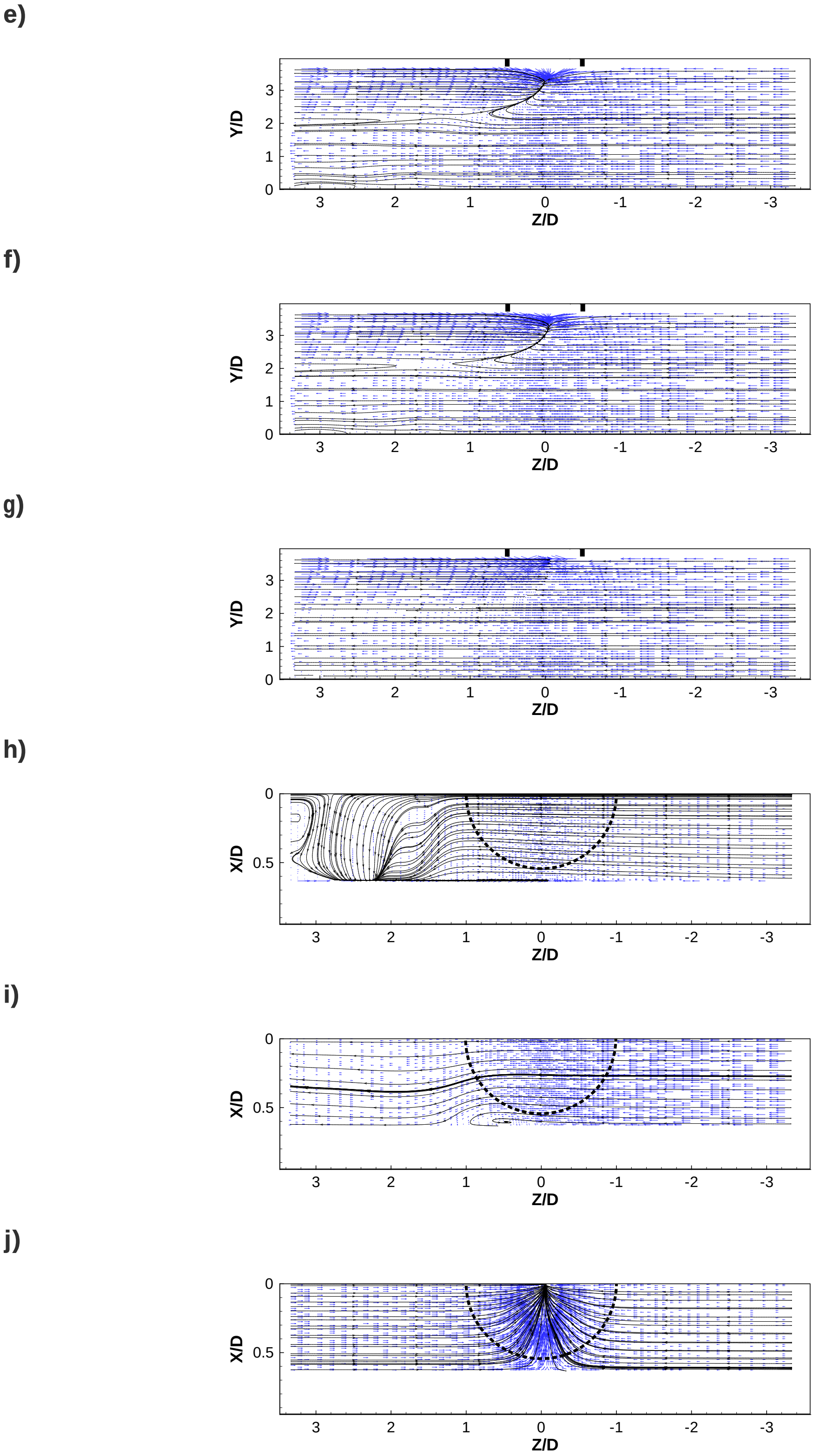

Figure 79: For h/D_i =0.63 and U_i/U_∞=9.09: a) 3D stream traces; b) 3D pressure distribution; c) pressure distribution in the ground plane; d) plane X=0.67XTOT(ground plane Y=0.05YTOT; i) plane Y=0.50YTOT; j) plane Y=0.95YTOT

A.2. One Vortex

a)

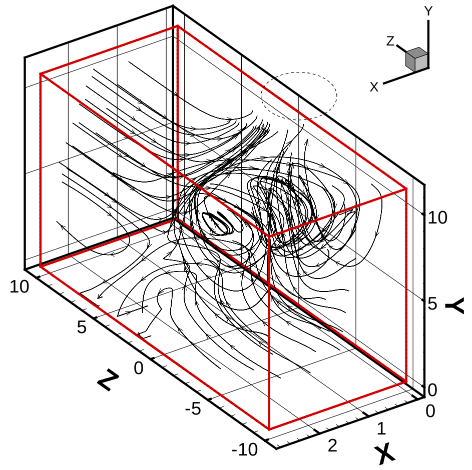

b)

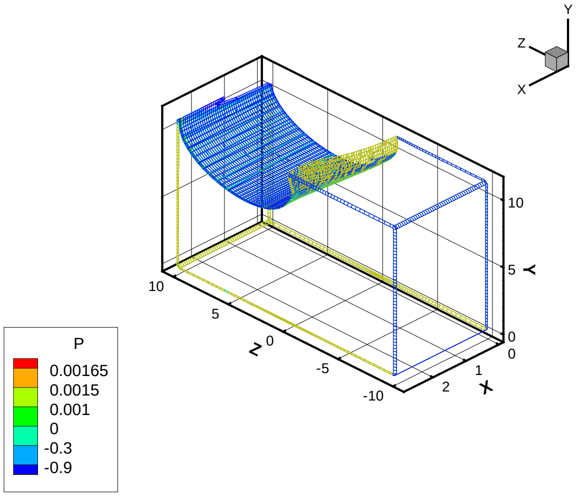

c)

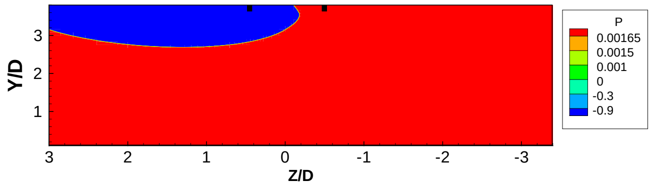

d)

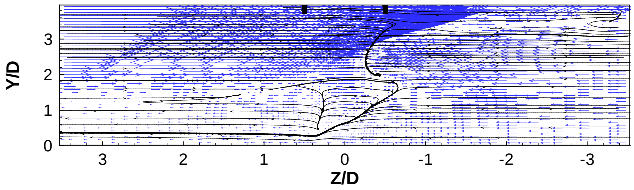

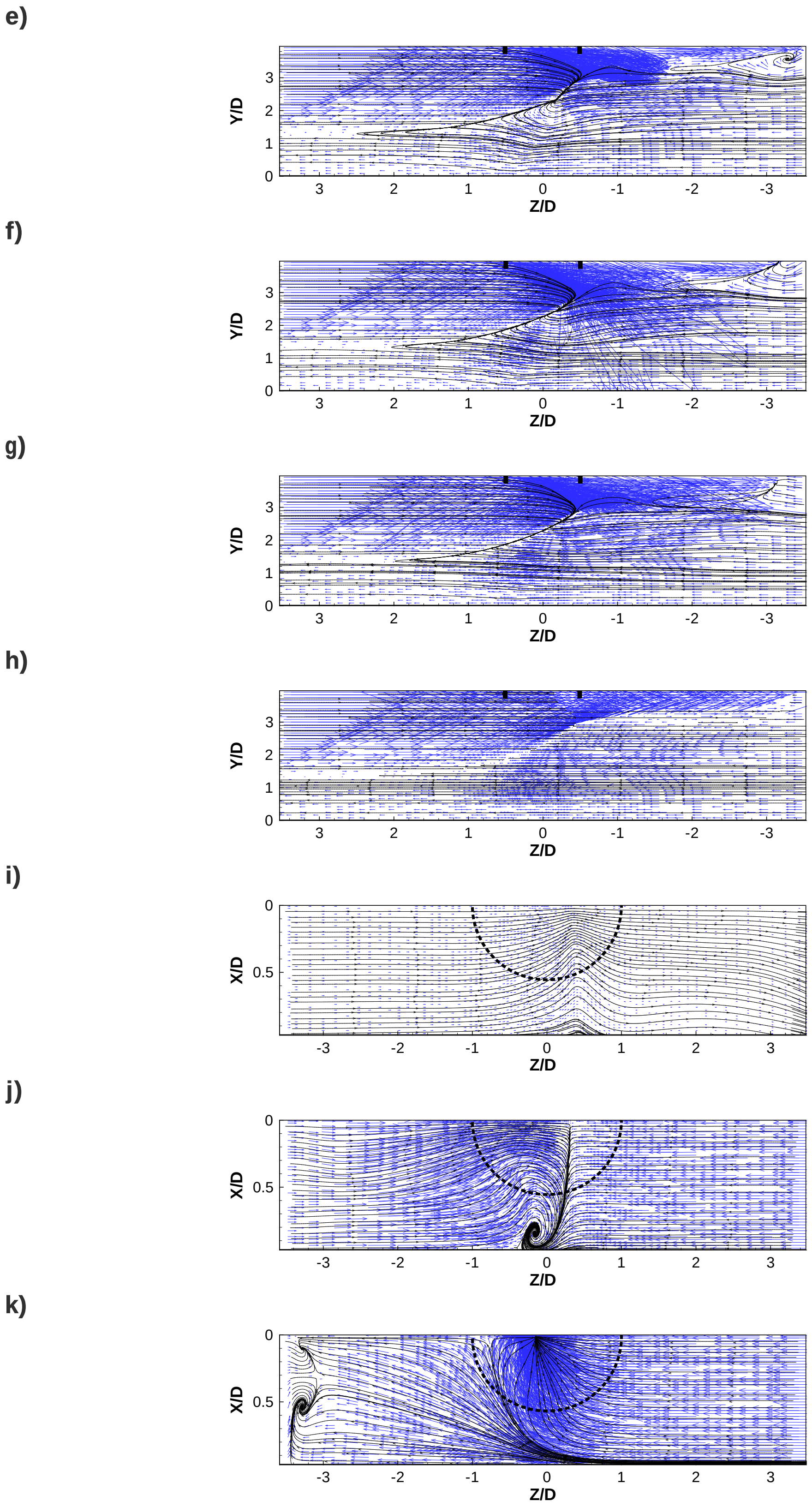

Figure 80: For $h/D_i h/D_i$=1.00 and U_i/U_∞=63.64: a) 3D stream traces; b) 3D pressure distribution; c) pressure distribution in the ground plane; d) plane X=0.95XTOT(ground plane); e) plane X=0.75XTOT; f) plane X=0.50XTOT; g) plane X=0.25XTOT; h) plane X=0.05XTOT; i) plane Y=0.05YTOT; j) plane Y=0.50YTOT; k) plane Y=0.95YTOT

a)

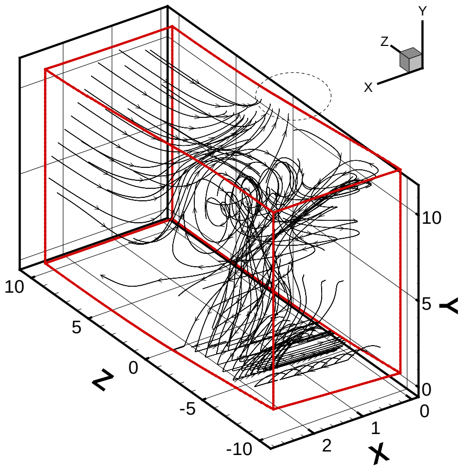
Y
Z
X
10
5
Y
0
0
1
2
X
10
5
0
Z
-5
-10

b)

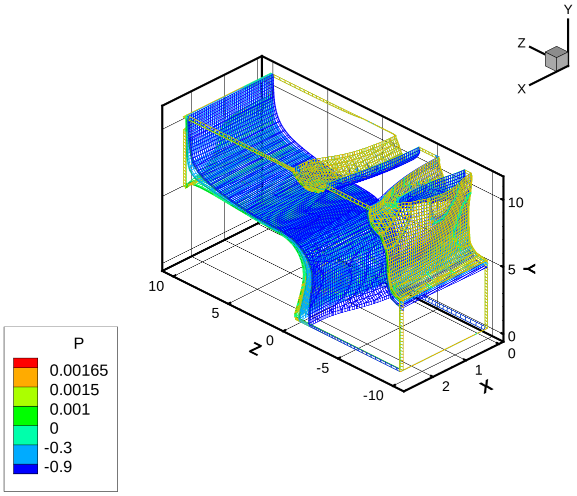
Y
Z
X
10
5
Y
0
0
1
2
X
10
5
Z
0
-5
-10
P
0.00165
0.0015
0.001
0
-0.3
-0.9

c)

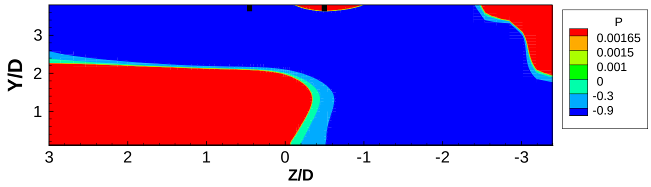
Y/D
3
2
1
3
2
1
0
-1
-2
-3
Z/D
P
0.00165
0.0015
0.001
0
-0.3
-0.9

d)

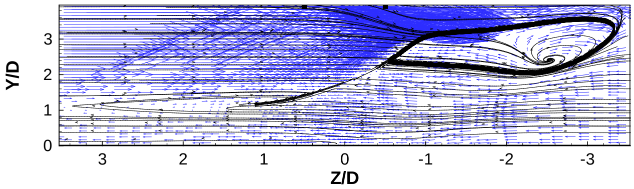
Y/D
3
2
1
0
3
2
1
0
-1
-2
-3
Z/D

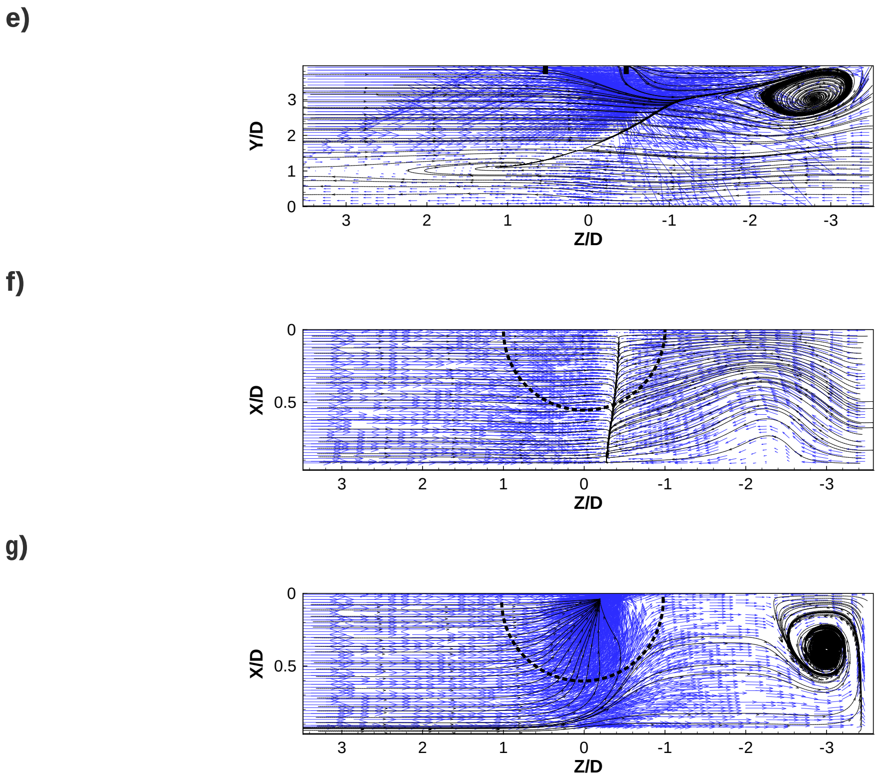

Figure 81: For h/D_i=0.93 and U_i/U_∞=63.64: a) 3D stream traces; b) 3D pressure distribution; c) pressure distribution in the ground plane; d) plane X=0.75XTOT; e) plane X=0.50XTOT; f) plane Y=0.50YTOT; g) plane Y=0.95YTOT

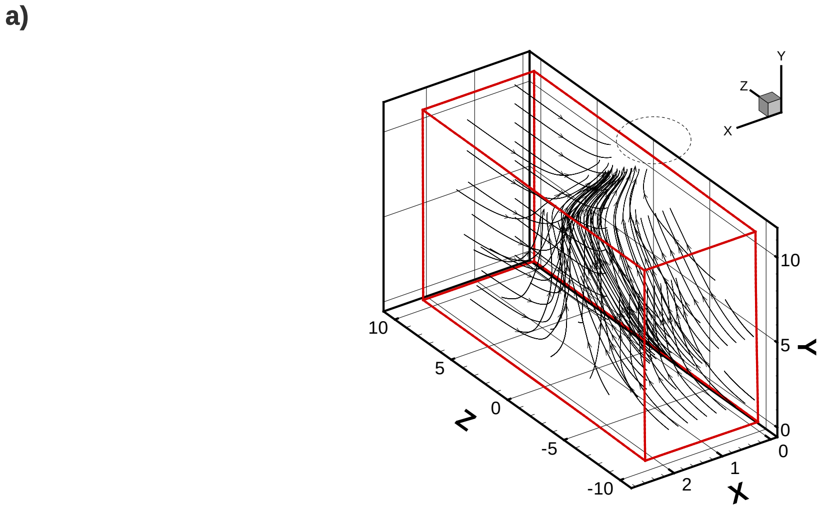

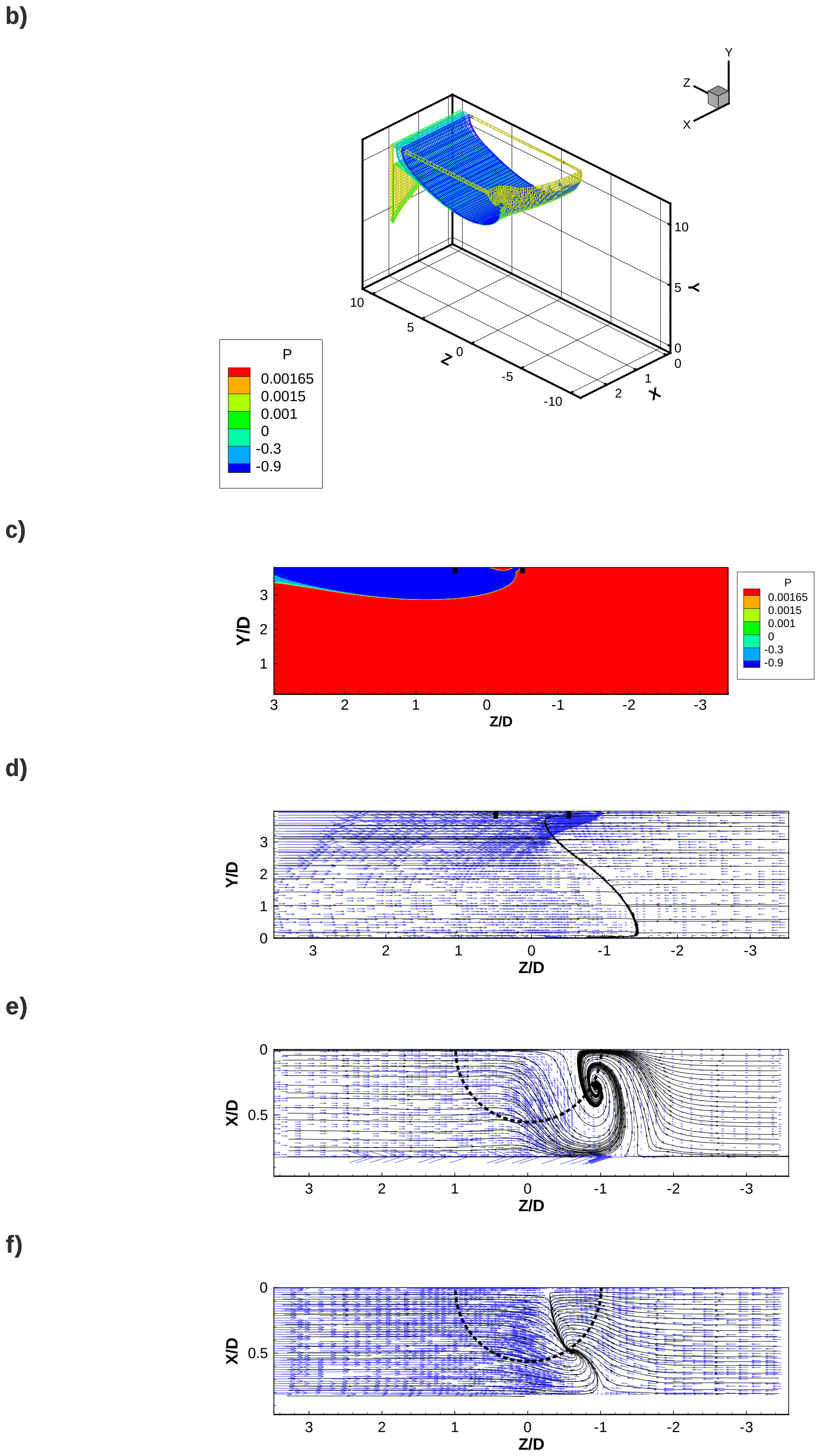

Figure 82: For h/D_i=0.82 and U_i/U_∞=63.64: a) 3D stream traces; b) 3D pressure distribution; c) pressure distribution in the ground plane; d) plane X=0.80XTOT(ground plane); h) plane Y=0.05YTOT; i) plane Y=0.50YTOT;

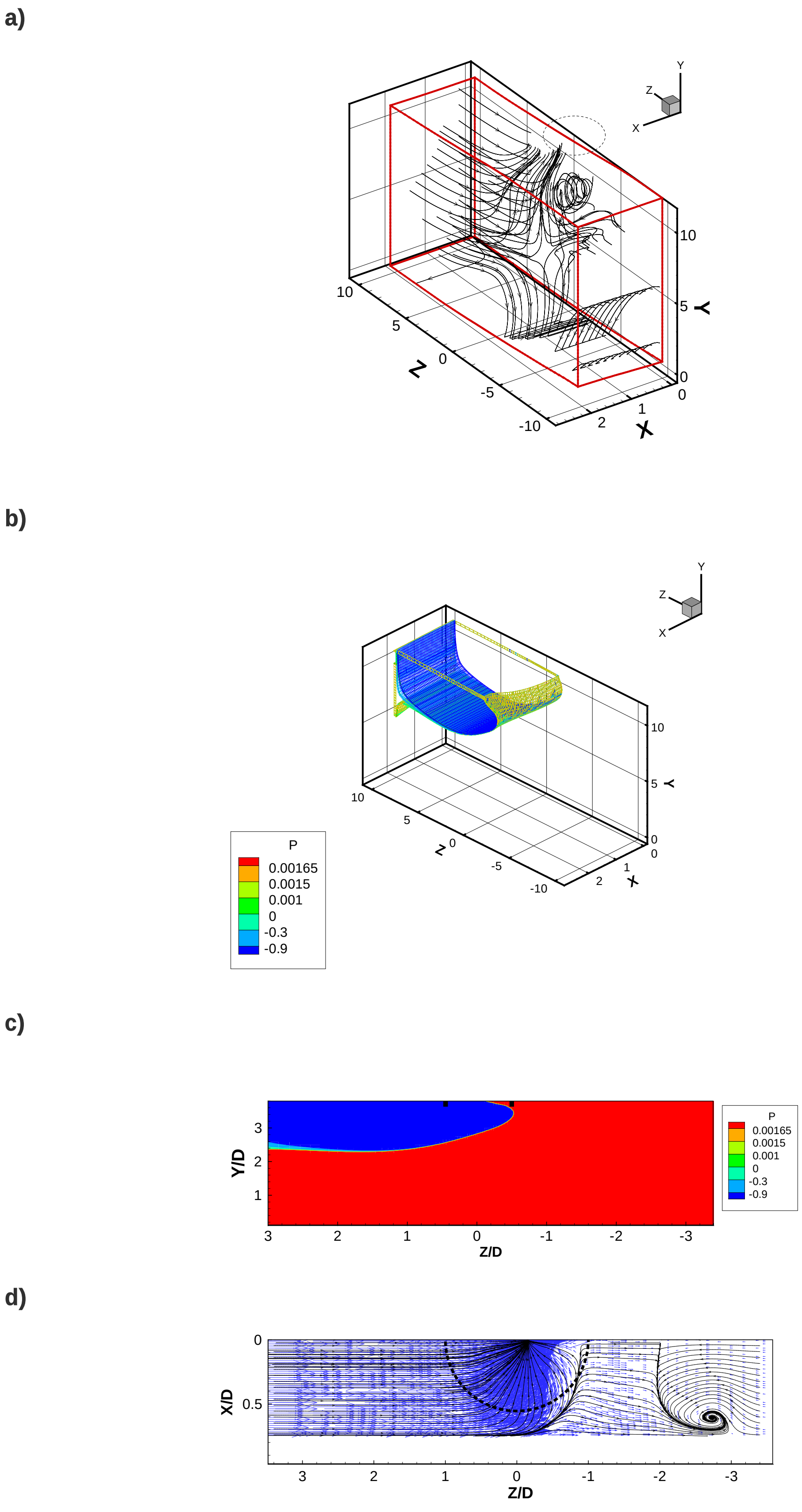

Figure 83: For h/D_i =0.75 and U_i/U_∞=63.64: a) 3D stream traces; b) 3D pressure distribution; c) pressure distribution in the ground plane; d) plane Y=0.95YTOT

a)

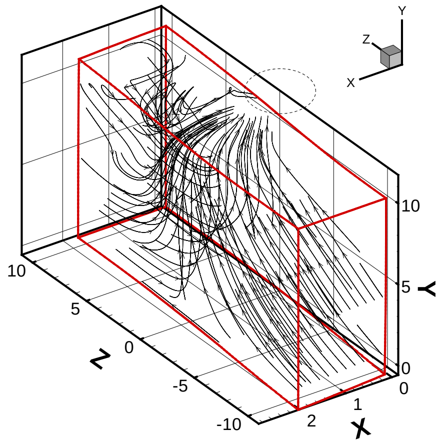
Y
Z
X
10
5
0
-5
-10
Z
10
5
Y
0
0
1
2
X

b)

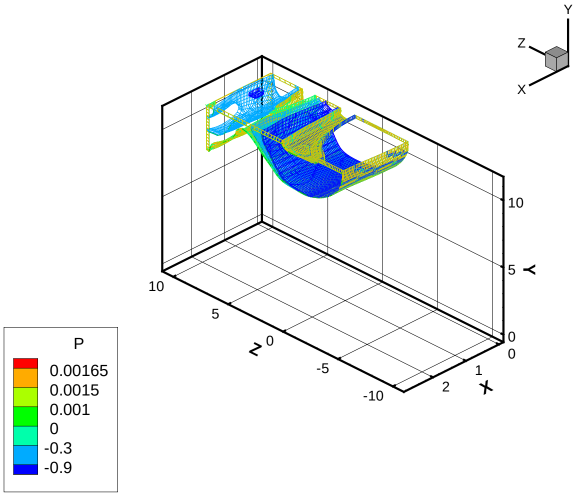
Y
Z
X
10
5
Y
0
0
1
2
X
10
5
Z
0
-5
-10
P
0.00165
0.0015
0.001
0
-0.3
-0.9

c)

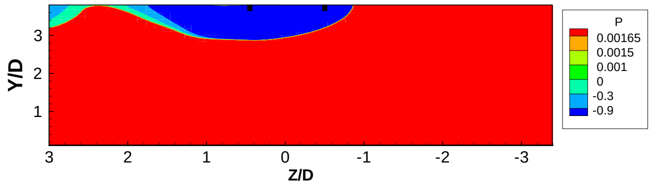
Y/D
3
2
1
3
2
1
0
-1
-2
-3
Z/D
P
0.00165
0.0015
0.001
0
-0.3
-0.9

d)

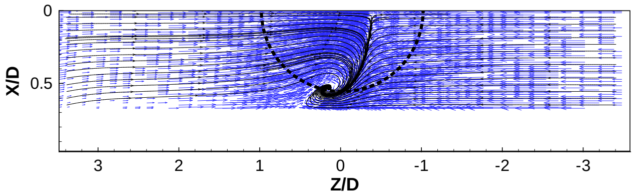
0
X/D
0.5
3
2
1
0
-1
-2
-3
Z/D

e)

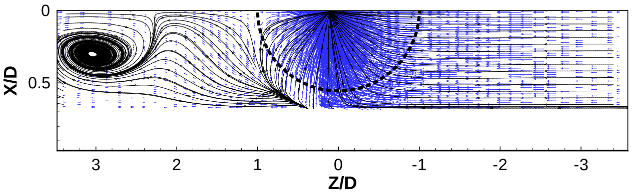

Figure 84: For h/D_i =0.68 and U_i/U_∞=63.64: a) 3D stream traces; b) 3D pressure distribution; c) pressure distribution in the ground plane; d) plane Y=0.50YTOT; e) plane Y=0.95YTOT

a)

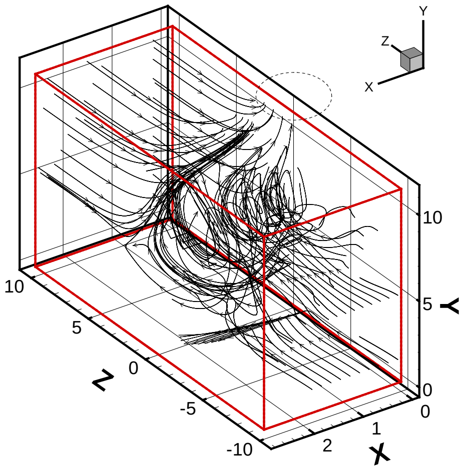

b)

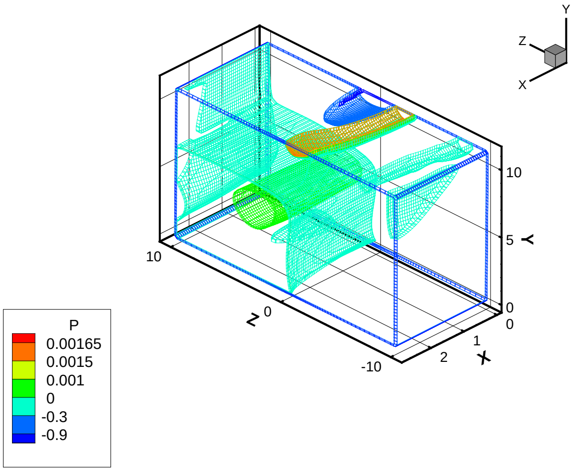

c)

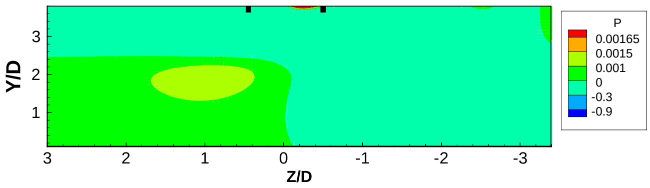

d)

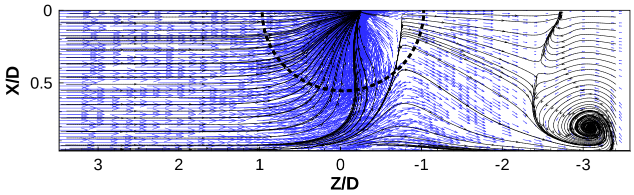

Figure 85: For h/D_i=1.00 and U_i/U_∞=72.73: a) 3D stream traces; b) 3D pressure distribution; c) pressure distribution in the ground plane; d) plane Y=0.95YTOT

a)

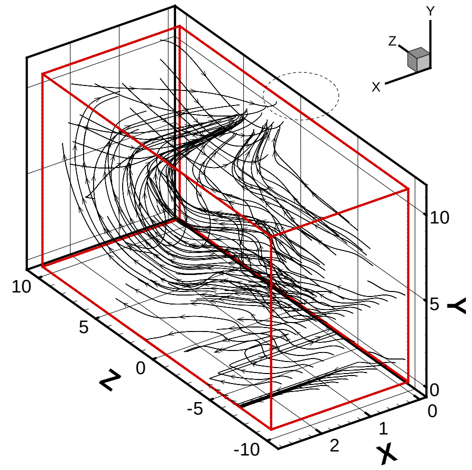

b)

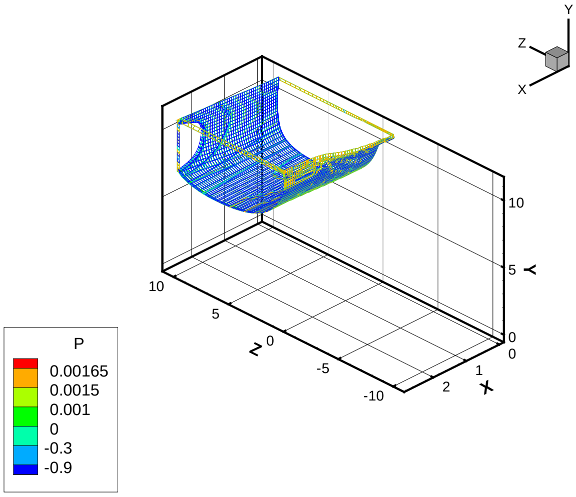

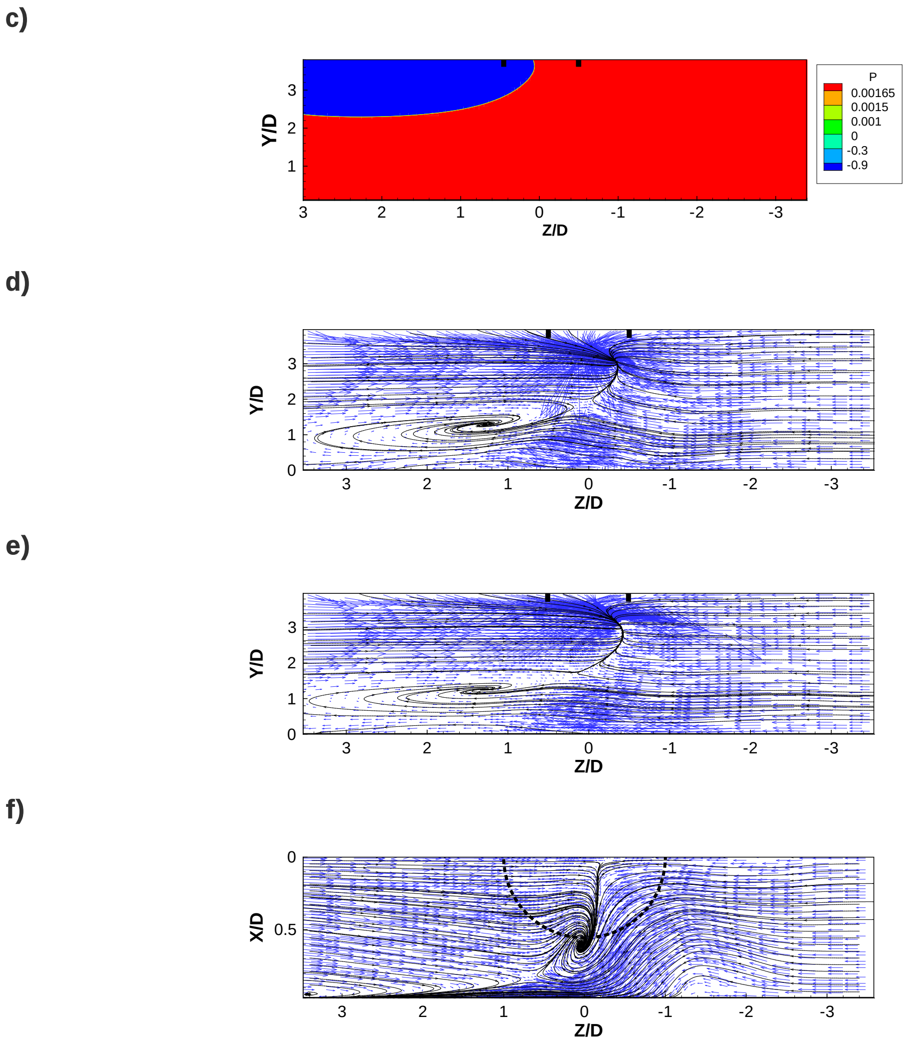

Figure 86: For h/D_i=1.00 and U_i/U_∞=36.36: a) 3D stream traces; b) 3D pressure distribution; c) pressure distribution in the ground plane; d) plane X=0.50XTOT; e) plane X=0.25XTOT; g) plane Y=0.50YTOT;

a)

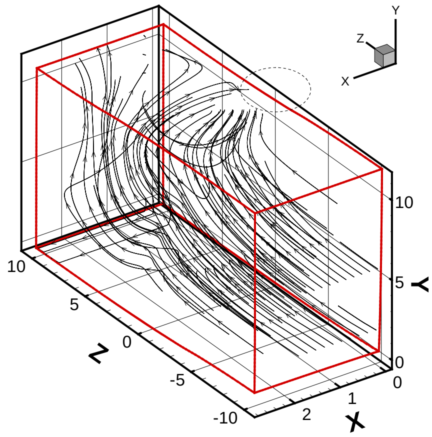

b)

c)

d)

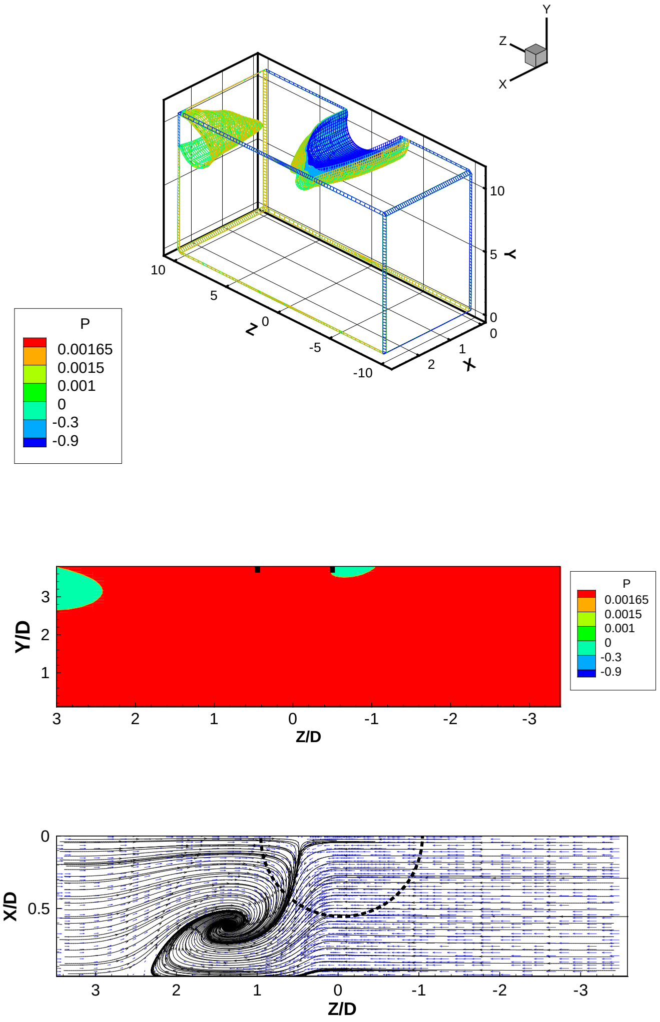

Figure 87: For h/D_i=1.00 and U_i/U_∞=9.09: a) 3D stream traces; b) 3D pressure distribution; c) pressure distribution in the ground plane; d) plane Y=0.50YTOT

a)

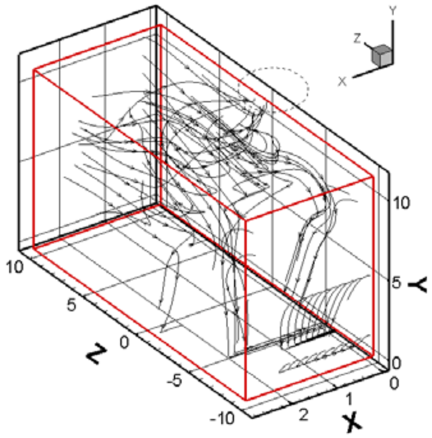

b)

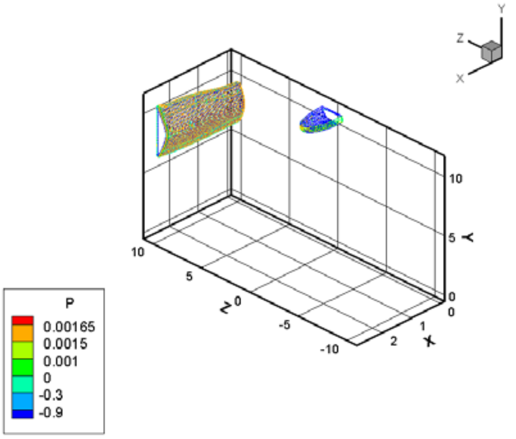

c)

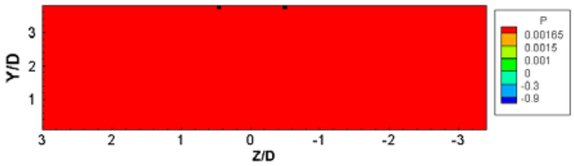

d)

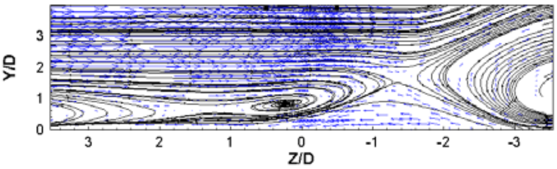

Figure 88: For h/D_i =1.87 and U_i/U_∞=45.45: a) 3D stream traces; b) 3D pressure distribution; c) pressure distribution in the ground plane; d) plane X=0.75XTOT

a)

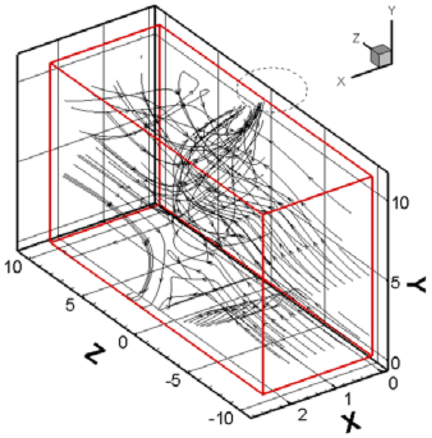

b)

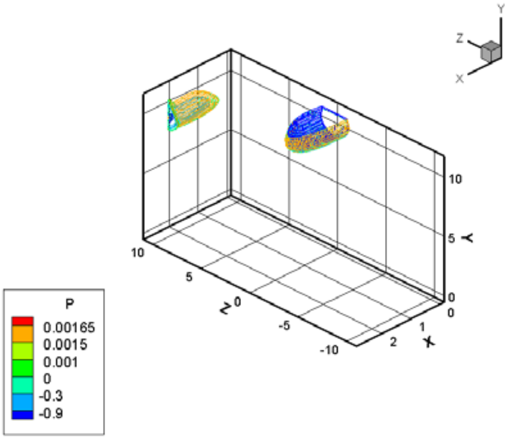

c)

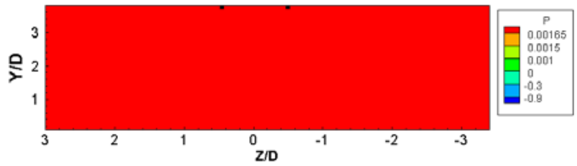

d)

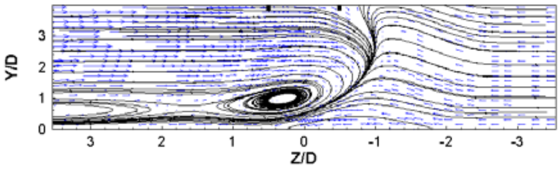

e)

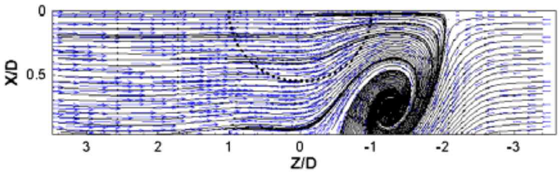

Figure 89: For h/D_i =1.60 and U_i/U_∞=45.45: a) 3D stream traces; b) 3D pressure distribution; c) pressure distribution in the ground plane; d) plane X=0.50XTOT; e) plane Y=0.50YTOT

a)

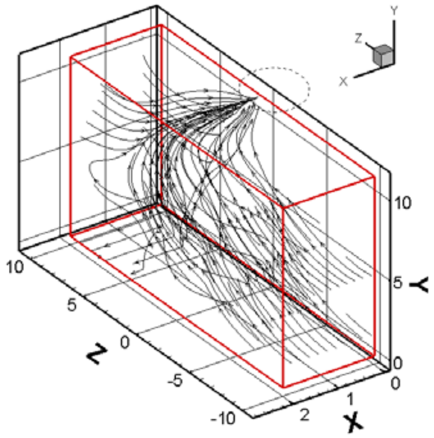

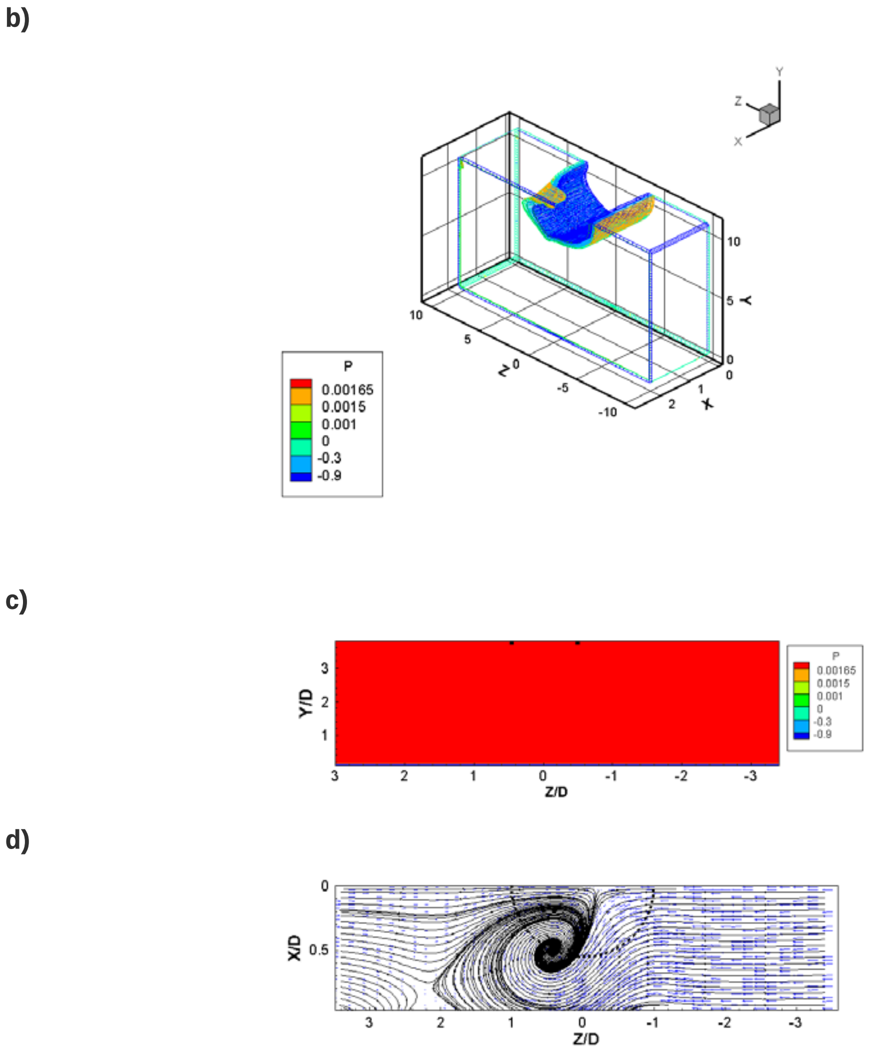

Figure 90: For h/Di =1.33 and =45.45: a) 3D stream traces; b) 3D pressure **distribution; c) pressure distribution in the ground plane; d) plane Y=0.50YTOT**

A.3. Two Vortices

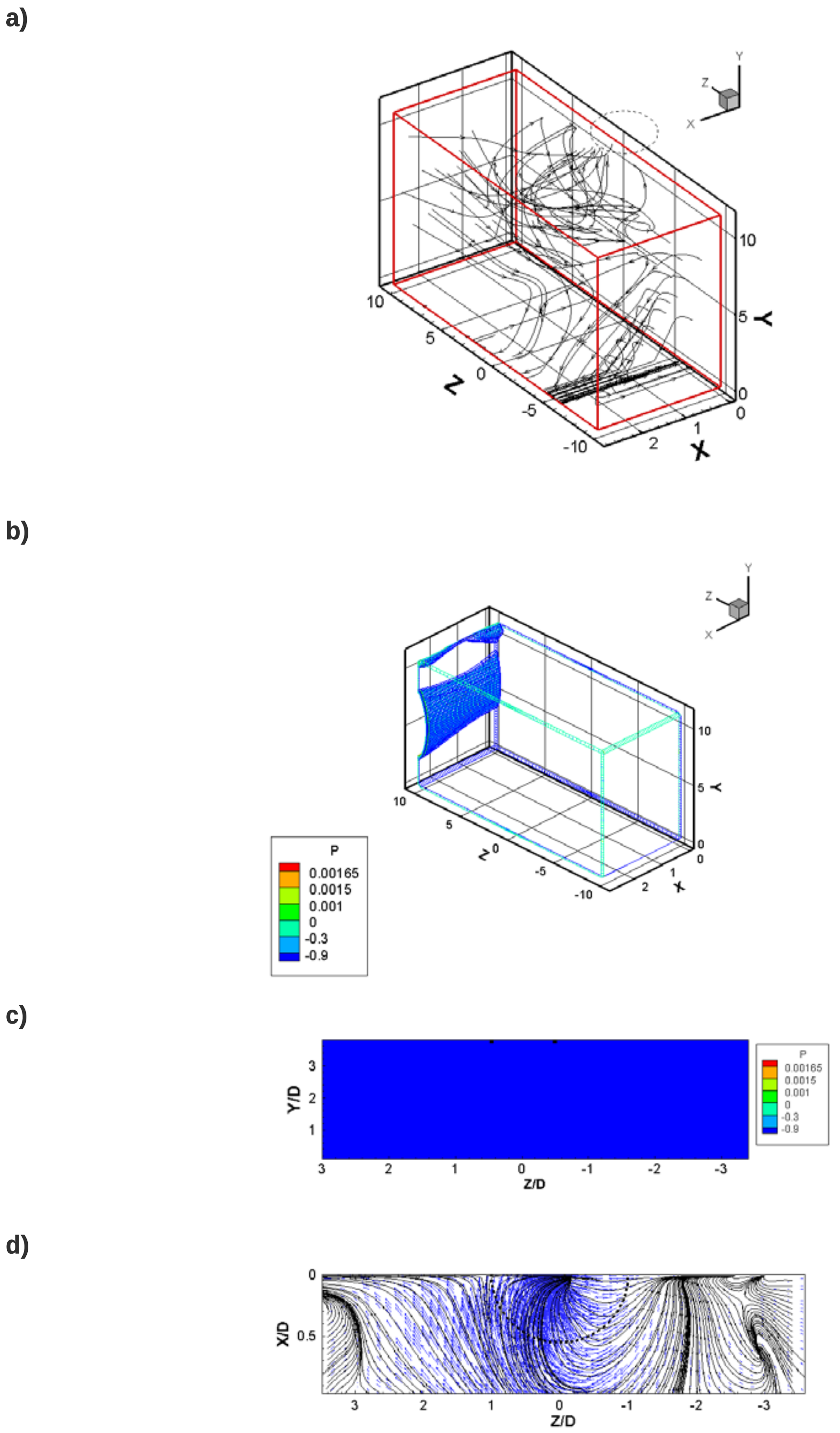

Figure 91: For h/D_i=1.4 and U_i/U_∞=45.45: a) 3D stream traces; b) 3D pressure distribution; c) pressure distribution in the ground plane; d) plane Y=0.95YTOT

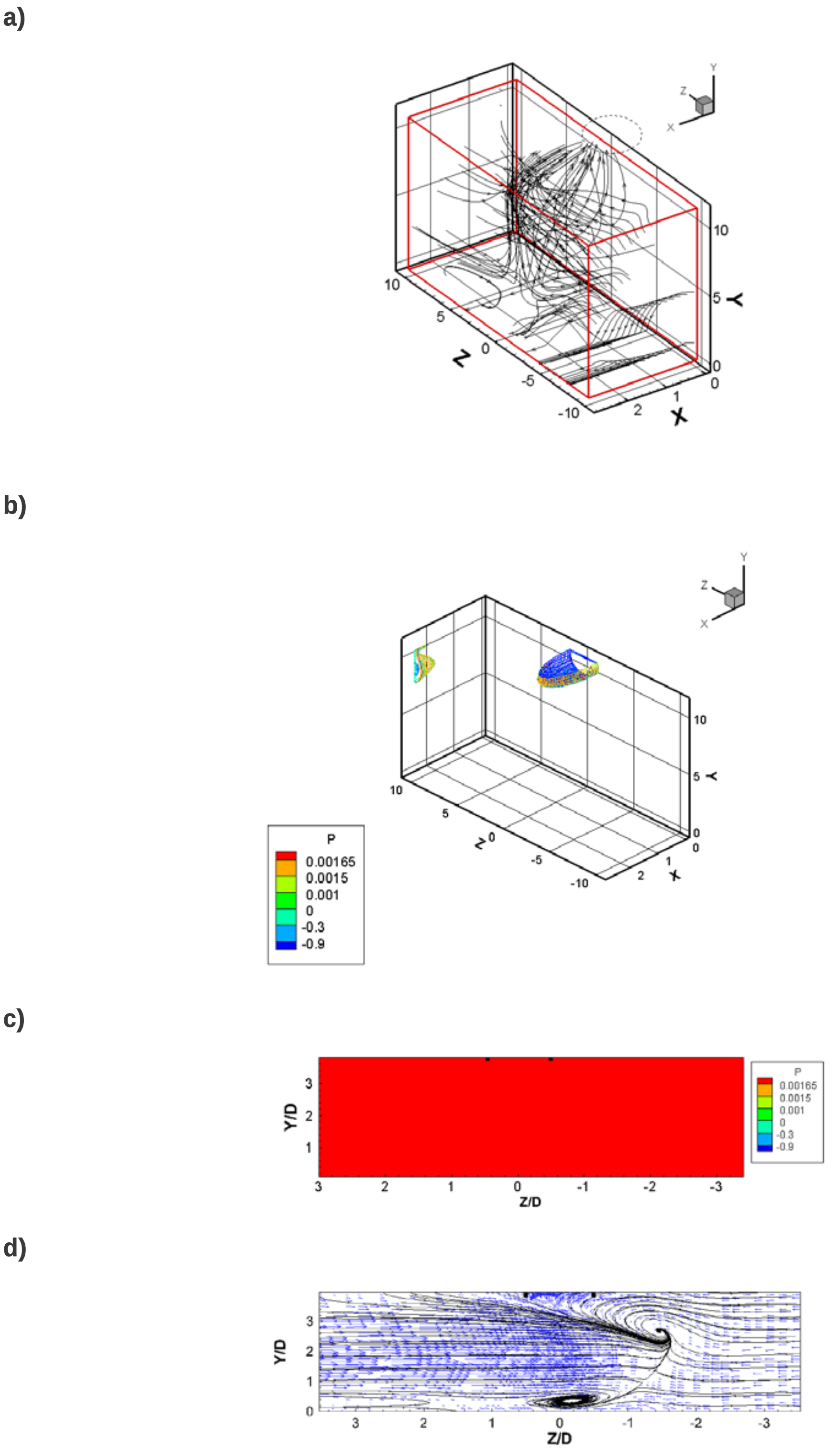

Figure 92: For h/D_i=1.17 and U_i/U_∞=18.18: a) 3D stream traces; b) 3D pressure distribution; c) pressure distribution in the ground plane; d) plane X=0.50XTOT

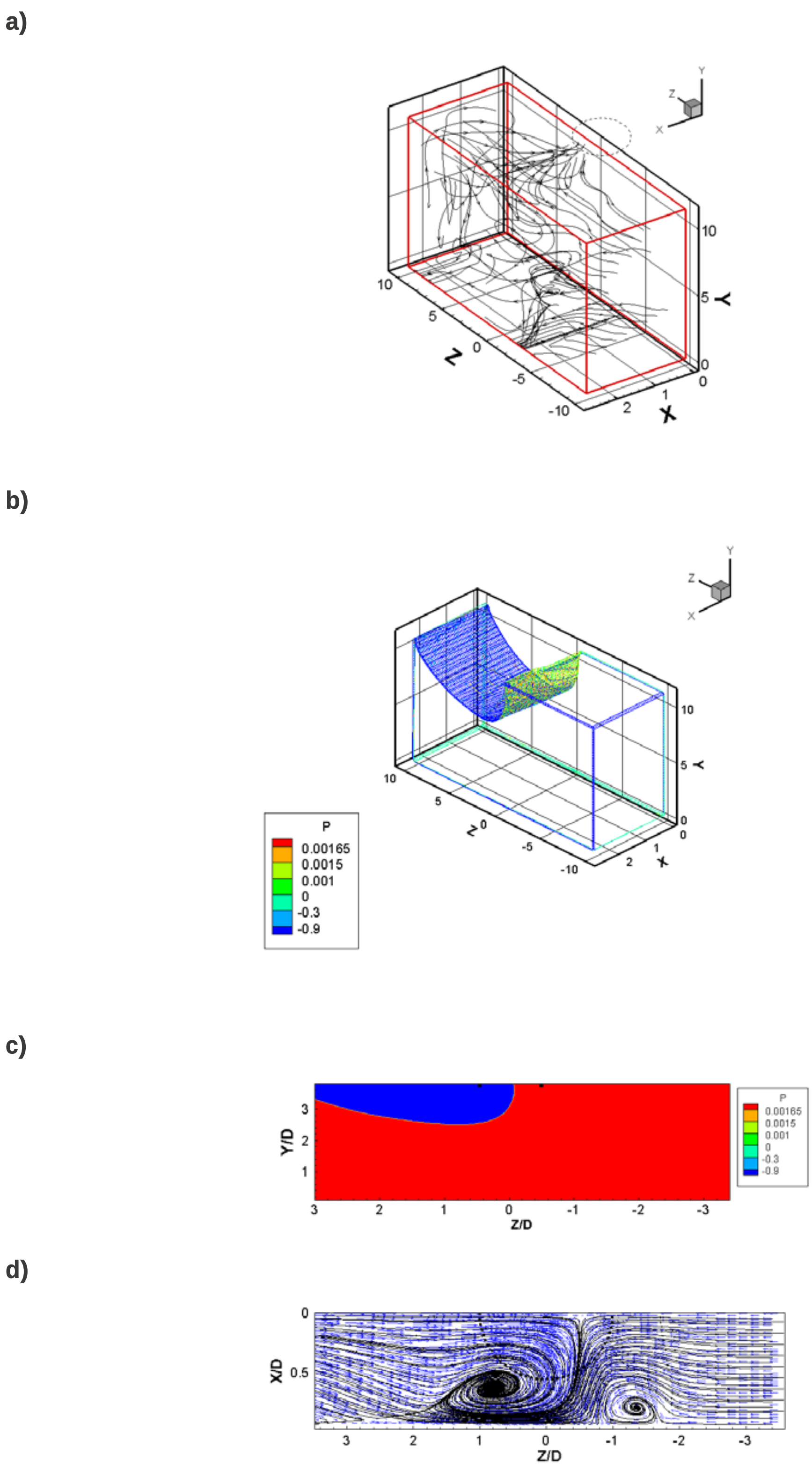

Figure 93: For h/D_i=0.93 and U_i/U_∞ =18.18: a) 3D stream traces; b) 3D pressure distribution; c) pressure distribution in the ground plane; d) plane Y=0.50YTOT

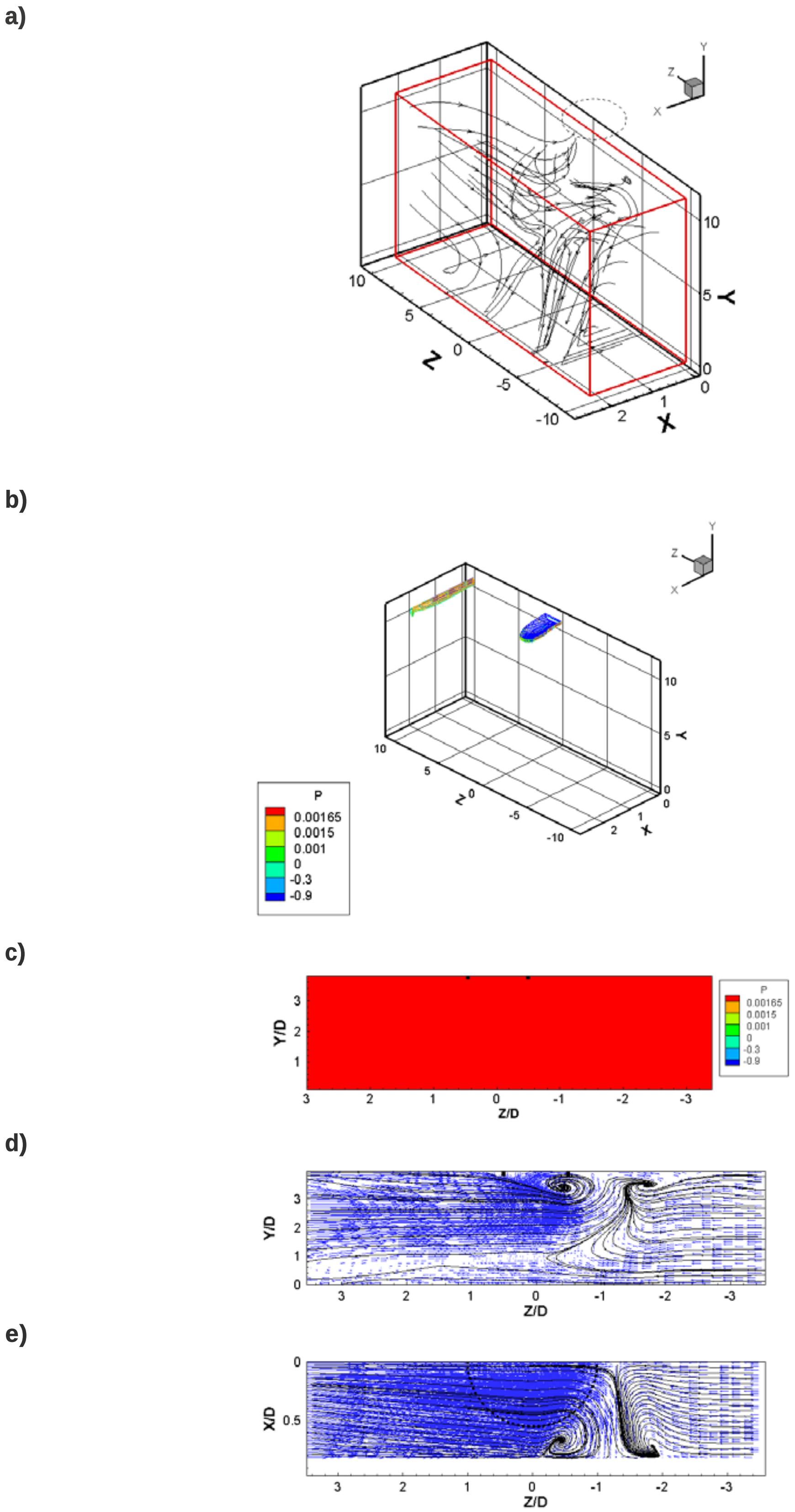

Figure 94: For h/D_i =0.82 and U_i/U_∞ =18.18: a) 3D stream traces; b) 3D pressure distribution; c) pressure distribution in the ground plane; d) plane_ X _0.50XTOT; e) plane Y=0.50YTOT

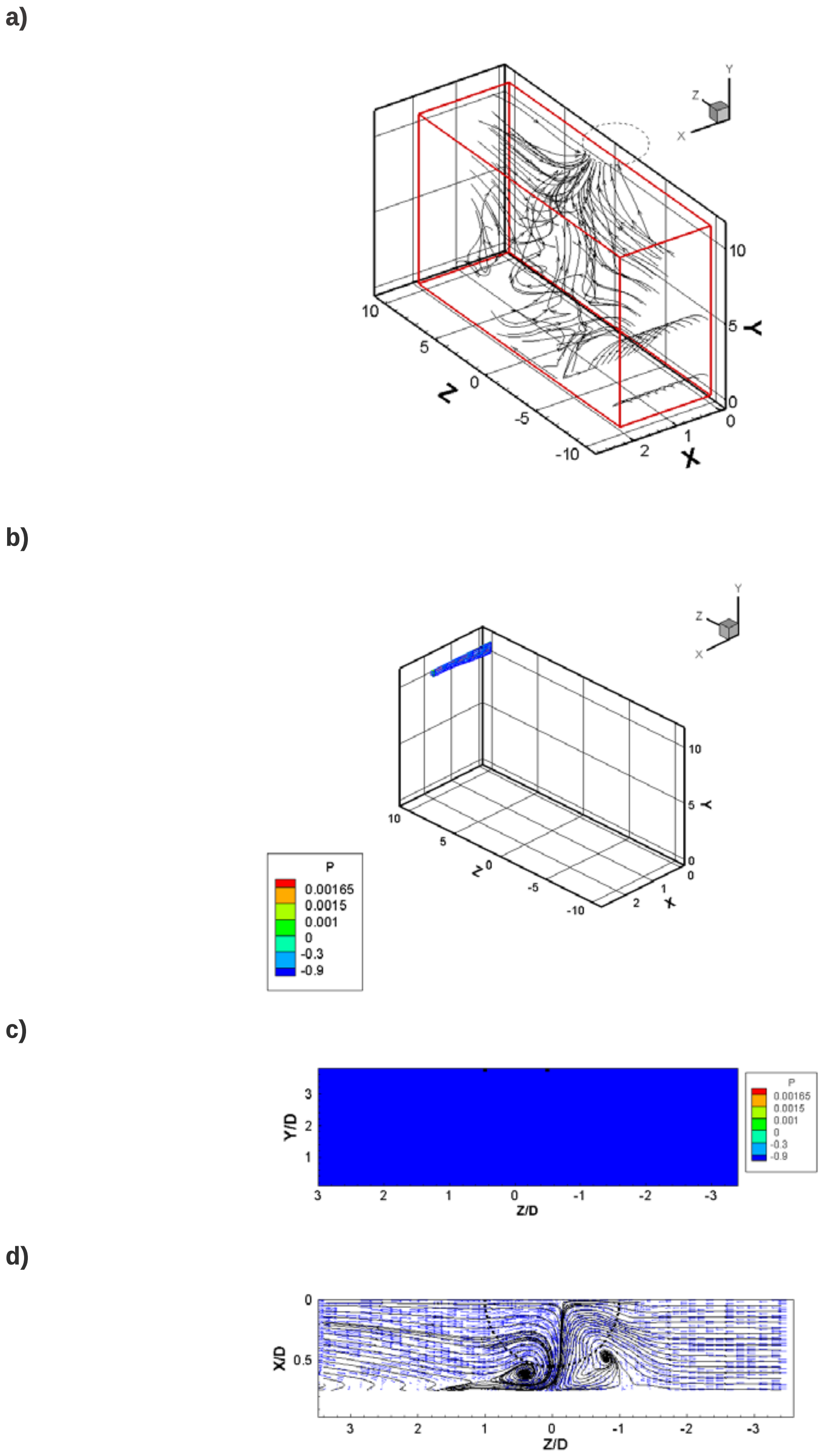

Figure 95: For h/D_i=0.75 and U_i/U_∞=18.18: a) 3D stream traces; b) 3D pressure distribution; c) pressure distribution in the ground plane; d) plane Y=0.50YTOT

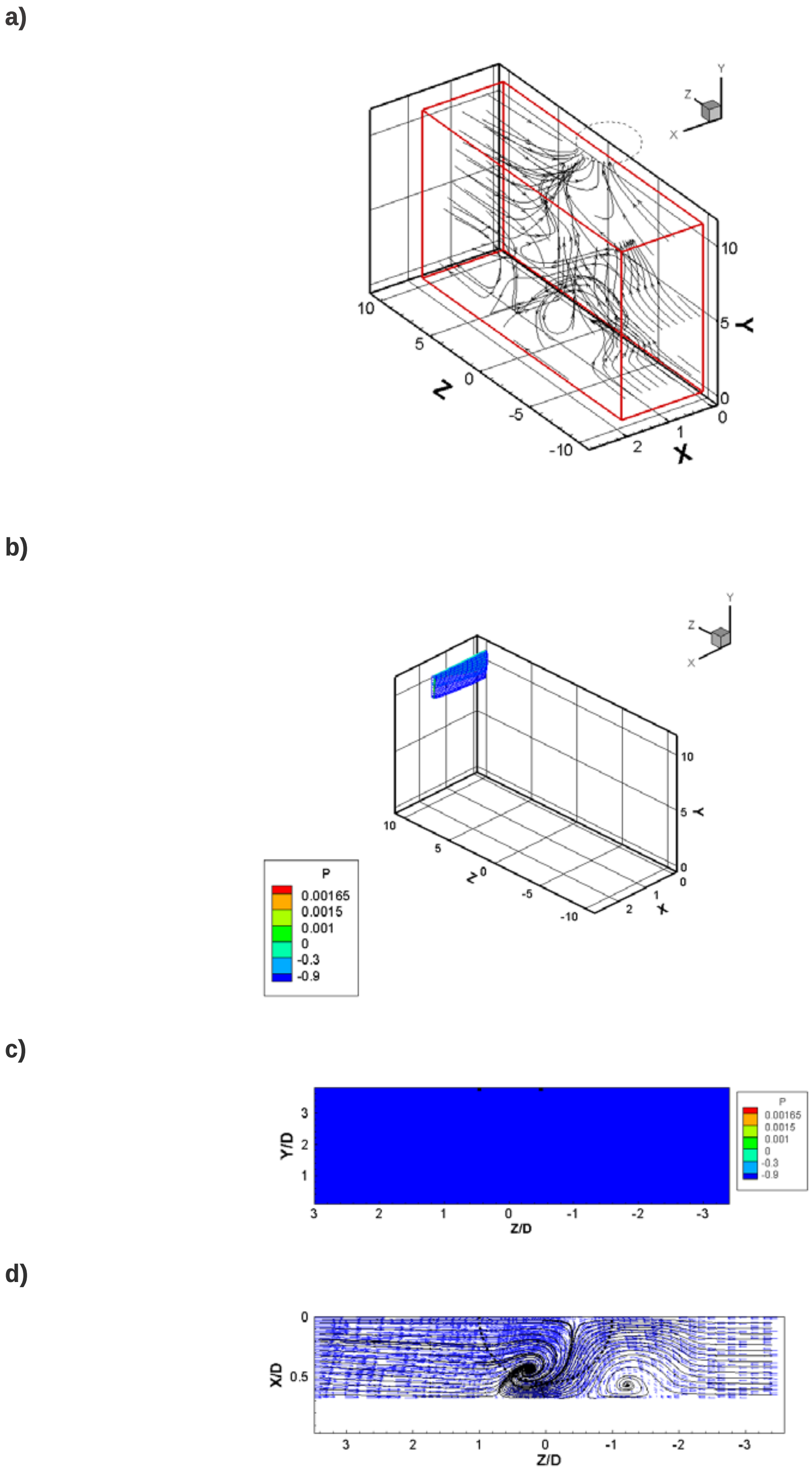

Figure 96: For h/D_i =0.68 and U_i/U_∞ =18.18: a) 3D stream traces; b) 3D pressure distribution; c) pressure distribution in the ground plane; d) plane Y=0.50YTOT

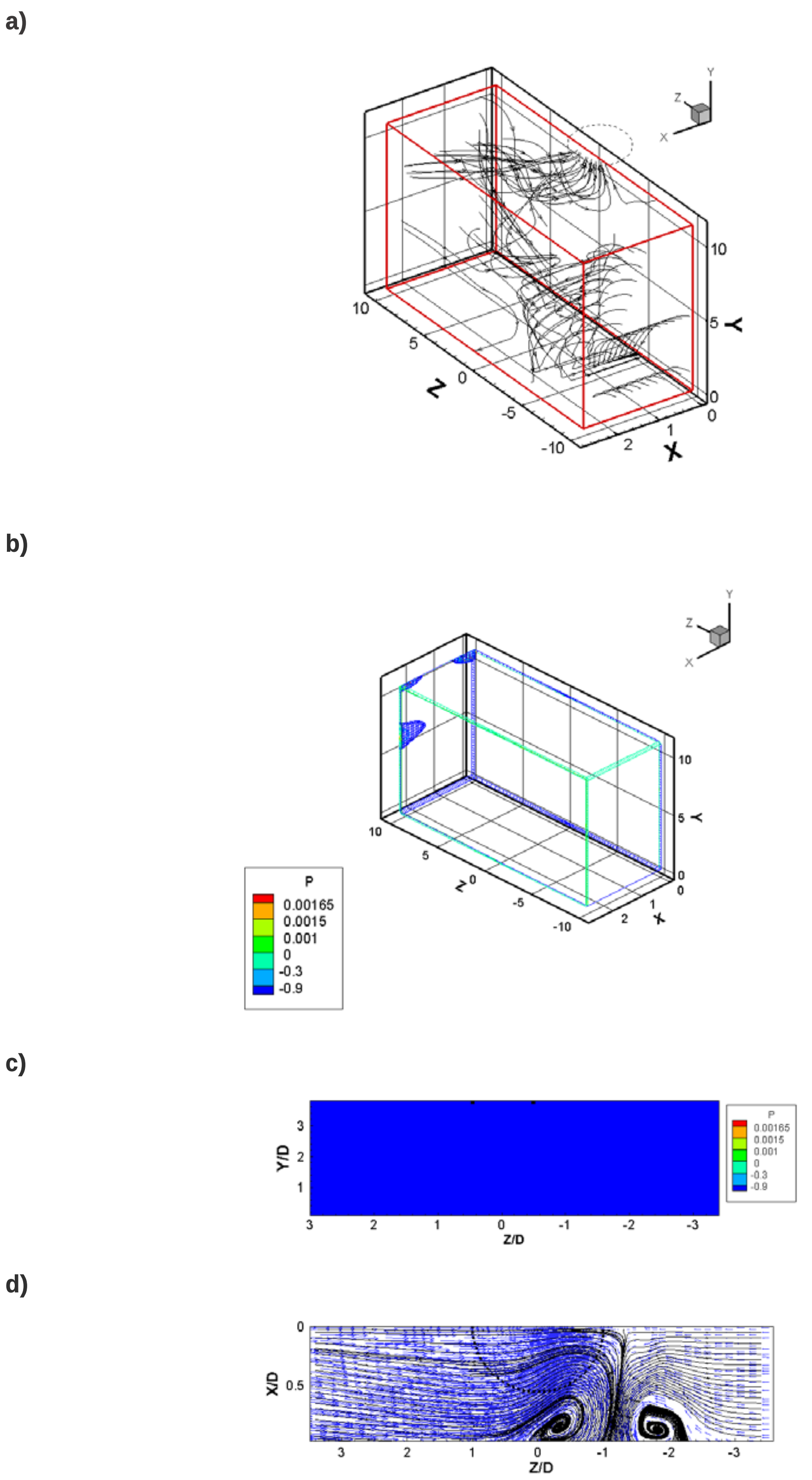

Figure 97: For h/D_i =1.08 and U_i/U_∞ =18.18: a) 3D stream traces; b) 3D pressure distribution; c) pressure distribution in the ground plane; d) plane Y=0.50YTOT

A.4. Three Vortices

a)

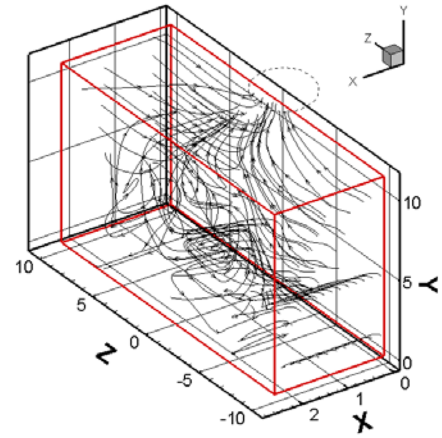

b)

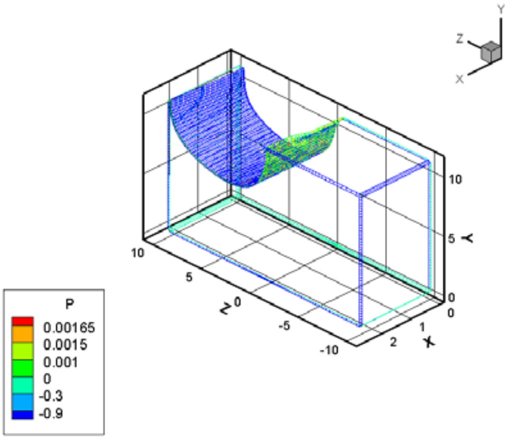

c)

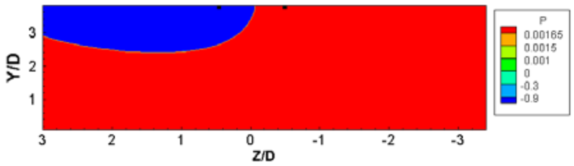

d)

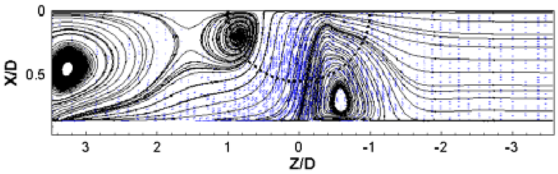

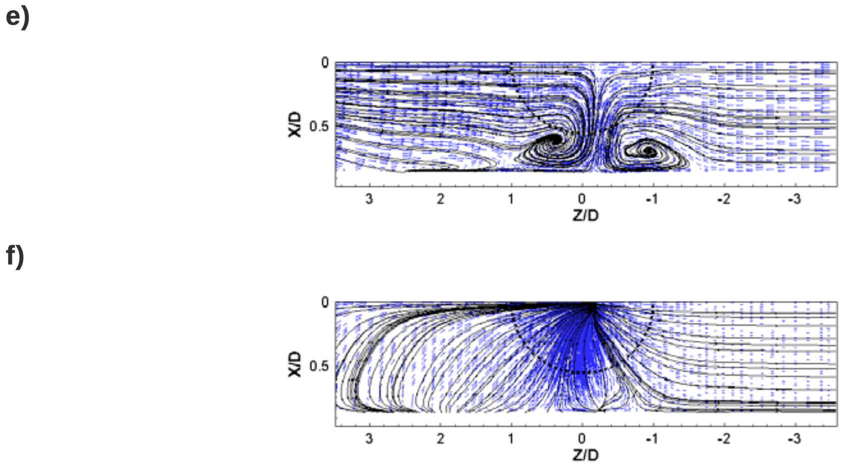

Figure 98: For h/D_i=0.86 and U_i/U_∞=27.27: a) 3D stream traces; b) 3D pressure distribution; c) pressure distribution in the ground plane; d) plane Y=0.05YTOT; e) plane Y=0.50YTOT; f) plane Y=0.95YTOT

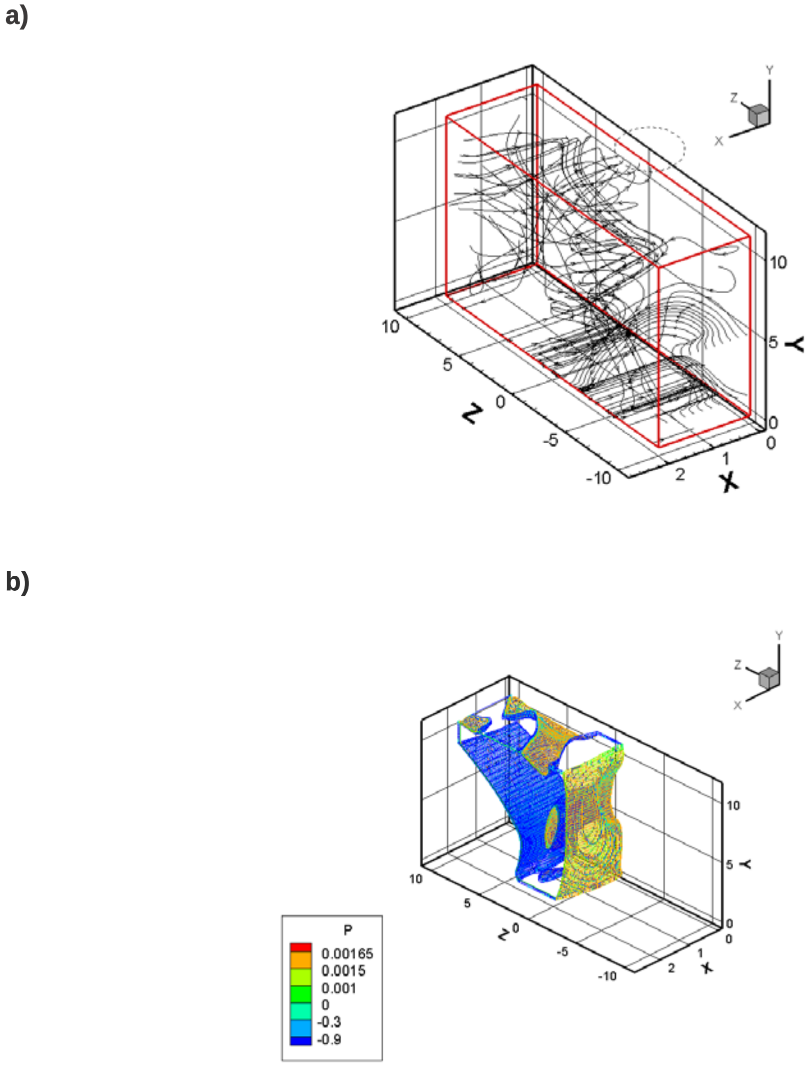

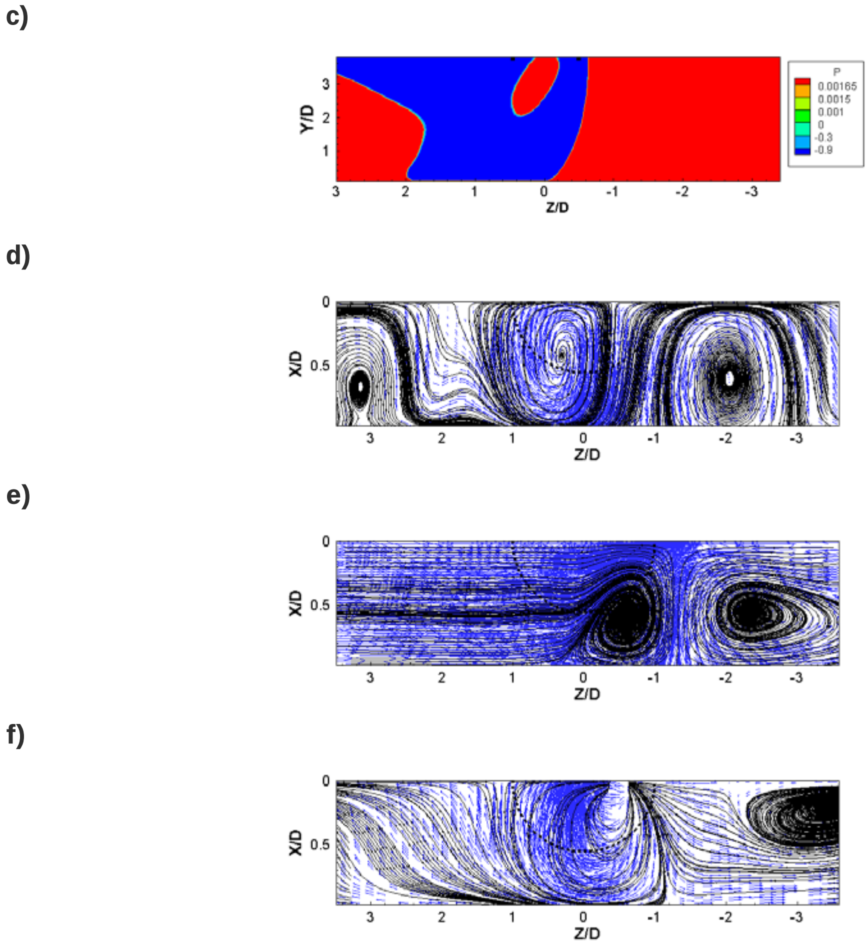

Figure 99: For h/D_i=1.00 and U_i/U_∞=27.27: a) 3D stream traces; b) 3D pressure distribution; c) pressure distribution in the ground plane; d) plane Y=0.05YTOT; e) plane Y=0.50YTOT; f) plane Y=0.95YTOT

a)

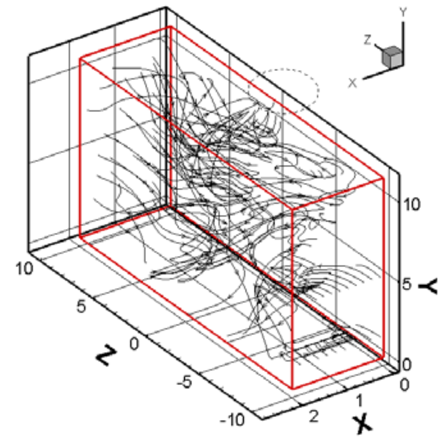

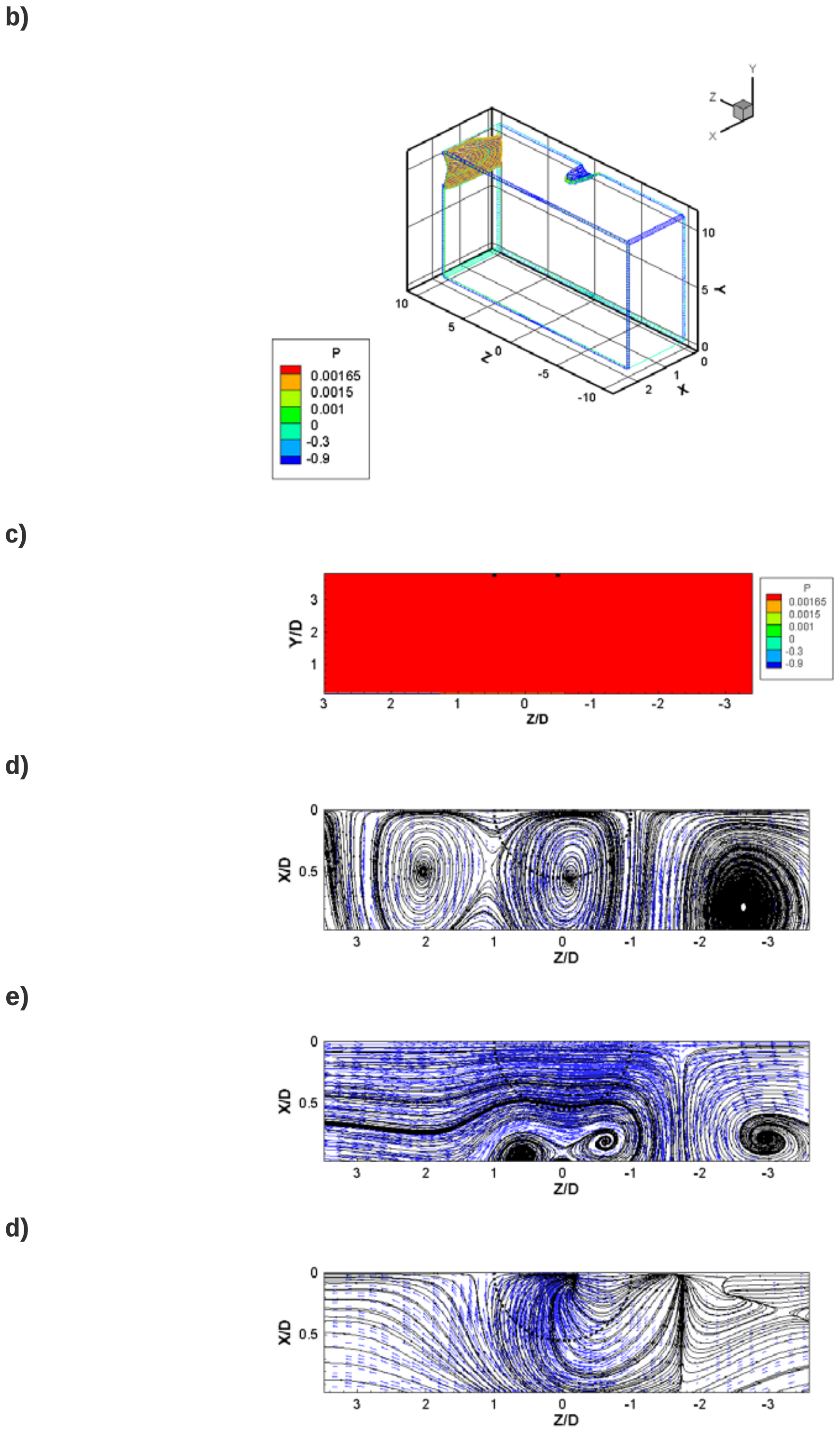

Figure 100: For h/D_i =1.25 and U_i/U_∞=27.27: a) 3D stream traces; b) 3D pressure distribution; c) pressure distribution in the ground plane; d) plane Y=0.05YTOT; e) plane Y=0.50YTOT; f) plane Y=0.95YTOT

a)

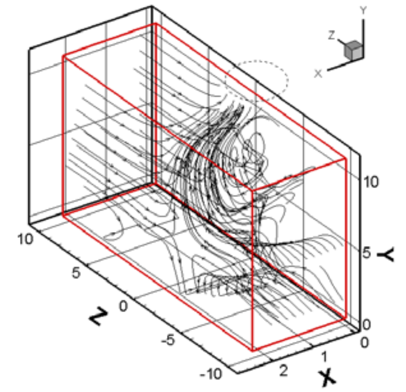
Y
Z
X
10
5
Y
0
10
5
0
Z
-5
-10
2
1
0
X

b)

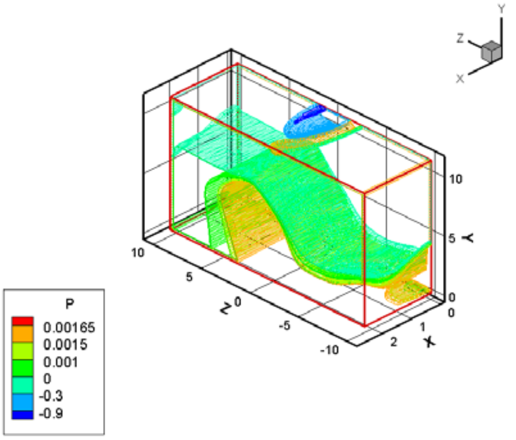
Y
Z
X
10
5
Y
0
10
5
0
Z
-5
-10
2
1
0
X
P
0.00165
0.0015
0.001
0
-0.3
-0.9

c)

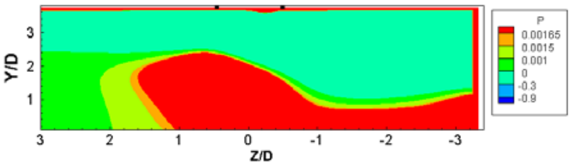
Y/D
3
2
1
3
2
1
0
-1
-2
-3
Z/D
P
0.00165
0.0015
0.001
0
-0.3
-0.9

d)

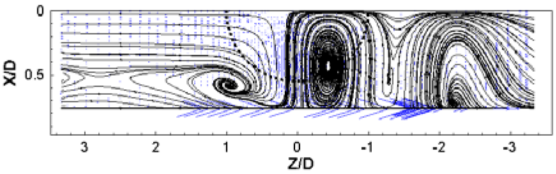
X/D
0
0.5
3
2
1
0
-1
-2
-3
Z/D

e)

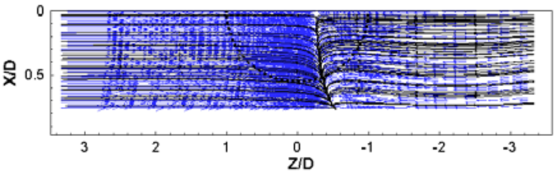
X/D
0
0.5
3
2
1
0
-1
-2
-3
Z/D

f)

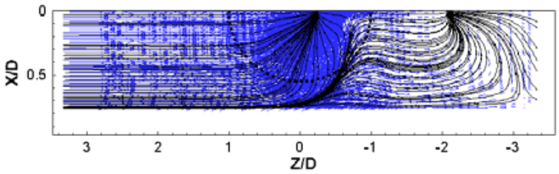

Figure 101: For h/D_i =0.77 and U_i/U_∞=72.73: a) 3D stream traces; b) 3D pressure distribution; c) pressure distribution in the ground plane; d) plane Y=0.05YTOT; e) plane Y=0.50YTOT; f) plane Y=0.95YTOT

a)

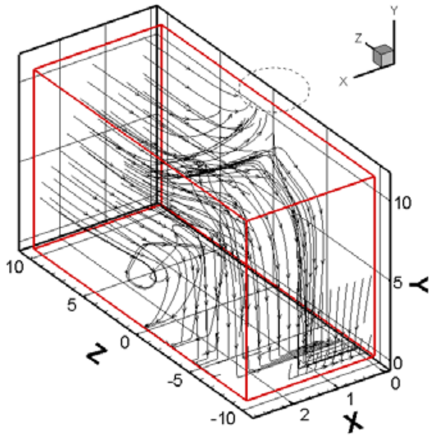

b)

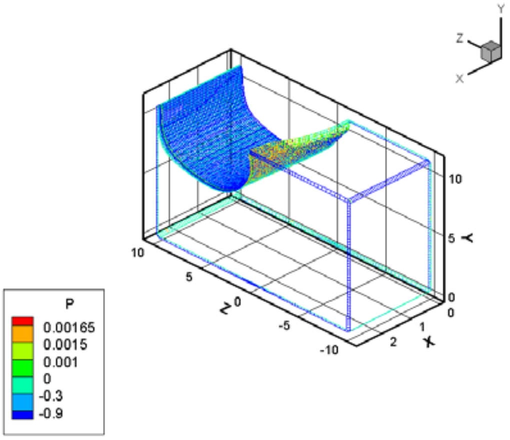

c)

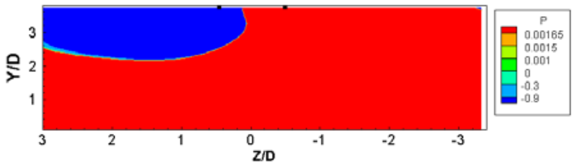

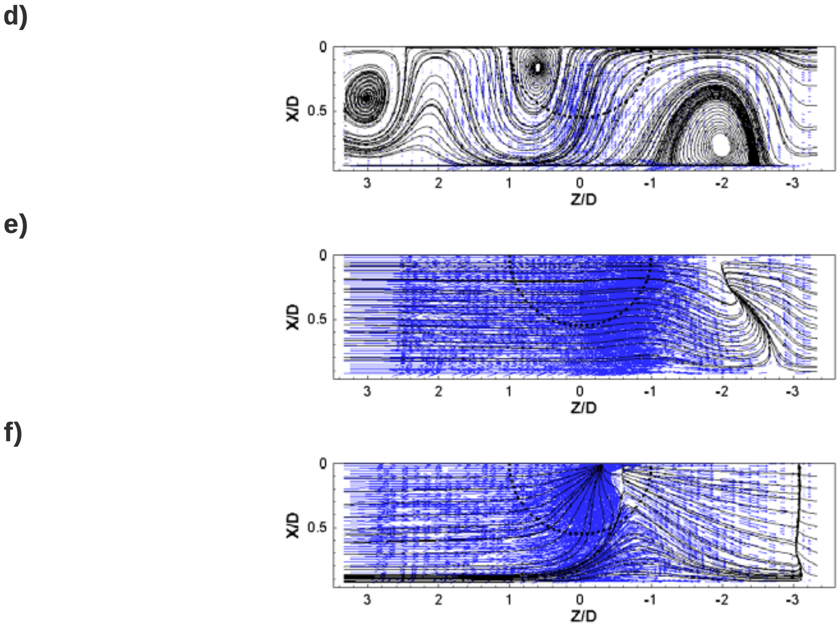

Figure 102: For h/D_i=0.93 and U_i/U_∞=45.45: a) 3D stream traces; b) 3D pressure distribution; c) pressure distribution in the ground plane; d) plane Y=0.05YTOT; e) plane Y=0.50YTOT; f) plane Y=0.95YTOT

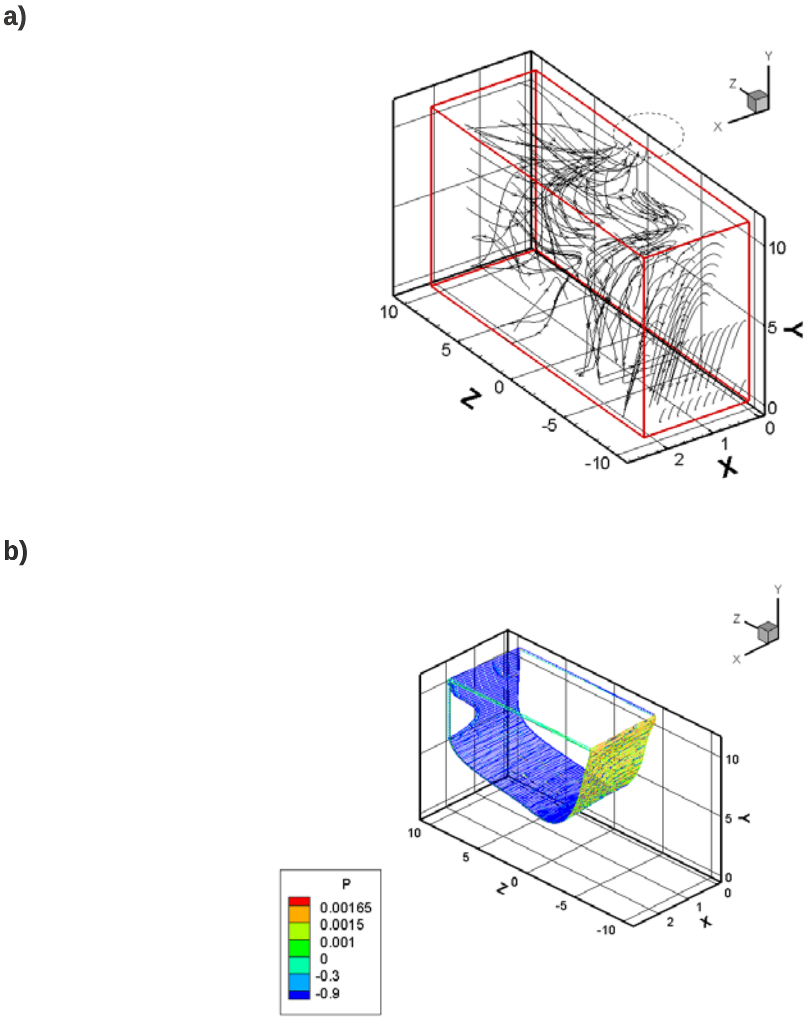

c)

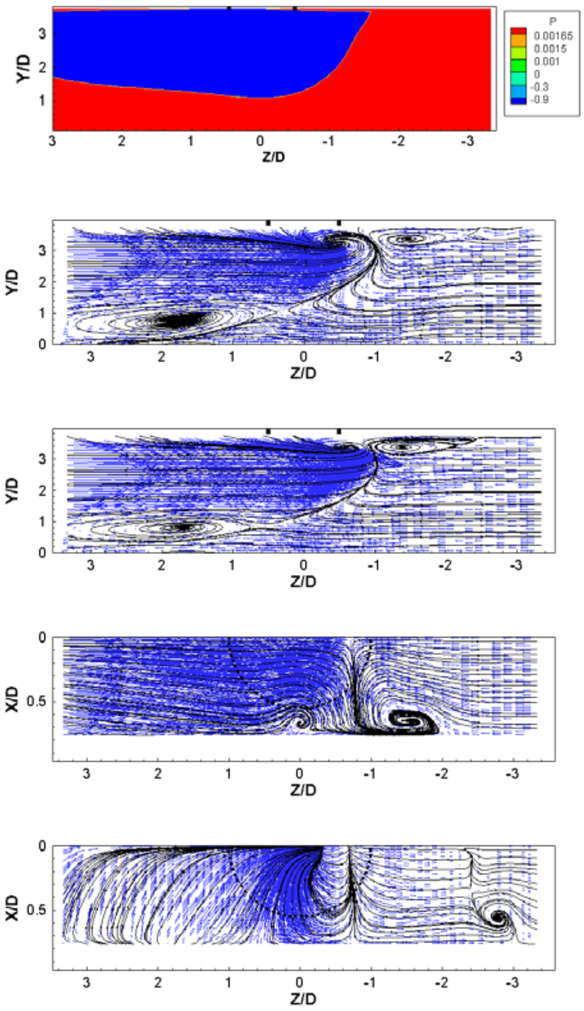

Figure 103: For h/D_i =0.77 and U_i/U_∞=27.27: a) 3D stream traces; b) 3D pressure distribution; c) pressure distribution in the ground plane; d) plane X=0.50XTOT; e) plane X=0.25XTOT; f) plane Y=0.50YTOT; g) plane Y=0.95YTOT

a)

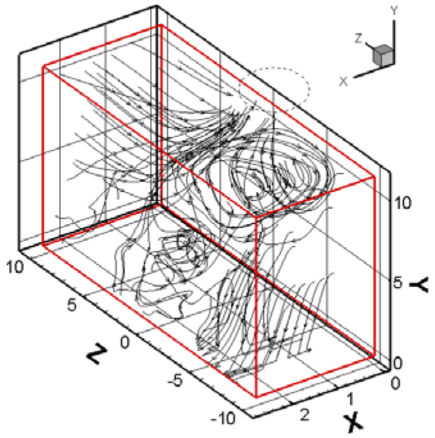

b)

c)

d)

e)

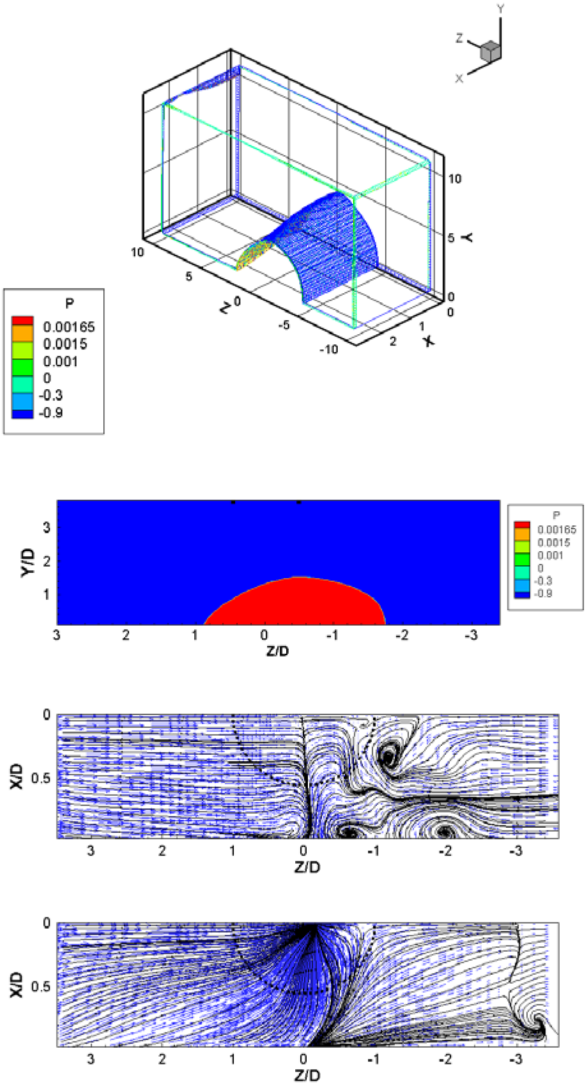

Figure 104: For h/D_i =1.00 and U_i/U_∞=54.55: a) 3D stream traces; b) 3D pressure distribution; c) pressure distribution in the ground plane; d) plane Y=0.50YTOT; e) plane Y=0.95YTOT

a)

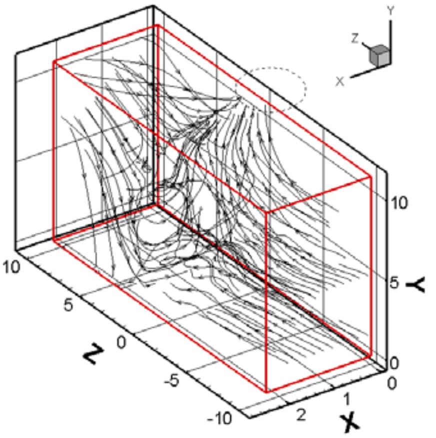

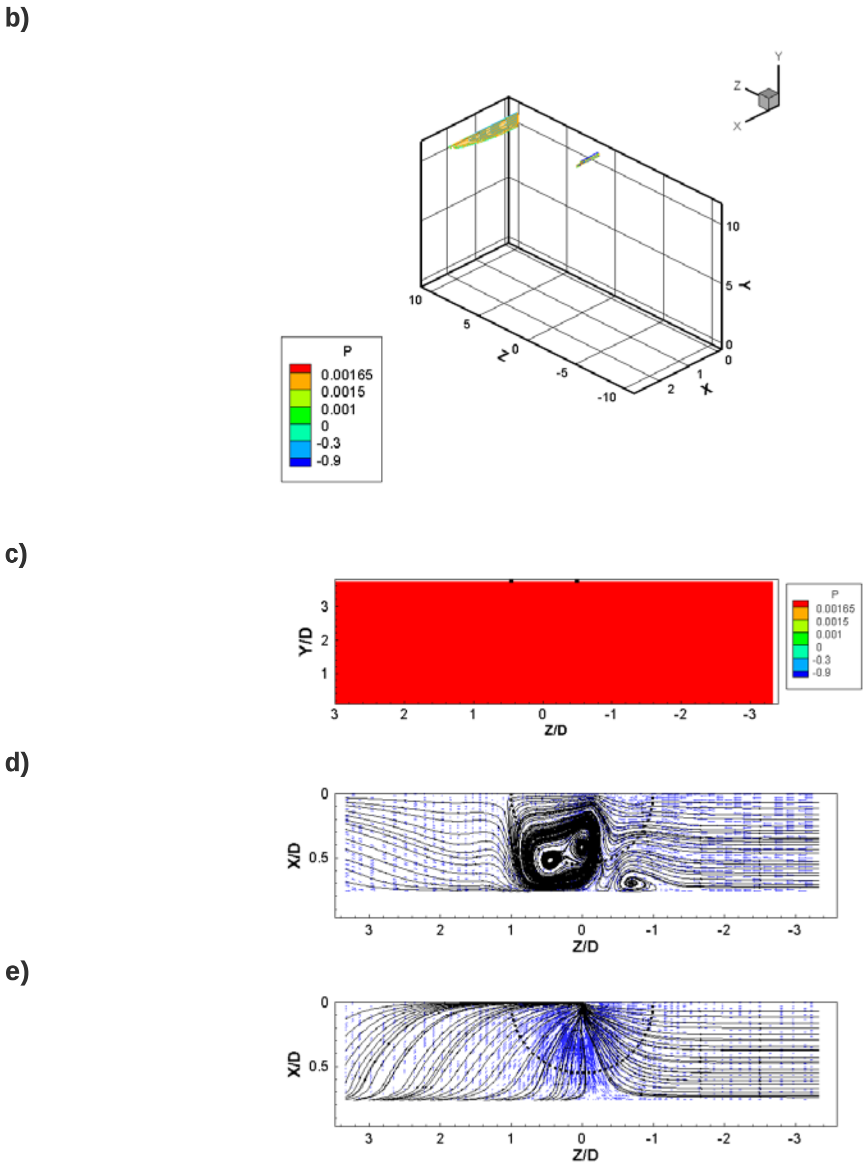

Figure 105: For h/D_i =0.77 and U_i/U_∞=9.09: a) 3D stream traces; b) 3D pressure distribution; c) pressure distribution in the ground plane; d) plane Y=0.50YTOT; e) plane Y=0.95YTOT

A.5. Four Vortices

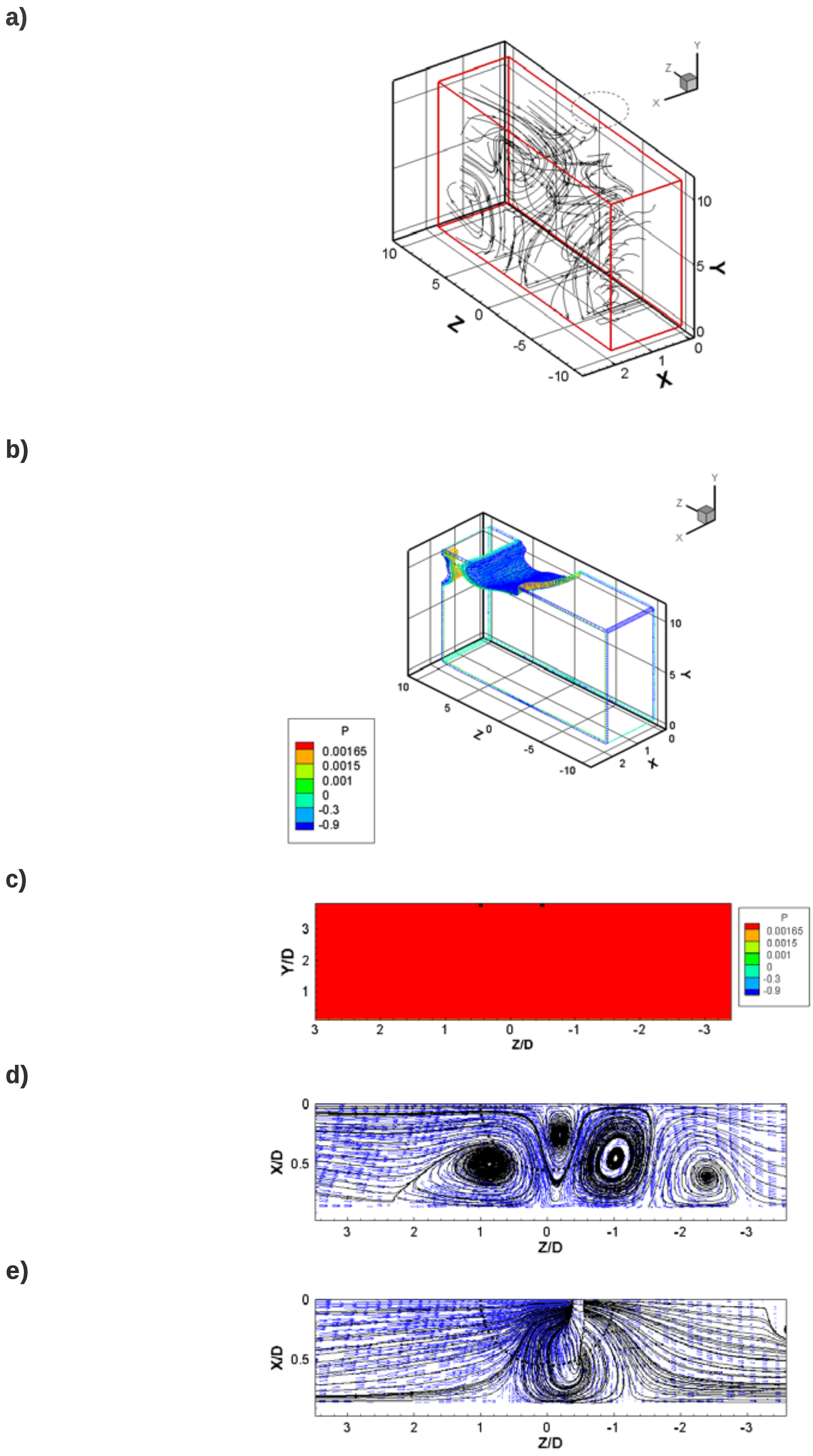

Figure 106: For h/D_i =0.86 and U_i/U_∞=18.18: a) 3D stream traces; b) 3D pressure distribution; c) pressure distribution in the ground plane; d) plane Y=0.50YTOT; e) plane Y=0.95YTOT

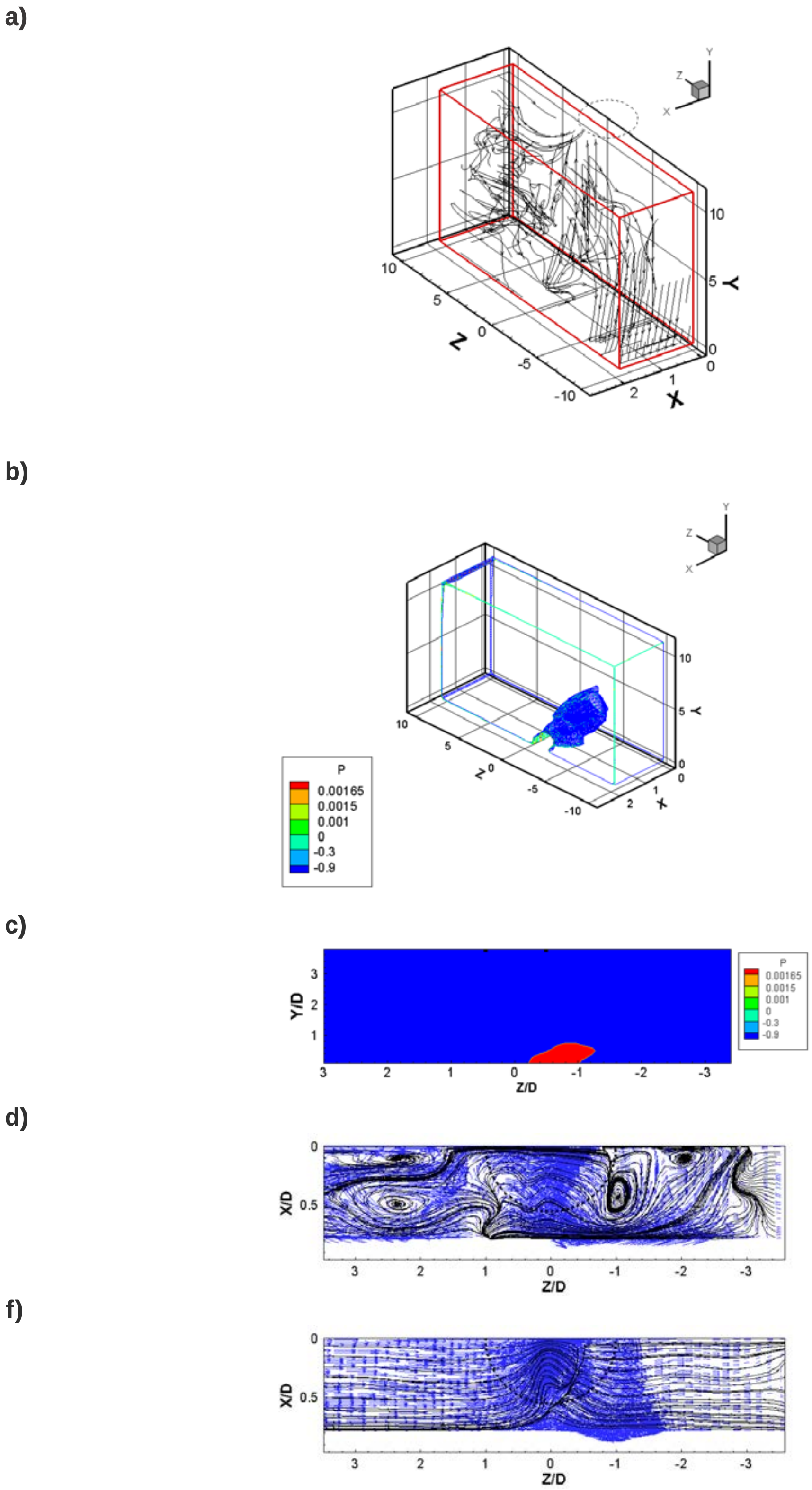

Figure 107: For h/D_i =0.79 and U_i/U_∞=72.73: a) 3D stream traces; b) 3D pressure distribution; c) pressure distribution in the ground plane; d) plane Y=0.50YTOT; e) plane Y=0.95YTOT

Annex B Papers Resulting from the Present Work

46th AIAA/ASME/SAE/ASEE Joint Propulsion Conference & Exhibit
25 - 28 July 2010, Nashville, TN

AIAA 2010-7116

A Comparison of Different Gas Turbine Engines Ground Vortex Flows

Jorge M. M. Barata[1], Pedro Manquinho[2] and André R. R. Silva[3]
Universidade da Beira Interior, Covilhã, 6201-001, Portugal

A computational method was used to predict and compare the ground vortices forming between the ground and a 1/1th scale model intake of different gas turbine engines. Calculations have been performed for the case of an irrotational crossflow mode of formation. Two different kinds of vortices appear around the intake: an inlet vortex and a trailing vortex. Away from the inlet plane other types of complex vortical structures were also identified. The computational method was found to describe all the main features of the flow for full scale geometry.

Nomenclature

A_i = intake area
A_∞ = frequency of oscillation of the ground vortex
D_i = inner diameter of the intake
h = height of the engine axis above the ground
$\boldsymbol{k}$ = turbulent kinetic energy
L_q = intake stream tube length
$\dot{m}$ = mass flow
U_i = intake throat velocity
U_∞ = free stream velocity
V_∞ = tangential velocity
Γ = vortex circulation
ζ = vorticity
ρ = density
μ = dynamic viscosity
ν = kinematic viscosity
ν_T = turbulent kinematic viscosity
ϕ = any dependent variable

I. Introduction

The design of an engine intake is a very important part of the aircraft engine design because it influences the overall performance. The inlet is designed to give the appropriate amount of airflow required from the free-stream conditions to the conditions required at the entrance of the compressor with minimal pressure loss by the engine[1]. Flow distortions at the inlet cause conditions that were not taken into account during the design process and usually represent a negative influence. So, to obtain the optimal engine conditions the airflow must be as uniform as possible when entering the compressor. This airflow condition is necessary in all flight configurations including when the aircraft is maneuvering on ground tasks where hazardous suction of objects may occur.

---

[1] Full Professor, Aerospace Sciences Department, Associate Fellow of AIAA.

[2] MEng Student, Aerospace Sciences Department, Rua Marques Avila e Bolama.

[3] Assistant Professor, Aerospace Sciences Department, AIAA Member.

The intake performance depends on the mass-flow delivered to the compressor. The internal mass-flow stays constant from the captured stream tube to the compressor face and assuming that the flow is incompressible due to low speed velocities, it will be given by $A_i U_i = A_\infty U_\infty$. Since the mass-flow is constant and the area ratio is related to the stream tube contraction ratio, the area ratio can be expressed as $\frac{A_\infty}{A_i} = \left(\frac{L_q}{D_i}\right)^2$. The capture ratio A_∞ / A_i is controlled by the engine, the engine mass-flow, the inlet diameter and the free-stream velocity. The area defined by the boundary between the air that enters in the engine and the air that does not is called the intake captured area. The flow ratio and the stream-tube shape vary with the operation conditions of the aircraft engine. In near static configuration since the ambient air is at rest, the engine must accelerate the air using maximum thrust. The extreme local acceleration of the flow at the inlet lip can lead to airflow separation in this region[2,3]. In cross-wind configuration, the shape of the stream tube is modified near the lip. The cross-flow leads to an increase in the flow velocity near the lip depending on the strength of the cross-flow, high velocity origins in flow separation leading to a total pressure loss at the engine fan.

The formation of ground vortices depends on engine power, wind velocity and engine inlet height and size. Previous published work show that the phenomenon can only occur with the presence of a stagnation streamline between the ground and the intake which is dependent on the velocity ratio U_i / U_∞ and the non-dimensional height of the engine axis above the ground, h/D_i (Fig. 1). In static conditions, the inlet airflow demand increases, and the inlet capture surface increases in diameter and starts including the ground to bring the necessary airflow to the fan[4,5]. Typically the formation of ground vortices is characterized by low h/D_i and high U_i / U_∞ that corresponds to an engine operating close to the ground at a high inlet mass flow[6]. Hence, the mechanism of intake formation is strongly dependant of the height of the engine axis above the ground, the velocity ratio and the presence of an upstream velocity.

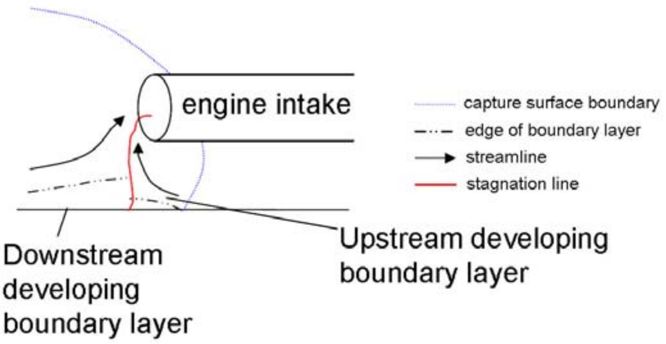

Figure 1. Ground vortex formation.

Four different types of conditions leading to the formation of inlet ground vortices have been identified. A vortex can be generated without ambient wind and with a low ratio h/D_i (typically less than one). Due to the ground proximity, high levels of suction beneath the engine inlet leads into a strong flow underneath the inlet upstream towards the intake lip[7]. In these conditions, it is possible to visualize at the engine intake and at the ground two upward spiraling vortices. Under no-wind condition, it appears that the two vortices are counter-rotating, and the vorticity is induced by the boundary layer. Is a head-wind flow, when the air is sucked into the engine inlet, the flow field underneath the intake starts to roll up into two upright counter-rotating vortices and a fast flow into the opposite direction of the wind appears between them[8,9]. For high velocity ratios (>20) the sense of rotation of the two vortices switches to the same as in the no-wind mechanism. With a 90° cross-wind two different kinds of vortices appear around the intake: an inlet vortex and a trailing vortex (Fig. 2). When the engine intake is oriented at a 90° yaw angle and with the presence of cross-wind with far upstream vertical vorticity, there is the formation of a single vortex inside the intake. In this case the sense of rotation of the vortex is opposite to the ambient vorticity.

Other mechanisms of formation also exist and can be considered as combinations of the previous ones that lead to a large number of possible combinations that are responsible for the need of more studies in order to understand all the physics involved. CFD tools have been applied recently to the understanding of the ground vortex with relative success. Nakayama & Jones[10] used panel methods to simulate the inlet and ground interaction, noting that the wind speed needed to blow the vortex away was lower than the measured experimentally. Barata et al.[11] report Reynolds Averaged Navier-Stokes calculations and predicted successfully the ground vortex phenomena using real operational conditions for the case of the engine Trent 900. The ground vortex formation in irrotational crosswind flow is analyzed in detail for this configuration and engine, and the formation of the trailing vortex was associated to a very complex flow.

In the present paper the previous work of Barata et al.[11] is extended to include several engines that have been used or will enter soon in service. The ground vortex flows produced by different engines are compared and discussed for each particular operational condition. These conditions are defined in terms of the real geometrical configuration, including diameter (D_i), clearance distance, height of the engine axis above the ground (H), etc. However, the inlet velocities correspond to the same selected jet-to-crosswind velocity ratios (U_i/U_∞ of 4.95, 9.8 and 19.8) to allow the comparison of the flow pattern generated by each particular engine.

The next section introduces the mathematical model. Section III presents the results which are followed by an analysis of the pressure field and the formation the ground vortex. The final section summarizes the main findings and conclusions of this work.

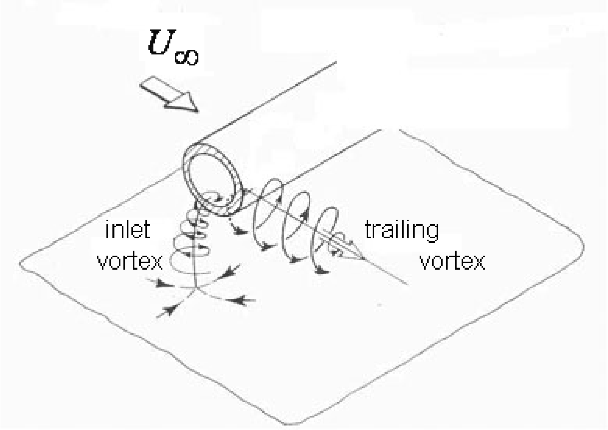

Figure 2. Sense of rotation of the inlet vortex and the trailing vortex (sketch adapted from Ref. 9).

II. Mathematical Model

The mathematical model used in the present study is described in detail in Ref. 11 and only the main features will be summarized here. The time averaged partial differential equations governing the steady, uniform-density isothermal three-dimensional flow

$$\rho \overline{U}_j \frac{\partial \overline{U}_i}{\partial X_j} = -\frac{\partial \overline{P}}{\partial X_i} + \frac{\partial}{\partial X_j}\left(\mu \frac{\partial \overline{U}_i}{\partial X_j} - \rho \overline{u'_i u'_j} \right) \qquad (1)$$

and the continuity equation,

$$\rho \overline{U}_j \frac{\partial \overline{U}_i}{\partial X_i} = 0 \qquad (2)$$

where solved together with the equations of transport of the turbulent kinetic energy and dissipation rate of the two-equation *"k-ε"* model[10]

$$\overline{U}_j \frac{\partial k}{\partial X_j} = \frac{\partial}{\partial X_j}\left(\frac{\upsilon_T}{\sigma_k} \frac{\partial k}{\partial X_j} \right) - \overline{u'_i u'_j} \frac{\partial \overline{U}_i}{\partial X_j} - \varepsilon \qquad (5)$$

$$\overline{U}_j \frac{\partial \varepsilon}{\partial X_j} = \frac{\partial}{\partial X_j}\left(\frac{\upsilon_T}{\sigma_\varepsilon} \frac{\partial \varepsilon}{\partial X_j} \right) - C_1 \frac{\varepsilon}{k} \overline{u'_i u'_j} \frac{\partial \overline{U}_i}{\partial X_j} - C_2 \frac{\varepsilon^2}{k} \qquad (6)$$

where C_1 and C_2 are additional dimensionless model constants, and σ_k and σ_ε are the turbulent Prandtl numbers for kinetic energy and turbulent dissipation.
The Reynolds stresses are expressed as

$$\overline{u'_i u'_j} = -\upsilon_T \left(\frac{\partial \overline{U}_i}{\partial X_j} + \frac{\partial \overline{U}_j}{\partial X_i} \right) + \frac{2}{3} k \delta_{ij} \qquad (3)$$

where υ_T is the turbulence kinematic viscosity, which is derived from the turbulence model and expressed by $C_\mu k^2/\varepsilon$.

The solution of the governing equations was obtained using a quadratic finite-difference method[12] that used discretized algebraic equations deduced from the exact differential equations that they represent.

The solution procedure is based on the SIMPLE algorithm widely used and reported in the literature (e.g. Ref. 13). It uses the staggered grid arrangement and a guess and correct procedure field such that the solution of the momentum equations satisfies continuity.

The computational domain has six boundaries where dependent values are specified: a free stream plane, a symmetry plane, and a solid wall. On the symmetry plane, the normal velocity vanishes, and the normal derivates of the other variables are zero. At the solid surface, the wall function method[14] is used to prescribe the boundary conditions for the velocity and turbulence quantities, assuming that the turbulence is in state of local equilibrium. The free stream plane is located at Z=0 and corresponds to the crossflow conditions. The engine intake boundary is represented by a right angled polygon and the mass flow rates and the momentum are matched to the experimental values. The intake represents a 1/1th scale model with a diameter that corresponds to each particular engine. The axis of the engine is located at a distance above the ground (h), which corresponds to the specific clearance distance. All the tests were performed for the case of irrotational crosswind, and the other conditions are shown in Table 1. The domain of solution, their dimensions and the system of axes are represented in Fig.3.

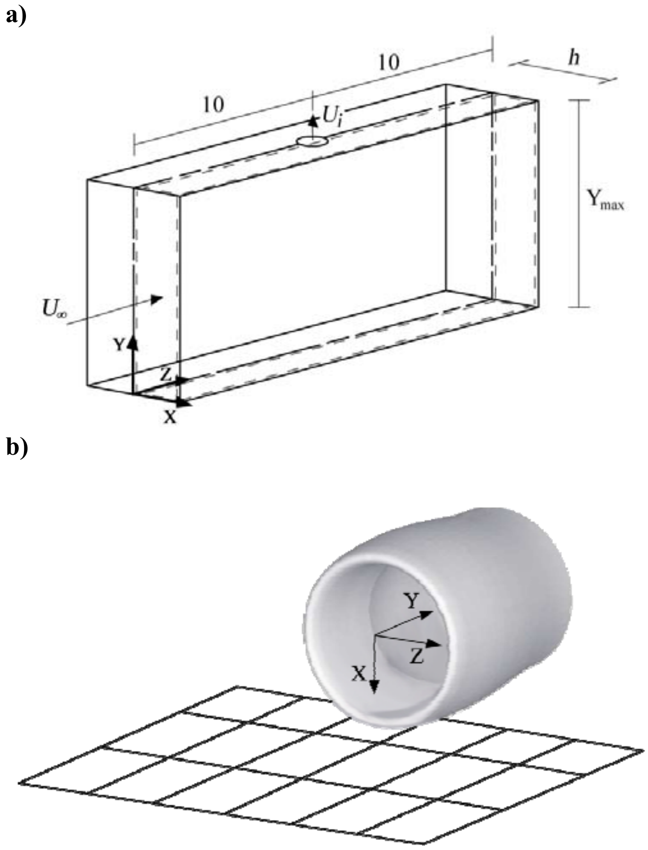

Figure 3. Domain of the solution a). Representation of the intake with referential at the center b).

Table 1. Summary of selected engine characteristics.

Engine	Diameter (m)	Clearance Distance (m)	Mass Flow (lb/s)	Mass Flow (Kg/s)	Radius (m)	Inlet Velocity (m/s)	H (m)
cf6-80a	2.667	0.654	1435	650.905	1.3335	43.14	1.988
trent 700	2.474	0.690	2030	920.793	1.2370	70.93	1.927
trent 900	2.946	1.030	2655	1204.288	1.4730	65.42	2.503
GE nx -1B64	2.819	0.740	2458	1114.930	1.4095	66.15	2.150

Grid independence tests were performed with different mesh sizes, and the results for a mesh with 33×59×33 were found to be independent of numerical influences. Nevertheless, a finer grid of 49×89×49 meshes was used to give a better description of the engine inlet.

III. Results

The ground vortex formation in irrotational crosswind flow is analyzed in the present section. In this configuration the ground vortex or inlet vortex that forms near the ground and is sucked by engine is accompanied by an additional feature which is the formation of the trailing vortex (see Fig. 2). This vortex develops from the lip of the inlet engine in the direction of the crossflow with its axis parallel to the ground.

Figure 4 shows three-dimensional particle tracks for the Trent 900 and the GE nx-1B64 engines for velocity ratios between the inlet and the crossflow, U_i/U_∞, of 4.95, 9.8 and 19.8. The vortex structure is detected for both engines for the highest velocity ratio (Fig. 4 e and f) with fluid being captured from both sides of the engine inlet that form a spiral directed towards the engine inlet. For an intermediate velocity ratio of 9.8 the intake fluid is also being sucked upstream and downstream of the engine inlet but the spiral tendency is only noticeable for the case of the GE nx-1B64 engine. For the smallest velocity ratio (U_i/U_∞ =4.95) the crossflow is less deflected by the engine for the Trent 900 case, while in the case of the GE nx-1B64 is deviated towards the vertical plane of symmetry to form an outwards jet-like flow (in the opposite direction of the engine inlet flow).

The flow pattern described before is associated with typical ground pressure distributions that are shown in Fig. 5. The static ground pressure nondimensionalized by the crossflow kinematic energy ($1/2\rho U_\infty^2$) is shown for the same conditions of Fig. 4 and both the Trent 900 and the GE nx-1B64 engines. For the smallest velocity ratio (Fig. 5a and b) the negative pressure region is about the same size with an intensity $(p - p_\infty)/(1/2\rho U_\infty^2) \approx -1.0$. For a velocity ratio, U_i/U_∞, of 9.9 (Fig. 5c and d), the negative region in the upstream side of the inlet becomes more intense with values of $(p - p_\infty)/(1/2\rho U_\infty^2)$ near -2.5, but in the downstream side the slight positive region also increases. Finally, for the highest velocity ratio of U_i/U_∞=19.8 (Fig. 5e and 5f) most of the ground floor is subjected to a relevant positive pressure, $0.25 < (p - p_\infty)/(1/2\rho U_\infty^2) < 0.5$, but a high suction region $(p - p_\infty)/(1/2\rho U_\infty^2) < -2.5$ in the inlet direction occurs. The negative region is located in the upstream side for the Trent 900 case and its extension is about ¾ of the inlet diameter while for the case of the GE nx-1B64 is considerably larger with a size slightly larger than one inlet diameter. In spite of these negative values a small high pressure region can be observed in the downstream side which is associated with the tendency for the formation of a stagnation line and the corresponding stagnation point.

The formation of the ground vortex near the wall is further analyzed with the help of Fig. 6 which shows near wall velocity vectors and particle streaks for the GE nx-1B64 case. The upstream and downstream flow converge to a line for the smallest and highest velocity ratio (Fig. 6a and c), while for U_i/U_∞=9.9 (Fig. 6b) converge to a stagnation saddle point indicating the presence of the inlet vortex formation. The main difference between the first and the third cases is the length of the diverted flow in the Y direction (horizontal parallel to the axis of the engine inlet) which increases from less than 1D to about twice with the velocity ratio. For the intermediate velocity ratio U_i/U_∞=9.9, Fig.7 shows the details of the flow pattern near the wall for the Trent 900 and the GE nx-1B64 engines. The stagnation point was detected for both engines but the misalignment with the crossflow is more pronounced for the GE nx-1B64. For this velocity ratio the flow pattern is completely different from the observed for the lowest and highest velocity ratios with the flow converging to a single point at about 0.5D from the inlet plane. It should be pointed out that from the three-dimensional perspectives of the flow (Fig. 4c and d) it is not possible to identify clearly any vertical structure, that can be detected from this kind of near wall flow patterns.

Figure 8 shows the typical flow development at the vertical plane near the engine inlet which assumes a similar pattern for all the test cases. The air is sucked in all directions towards the center of the inlet in a slightly distorted radial direction.

Away from the engine inlet at a distance of Y=5.6m measured along the axis, the flow is considerably different for each engine and test case (Fig. 9). The core of a spiral can be identified for both the Trent 900 and the GE nx-1B64 engines, but its center is closer to the ground in the former case. It should be pointed out also that the cross-section of the flow is considerably larger for the case of the GE nx-1B64. For the Trent 700 engine the vortex flow exists near the ground at the same plane but with an opposite sign (clockwise). This is an interesting result because it reveals that away from the inlet and depending on the clearance distance the sign of a third vortex flow can change.

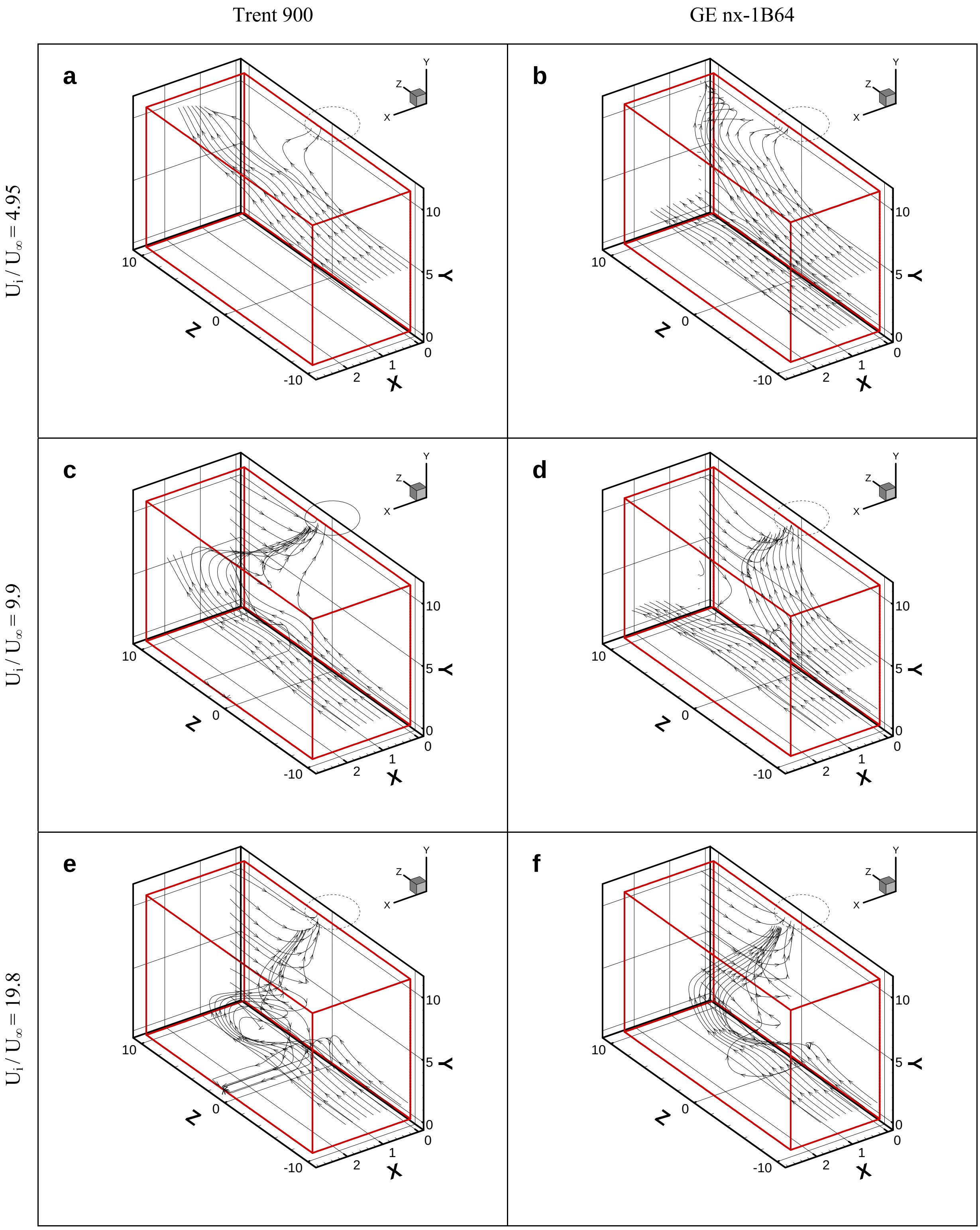

Figure 4. Three-dimensional particle tracks.

a	$U_i / U_\infty = 4.95$	Trent 900	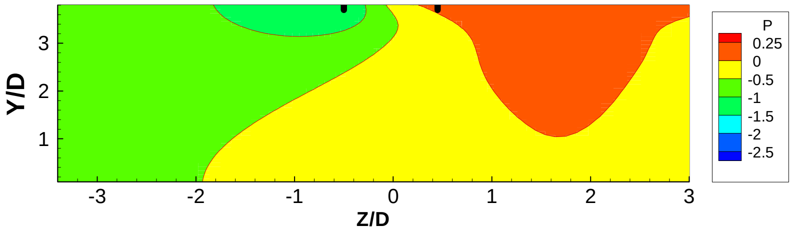
b		GE nx-1B64	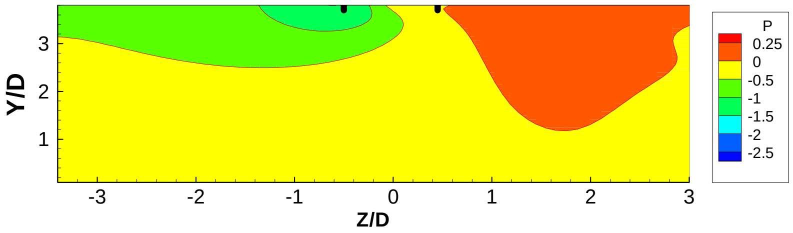
c	$U_i / U_\infty = 9.9$	Trent 900	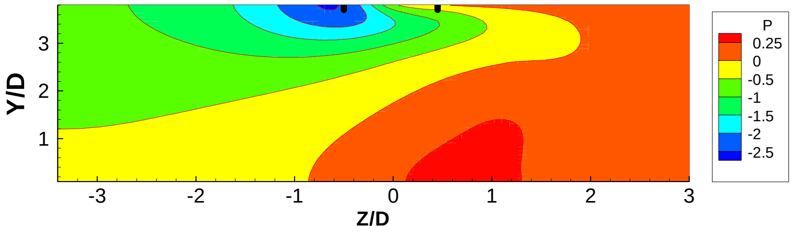
d		GE nx-1B64	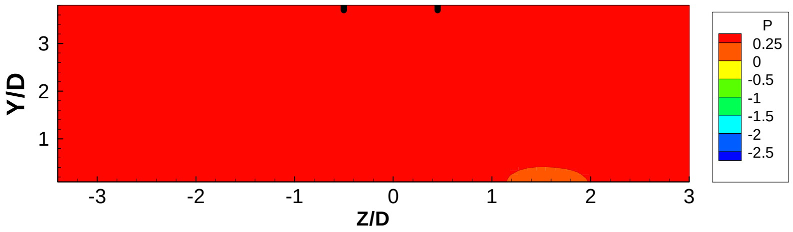
e	$U_i / U_\infty = 19.8$	Trent 900	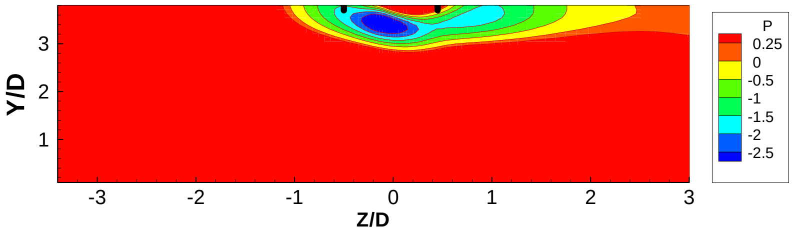
f		GE nx-1B64	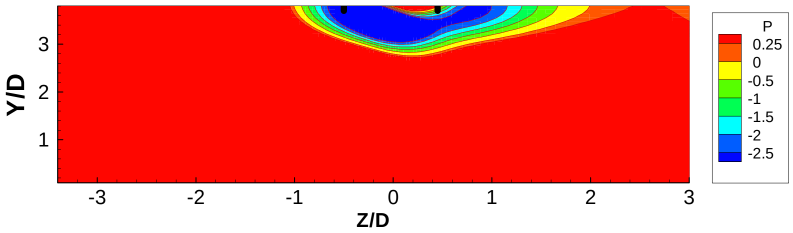

Figure 5. Ground pressure distribution $(p - p_\infty)/(1/2\rho U_\infty^2)$ **.**

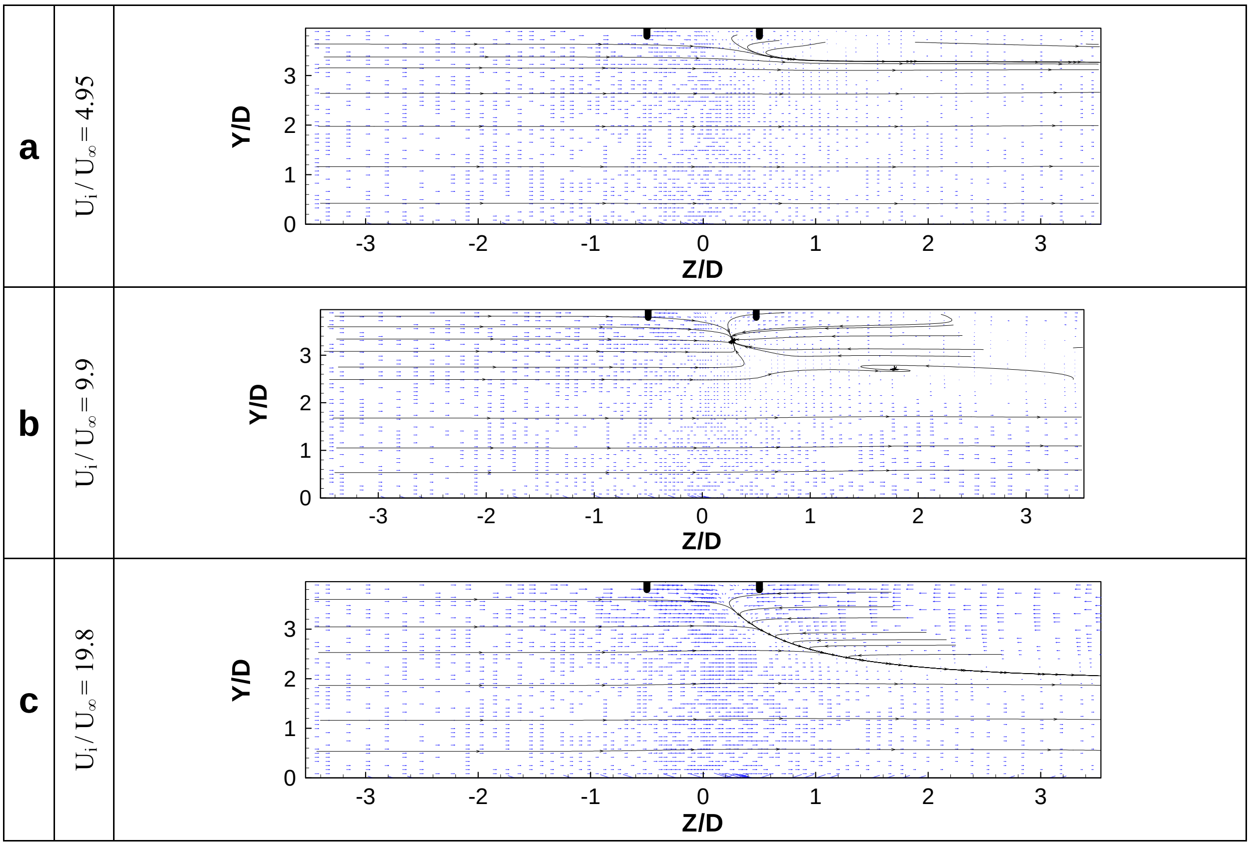

Figure 6. Near wall velocity vectors and particle streaks for GE nx-1B64 test case.

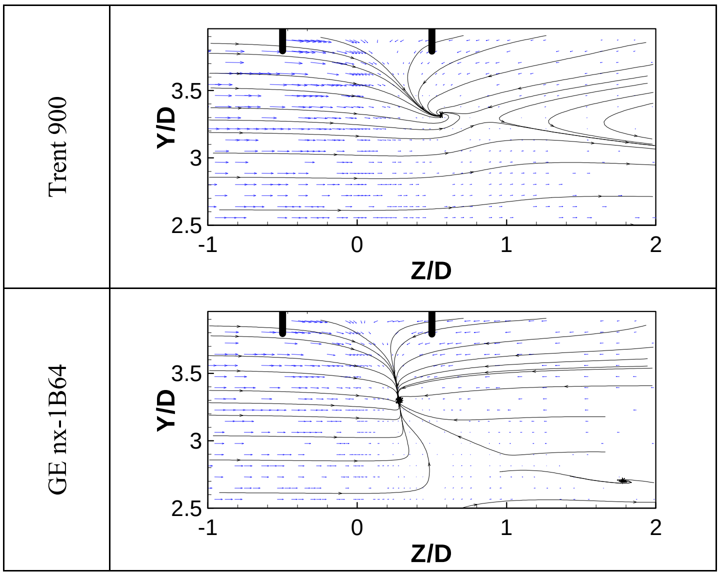

Figure 7. Detail of the near wall velocity vectors and particle streaks for U_i/U_∞=9.9.

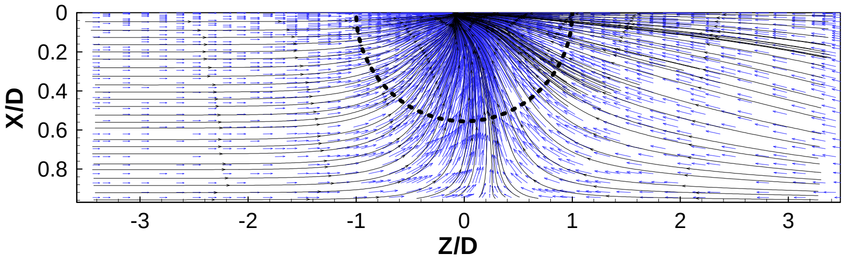

Figure 8. Typical Flow pattern at the vertical plane near the engine inlet for all the test cases (present results for Trent 900, Uin/U∞=19.8 and h/Di=0.97, vertical plane parallel to the engine inlet at 56mm of distance).

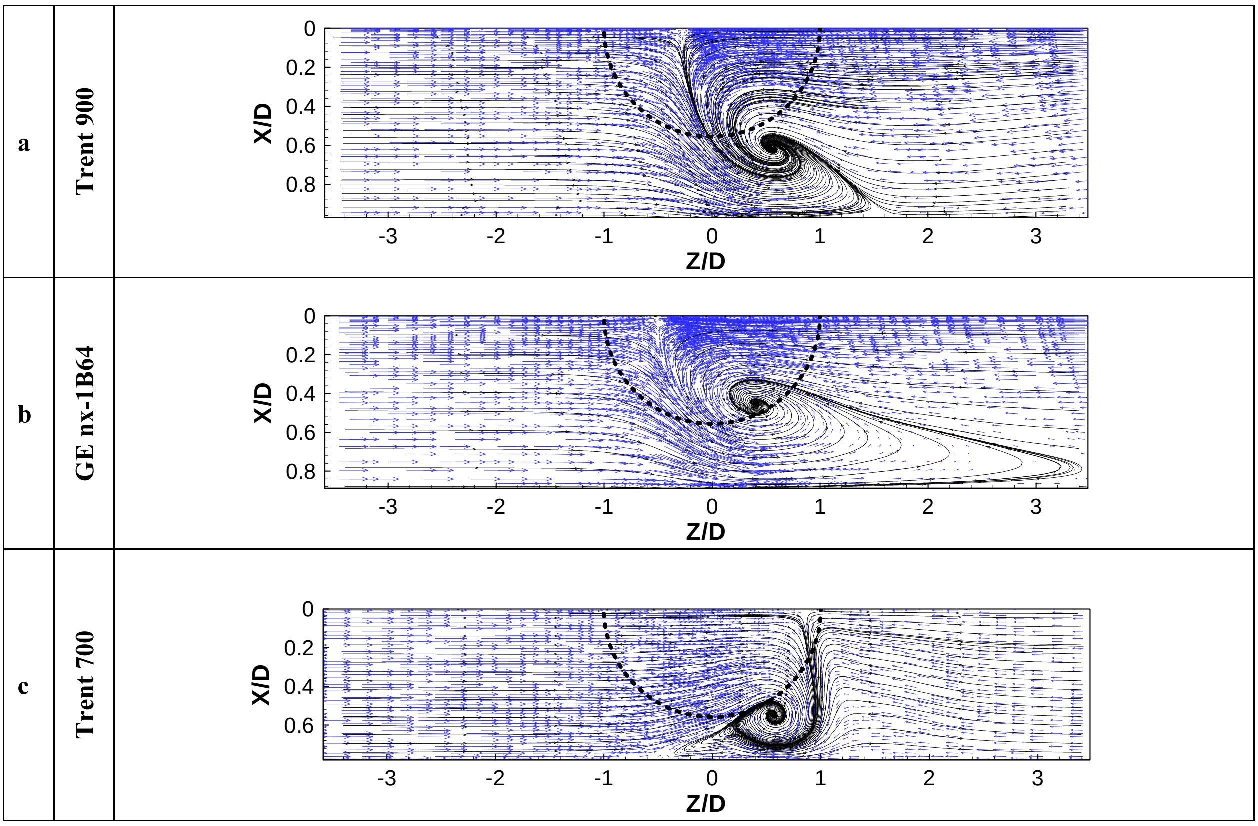

Figure 9. Velocity vectors and particle tracks in a vertical plane parallel to the engine inlet at 5.6m of distance ($U_i / U_\infty = 19.8$).

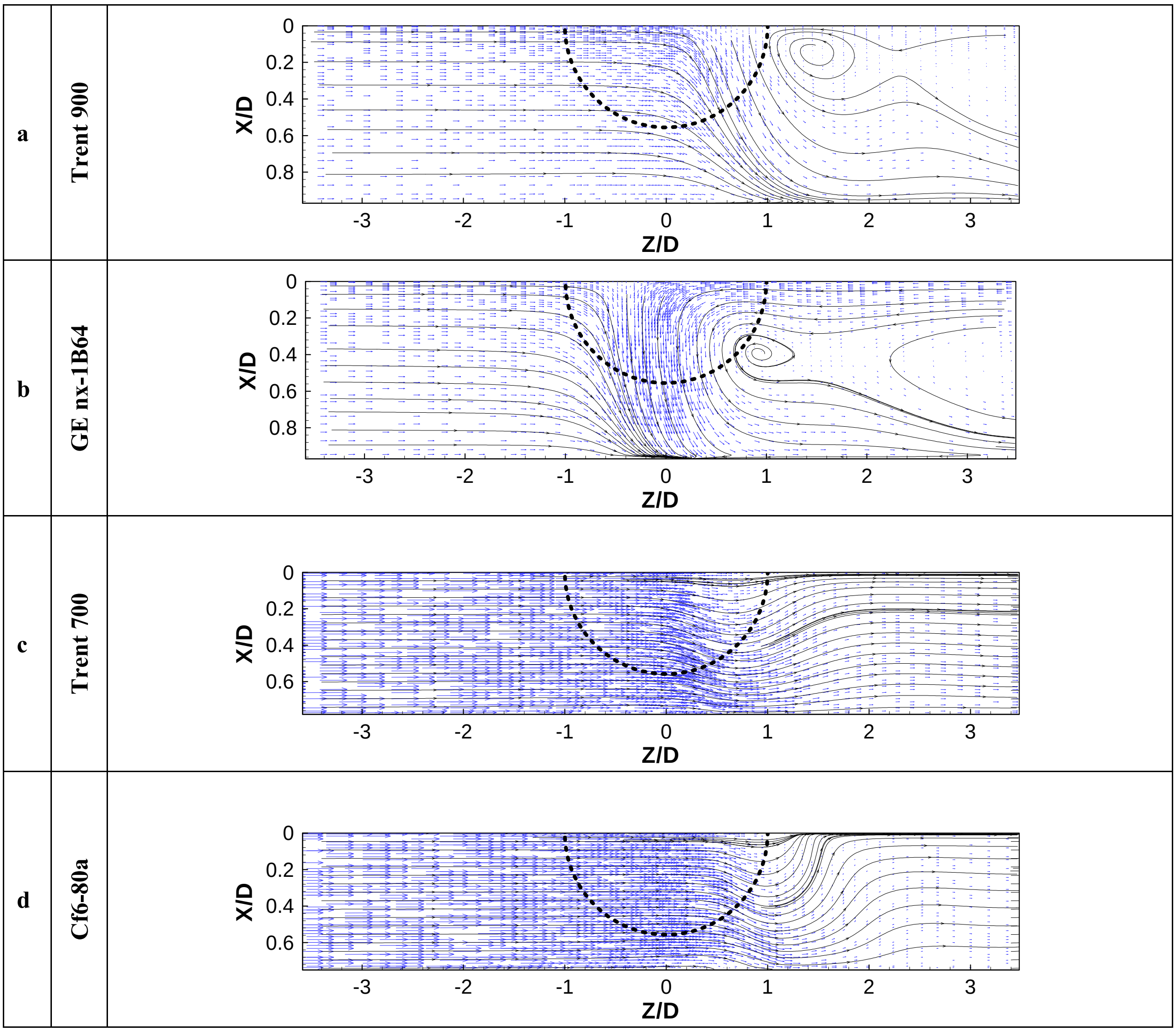

Figure 10. Velocity vectors and particle tracks in a vertical plane parallel to the engine inlet at 5.6m of distance ($U_i / U_\infty = 9.9$).

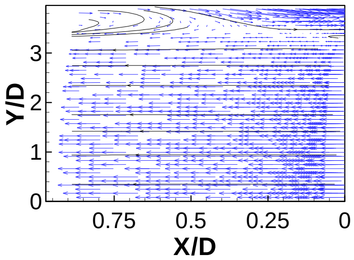

Figure 11. Velocity vectors and particle tracks in a vertical plane parallel to the engine axis at $Z=0.57D_i$ (GE nx-1B64 test case, $h/D_i=0.89$, $U_i / U_\infty = 9.9$).

With a smaller velocity ratio ($U_i / U_\infty = 9.9$) the vortex flow becomes weaker (Fig. 9) and for the Trent 700 and cf6-80a totally disappears. In this cases the crossflow is only slightly distorted but in general keeps its initial direction. For the Trent 900 and GE nx-1B64 the vortex flow can be already identified at 5.6m of distance from the inlet (Figs. 10a and b).

The existence of the trailing vortex was also investigated for all the test cases since it should be present all of the engine/test cases. Nevertheless, it was only clearly identified for the GE nx-1B64, $h/D_i=0.89$, $U_i/U_\infty=9.9$ combination (Fig. 11) and more study is still needed.

IV. Conclusions

The present study has shown that the inlet flow of a gas turbine engine is strongly dependent on the velocity ratio between the inlet and any crosswind as well as on the diameter at its position above the ground. Different engines have been studied and the formation of the ground vortex was identified for all engines. The affected flow region was found to be considerably larger for the case of the GE nx-1B64. The trailing vortex could be clearly noticed for this engine. Away from the inlet plane other types of complex vortical structures were identified that have different signs depending on the clearance distance of each particular engine and initial conditions.

References

[1] Hünecke, K. "Jet Engines: Fundamental of theory, design and operation", Airlife publishing, UK, 1997.

[2] Mattingly, J.D., Heiser, W.H., Daley, D.H. "Aircraft Engine Design", AIAA Education Series, New York, 1987.

[3] Mattingly, J.D. "Elements of Gas Turbine Propulsion", Singapore: McGraw-Hill, 1996.

[4] Johns, C. "The Aircraft Engine Inlet Vortex Problem", AIAA's Aircraft Technology, Integrations and Operations (ATIO) 2002 Technical, 1-3rd 2002, Los Angles, California, AIAA Paper 2002-5894.

[5] Swainston, M. "Vortex Formation Near Intakes to Turbomachinery and Duct Systems", Heat and Fluid Flow, Vol. 4, No. 2, 1974.

[6] Nakayama, A. & Jones, J. "Correlation for Formation of Inlet Formation", AIAA Journal, Vol. 37, No. 4: Technical Notes, 1998.

[7] Motycka, D. & Walter, W. "An Experimental Investigation of Ground Vortex Formation During Reverse Thrust Operation", AIAA Paper No. 75/1322, AIAA/SAE 11th Propulsion Conference, 1975

[8] Brix, S., Neuwerth, G. & Jacob, D. "The Inlet-Vortex System of Jet Engines Operating Near the Ground", AIAA Paper 2000-3998, 2000

[9] De Siervi, F., Viguier, H., Greitzer, E. & Tan, C. "Mechanisms of Inlet Vortex Formation", J. Fluid Mech., Vol. 124, pp. 173-207, 1982

[10] Nakayama, A. & Jones, J. "Correlation for Formation of Inlet Formation", AIAA Journal, Vol. 37, No. 4: Technical Notes, 1998.

[11] Barata, J. M. M., Maneta, A.M., Silva, A.R.R. " Numerical Study of Single Impinging Jets Through a Crossflow", AIAA Paper no. 2009-4801, 45th AIAA/ASME/SAE/ASEE Joint propulsion Conference & Exhibit, Denver, CO, 2-5 Aug., 2009.

[12] Leonard, B. P. "A Stable and Accurate Convective Modelling Procedure Based on Quadratic Upstream Interpolation", Computer Methods in Applied Mechanics and Engineering, Vol. 19, No.1, pp. 59-98, 1979

[12] Patankar, S. V. and Spalding, D. B. "A Calculation Procedure for Heat, Mass and Momentum Transfer in Three-Dimensional Parabolic Flows", *International Journal of Heat and Mass Transfer*, Vol. 15, No. 10, pp. 1787-1805, 1972.

II LAETA Young Researchers Meeting
FEUP, Porto, 10-11 April 2012

IDENTIFICATION OF GAS TURBINE GROUND VORTEX FORMATION REGIMES

Jorge M. M. Barata , Pedro Manquinho and André R. R. Silva

AeroG/UBI, Universidade da Beira Interior, Covilhã, 6201-1, Portugal
e-mail: pedro.manquinho@gmail.com

Key words: ground vortex, vortexes, engine-velocity, ratio-clearance distance, inlet engine

Abstract. *In the present paper the previous work of Barata et al.11 is extended to include eighteen engines that are being used in the present. The ground vortex flows produced by the different engines are compared and discussed for each operational condition. The results have shown that more than one mode can occur for a particular engine-velocity ratio-clearance distance combination with 1, 2 or 3 vortexes that may merge before entering the.*

1 INTRODUCTION

The design of an engine intake is very important because, it is one of the engine components that directly interface with the flow around the engine and the internal airflow. The inlet is designed to give the appropriate amount of airflow required from the free-stream conditions to the conditions required at the entrance of the compressor with minimal pressure loss by the engine[1]. When the pressure losses and the flow distortions are very low, the performance of the engine is optimal, and that is the reason why the airflow has to be as uniform as possible when entering into the compressor. This airflow condition is necessary in all flight configurations including when the aircraft is maneuvering on ground tasks. The intake performance depends on the mass-flow delivered to the compressor. The internal mass-flow stays constant from the captured stream tube to the compressor face and assuming that the flow is incompressible due to low speed velocities, it will be given by $A_i U_i = A_\infty U_\infty$. Since the mass-flow is constant and the area ratio is related to the stream tube contraction ratio, the area ratio can be expressed as $\frac{A_\infty}{A_i} = \left(\frac{L_q}{D_i}\right)^2$. The capture ratio A_∞ / A_i is controlled by the engine, the engine mass-flow, the inlet diameter and the free-stream velocity. The area defined by the boundary between the air that enters in the engine and the air that does not is called the intake captured area. The flow ratio and the stream-tube shape vary with the operation conditions of the aircraft engine. In near static configuration since the ambient air is at rest, the engine must accelerate the air using maximum thrust. The extreme local acceleration of the flow at the inlet lip can lead to airflow separation in this region[2,3]. In cross-wind configuration, the shape of the stream tube is modified near the lip. The cross-flow leads to an increase in the flow velocity near the lip depending on the strength of the cross-flow, high velocity origins in flow separation leading to a total pressure loss at the engine fan.

The formation of ground vortices depends on engine power, wind velocity and engine inlet height and size. Previous published work show that the phenomenon can only occur with the presence of a stagnation streamline between the ground and the intake which is dependent on the velocity ratio U_i/U_∞ and the non-dimensional height of the engine axis above the ground, h/D_i (Fig. 1). In static conditions, the inlet airflow demand increases, and the inlet capture surface increases in diameter and starts including the ground to bring the necessary airflow to the fan[4,5]. Typically the formation of ground vortices is characterized by low h/D_i and high U_i/U_∞ that corresponds to an engine operating close to the ground at a high inlet mass flow[6]. Hence, the mechanism of intake formation is strongly dependant of the height of the engine axis above the ground, the velocity ratio and the presence of an upstream velocity.

Four different types of conditions leading to the formation of inlet ground vortices have been identified. A vortex can be generated without ambient wind and with a low ratio h/D_i (typically less than one). Due to the ground proximity, high levels of suction beneath the engine inlet leads into a strong flow underneath the inlet upstream towards the intake lip[7]. In these conditions, it is possible to visualize at the engine intake and at the ground two upward spiraling vortices. Under no-wind condition, it appears that the two vortices are counter-rotating, and the vorticity is induced by the boundary layer. Is a head-wind flow, when the air is sucked into the engine inlet, the flow field underneath the intake starts to roll up into two upright counter-rotating vortices and a fast flow into the opposite direction of the wind appears between them[8,9]. For high velocity ratios (>20) the sense of rotation of the two vortices switches to the same as in the no-wind mechanism. With a 90° cross-wind two different kinds of vortices appear around the intake: an inlet vortex and a trailing vortex (Fig.2). When the engine intake is oriented at a 90° yaw angle and with the presence of cross-wind with far upstream vertical vorticity, there is the formation of a single vortex inside the intake. In this case the sense of rotation of the vortex is opposite to the ambient vorticity. Other mechanisms of formation also exist and can be considered as combinations of the previous ones that lead to a large number of possible combinations that are responsible for the need of more studies in order to understand all the physics involved.

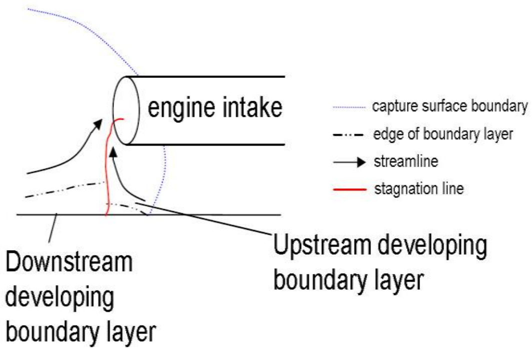

Figure 1. Ground vortex formation.

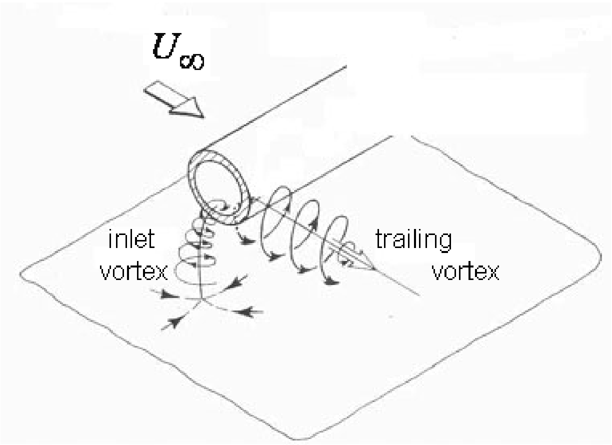

Figure 2. Sense of rotation of the inlet vortex and the trailing vortex (sketch adapted from Ref. 9).

CFD tools have been applied recently to the understanding of the ground vortex with relative success. Nakayama & Jones10 used panel methods to simulate the inlet and ground interaction, noting that the wind speed needed to blow the vortex away was lower than the measured experimentally. Barata et al.11 report Navier-Stokes calculations and predicted successfully the ground vortex phenomena using real operational conditions for the case of the engine Trent 9 and GE nx-1B64. The ground vortex formation in irrotational crosswind flow is analyzed in detail for this configuration, and the formation of the trailing vortex was associated to a very complex flow. In the present paper the previous work of Barata et al.11 is extended to include eighteen engines that are being used in the present (Table 1). The ground vortex flows produced by the different engines are compared and discussed for each operational condition. The results have shown that more than one mode can occur for a particular engine-velocity ratio-clearance distance combination with 1, 2 or 3 vortexes that may merge before entering the inlet engine (Fig. 3).

Table 1. Characteristics of engines tested.

Engine	**Diameter (m)**	**Clearance Distance**	**Mass Flow (lb/s)**	**Mass Flow (Kg/s)**	**Radius (m)**	**Inlet Velocity (m/s)**	**H (m)**
cf6-50	2.667	0.83	1450	657.7089	1.3335	43.5947	2.1635
cf6-6	2.667	0.84	1300	589.6701	1.3335	39.0849	2.1735
cf6-80a	2.667	0.654	1435	650.9051	1.3335	43.1437	1.9875
cf6-80c2	2.690	0.65	1750	793.7866	1.3450	51.7184	1.9950
cf6-8oe1	2.689	0.76	1925	873.1653	1.3445	56.9326	2.1045
cfm56-2	1.735	0.56	784	355.6164	0.8675	55.6966	1.4275
cfm56-3	1.524	0.46	638	289.3919	0.7620	58.7439	1.2220
cfm56-5a	1.735	0.58	816	370.1314	0.8675	57.97	1.4475
cfm56-5b	1.735	0.58	811	367.8634	0.8675	57.6148	1.4475
cfm56-5c	1.836	1.22	1027	465.8394	0.9180	65.1534	2.1380
cfm56-7	1.549	0.46	677	307.0820	0.7745	60.3389	1.2345
rb211-535e4	1.882	0.74	1177	533.8782	0.9410	71.0639	1.6810
trent 5	2.474	0.48	1897	860.4647	1.2370	66.2796	1.7170
trent 7	2.474	0.69	2030	920.7925	1.2370	70.9265	1.9270
trent 8	2.794	1.09	2378	1078.6427	1.3970	65.1435	2.4870
trent 9	2.946	1.03	2655	1204.2877	1.4730	65.4201	2.5030
trent 10	2.845	0.71	2400	1088.6217	1.4225	63.4101	2.1325
GE nx	2.819	0.74	2458	1114.93	1.4095	66.1460	2.1495

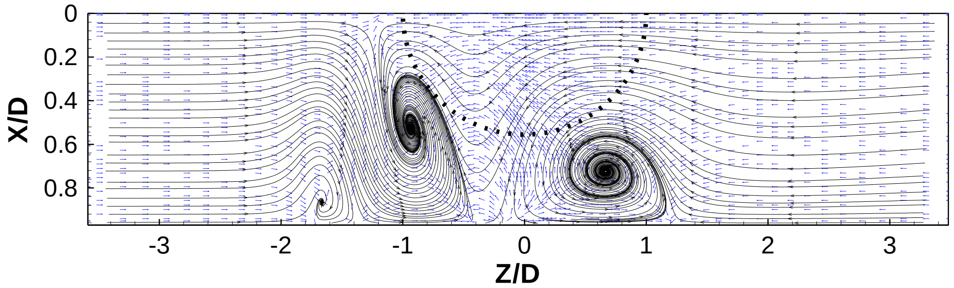

Figure 3. Two-dimensional velocity vectors in the vertical plane parallel to the engine inlet at Y=0.5Y_{TOT} (Engine cf6-80c2, h/D_i=0.97, $U_i / U_\infty = 9.9$).

2 MATHEMATICAL MODEL

The mathematical model used in the present study is described in detail in Ref. 11 and only the main features will be summarized here. The time averaged partial differential equations governing the steady, uniform-density isothermal three-dimensional flow

$$\rho \overline{U}_j \frac{\partial \overline{U}_i}{\partial X_j} = -\frac{\partial \overline{P}}{\partial X_i} + \frac{\partial}{\partial X_j}\left(\mu \frac{\partial \overline{U}_i}{\partial X_j} - \rho \overline{u'_i u'_j} \right) \qquad (1)$$

and the continuity equation,

$$\rho \overline{U}_j \frac{\partial \overline{U}_i}{\partial X_i} = 0 \qquad (2)$$

where solved together with the equations of transport of the turbulent kinetic energy and dissipation rate of the two-equation *“k-ε”* model[10]

$$\overline{U}_j \frac{\partial k}{\partial X_j} = \frac{\partial}{\partial X_j}\left(\frac{\upsilon_T}{\sigma_k} \frac{\partial k}{\partial X_j} \right) - \overline{u'_i u'_j} \frac{\partial \overline{U}_i}{\partial X_j} - \varepsilon \qquad (5)$$

$$\overline{U}_j \frac{\partial \varepsilon}{\partial X_j} = \frac{\partial}{\partial X_j}\left(\frac{\upsilon_T}{\sigma_\varepsilon} \frac{\partial \varepsilon}{\partial X_j} \right) - C_1 \frac{\varepsilon}{k} \overline{u'_i u'_j} \frac{\partial \overline{U}_i}{\partial X_j} - C_2 \frac{\varepsilon^2}{k} \qquad (6)$$

where C_1 and C_2 are additional dimensionless model constants, and σ_k and σ_ε are the turbulent Prandtl numbers for kinetic energy and turbulent dissipation.
The Reynolds stresses are expressed as

$$\overline{u'_i u'_j} = -\upsilon_T \left(\frac{\partial \overline{U}_i}{\partial X_j} + \frac{\partial \overline{U}_j}{\partial X_i} \right) + \frac{2}{3} k \delta_{ij} \qquad (3)$$

where υ_T is the turbulence kinematic viscosity, which is derived from the turbulence model and expressed by $C_\mu k^2/\varepsilon$.

The solution of the governing equations was obtained using a quadratic finite-difference method[12] that used discretized algebraic equations deduced from the exact differential equations that they represent.

The solution procedure is based on the SIMPLE algorithm widely used and reported in the literature (e.g. Ref. 13). It uses the staggered grid arrangement and a guess and correct procedure field such that the solution of the momentum equations satisfies continuity.

The computational domain has six boundaries where dependent values are specified: a free stream plane, a symmetry plane, and a solid wall. On the symmetry plane, the normal velocity vanishes, and the normal derivates of the other variables are zero. At the solid surface, the wall function method[14] is used to prescribe the boundary conditions for the velocity and turbulence quantities, assuming that the turbulence is in state of local equilibrium. The free stream plane is located at *Z*=0 and corresponds to the crossflow conditions. The engine intake boundary is represented by a right angled polygon and the mass flow rates and the momentum are matched to the experimental values. The intake represents a 1/1th scale model with a diameter that corresponds to each particular engine. The axis of the engine is located at a distance above the ground (h), which corresponds to the specific clearance distance. All the tests were performed for the case of irrotational crosswind, and the other conditions are shown in Table 1.

The domain of solution, their dimensions and the system of axes are represented in Fig.4

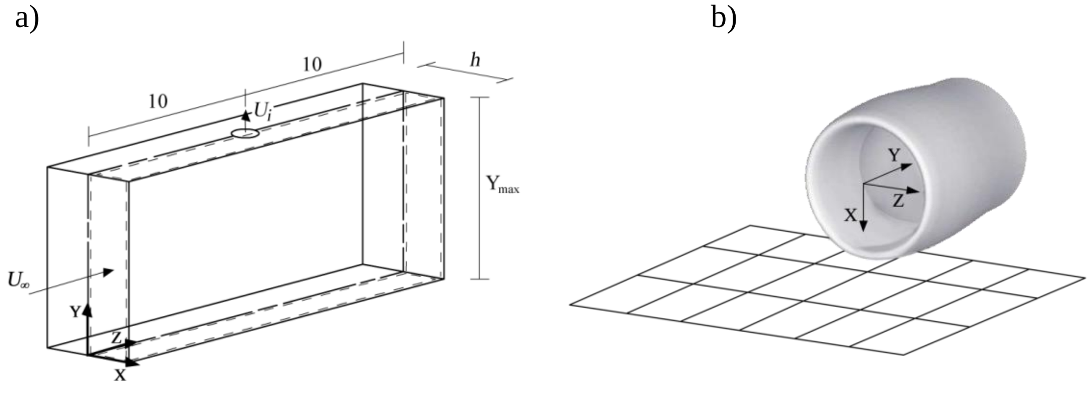

Figure 4: a) Domain of the solution. b) Representation of the intake with referential at the

3 RESULTS

The ground vortex formation in irrotational crosswind flow is analyzed in the present section. In this configuration the ground vortex or inlet vortex that forms near the ground and is sucked by engine is accompanied by an additional feature which is the formation of the trailing vortex (see Fig. 2). This vortex develops from the lip of the inlet engine in the direction of the crossflow with its axis parallel to the ground.

3.1 Ui/U∞ Max and h/Di=0.97

Engine	XZ	YZ	3D	Nº of vortex	Vi/V∞	H/Di
cf6-50	X			1	43,6863	0.97
cf6-6	X			3	39,1670	0.97
cf6-80a	X	X		2	43,2344	0.97
cf6-80c2				0	51,8271	0.97
cf6-8oe1				0	57,0522	0.97
cfm56-2				0	55,8137	0.97
cfm56-3				0	58,8673	0.97
cfm56-5a	X			1	58,0918	0.97
cfm56-5b	X			1	57,7358	0.97
cfm56-5c				0	65,2903	0.97
cfm56-7	X			1	60,4657	0.97
rb211-535e4				0	71,2132	0.97
trent 500	X			1	66,4189	0.97
trent 700	X			1	71,0755	0.97
trent 800				0	65,2804	0.97
trent 1000				0	63,5434	0.97
GE nx				0	66,2850	0.97

Table 2. Summary of results for the selected conditions.

How can we see after a brief review of table 2 and for the conditions mentioned above (Vi/V ∞ Max engine and H/Di = 0.97) there are four sets of results obtained. The largest group is the single vortex in the plane XZ which shows some examples

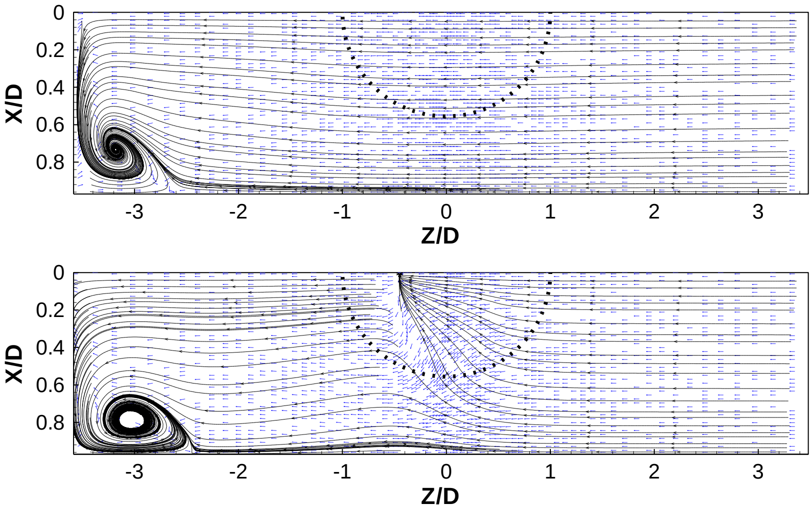

Figure 4. Engine Cf6-50 for U_i/U_∞ Max and H/Di=0.97 Y=0.5YTOT and Y=0.95YTOT

It is perfectly visible a ground vortex at position X/D = 0.8 Z/D =-3.
In the case of Figure 5 we can observe the same situation but on the opposite side of the stream

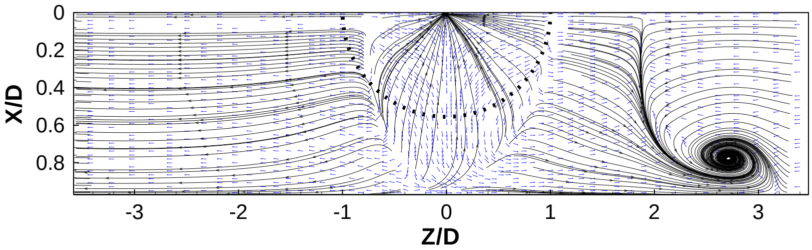

Figure 5. Engine Cfm56-7 for U_i/U_∞ Max and H/Di=0.97, Y=0.95YTOT

Still in the group of single vortex engines, there is the situation of Trent 700 engine where the Vortex arises in a central position (Figure 6) and Trent 500 where this vortex in a higher position (Figure 7). It should be noted that the vortex of Figure 7 has a different sign (clockwise) which also applies in the Cfm56-5a.

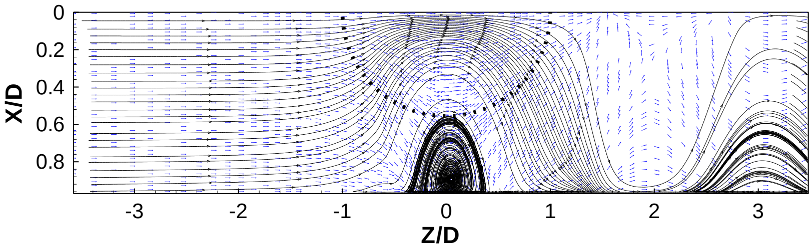

Figure 6. Engine Trent 700 for U_i/U_∞ Max and H/Di=0.97, Y=0.05YTOT

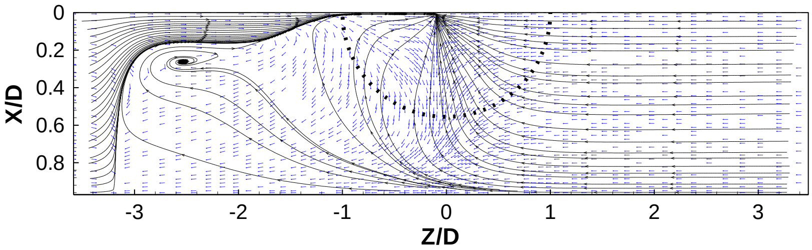

Figure 7. Engine Trent 500 for U_i/U_∞ Max and H/Di=0.97, Y=0.95YTOT

In table 2 we can see two more vorticity situations. In the case of the Cf6-80a engine where there are two vorticity structures, one in the XZ plane and the other in YZ plane with can be seen in Figure 8 and Figure 9.

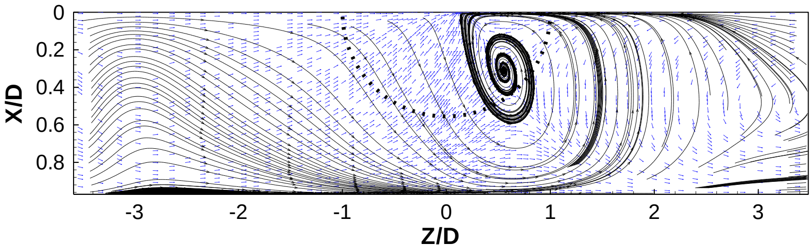

Figure 8. Engine Cf6-80a for U_i/U_∞ Max and H/Di=0.97, Y=0.05YTOT

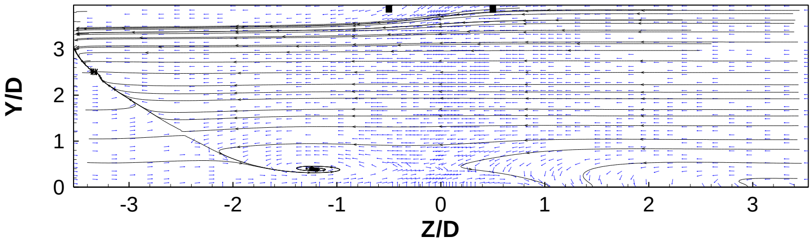

Figure 9. Engine Cf6-80a for U_i/U_∞ Max and H/Di=0.97, X=0.5XTOT

And in the case of Cf6-6 engine there is the formation of three weak ground vortex at the same time, calling attention to the fact that two of them have a clockwise direction and not the third, as shown in Figure 10.

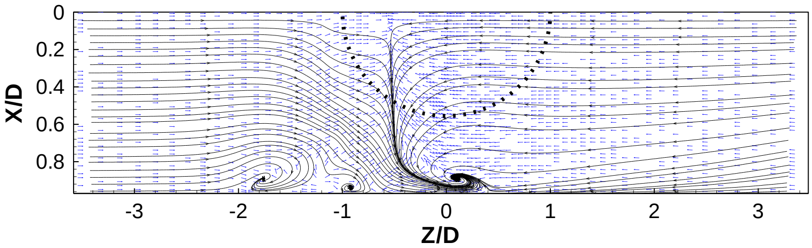

Figure 10. Engine Cf6-6 for U_i/U_∞ Max and H/Di=0.97, Y=0.05YTOT

3.2 Ui/U∞=9.9 and h/Di=0.97

Engine	XZ	YZ	3D	Nº of vortex	Vi/V∞	H/Di
cf6-50	X(2)	X		3	9.9	0.97
cf6-6	X(2)	X		3	9.9	0.97
cf6-80a	X(2)	X		3	9.9	0.97
cf6-80c2	X(2)	X		3	9.9	0.97
cf6-8oe1				0	9.9	0.97
cfm56-2				0	9.9	0.97
cfm56-3				0	9.9	0.97
cfm56-5a				0	9.9	0.97
cfm56-5b				0	9.9	0.97
cfm56-5c				0	9.9	0.97
cfm56-7				0	9.9	0.97
rb211-535e4				0	9.9	0.97
trent 500		X	X	2	9.9	0.97
trent 700		X	X	2	9.9	0.97
trent 800	X(2)	X		3	9.9	0.97
trent 1000	X	X		2	9.9	0.97
GE nx	X(2)	X		3	9.9	0.97

Table 3. Summary of results for the selected conditions.

For the case of table 3 we can again separate the results into three groups.

There is a group where in the XZ plane there are two vortical structures and one in the YZ plane. In the situation of the YZ plane four situations that occur should be described. The first is one in which the vortex changes direction of rotation as shown in Figure 11 and 12.

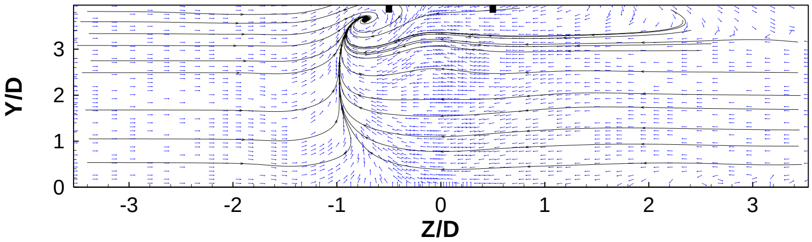

Figure 11. Engine Cf6-6 for U_i/U_∞=9.9 and H/Di=0.97, X=0.25XTOT

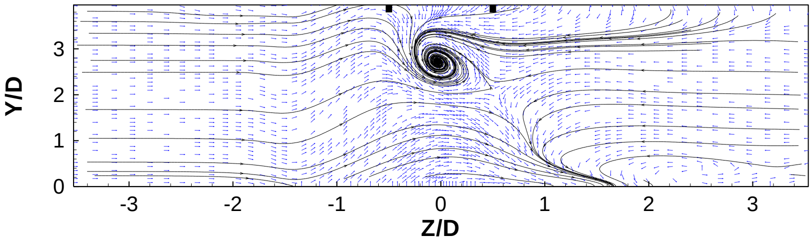

Figure 12. Engine Cf6-6 for U_i/U_∞=9.9 and H/Di=0.97, X=0.5XTOT

The second is that where the vortex with the clockwise rotation disappears from the first to the second graph causing increased disruption of the flow (Figure 13 and 14).

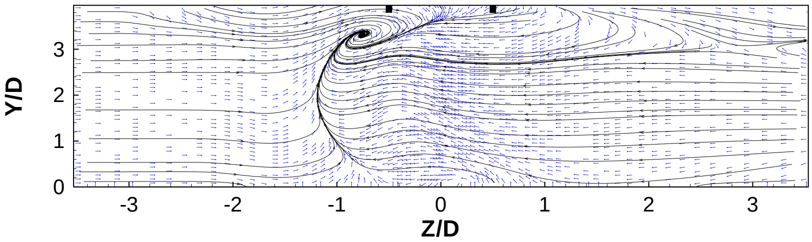

Figure 13. Engine Cf6-80c2 para U_i/U_∞=9.9 e H/Di=0.97, X=0.25XTOT

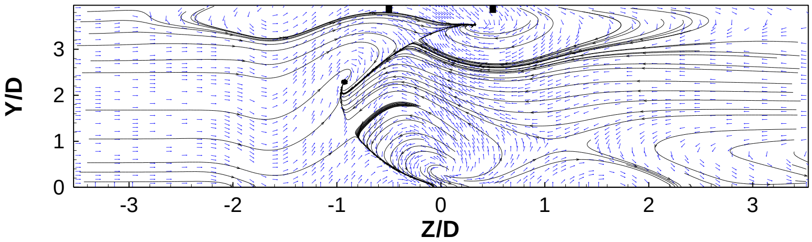

Figure 14. Engine Cf6-80c2 para U_i/U_∞ =9.9 e H/Di=0.97, X=0.5XTOT

In the third situation where the case of the Trent 800 engine where the vortex occurs in the central area and far away from the engine (Figure 15).

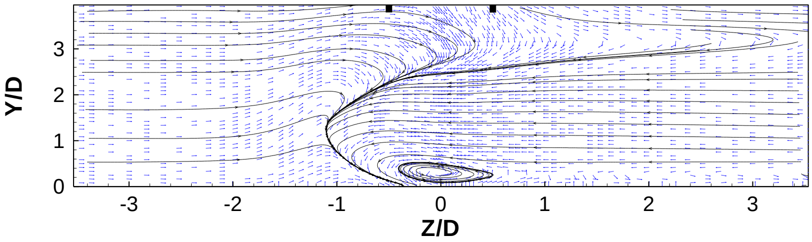

Figure 15. Engine Trent 800 for U_i/U_∞ =9.9 and H/Di=97, X=0.5XTOT

In the latter situation we have the Ge-nx engine where you can see the vortex with a clockwise direction along the plane of the face of the engine and with the increase of X there is a Y/D decrease.

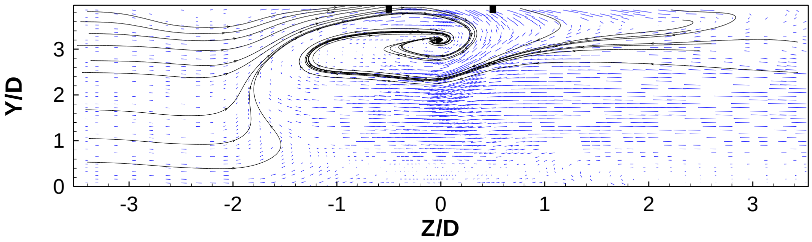

Figure 16. Engine GE-nx for U_i/U_∞ =9.9 and H/Di=0.97, X=0.5XTOT

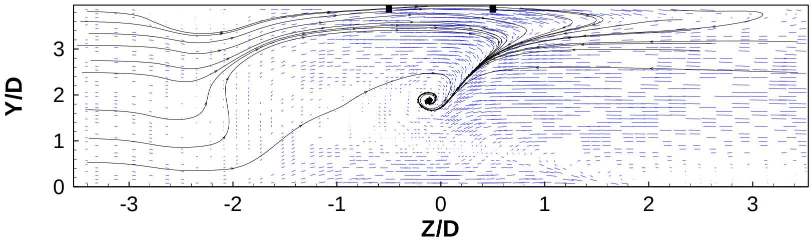

Figure 17. Engine Ge-nx for U_i/U_∞ =9.9 and H/Di=0.97, X=0.75XTOT

In the YZ plane there are four situations to be described. In Figure 18 the position of the vortex is near the edge of the inlet nozzle. In Figure 19 we can see the difference in the position of the two vortexes. In Figure 20 we can see the difference in intensity of vortex and in Figure 21 can verify the big difference compared to previous situations because there is a ground vortex of great intensity and another of weak intensity with an opposite rotation.

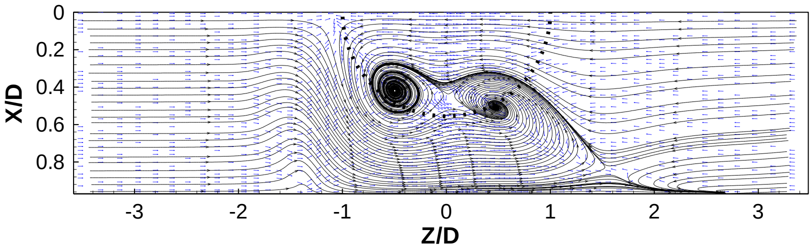

Figure 18. Engine Cf6-6 for U_i/U_∞ =9.9 and H/Di=0.97, Y=0.5YTOT

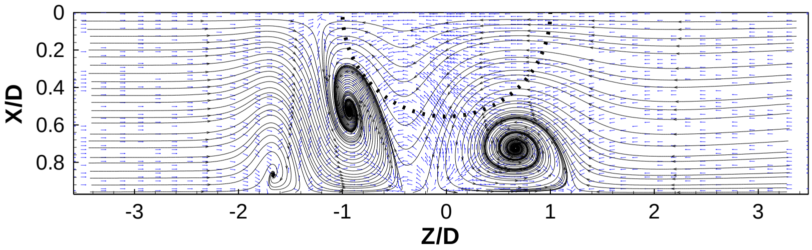

Figure 19. Engine cf6-80c2 for U_i/U_∞ =9.9 and H/Di=0.97, Y=0.5YTOT

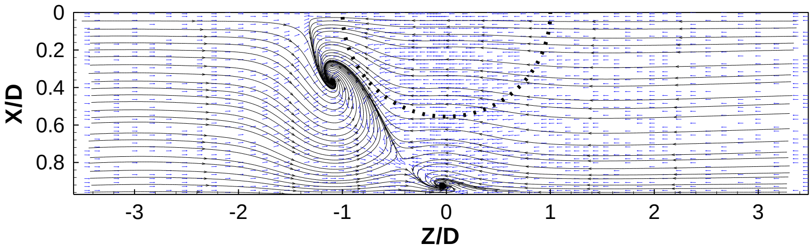

Figure 20. Engine Ge-nx for U_i/U_∞ =9.9 and H/Di=0.97, Y=0.5YTOT

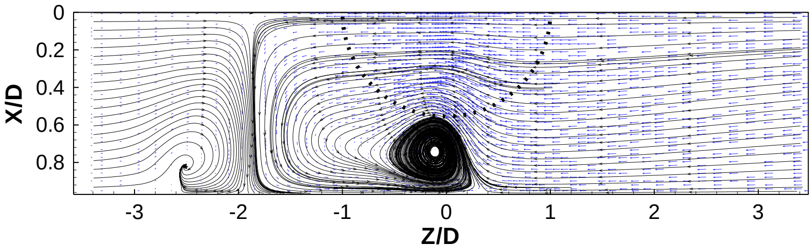

Figure 21. Engine Ge-nx for U_i/U_∞ =9.9 and H/Di=0.97, Y=0.5YTOT

In the case of the Trent 1000 engine there is a vortex in the YZ plane and another in the XZ plane. In relation to the XZ plane can see a vortex of high intensity near the inlet nozzle of the engine (Figure 22) and the YZ plane the vortex moves from one central location in the flow for a more lateral one and changing the direction of rotation (Figure 23 and 24).

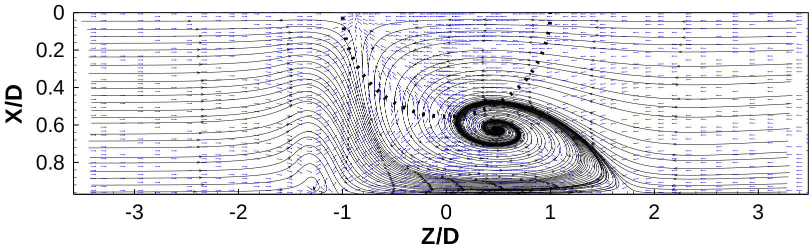

Figure 22. Engine Trent 1000 for U_i/U_∞ =9.9 and H/Di=0.97, Y=0.5YTOT

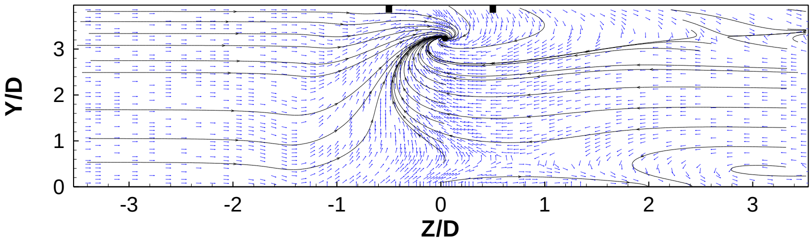

Figure 23. Engine Trent 1000 for U_i/U_∞ =9.9 and H/Di=0.97, X=0.5XTOT

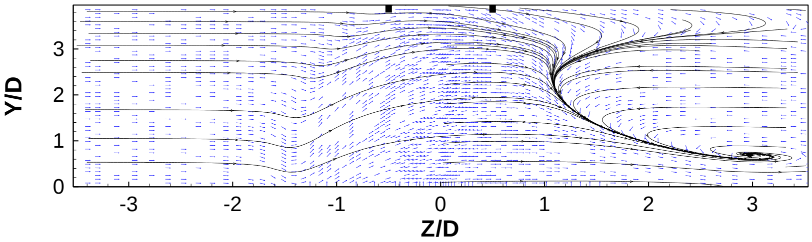

Figure 24. Engine Trent 1000 for U_i/U_∞ =9.9 and H/Di=0.97, X=0.75XTOT

In the last group on Table 3 appears a result never observed until now, we can see in Figure 25 the return flow coming from the area downstream in the vicinity of Y/D = 0 and coming out near Y/D = 10.

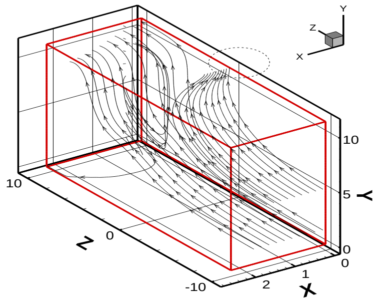

Figure 25. Engine Trent 500 for U_i/U_∞ =9.9 and H/Di=0.97

In the YZ plane we can see a small vortex in the downstream of the nozzle (Figure 26).

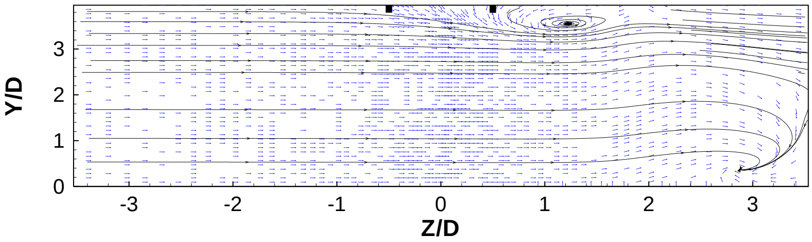

Figure 26. Engine Trent 500 for U_i/U_∞ =9.9 and H/Di=0.97, X=0.5XTOT

3.3 Ui/U∞= 4.95 and h/Di=0.97

Engine	XZ	YZ	3D	Nº of vortex	Vi/V∞	H/Di
cf6-50				0	4.95	0.97
cf6-6				0	4.95	0.97
cf6-80a				0	4.95	0.97
cf6-80c2				0	4.95	0.97
cf6-8oe1				0	4.95	0.97
cfm56-2				0	4.95	0.97
cfm56-3				0	4.95	0.97
cfm56-5a				0	4.95	0.97
cfm56-5b				0	4.95	0.97
cfm56-5c				0	4.95	0.97
cfm56-7				0	4.95	0.97
rb211-535e4				0	4.95	0.97
trent 500				0	4.95	0.97
trent 700				0	4.95	0.97
trent 800				0	4.95	0.97
trent 1000				0	4.95	0.97
GE nx				0	4.95	0.97

Table 4. Summary of results for the selected conditions.

In table 4 we verified no vortex results.

3.4 Ui/U∞=9.9 and h/Di=1.2

Engine	XZ	YZ	3D	Nº of vortex	Vi/V∞	H/Di
cf6-50				0	9.9	1.2
cf6-6				0	9.9	1.2
cf6-80ª				0	9.9	1.2
cf6-80c2	X(2)	X		3	9.9	1.2
cf6-8oe1	X	X	X	3	9.9	1.2
cfm56-2			X	1	9.9	1.2
cfm56-3				0	9.9	1.2
cfm56-5ª			X	1	9.9	1.2
cfm56-5b			X	1	9.9	1.2
cfm56-5c			X	1	9.9	1.2
cfm56-7				0	9.9	1.2
rb211-535e4			X	1	9.9	1.2
trent 500		X	X	2	9.9	1.2
trent 700				0	9.9	1.2
trent 800		X		1	9.9	1.2
trent 1000		X		1	9.9	1.2
GE nx		X		1	9.9	1.2

Table 5. Summary of results for the selected conditions.

Regarding the results of Table 5 we can check the increasing of vortical structures mentioned before and the decrease of ground vortex. In Table 5 we can see five relevant result sets, two vortex in the XZ plane and one in the YZ plane. A vortex in the XZ plane one in the YZ plane and one in 3D. A 3D one. One 3D and one in the YZ plane and finally one in the YZ plane.

For the first situation we have the CF6-80C2 engine with two vortex in XZ and one in YZ. In the YZ plane emerges a structure similar to that described in Figures 13 and 14, and in relation to the XZ plane again there are two structures that look similar to those in Figure 19.

In the second situation three structures are visible in XZ and YZ and another one in 3D. In XZ a vortex arises in the area downstream of the stream as it is clearly visible in Figure 27.

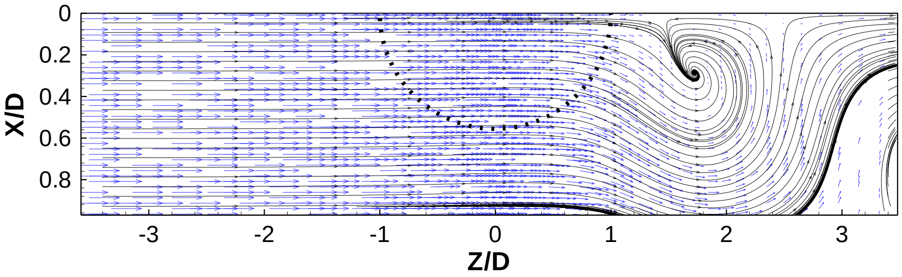

Figure 27. Engine Cf6-80c2 for U_i/U_∞ =9.9 and H/Di=1.2, Y=0.5YTOT

In the YZ plane appears a weak vortex and an area where the flow enters a plane coming from behind the plane of the face of the engine and follows in main the flow direction (Figure 28).

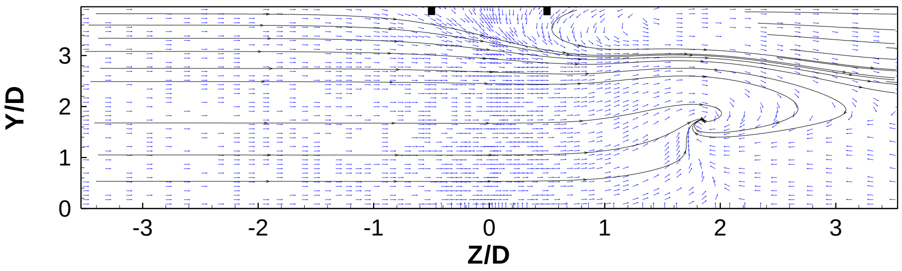

Figure 28. Engine Cf6-80c2 for U_i/U_∞ =9.9 and H/Di=1.2, X=0.5XTOT

The 3D structure is identical to one already mentioned above in relation to Figure 25.

In the third set only arise visible structures in 3D perspective, which may be of three types. One already referenced above (Figure 15). A flow in the same area but weaker (Fig. 29) and a third is already well defined vortex and strong influence on the flow (Figure 30).

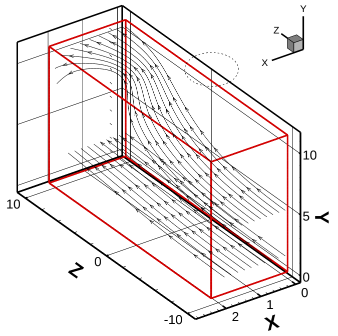

Figure 29. Engine Cf56-2
for U_i/U_∞ =9.9 and H/Di=1.2

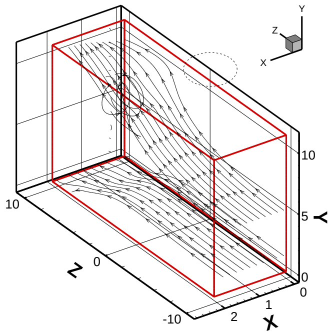

Figure 30. Engine Cf56-5c
for U_i/U_∞ =9.9 and H/Di=1.2

The fourth set of results is the Trent 500 where the structures are of the same kind found in Figure 25 and Figure 26.

Finally the fifth set of results which has only one YZ vortex, which is similar to others previously mentioned in terms of position but of greater intensity (Figure 31).

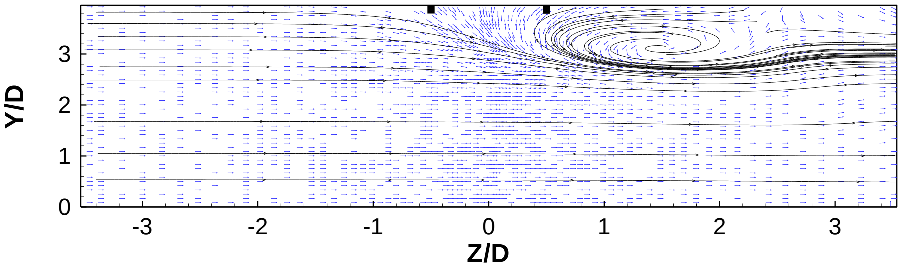

Figure 31. Engine Trent 800 for U_i/U_∞ =9.9 and H/Di=1.2, X=0.5XTOT

3.5 VORTICITY DISTRIBUTION

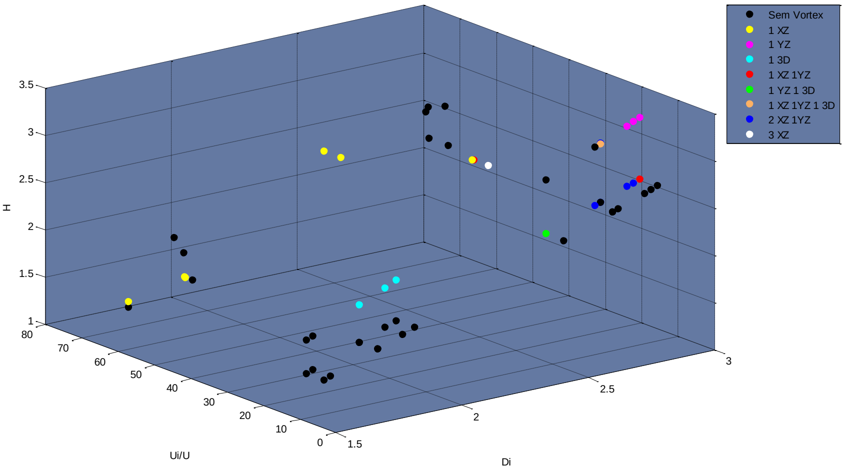

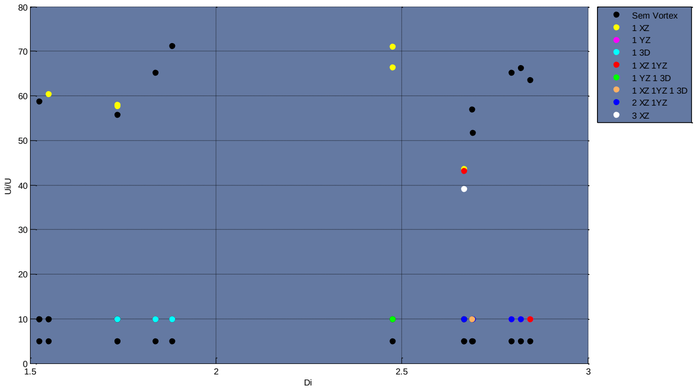

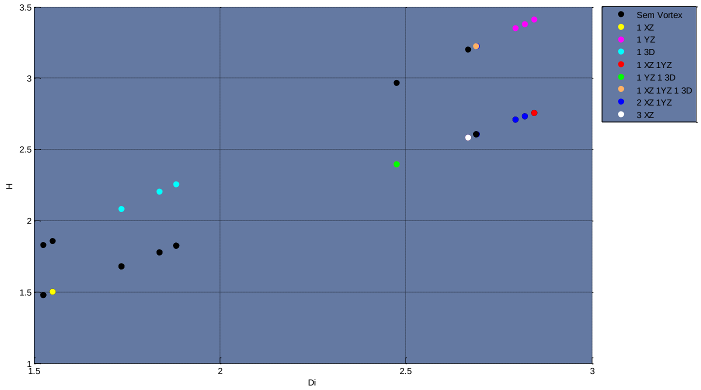

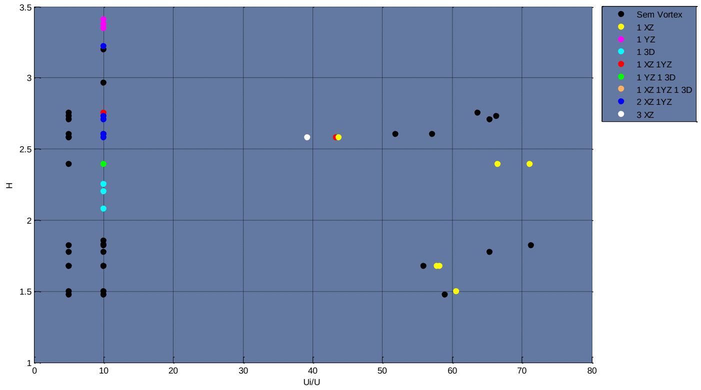

4 CONCLUSIONS

The present study has shown that the inlet flow of a gas turbine engine is strongly dependent on the velocity ratio between the inlet and any crosswind as well as on the diameter at its position above the ground.

Different engines have been studied and the formation of vortex was identified for all engines. The affected flow region was found to be considerably different in size. The trailing vortex could be clearly noticed for some engines.

Away from the inlet plane other types of complex vortical structures were identified that have different signs depending on the clearance distance of each particular engine and initial conditions.

By analyzing the different tables we can see the influence of inlet velocity and H in vortical structures.

We can conclude that for high inlet velocities vortical structures are almost exclusive to the XZ plane and with its decrease the formation of vortex passes through two stages one intermediate of an increase in vorticity at all levels and the second for low inlet velocities of almost absence of vortex.

With increased ground clearance to the shaft of the engines we see a change in the type of vortex that arise, with a decrease of it in the XZ plane, roughly the same number of structures in the YZ plane and big structures that are only possible to visualize in 3D perspective.

ACKNOWLEDGEMENTS

The present work has been performed in the scope of the activities of the Aeronautics and Astronautics Research Center – AeroG of the University of Beira Interior, Covilhã, Portugal.

REFERENCES

[1] Hünecke, K. “Jet Engines: Fundamental of theory, design and operation”, Airlife publishing, UK, 1997.

[2] Mattingly, J.D., Heiser, W.H., Daley, D.H. “Aircraft Engine Design”, AIAA Education Series, New York, 1987.

[3] Mattingly, J.D. “Elements of Gas Turbine Propulsion”, Singapore: McGraw-Hill, 1996.

[4] Johns, C. “The Aircraft Engine Inlet Vortex Problem”, AIAA’s Aircraft Technology, Integrations and Operations (ATIO) 22 Technical, 1-3rd 22, Los Angles, California, AIAA Paper 22-5894.

[5] Swainston, M. “Vortex Formation Near Intakes to Turbomachinery and Duct Systems”, Heat and Fluid Flow, Vol. 4, No. 2, 1974.

[6] Nakayama, A. & Jones, J. “Correlation for Formation of Inlet Formation”, AIAA Journal, Vol. 37, No. 4: Technical Notes, 1998.

[7] Motycka, D. & Walter, W. “An Experimental Investigation of Ground Vortex Formation During Reverse Thrust Operation”, AIAA Paper No. 75/1322, AIAA/SAE 11th Propulsion Conference, 1975

[8] Brix, S., Neuwerth, G. & Jacob, D. “The Inlet-Vortex System of Jet Engines Operating Near the Ground”, AIAA Paper 20-3998, 20

[9] De Siervi, F., Viguier, H., Greitzer, E. & Tan, C. “Mechanisms of Inlet Vortex Formation”, J. Fluid Mech., Vol. 124, pp. 173-207, 1982

[10] Nakayama, A. & Jones, J. “Correlation for Formation of Inlet Formation”, AIAA Journal, Vol. 37, No. 4: Technical Notes, 1998.

[11] Barata, J. M. M., Manquinho, P. e Silva, A.R.R., “A Comparison of Different Gas Turbine Engines Ground Vortex Flows”. Artigo AIAA 2010-7116, 46th AIAA/ASME/ SAE/ASEE Joint Propulsion Conference and Exhibit, Nashville, Tennessee, 25-28 Julho, 2010.

Praise Worthy Prize

International Review of Aerospace Engineering (I.RE.AS.E), Vol. 5, N. 4
ISSN 1973-7459
August 2012

Identification of Gas Turbine Ground Vortex Formation Regimes

Jorge M. M. Barata, Pedro Manquinho, André R. R. Silva

Abstract – *In the present paper the previous work of Barata et al. is extended to include eighteen engines that are being used in the present. The ground vortex flows produced by the different engines are compared and discussed for each operational condition. The results have shown that more than one mode can occur for a particular engine-velocity ratio-clearance distance combination with 1, 2 or 3 vortexes that may merge before entering the inlet engine.* ***Copyright © 2012 Praise Worthy Prize S.r.l. - All rights reserved.***

***Keywords**: Ground Vortex, Vortexes, Engine-Velocity, Ratio-Clearance Distance, Inlet Engine*

Nomenclature

A_i	Intake Area
A_∞	Frequency of Oscillation of the Ground Vortex
D_i	Inner Diameter of the Intake
h	Height of the Engine Axis Above the Ground
k	Turbulent Kinetic Energy
L_q	Intake Stream Tube Length
$\dot{m}$	Mass Flow
U_i	Intake Throat Velocity
U_∞	Free Stream Velocity
V_∞	Tangential Velocity
Γ	Vortex Circulation
ζ	Vorticity
ρ	Density
μ	Dynamic Viscosity
ν	Kinematic Viscosity
ν_T	Turbulent Kinematic Viscosity
ϕ	Any Dependent Variable

I. Introduction

The design of an engine intake is very important because, it is one of the engine components that directly interface with the flow around the engine and the internal airflow. The inlet is designed to give the appropriate amount of airflow required from the free-stream conditions to the conditions required at the entrance of the compressor with minimal pressure loss by the engine [1]. When the pressure losses and the flow distortions are very low, the performance of the engine is optimal, and that is the reason why the airflow has to be as uniform as possible when entering into the compressor. This airflow condition is necessary in all flight configurations including when the aircraft is maneuvering on ground tasks. The intake performance depends on the mass-flow delivered to the compressor.

The internal mass-flow stays constant from the captured stream tube to the compressor face and assuming that the flow is incompressible due to low speed velocities, it will be given by $A_i U_i = A_\infty U_\infty$. Since the mass-flow is constant and the area ratio is related to the stream tube contraction ratio, the area ratio can be expressed as $\frac{A_\infty}{A_i} = \left(\frac{L_q}{D_i}\right)^2$. The capture ratio A_∞ / A_i is controlled by the engine, the engine mass-flow, the inlet diameter and the free-stream velocity. The area defined by the boundary between the air that enters in the engine and the air that does not is called the intake captured area. The flow ratio and the stream-tube shape vary with the operation conditions of the aircraft engine. In near static configuration since the ambient air is at rest, the engine must accelerate the air using maximum thrust. The extreme local acceleration of the flow at the inlet lip can lead to airflow separation in this region [2]-[4]. In cross-wind configuration, the shape of the stream tube is modified near the lip.

The cross-flow leads to an increase in the flow velocity near the lip depending on the strength of the cross-flow, high velocity origins in flow separation leading to a total pressure loss at the engine fan.

The formation of ground vortices depends on engine power, wind velocity and engine inlet height and size. Previous published work show that the phenomenon can only occur with the presence of a stagnation streamline between the ground and the intake which is dependent on the velocity ratio U_i / U_∞ and the non-dimensional height of the engine axis above the ground, h/D_i (Fig. 1). In static conditions, the inlet airflow demand increases, and the inlet capture surface increases in diameter and starts including the ground to bring the necessary airflow to the fan [5],[6]. Typically the formation of ground vortices [7] is characterized by low h/D_i and high U_i / U_∞ that corresponds to an engine operating close to the ground at a high inlet mass flow [8]. Hence, the

Manuscript received and revised July 2012, accepted August 2012

mechanism of intake formation is strongly dependant of the height of the engine axis above the ground, the velocity ratio and the presence of an upstream velocity.

Four different types of conditions leading to the formation of inlet ground vortices have been identified. A vortex can be generated without ambient wind and with a low ratio h/D_i (typically less than one). Due to the ground proximity, high levels of suction beneath the engine inlet leads into a strong flow underneath the inlet upstream towards the intake lip [9]. In these conditions, it is possible to visualize at the engine intake and at the ground two upward spiraling vortices. Under no-wind condition, it appears that the two vortices are counter-rotating, and the vorticity is induced by the boundary layer. Is a head-wind flow, when the air is sucked into the engine inlet, the flow field underneath the intake starts to roll up into two upright counter-rotating vortices and a fast flow into the opposite direction of the wind appears between them [10],[11]. For high velocity ratios (>20) the sense of rotation of the two vortices switches to the same as in the no-wind mechanism. With a 90° cross-wind two different kinds of vortices appear around the intake: an inlet vortex and a trailing vortex (Fig. 2). When the engine intake is oriented at a 90° yaw angle and with the presence of cross-wind with far upstream vertical vorticity, there is the formation of a single vortex inside the intake. In this case the sense of rotation of the vortex is opposite to the ambient vorticity. Other mechanisms of formation also exist and can be considered as combinations of the previous ones that lead to a large number of possible combinations that are responsible for the need of more studies in order to understand all the physics involved. CFD tools have been applied recently to the understanding of the ground vortex with relative success. Nakayama & Jones [12] used panel methods to simulate the inlet and ground interaction, noting that the wind speed needed to blow the vortex away was lower than the measured experimentally. Barata et al. [13] report Navier-Stokes calculations and predicted successfully the ground vortex phenomena using real operational conditions for the case of the engine Trent 9 and GE nx-1B64. The ground vortex formation in irrotational crosswind flow is analyzed in detail for this configuration, and the formation of the trailing vortex was associated to a very complex flow. In the present paper the previous work of Barata et al. [13] is extended to include eighteen engines that are being used in the present (Table I).

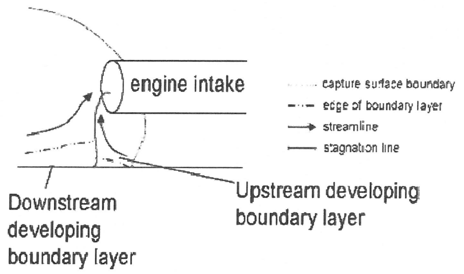

Fig. 1. Ground vortex formation

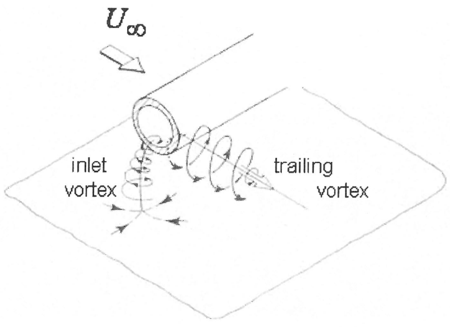

Fig. 2. Sense of rotation of the inlet vortex and the trailing vortex (sketch adapted from Ref. [9])

The ground vortex flows produced by the different engines are compared and discussed for each operational condition. The results have shown that more than one mode can occur for a particular engine-velocity ratio-clearance distance combination with 1, 2 or 3 vortexes that may merge before entering the inlet engine (Fig. 3).

TABLE I
CHARACTERISTICS OF ENGINES TESTED

Engine	Diameter (m)	Clearance Distance	Mass Flow (lb/s)	Mass Flow (kg/s)	Radius (m)	Inlet Velocity (m/s)	H (m)
cf6-50	2.667	0.83	1450	657.7089	1.3335	43.5947	2.1635
cf6-6	2.667	0.84	1300	589.6701	1.3335	39.0849	2.1735
cf6-80a	2.667	0.654	1435	650.9051	1.3335	43.1437	1.9875
cf6-80c2	2.690	0.65	1750	793.7866	1.3450	51.7184	1.9950
cf6-8oe1	2.689	0.76	1925	873.1653	1.3445	56.9326	2.1045
cfm56-2	1.735	0.56	784	355.6164	0.8675	55.6966	1.4275
cfm56-3	1.524	0.46	638	289.3919	0.7620	58.7439	1.2220
cfm56-5a	1.735	0.58	816	370.1314	0.8675	57.97	1.4475
cfm56-5b	1.735	0.58	811	367.8634	0.8675	57.6148	1.4475
cfm56-5c	1.836	1.22	1027	465.8394	0.9180	65.1534	2.1380
cfm56-7	1.549	0.46	677	307.0820	0.7745	60.3389	1.2345
rb211-535e4	1.882	0.74	1177	533.8782	0.9410	71.0639	1.6810
trent 5	2.474	0.48	1897	860.4647	1.2370	66.2796	1.7170
trent 7	2.474	0.69	2030	920.7925	1.2370	70.9265	1.9270
trent 8	2.794	1.09	2378	1078.6427	1.3970	65.1435	2.4870
trent 9	2.946	1.03	2655	1204.2877	1.4730	65.4201	2.5030
trent 10	2.845	0.71	2400	1088.6217	1.4225	63.4101	2.1325
GE nx	2.819	0.74	2458	1114.93	1.4095	66.1460	2.1495

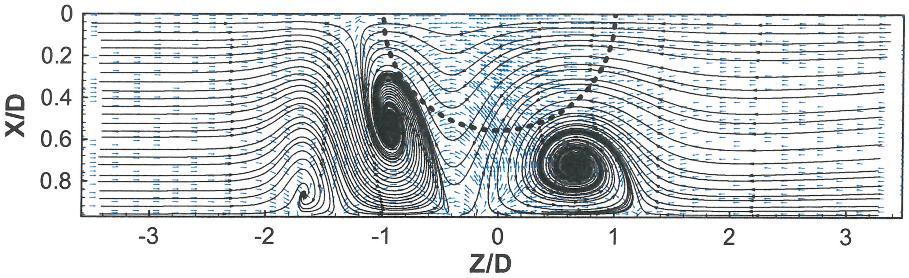

Fig. 3. Two-dimensional velocity vectors in the vertical plane parallel to the engine inlet at Y=0.5Y_{TOT} (Engine cf6-80c2, h/D_i=0.97, $U_i / U_\infty = 9.9$)

II. Mathematical Model

The mathematical model used in the present study is described in detail in [13] and only the main features will be summarized here. The time averaged partial differential equations governing the steady, uniform-density isothermal three-dimensional flow:

$$\rho \bar{U}_j \frac{\partial \bar{U}_i}{\partial X_j} = -\frac{\partial \bar{P}}{\partial X_i} + \frac{\partial}{\partial X_j}\left(\mu \frac{\partial \bar{U}_i}{\partial X_j} - \rho \overline{u'_i u'_j} \right) \qquad (1)$$

and the continuity equation:

$$\rho \bar{U}_j \frac{\partial \bar{U}_i}{\partial X_i} = 0 \qquad (2)$$

where solved together with the equations of transport of the turbulent kinetic energy and dissipation rate of the two-equation *"k-ε"* model [12]:

$$\bar{U}_j \frac{\partial k}{\partial X_j} = \frac{\partial}{\partial X_j}\left(\frac{\upsilon_T}{\sigma_k} \frac{\partial k}{\partial X_j} \right) - \overline{u'_i u'_j} \frac{\partial \bar{U}_i}{\partial X_j} - \varepsilon \qquad (3)$$

$$\begin{aligned} \bar{U}_j \frac{\partial \varepsilon}{\partial X_j} = \frac{\partial}{\partial X_j}\left(\frac{\upsilon_T}{\sigma_\varepsilon} \frac{\partial \varepsilon}{\partial X_j} \right) + \\ - C_1 \frac{\varepsilon}{k} \overline{u'_i u'_j} \frac{\partial \bar{U}_i}{\partial X_j} - C_2 \frac{\varepsilon^2}{k} \end{aligned} \qquad (4)$$

where C_1 and C_2 are additional dimensionless model constants, and σ_k and σ_ε are the turbulent Prandtl numbers for kinetic energy and turbulent dissipation.

The Reynolds stresses are expressed as:

$$\overline{u'_i u'_j} = -\upsilon_T \left(\frac{\partial \bar{U}_i}{\partial X_j} + \frac{\partial \bar{U}_j}{\partial X_i} \right) + \frac{2}{3} k \delta_{ij} \qquad (5)$$

where υ_T is the turbulence kinematic viscosity, which is derived from the turbulence model and expressed by $C_\mu k^2/\varepsilon$.

The solution of the governing equations was obtained using a quadratic finite-difference method [14] that used discretized algebraic equations deduced from the exact differential equations that they represent.

The solution procedure is based on the SIMPLE algorithm widely used and reported in the literature (e.g. [13]). It uses the staggered grid arrangement and a guess and correct procedure field such that the solution of the momentum equations satisfies continuity.

The computational domain has six boundaries where dependent values are specified: a free stream plane, a symmetry plane, and a solid wall. On the symmetry plane, the normal velocity vanishes, and the normal derivates of the other variables are zero. At the solid surface, the wall function method [16] is used to prescribe the boundary conditions for the velocity and turbulence quantities, assuming that the turbulence is in state of local equilibrium.

The free stream plane is located at Z=0 and corresponds to the crossflow conditions. The engine intake boundary is represented by a right angled polygon and the mass flow rates and the momentum are matched to the experimental values. The intake represents a 1/1th scale model with a diameter that corresponds to each particular engine.

The axis of the engine is located at a distance above the ground (h), which corresponds to the specific clearance distance. All the tests were performed for the case of irrotational crosswind, and the other conditions are shown in Table I. The domain of solution, their dimensions and the system of axes are represented in Figs. 4

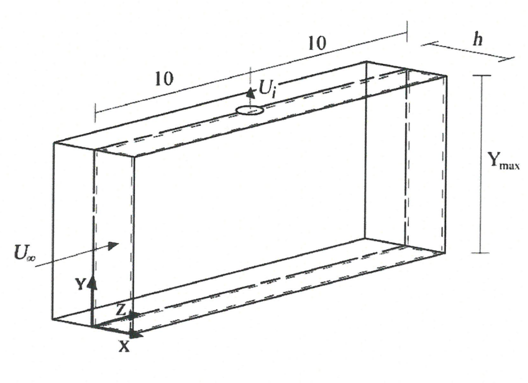

Fig. 4(a). Domain of the solution

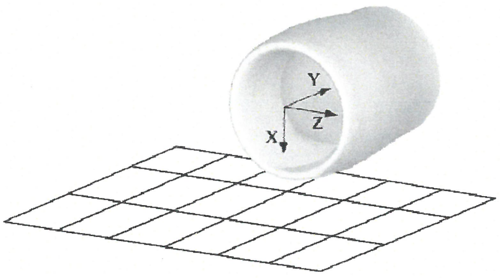

Fig. 4(b). Representation of the intake with referential at the center

III. Results

The ground vortex formation in irrotational crosswind flow is analyzed in the present section. In this configuration the ground vortex or inlet vortex that forms near the ground and is sucked by engine is accompanied by an additional feature which is the formation of the trailing vortex (see Fig. 2).

This vortex develops from the lip of the inlet engine in the direction of the crossflow with its axis parallel to the ground.

III.1. Ui/U∞ Max and h/Di=0.97

How can we see after a brief review of Table II and for the conditions mentioned above (V_i/V_∞ Max engine and H/Di = 0.97) there are four sets of results obtained.

The largest group is the single vortex in the plane XZ which shows some examples. It is perfectly visible a ground vortex at position X/D = 0.8 Z/D =-3 (Fig. 5(a)).

In the case of Fig. 5(b) we can observe the same situation but on the opposite side of the stream.

Still in the group of single vortex engines, there is the situation of Trent 700 engine where the Vortex arises in a central position (Fig. 6) and Trent 500 where this vortex in a higher position (Fig. 7). It should be noted that the vortex of Fig. 7 has a different sign (clockwise) which also applies in the Cfm56-5a.

TABLE II
SUMMARY OF RESULTS FOR THE SELECTED CONDITIONS

Engine	XZ	YZ	3D	N° of vortex	Vi/V∞	H/Di
cf6-50	X			1	43,6863	0.97
cf6-6	X			3	39,1670	0.97
cf6-80a	X	X		2	43,2344	0.97
cf6-80c2				0	51,8271	0.97
cf6-8oe1				0	57,0522	0.97
cfm56-2				0	55,8137	0.97
cfm56-3				0	58,8673	0.97
cfm56-5a	X			1	58,0918	0.97
cfm56-5b	X			1	57,7358	0.97
cfm56-5c				0	65,2903	0.97
cfm56-7	X			1	60,4657	0.97
rb211-535e4				0	71,2132	0.97
trent 500	X			1	66,4189	0.97
trent 700	X			1	71,0755	0.97
trent 800				0	65,2804	0.97
trent 1000				0	63,5434	0.97
GE nx				0	66,2850	0.97

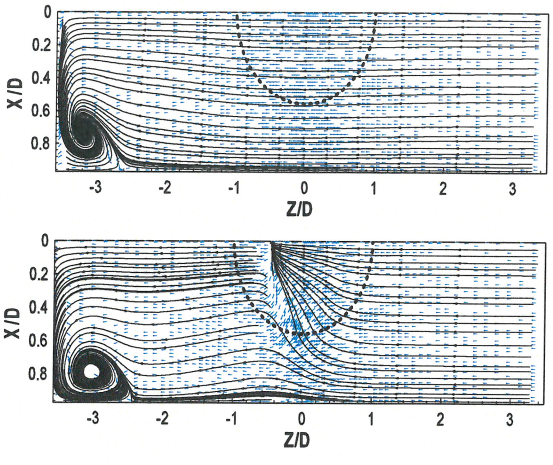

Fig. 5(a). Engine Cf6-50 for U_i/U_∞ Max and H/Di=0.97 Y=0.5YTOT and Y=0.95YTOT

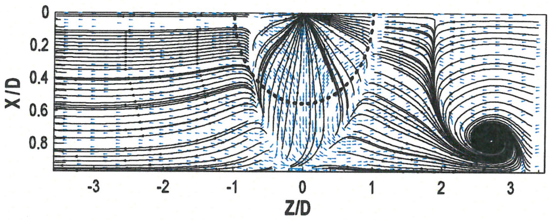

Fig. 5(b). Engine Cfm56-7 for U_i/U_∞ Max and H/Di=0.97, Y=0.95YTOT

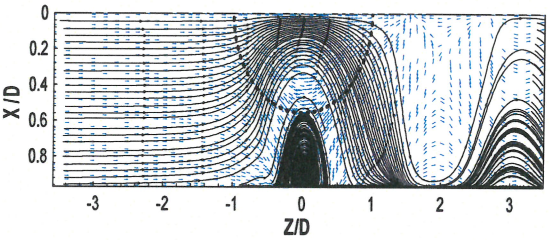

Fig. 6. Engine Trent 700 for U_i/U_∞ Max and H/Di=0.97, Y=0.05YTOT

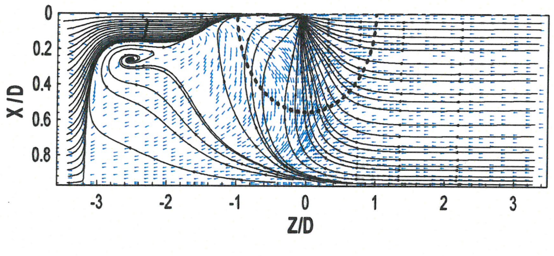

Fig. 7. Engine Trent 500 for U_i/U_∞ Max and H/Di=0.97, Y=0.95YTOT

In Table II we can see two more vorticity situations. In the case of the Cf6-80a engine where there are two vorticity structures, one in the XZ plane and the other in YZ plane with can be seen in Fig. 8 and Fig. 9.

And in the case of Cf6-6 engine there is the formation of three weak ground vortex at the same time, calling attention to the fact that two of them have a clockwise direction and not the third, as shown in Fig. 10.

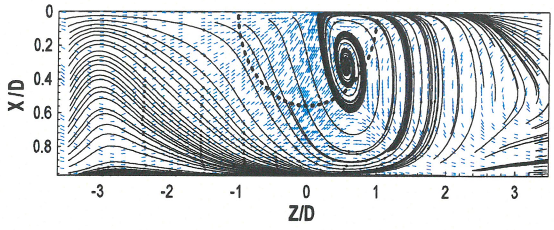

Fig. 8. Engine Cf6-80a for U_i/U_∞ Max and H/Di=0.97, Y=0.05YTOT

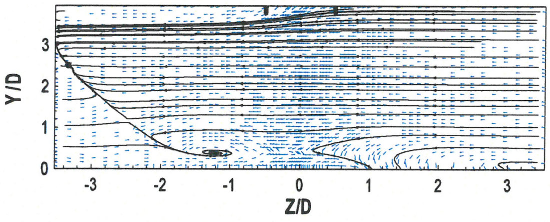

Fig. 9. Engine Cf6-80a for U_i/U_∞ Max and H/Di=0.97, X=0.5XTOT

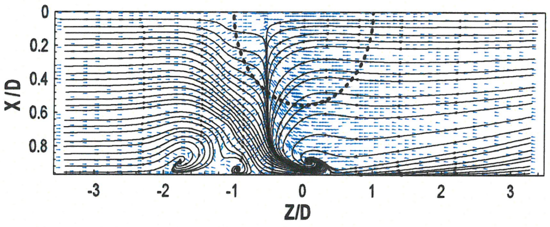

Fig. 10. Engine Cf6-6 for U_i/U_∞ Max and H/Di=0.97, Y=0.05YTOT

III.2. Ui/U∞=9.9 and h/Di=0.97

For the case of Table III we can again separate the results into three groups.

There is a group where in the XZ plane there are two vortical structures and one in the YZ plane. In the situation of the YZ plane four situations that occur should be described. The first is one in which the vortex changes direction of rotation as shown in Figures 11 and 12.

TABLE III
SUMMARY OF RESULTS FOR THE SELECTED CONDITIONS

Engine	XZ	YZ	3D	N° of vortex	Vi/V∞	H/Di
cf6-50	X(2)	X		3	9.9	0.97
cf6-6	X(2)	X		3	9.9	0.97
cf6-80a	X(2)	X		3	9.9	0.97
cf6-80c2	X(2)	X		3	9.9	0.97
cf6-8oe1				0	9.9	0.97
cfm56-2				0	9.9	0.97
cfm56-3				0	9.9	0.97
cfm56-5a				0	9.9	0.97
cfm56-5b				0	9.9	0.97
cfm56-5c				0	9.9	0.97
cfm56-7				0	9.9	0.97
rb211-535e4				0	9.9	0.97
trent 500		X	X	2	9.9	0.97
trent 700		X	X	2	9.9	0.97
trent 800	X(2)	X		3	9.9	0.97
trent 1000	X	X		2	9.9	0.97
GE nx	X(2)	X		3	9.9	0.97

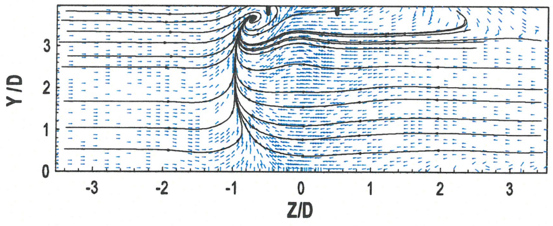

Fig. 11. Engine Cf6-6 for U_i/U_∞=9.9 and H/Di=0.97, X=0.25XTOT

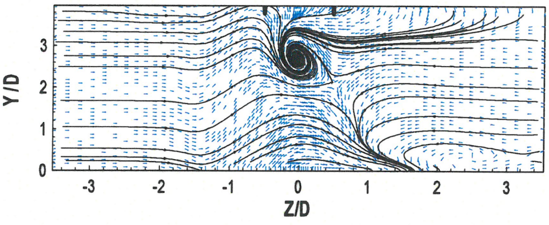

Fig. 12. Engine Cf6-6 for U_i/U_∞=9.9 and H/Di=0.97, X=0.5XTOT

The second is that where the vortex with the clockwise rotation disappears from the first to the second graph causing increased disruption of the flow (Figs. 13 and 14).

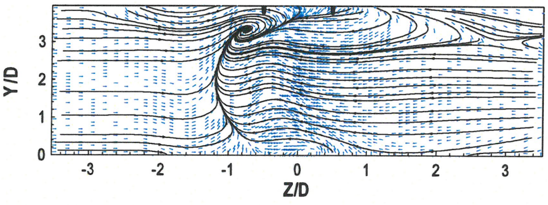

Fig. 13. Engine Cf6-80c2 para U_i/U_∞=9.9 e H/Di=0.97, X=0.25XTOT

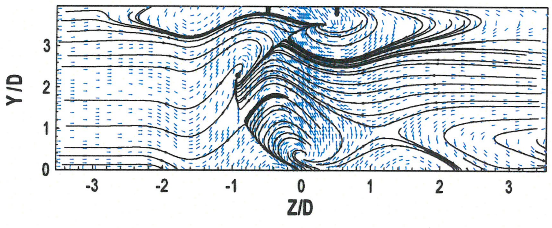

Fig. 14. Engine Cf6-80c2 para U_i/U_∞ =9.9 e H/Di=0.97, X=0.5XTOT

In the third situation where the case of the Trent 800 engine where the vortex occurs in the central area and far away from the engine (Fig. 15).

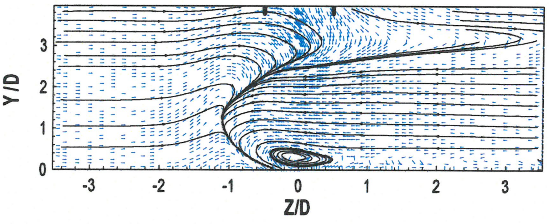

Fig. 15. Engine Trent 800 for U_i/U_∞ =9.9
and H/Di=97, X=0.5XTOT

In the latter situation we have the Ge-nx engine where you can see the vortex with a clockwise direction along the plane of the face of the engine and with the increase of X there is a Y/D decrease.

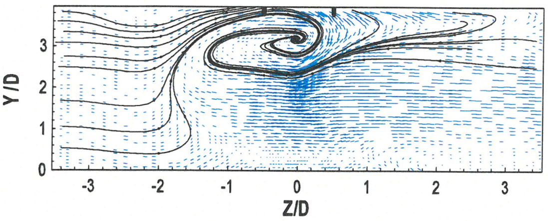

Fig. 16. Engine GE-nx for U_i/U_∞ =9.9 and H/Di=0.97, X=0.5XTOT

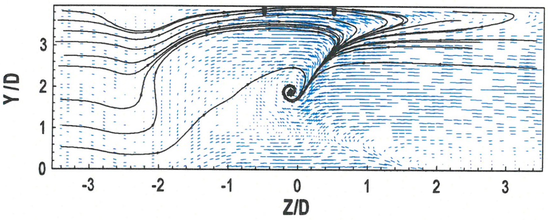

Fig. 17. Engine Ge-nx for U_i/U_∞ =9.9 and H/Di=0.97, X=0.75XTOT

In the YZ plane there are four situations to be described. In Fig. 18 the position of the vortex is near the edge of the inlet nozzle.

In Fig. 19 we can see the difference in the position of the two vortexes.

In Fig. 20 we can see the difference in intensity of vortex and in Fig. 21 can verify the big difference compared to previous situations because there is a ground vortex of great intensity and another of weak intensity with an opposite rotation.

In the case of the Trent 1000 engine there is a vortex in the YZ plane and another in the XZ plane.

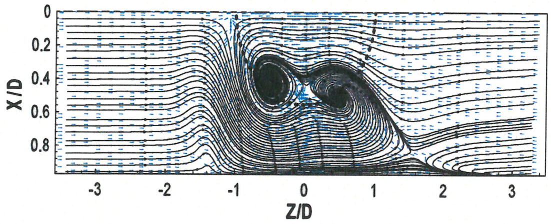

Fig. 18. Engine Cf6-6 for U_i/U_∞ =9.9
and H/Di=0.97, Y=0.5YTOT

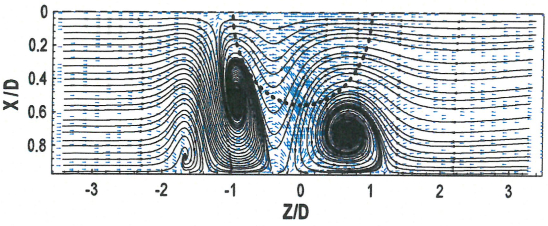

Fig. 19. Engine cf6-80c2 for U_i/U_∞ =9.9
and H/Di=0.97, Y=0.5YTOT

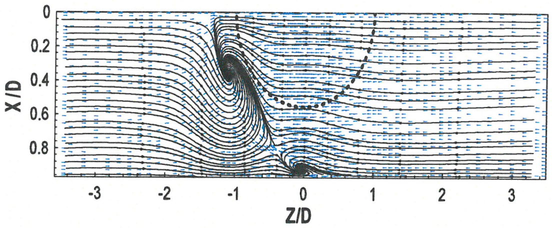

Fig. 20. Engine Ge-nx for U_i/U_∞ =9.9 and H/Di=0.97, Y=0.5YTOT

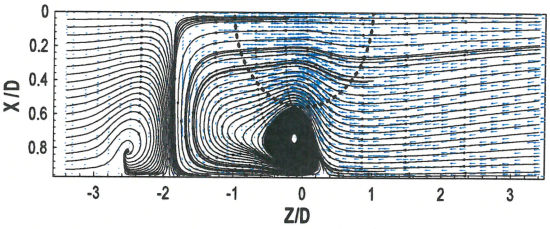

Fig. 21. Engine Ge-nx for U_i/U_∞ =9.9 and H/Di=0.97, Y=0.5YTOT

In relation to the XZ plane can see a vortex of high intensity near the inlet nozzle of the engine (Fig. 22) and the YZ plane the vortex moves from one central location in the flow for a more lateral one and changing the direction of rotation (Figs. 23 and 24).

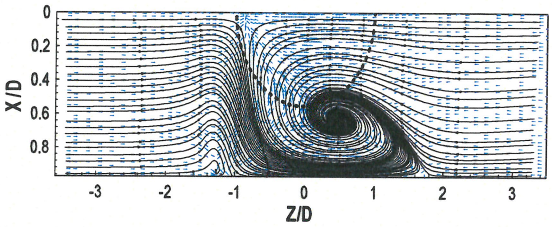

Fig. 22. Engine Trent 1000 for U_i/U_∞ =9.9
and H/Di=0.97, Y=0.5YTOT

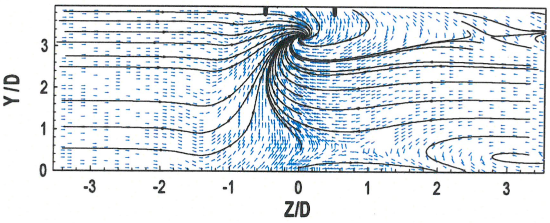

Fig. 23. Engine Trent 1000 for U_i/U_∞ =9.9
and H/Di=0.97, X=0.5XTOT

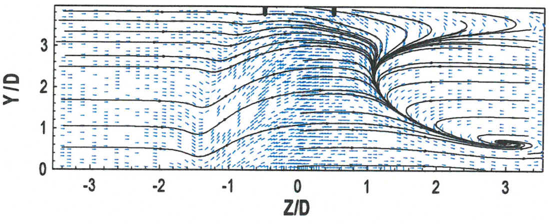

Fig. 24. Engine Trent 1000 for U_i/U_∞ =9.9
and H/Di=0.97, X=0.75XTOT

In the last group on Table III appears a result never observed until now, we can see in Fig. 25 the return flow coming from the area downstream in the vicinity of Y/D = 0 and coming out near Y/D = 10.

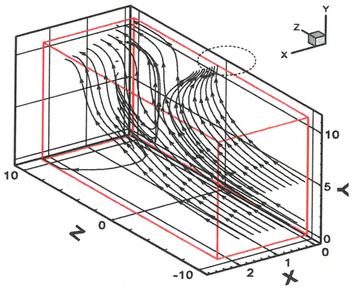

Fig. 25. Engine Trent 500 for U_i/U_∞ =9.9 and H/Di=0.97

In the YZ plane we can see a small vortex in the downstream of the nozzle (Fig. 26).

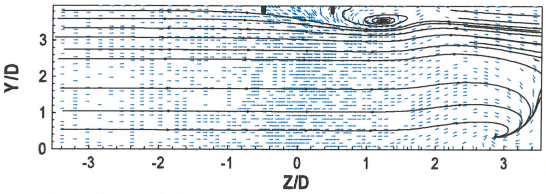

Fig. 26. Engine Trent 500 for U_i/U_∞ =9.9 and H/Di=0.97, X=0.5XTOT

III.3. $Ui/U\infty= 4.95$ and $h/Di=0.97$

In Table IV we verified no vortex results, for the case U_i/U_∞= 4.95 and h/D_i=0.97

TABLE IV
SUMMARY OF RESULTS FOR THE SELECTED CONDITIONS

Engine	XZ	YZ	3D	N° of vortex	Vi/V∞	H/Di
cf6-50				0	4.95	0.97
cf6-6				0	4.95	0.97
cf6-80a				0	4.95	0.97
cf6-80c2				0	4.95	0.97
cf6-8oe1				0	4.95	0.97
cfm56-2				0	4.95	0.97
cfm56-3				0	4.95	0.97
cfm56-5a				0	4.95	0.97
cfm56-5b				0	4.95	0.97
cfm56-5c				0	4.95	0.97
cfm56-7				0	4.95	0.97
rb211-535e4				0	4.95	0.97
trent 500				0	4.95	0.97
trent 700				0	4.95	0.97
trent 800				0	4.95	0.97
trent 1000				0	4.95	0.97
GE nx				0	4.95	0.97

III.4. $Ui/U\infty=9.9$ and $h/Di=1.2$

Regarding the results of Table V we can check the increasing of vortical structures mentioned before and the decrease of ground vortex.

In Table V we can see five relevant result sets, two vortex in the XZ plane and one in the YZ plane. A vortex in the XZ plane one in the YZ plane and one in 3D. A 3D one. One 3D and one in the YZ plane and finally one in the YZ plane.

TABLE V
SUMMARY OF RESULTS FOR THE SELECTED CONDITIONS

Engine	XZ	YZ	3D	N° of vortex	Vi/V∞	H/Di
cf6-50				0	9.9	1.2
cf6-6				0	9.9	1.2
cf6-80^a				0	9.9	1.2
cf6-80c2	X(2)	X		3	9.9	1.2
cf6-8oe1	X	X	X	3	9.9	1.2
cfm56-2			X	1	9.9	1.2
cfm56-3				0	9.9	1.2
cfm56-5^a			X	1	9.9	1.2
cfm56-5b			X	1	9.9	1.2
cfm56-5c			X	1	9.9	1.2
cfm56-7				0	9.9	1.2
rb211-535e4			X	1	9.9	1.2
trent 500		X	X	2	9.9	1.2
trent 700				0	9.9	1.2
trent 800		X		1	9.9	1.2
trent 1000		X		1	9.9	1.2
GE nx		X		1	9.9	1.2

For the first situation we have the CF6-80C2 engine with two vortex in XZ and one in YZ. In the YZ plane emerges a structure similar to that described in Figures 13 and 14, and in relation to the XZ plane again there are two structures that look similar to those in Fig. 19.

In the second situation three structures are visible in XZ and YZ and another one in 3D. In XZ a vortex arises in the area downstream of the stream as it is clearly visible in Fig. 27.

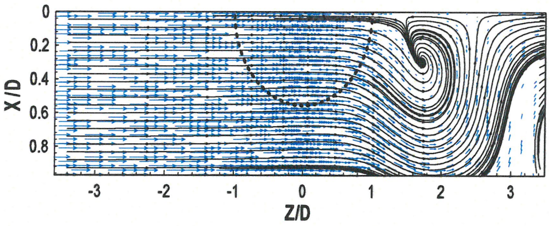

Fig. 27. Engine Cf6-80c2 for U_i/U_∞ =9.9 and H/Di=1.2, Y=0.5YTOT

In the YZ plane appears a weak vortex and an area where the flow enters a plane coming from behind the plane of the face of the engine and follows in main the flow direction (Fig. 28).

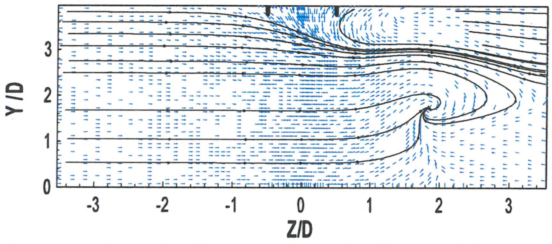

Fig. 28. Engine Cf6-80c2 for U_i/U_∞ =9.9 and H/Di=1.2, X=0.5XTOT

The 3D structure is identical to one already mentioned above in relation to Fig. 25.

In the third set only arise visible structures in 3D perspective, which may be of three types. One already referenced above (Fig. 15). A flow in the same area but weaker (Fig. 29) and a third is already well defined vortex and strong influence on the flow (Fig. 30).

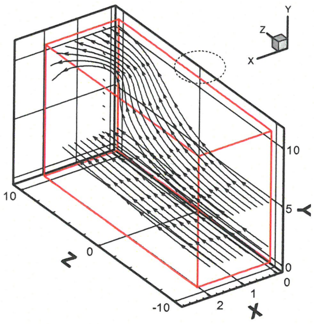

Fig. 29. Engine Cf56-2 for U_i/U_∞ =9.9 and H/Di=1.2

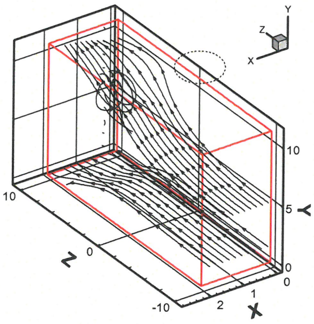

Fig. 30. Engine Cf56-5c for U_i/U_∞ =9.9 and H/Di=1.2

The fourth set of results is the Trent 500 where the structures are of the same kind found in Fig. 25 and Fig. 26.

Finally the fifth set of results which has only one YZ vortex, which is similar to others previously mentioned in terms of position but of greater intensity (Fig. 31).

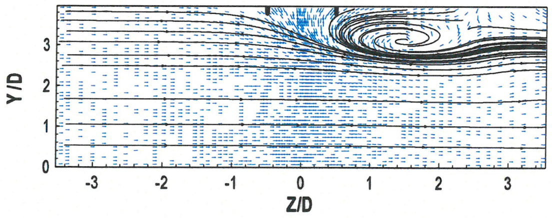

Fig. 31. Engine Trent 800 for U_i/U_∞ =9.9 and H/Di=1.2, X=0.5XTOT

III.5. Vorticity Distribution

We can see from analyzing the last figures (Figure 32 to Figure 36) that despite the results obtain concurred whit the perversely presented results by other authors has cam be seen in Figure 36, where below the line is an non vorticity area and above the line is an vorticity area, there are some engines who present no vorticity in a clearly vorticity area, so future work should be done to appraise that.

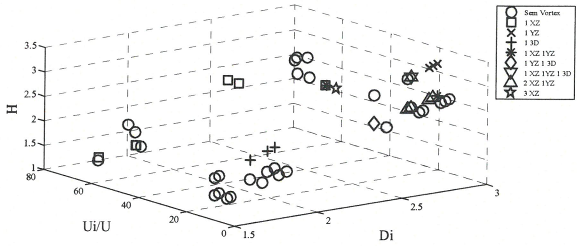

Fig. 32. Vorticity distribution whit H, Ui/U and Di

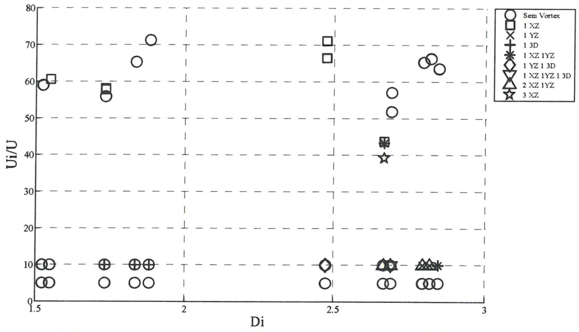

Fig. 33. Vorticity distribution whit Ui/U, Di

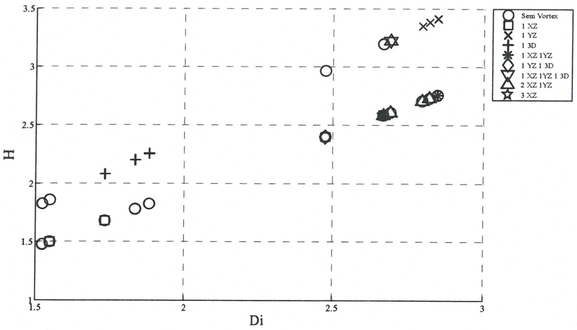

Fig. 34. Vorticity distribution whit H, Di

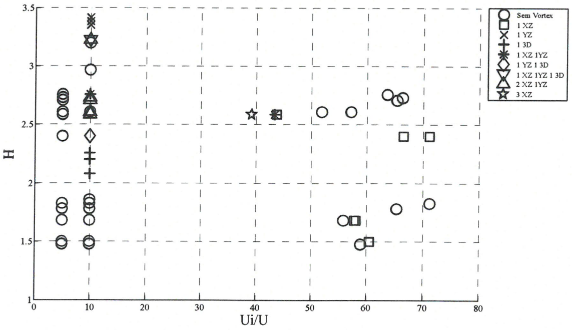

Fig. 35. Vorticity distribution whit H, Ui/U

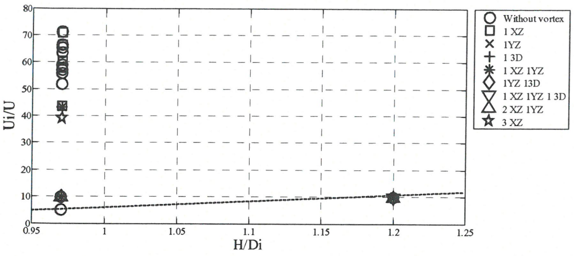

Fig. 36. Vorticity distribution whit H/Di, Ui/U

IV. Conclusion

The present study has shown that the inlet flow of a gas turbine engine is strongly dependent on the velocity ratio between the inlet and any crosswind as well as on the diameter at its position above the ground.

Different engines have been studied and the formation of vortex was identified for all engines. The affected flow region was found to be considerably different in size. The trailing vortex could be clearly noticed for some engines.

Away from the inlet plane other types of complex vortical structures were identified that have different signs depending on the clearance distance of each particular engine and initial conditions.

By analyzing the different tables we can see the influence of inlet velocity and H in vortical structures.

We can conclude that for high inlet velocities vortical structures are almost exclusive to the XZ plane and with its decrease the formation of vortex passes through two stages one intermediate of an increase in vorticity at all levels and the second for low inlet velocities of almost absence of vortex.

With increased ground clearance to the shaft of the engines we see a change in the type of vortex that arise, with a decrease of it in the XZ plane, roughly the same number of structures in the YZ plane and big structures that are only possible to visualize in 3D perspective.

Acknowledgements

The present work has been performed in the scope of the activities of the Aeronautics and Astronautics Research Center – AeroG of the University of Beira Interior, Covilhã, Portugal.

References

[1] Hünecke, K. "Jet Engines: Fundamental of theory, design and operation", Airlife publishing, UK, 1997.

[2] Mattingly, J.D., Heiser, W.H., Daley, D.H. "Aircraft Engine Design", AIAA Education Series, New York, 1987.

[3] Mattingly, J.D. "Elements of Gas Turbine Propulsion", Singapore: McGraw-Hill, 1996.

[4] Belkacem, B., Amina, B. & Rachid, S. "Scale Factor Elaboration of Gas Turbines Design by Meridian Flow Analysis" *International Review in Aerospace Engineering (IREASE)*, Vol. 5 no.3, 2012, pp. 101-108.

[5] Johns, C. "The Aircraft Engine Inlet Vortex Problem", AIAA's Aircraft Technology, Integrations and Operations (ATIO) 22 Technical, 1-3rd 22, Los Angles, California, AIAA Paper 22-5894.

[6] Swainston, M. "Vortex Formation Near Intakes to Turbomachinery and Duct Systems", Heat and Fluid Flow, Vol. 4, No. 2, 1974.

[7] Silva, A.R.R., Durão, D.F.G., Barata, J.M.M. & Ribeiro, S. "Laser-Doppler Analysis of the Separation Zone of a Ground Vortex Flow", *International Review in Aerospace Engineering (IREASE)*, Vol. 2 no.3, 2009, pp. 167-174.

[8] Nakayama, A. & Jones, J. "Correlation for Formation of Inlet Formation", AIAA Journal, Vol. 37, No. 4: Technical Notes, 1998.

[9] Motycka, D. & Walter, W. "An Experimental Investigation of Ground Vortex Formation During Reverse Thrust Operation", AIAA Paper No. 75/1322, AIAA/SAE 11th Propulsion Conference, 1975

[10] Brix, S., Neuwerth, G. & Jacob, D. "The Inlet-Vortex System of Jet Engines Operating Near the Ground", AIAA Paper 20-3998, 20

[11] De Siervi, F., Viguier, H., Greitzer, E. & Tan, C. "Mechanisms of Inlet Vortex Formation", J. Fluid Mech., Vol. 124, pp. 173-207, 1982

[12] Nakayama, A. & Jones, J. "Correlation for Formation of Inlet Formation", AIAA Journal, Vol. 37, No. 4: Technical Notes, 1998.

[13] Barata, J. M. M., Manquinho, P. e Silva, A.R.R., "A Comparison of Different Gas Turbine Engines Ground Vortex Flows". Artigo AIAA 2010-7116, 46th AIAA/ASME/ SAE/ASEE Joint Propulsion Conference and Exhibit, Nashville, Tennessee, 25-28 Julho, 2010.

Authors' information

Aerospace Science Department, University of Beira Interior, Calçada Fonte do Lameiro, 6200-358 Covilhã, Portugal.

Jorge Jorge M. M. Barata, Portugal, 17th December 1959. Habilitation on Aerospace Sciences, University of Beira Interior, Covilhã, 1999. PhD in Mechanical Engineering, Instituto Superior Técnico, Technical University of Lisbon, Portugal, 1989. Master on Energy Transfer and Conversion, Instituto Superior Técnico, Technical University of Lisbon, Portugal, 1985. BEng on Mechanical Engineering, University of Coimbra, Portugal, 1982.

He published more than 150 publications including books, chapter of books, papers on journals and scientific meetings in the areas of V/STOL aerodynamics and propulsion. Has been member of the editorial board and reviewer of scientific journals (IMechE Journal of Aerospace Engineering, Atomization and Sprays, among others) and scientific congresses.

Professor Barata is a full professor of the Aerospace Sciences Department of the University of Beira Interior, Covilhã, Portugal, scientific coordinator of the AeroG-Aeronautics and Astronautics Research Center, and an Associate Fellow of the American Institute of Aeronautics and Astronautics.

Andre R. R. Silva, Portugal, 10th July 1973. PhD in Aeronautical Engineering, University of Beira Interior, Covilhã, Portugal, 2007. BEng on Aeronautical Engineering, University of Beira Interior, Covilhã, Portugal, 1999.

He published more than 30 publications including chapter of books, papers on journals and scientific meetings in the areas of V/STOL aerodynamics and propulsion.

Professor Silva is an assistant professor of the Aerospace Sciences Department of the University of Beira Interior, Covilhã, Portugal, member of the AeroG-Aeronautics and Astronautics Research Center, and a Professional Membership of the American Institute of Aeronautics and Astronautics.

Pedro A. R. Manquinho, Portugal, 06th August 1976. Master in Aeronautical Engineering, University of Beira Interior, Covilhã, Portugal, 2010. BEng on Aeronautical Engineering, University of Beira Interior, Covilhã, Portugal, 2009.

Pedro Manquinho is an member of the AeroG-Aeronautics and Astronautics Research Center, and a Student Membership of the American Institute of Aeronautics and Astronautics.

STUDIES OF THE VORTEX FORMATION IN IRROTATIONAL WIND

Pedro Manquinho[a*], **Jorge M. M. Barata**[a], **André R. R. Silva**[a]
a) Universidade da Beira Interior, Covilhã, 6201-001, Portugal
* e-mail: pedro.manquinho@gmail.com

Key words: cross-wind, ground, vortex, inlet

Abstract. *The present paper has the previous work of Barata et al in mind and has the purpose of analyzing the behavior of ground vortex flows through several values of height of the engine axis above the ground, diameter of engine intake and inlet airflow velocity.*

1 INTRODUCTION

The inlet is designed to give the appropriate amount of airflow required with minimal pressure loss by the engine. If the pressure losses and the flow distortions are very low, the performance of the engine is optimal. This airflow condition is necessary in all flight configurations including when the aircraft is maneuvering on the ground. The performance of the intake depends on the mass-flow delivered to the compressor. The internal mass-flow stays constant and assuming that the flow is incompressible due to low speed velocities, it will be given by $A_i U_i = A_\infty U_\infty$. Since the mass-flow is constant and the area ratio is related to the stream tube contraction ratio, the area ratio can be expressed as $\frac{A_\infty}{A_i} = \left(\frac{L_q}{D_i}\right)^2$. The capture ratio A_∞ / A_i is controlled by the engine, the engine mass-flow, the inlet diameter and the free-stream velocity. The area called the intake captured area is defined by the boundary between the air that enters in the engine and the air that does not. The flow ratio and the stream-tube shape vary with the operation conditions of the aircraft engine. In near static configuration, the engine must accelerate the air using maximum thrust since the ambient air is at rest. The extreme local acceleration of the flow at the inlet lip can cause airflow separation in this region[2,3]. The shape of the stream tube is modified near the lip in cross-wind configuration,. The cross-flow causes an increase in the flow velocity near the lip depending on the strength of the cross-flow, high velocity origins in flow separation leading to a total pressure loss at the engine fan.

The formation of ground vortices depends on engine power, wind velocity and engine inlet height and size. Previous published work show that the phenomenon can only occur with the presence of a stagnation streamline between the ground and the intake which is dependent on the velocity ratio U_i / U_∞ and the non-dimensional height of the engine axis above the ground, h/D_i (Fig. 1). In static conditions, the inlet airflow demand increases, and the inlet capture surface increases in diameter and starts including the ground to bring the necessary airflow to the fan[4,5]. The typical formation of ground vortices is defined by low h/D_i and high U_i/U_∞ and that is the same has saying the engine is operating close to the ground at a high inlet mass flow[6]. Hence, the mechanism of intake formation is strongly dependent of the height of the engine axis above the ground, the velocity ratio and the presence of an upstream velocity.

Four different types of conditions leading to the formation of inlet ground vortices have been identified. A vortex can be generated without ambient wind and with a low ratio h/D_i (typically less than one). Due to the ground proximity, high levels of suction beneath the engine inlet leads into a strong flow underneath the inlet upstream towards the intake lip[7]. In these conditions, it is possible to visualize at the engine intake and at the ground two upward spiraling vortices. Under no-wind condition, it appears that the two vortices are counter-rotating, and the vorticity is induced by the boundary layer. Is a head-wind flow, when the air is sucked into the engine inlet, the flow field underneath the intake starts to roll up into two upright counter-rotating vortices and a fast flow into the opposite direction of the wind appears between them[8,9]. For high velocity ratios (>20) the sense of rotation of the two vortices switches to the same as in the no-wind mechanism. With a 90° cross-wind two different kinds of vortices appear around the intake: an inlet vortex and a trailing vortex (Fig.2). When the engine intake is oriented at a 90° yaw angle and with the presence of cross-wind with far upstream vertical vorticity, there is the formation of a single vortex inside the intake. In this case the sense of rotation of the vortex is opposite to the ambient vorticity. Other mechanisms of formation also exist and can be considered as combinations of the previous ones that lead to a large number of possible combinations that are responsible for the need of more studies in order to understand all the physics involved.

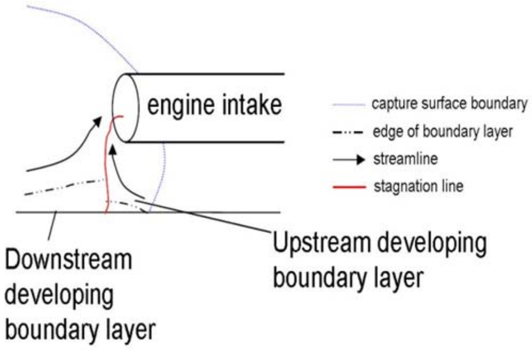

Figure 1. Ground vortex formation.

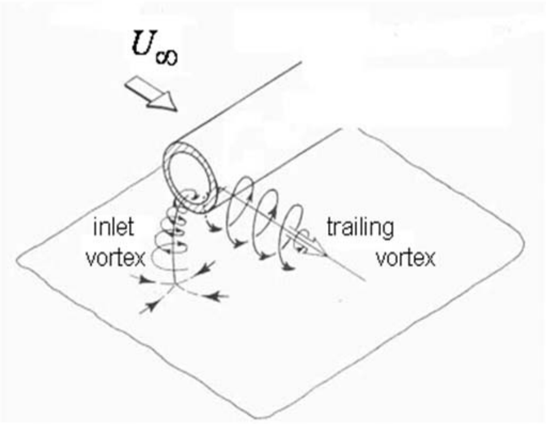

Figure 2. Sense of rotation of the inlet vortex and the trailing vortex (sketch adapted from Ref. 9).

CFD tools have been applied recently to the understanding of the ground vortex with relative success. Nakayama & Jones[10] used panel methods to simulate the inlet and ground interaction, noting that the wind speed needed to blow the vortex away was lower than the measured experimentally. Barata et al.[11] report Navier-Stokes calculations and predicted successfully the ground vortex phenomena using real operational conditions for the case of the engine Trent 9 and GE nx-1B64. The ground vortex formation in irrotational crosswind flow is analyzed in detail for this configuration, and the formation of the trailing vortex was associated to a very complex flow. In the present paper the work of Barata et al.[11, 12, 13] is extended to 572 simulations for different values of inlet diameter, height of the engine axis above the ground and inlet velocity (Table 1). The ground vortex flows produced by the different engine-velocity ratio-clearance distance combination are compared and discussed using pressure has base of comparison. The results have shown that is very difficult to analyze in most cases ground vortex flows using only pressure so we used two-dimensional velocity vectors in the vertical and horizontal planes to determine the existence of vorticity and then draw our conclusions for the pressure. In some cases it was easy to determine the existence of vorticity (Fig. 3).

Table 1. Values tested.

r (m)	D_i (m)	h (m)	U_i (m/s)	U_∞ (m/s)
1,5000	**3,0000**	**2,8000**	**160,0000**	**2,2000**
1,4000	**2,8000**	**2,6000**	**140,0000**	
1,3000	**2,6000**	**2,4000**	**120,0000**	
1,2000	**2,4000**	**2,3000**	**100,0000**	
1,1000	**2,2000**	**2,2000**	**80,0000**	
1,0000	**2,0000**	**2,1000**	**60,0000**	
0,9000	**1,8000**	**2,0000**	**40,0000**	
0,8000	**1,6000**	**1,9000**	**20,0000**	
0,7500	**1,5000**			

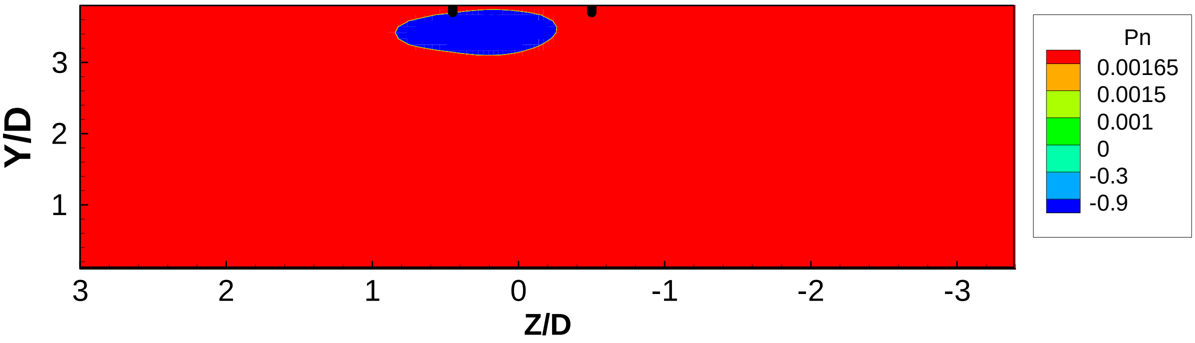

Figure 3. Two-dimensional pressure contours in the horizontal plane parallel to the ground. (D_i=2,800; h=1,900; U_i=160,000; U_∞=2,200)

2 MATHEMATICAL MODEL

The mathematical model used in the present study is described in detail in Ref. 11 and only the main features will be summarized here. The time averaged partial differential equations governing the steady, uniform-density isothermal three-dimensional flow

$$\rho \overline{U}_j \frac{\partial \overline{U}_i}{\partial X_j} = -\frac{\partial \overline{P}}{\partial X_i} + \frac{\partial}{\partial X_j}\left(\mu \frac{\partial \overline{U}_i}{\partial X_j} - \rho \overline{u'_i u'_j} \right) \qquad (1)$$

and the continuity equation,

$$\rho \overline{U}_j \frac{\partial \overline{U}_i}{\partial X_i} = 0 \qquad (2)$$

where solved together with the equations of transport of the turbulent kinetic energy and dissipation rate of the two-equation *"k-ε"* model[10]

$$\overline{U}_j \frac{\partial k}{\partial X_j} = \frac{\partial}{\partial X_j}\left(\frac{\upsilon_T}{\sigma_k} \frac{\partial k}{\partial X_j} \right) - \overline{u'_i u'_j} \frac{\partial \overline{U}_i}{\partial X_j} - \varepsilon \qquad (5)$$

$$\overline{U}_j \frac{\partial \varepsilon}{\partial X_j} = \frac{\partial}{\partial X_j}\left(\frac{\upsilon_T}{\sigma_\varepsilon} \frac{\partial \varepsilon}{\partial X_j} \right) - C_1 \frac{\varepsilon}{k} \overline{u'_i u'_j} \frac{\partial \overline{U}_i}{\partial X_j} - C_2 \frac{\varepsilon^2}{k} \qquad (6)$$

where C_1 and C_2 are additional dimensionless model constants, and σ_k and σ_ε are the turbulent Prandtl numbers for kinetic energy and turbulent dissipation.
The Reynolds stresses are expressed as

$$\overline{u'_i u'_j} = -\upsilon_T \left(\frac{\partial \overline{U}_i}{\partial X_j} + \frac{\partial \overline{U}_j}{\partial X_i} \right) + \frac{2}{3} k \delta_{ij} \qquad (3)$$

where υ_T is the turbulence kinematic viscosity, which is derived from the turbulence model and expressed by $C_\mu k^2/\varepsilon$.

The solution of the governing equations was obtained using a quadratic finite-difference method that used discretized algebraic equations deduced from the exact differential equations that they represent.

The solution procedure is based on the SIMPLE algorithm widely used and reported in the literature. It uses the staggered grid arrangement and a guess and correct procedure field such that the solution of the momentum equations satisfies continuity.

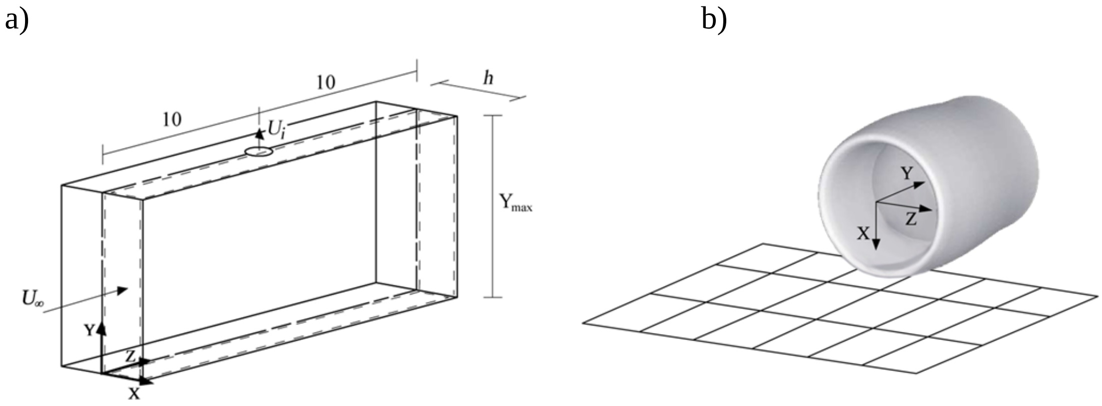

Figure 4. Domain of the solution a). Representation of the intake with referential at the center b).

The computational domain has six boundaries where dependent values are specified: a free stream plane, a symmetry plane, and a solid wall.

On the symmetry plane, the normal velocity vanishes, and the normal derivates of the other variables are zero.

At the solid surface, the wall function method is used to prescribe the boundary conditions for the velocity and turbulence quantities, assuming that the turbulence is in state of local equilibrium. The free stream plane is located at Z=0 and corresponds to the crossflow conditions.

The engine intake boundary is represented by a right angled polygon and the mass flow rates and the momentum are matched to the experimental values.

The intake represents a 1/1th scale model with a diameter that corresponds to each particular engine. The axis of the engine is located at a distance above the ground (h), which corresponds to the specific clearance distance.

All the tests were performed for the case of irrotational crosswind, and the other conditions are shown in Table 1. The domain of solution, their dimensions and the system of axes are represented in Fig.4

3 RESULTS

The ground vortex formation in irrotational crosswind flow is the only mode analyzed in the present paper. In this configuration the ground vortex or inlet vortex that forms near the ground and is sucked by engine is accompanied by an additional feature which is the formation of the trailing vortex (see Fig. 2).

In this section we analyze the various types of pressure distribution for the different velocity ratio-clearance distance combination.

We have types of pressure distribution that always have vorticity for all the cases analyzed others that do not have any or almost any vorticity and cases where the existence of vorticity varies in different combinations.

When the floor is all a low pressure area there is always vorticity present in the flow (Fig. 4 and Fig. 5).

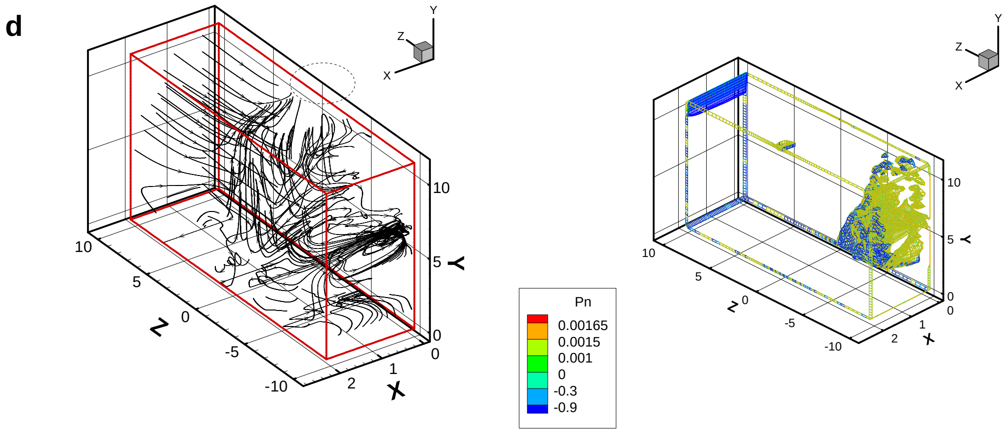

Figure 4. D_i=2,800; h=2,100; U_i=160,000; U_∞=2,200

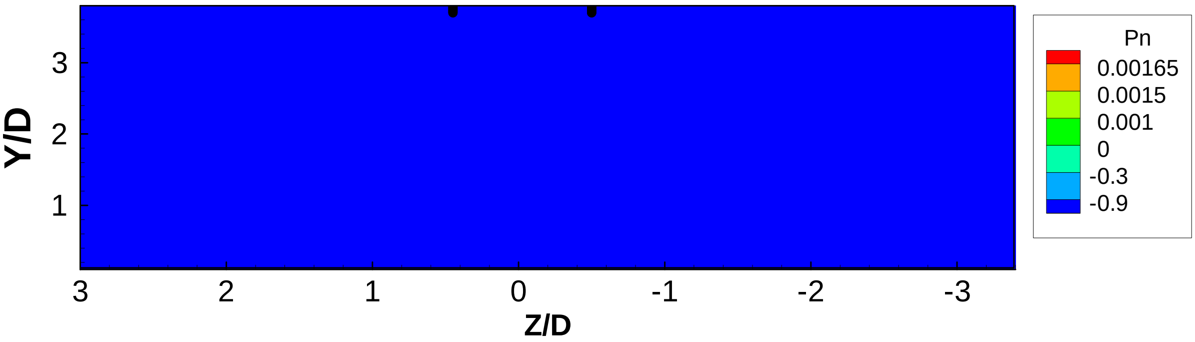

Figure 5. D_i=2,800; h=2,100; U_i=160,000; U_∞=2,200

It is perfectly visible in Fig. 4 an area of vorticity in the flow. All the cases equal or must alike figures 4 and 5 may have vorticity be visible in 3D grafic or not. An exemple of that is Fig. 6 and 7 where nothing is visible but there is vorticity present.

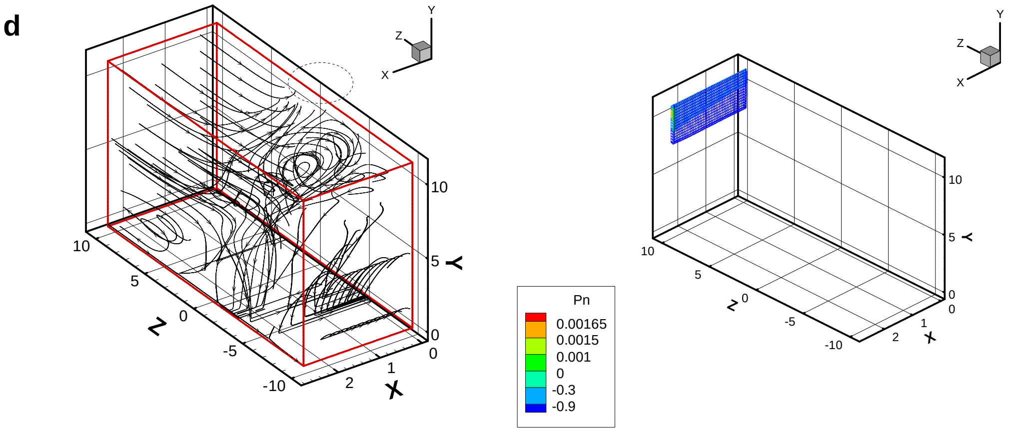

Figure 6. D_i=2,600; h=2,600; U_i=160,000; U_∞=2,200

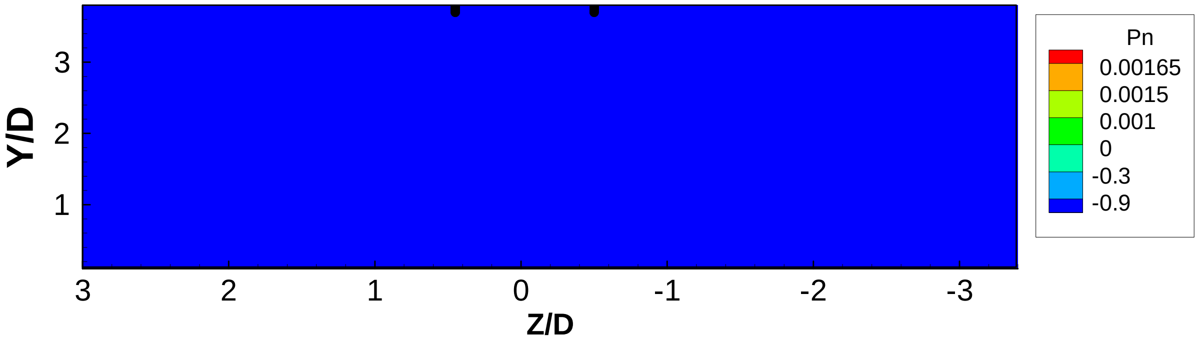

Figure 7. D_i=2,600; h=2,600; U_i=160,000; U_∞=2,200

Still in the same group that always have vorticity we find a case that has two different areas of pressure one high and very low separated be a plane almost perpendicular to the plane of the inlet (Fig. 8 and Fig. 9)

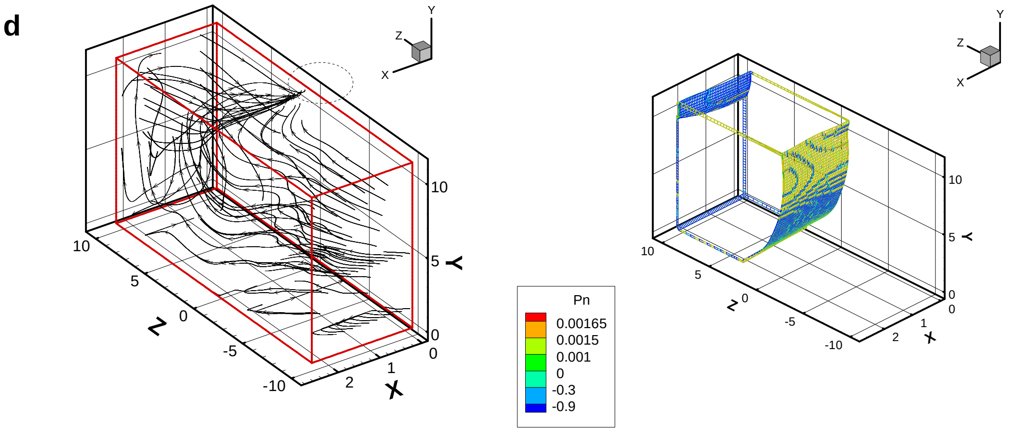

Figure 8. D_i=1,800; h=2,400; U_i=100,000; U_∞=2,200

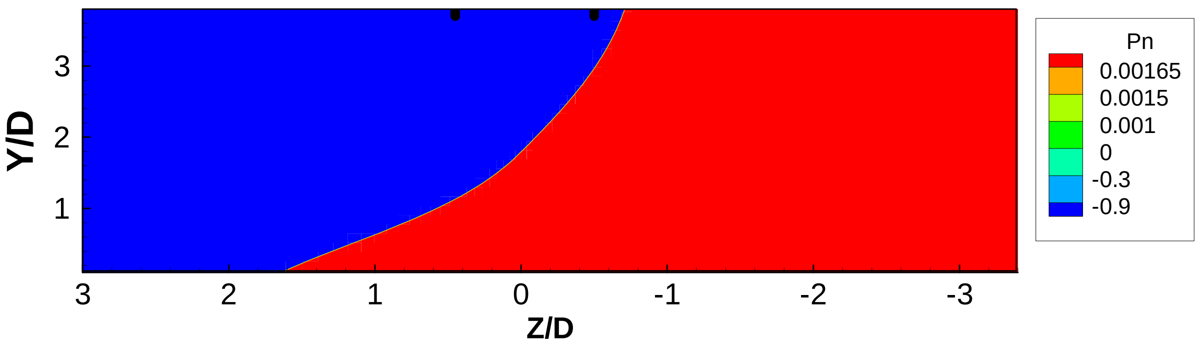

Figure 9. D_i=1,800; h=2,400; U_i=100,000; U_∞=2,200

In next cases there is a high pressure area near the inlet and a low pressure area surrounding it (Fig. 10, 11, 12 and 13).

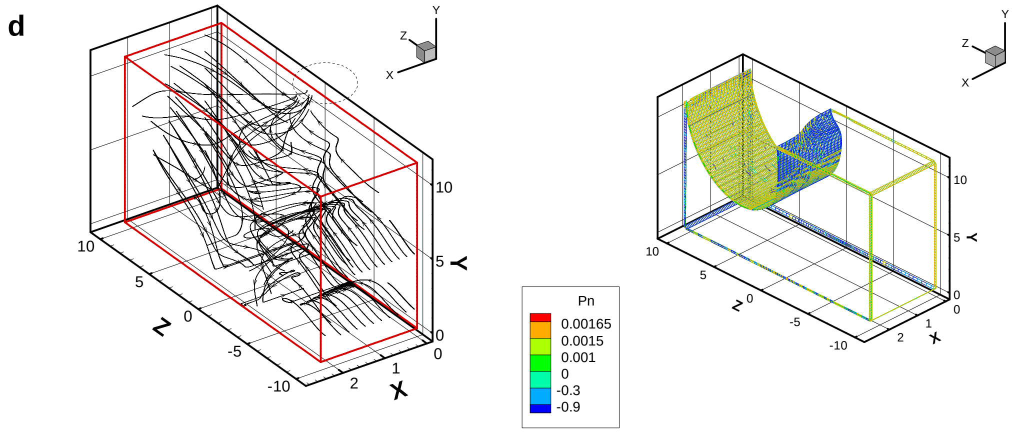

Figure 11. D_i=1,600; h=2,300; U_i=120,000; U_∞=2,200

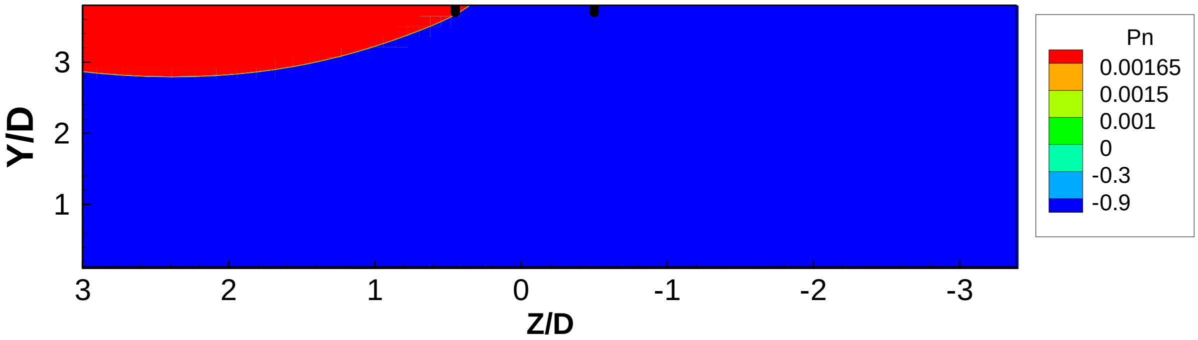

Figure 10. D_i=1,600; h=2,300; U_i=120,000; U_∞=2,200

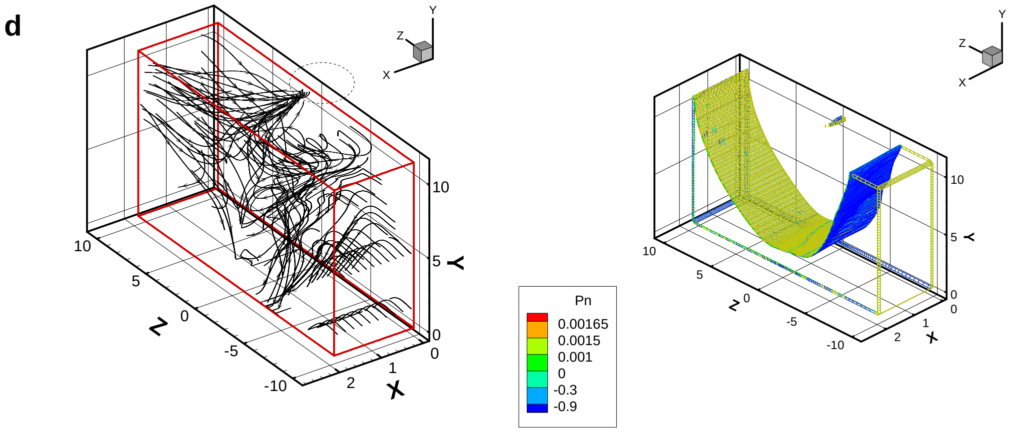

Figure 12. D_i=1,600; h=1,900; U_i=80,000; U_∞=2,200

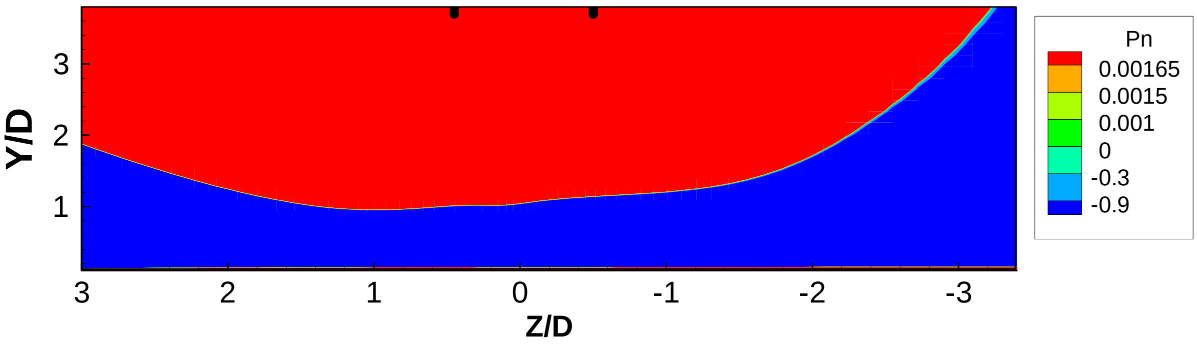

Figure 13. D_i=1,600; h=1,900; U_i=80,000; U_∞=2,200

In figure 14 and 15 it can be seen that the fact of the pressure being lower does not change the behavior of flow the same has seen before (Fig.6 and 7).

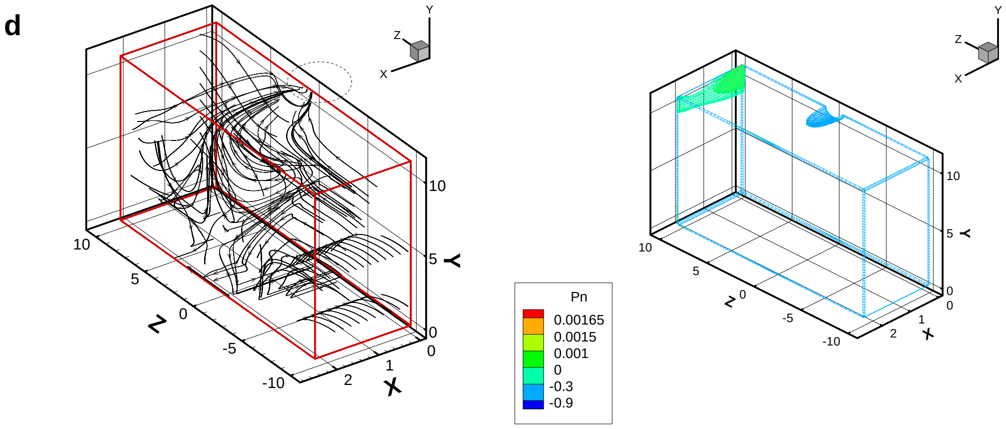

Figure 14. D_i=1,600; h=2,300; U_i=80,000; U_∞=2,200

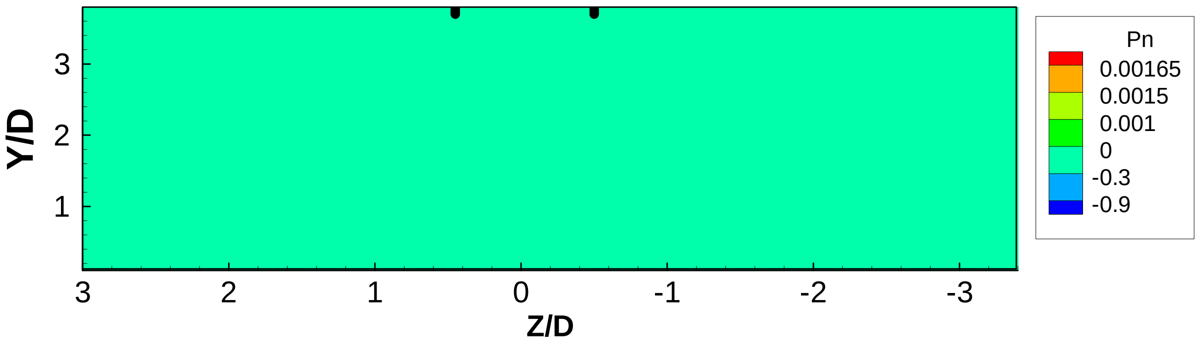

Figure 15. D_i=1,600; h=2,300; U_i=80,000; U_∞=2,200

The next combination has a similar behavior to that showed in figures 8 and 9 but the areas of high and low pressure have changed position (Fig. 16 and 17).

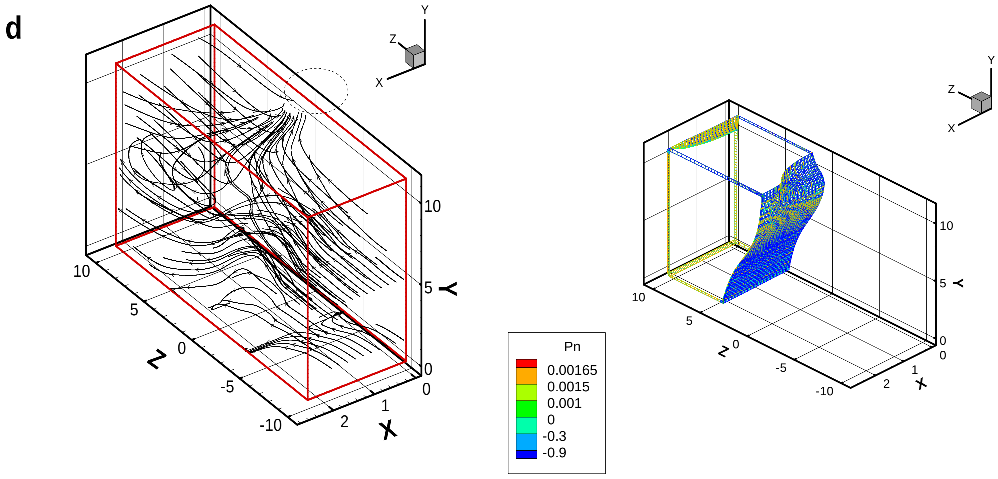

Figure 16. D_i=2,200; h=2,400; U_i=80,000; U_∞=2,200

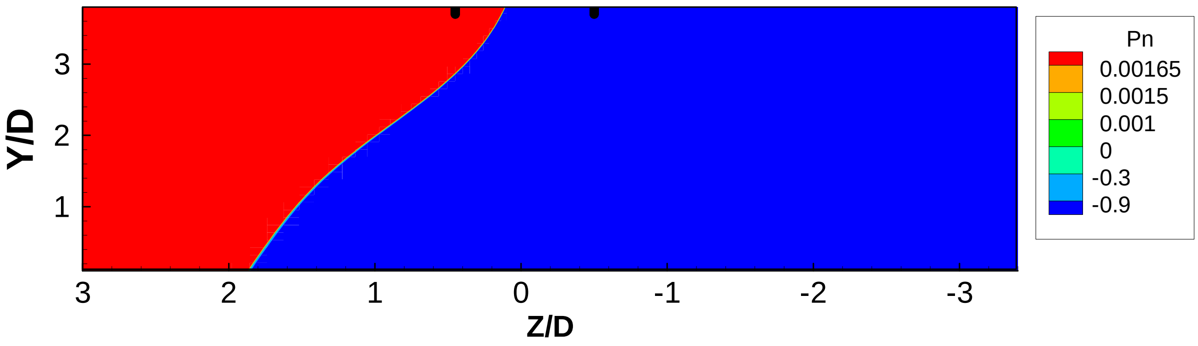

Figure 17. D_i=2,200; h=2,400; U_i=80,000; U_∞=2,200

In figures 18 and 19 we can see the two areas of pressure and the vorticity is present.

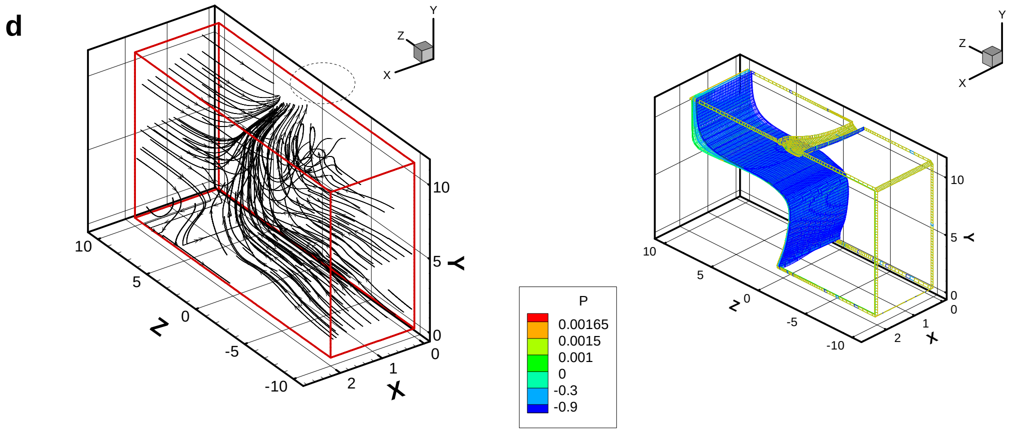

Figure 18. D_i=2,200; h=2,000; U_i=160,000; U_∞=2,200

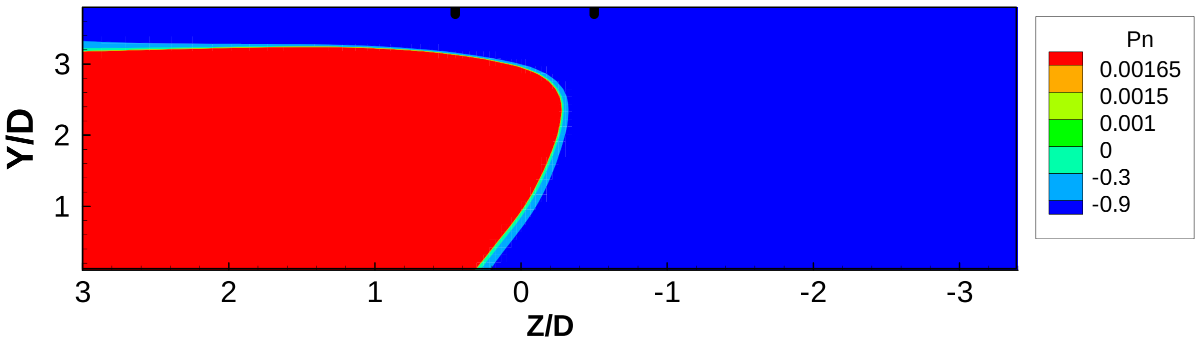

Figure 19. D_i=2,200; h=2,000; U_i=160,000; U_∞=2,200

The next example has the same behavior has the figures 6 and 7 with the obvious difference that the floor is now an high pressure area (Fig. 20 and 21).

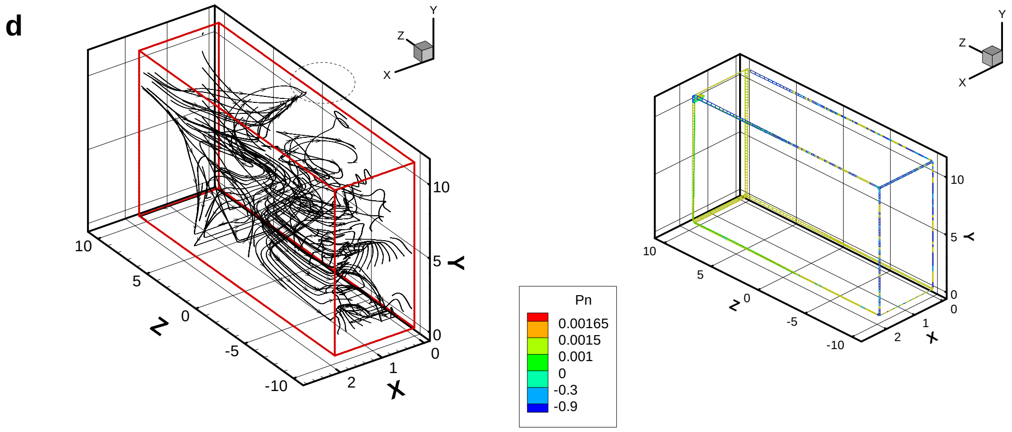

Figure 20. D_i=1,800; h=1,900; U_i=40,000; U_∞=2,200

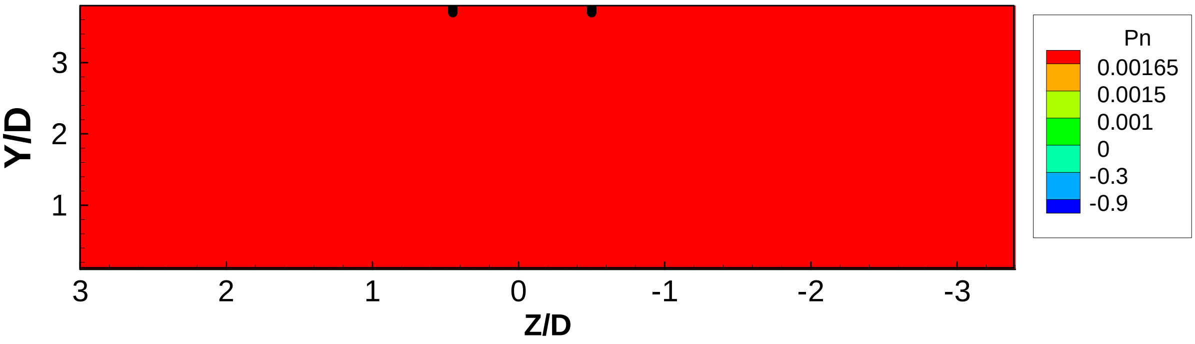

Figure 21. D_i=1,800; h=1,900; U_i=40,000; U_∞=2,200

on the following figures (Fig. 22, 23, 24 and 25) we see that the flow has no pattern and in such a case we have always vorticity present non the flow.

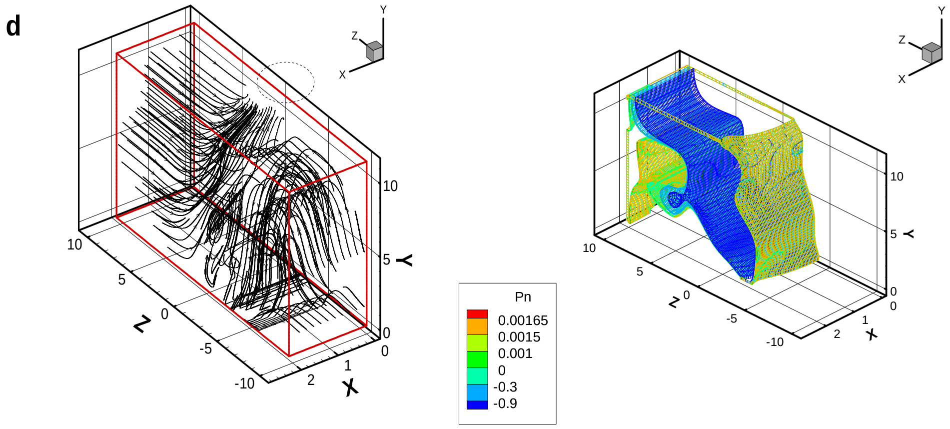

Figure 22. D_i=3,000; h=2,100; U_i=100,000; U_∞=2,200

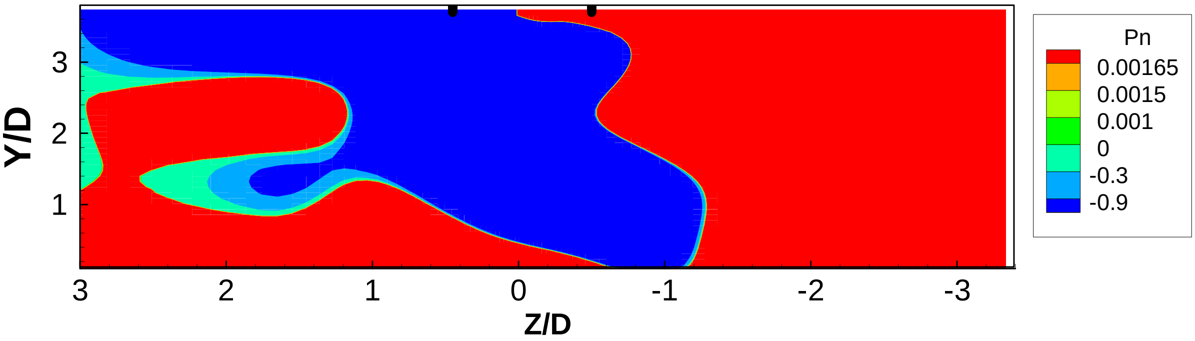

Figure 23. D_i=3,000; h=2,100; U_i=100,000; U_∞=2,200

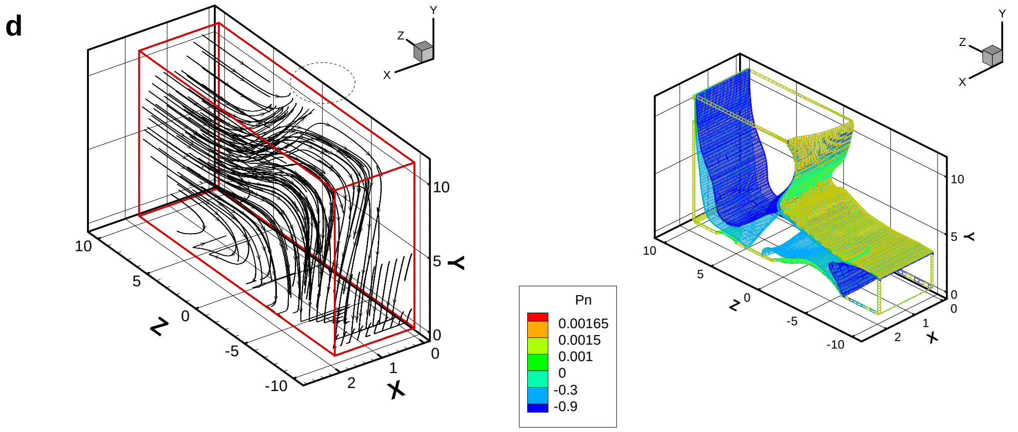

Figure 24. D_i=2,600; h=1,900; U_i=100,000; U_∞=2,200

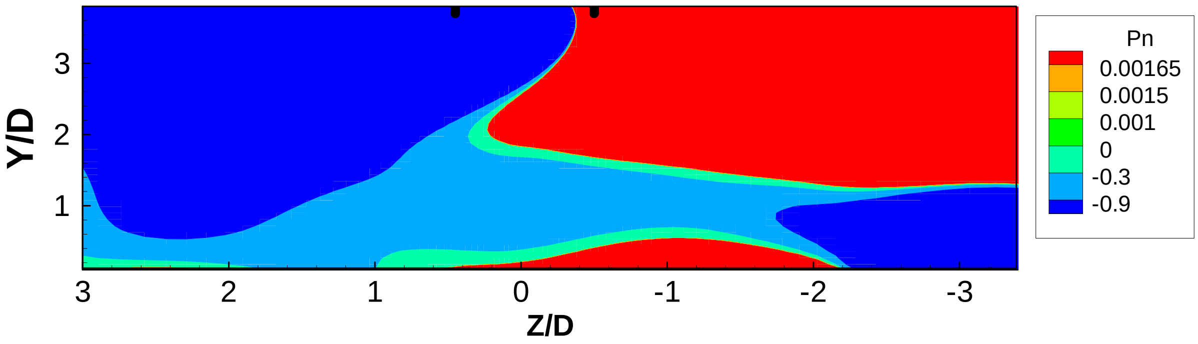

Figure 25. D_i=2,600; h=1,900; U_i=100,000; U_∞=2,200

For the next example we encounter a situation where for basically the same type of pressure pattern there are combinations with vorticity and others with no vorticity.

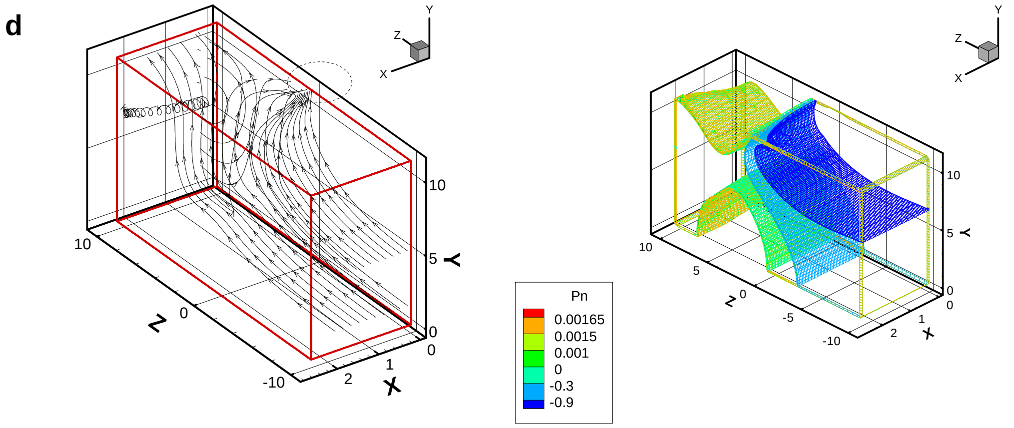

Figure 26. D_i=1,500; h=2,400; U_i=60,000; U_∞=2,200

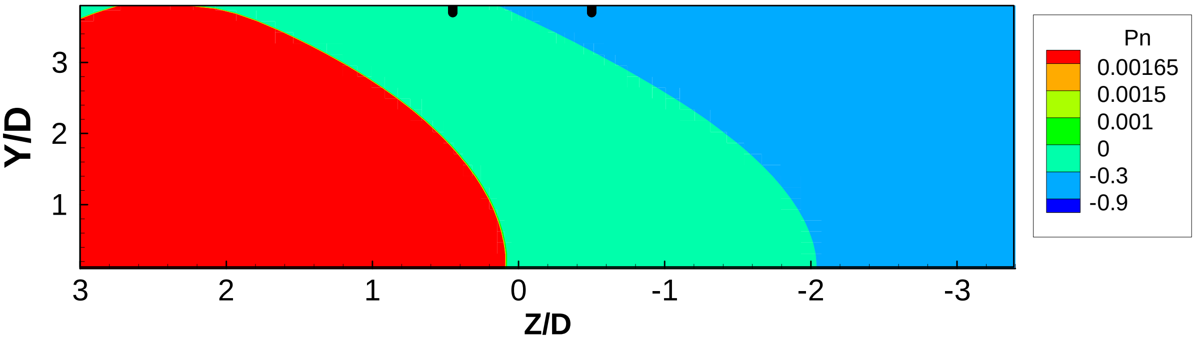

Figure 27. D_i=1,500; h=2,400; U_i=60,000; U_∞=2,200

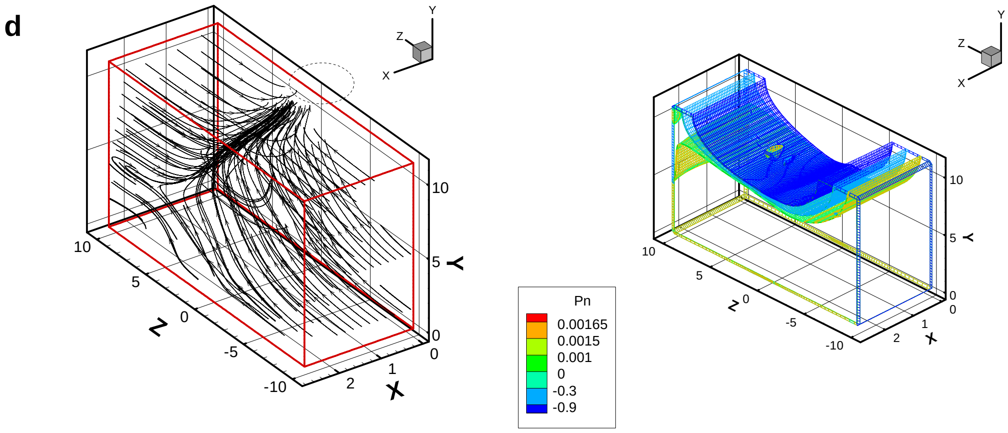

Figure 28. D_i=2,600; h=2,600; U_i=80,000; U_∞=2,200

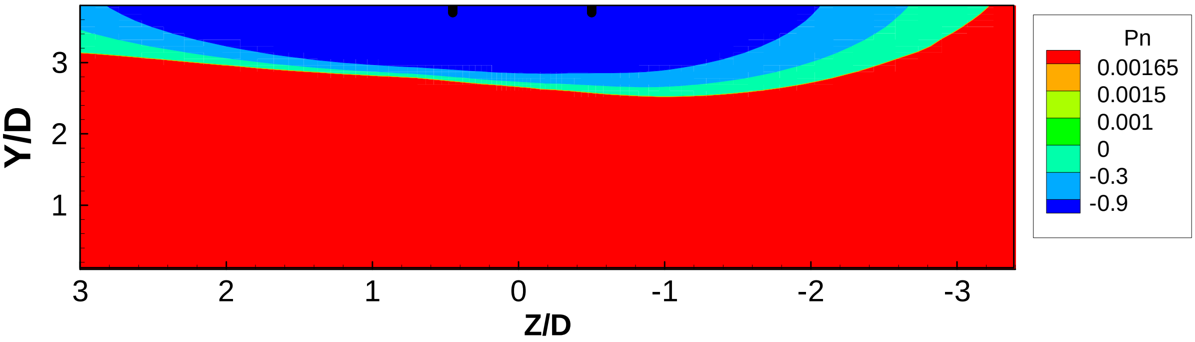

Figure 29. D_i=2,600; h=2,600; U_i=80,000; U_∞=2,200

Now we will show the situations where there is very low vorticity or no vorticity. For our first situation we have figures 30 and 31 where despite the fact of the ground being all a low pressure area there is no vorticity present.

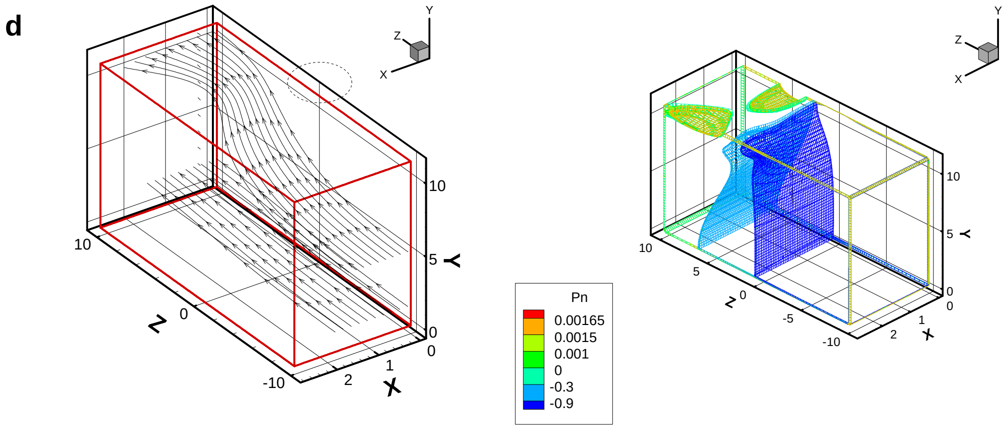

Figure 30. D_i=2,200; h=2,800; U_i=20,000; U_∞=2,200

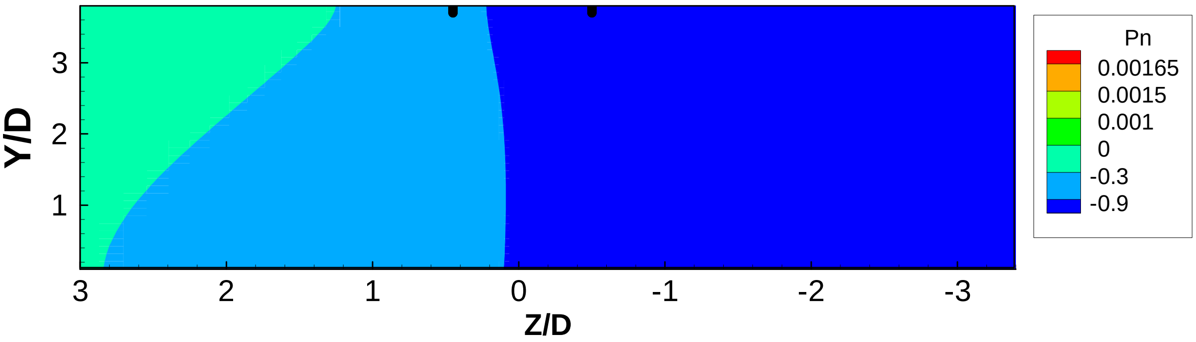

Figure 31. D_i=2,200; h=2,800; U_i=20,000; U_∞=2,200

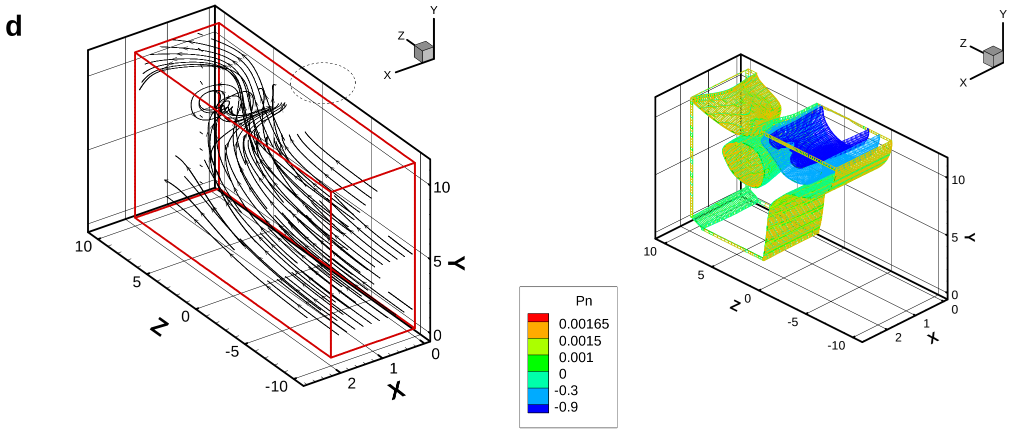

Figure 32. D_i=2,000; h=1,900; U_i=20,000; U_∞=2,200

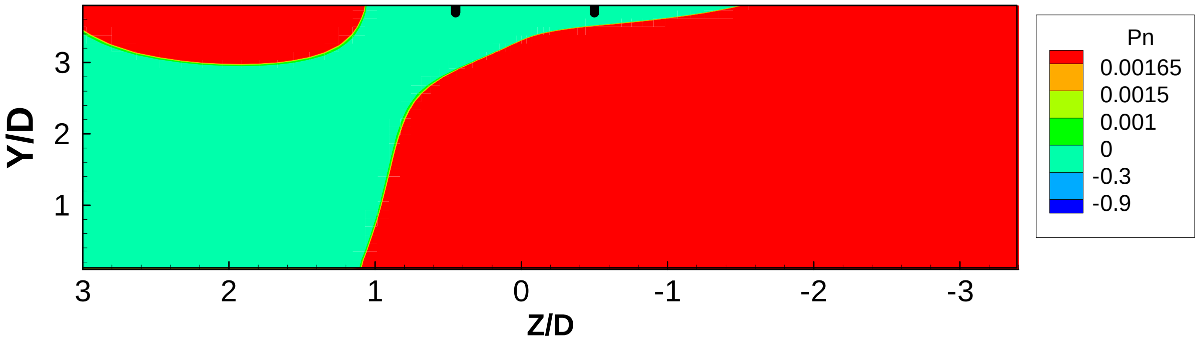

Figure 33. D_i=2,000; h=1,900; U_i=20,000; U_∞=2,200

Regarding the two previous figures (Fig. 32 and 33) in the presence of this type of pattern we never encounter the existence of vorticity on the flow.

The other pattern that we encounter that reveal no existence of vorticity is shown in the figures 34 and 35

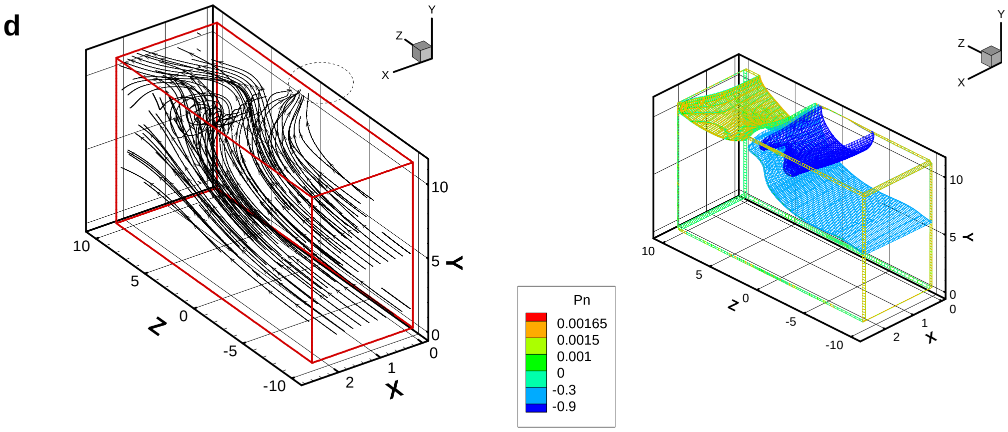

Figure 34. D_i=2,000; h=2,400; U_i=20,000; U_∞=2,200

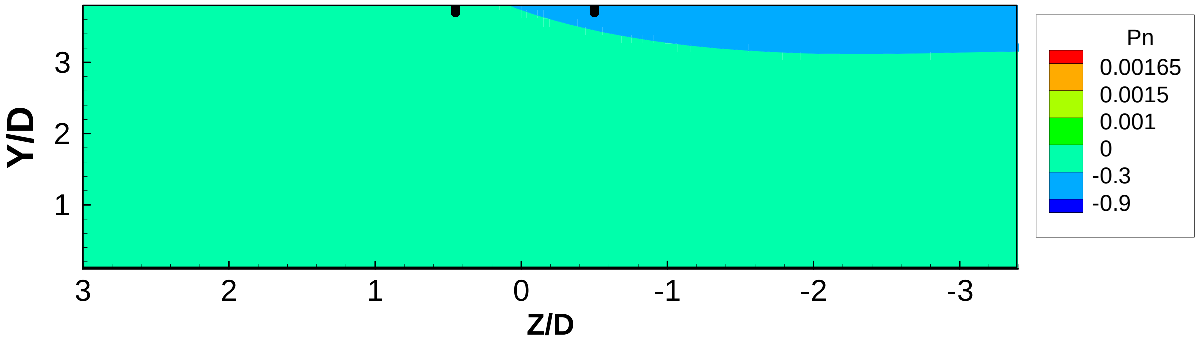

Figure 35. D_i=2,000; h=2,400; U_i=20,000; U_∞=2,200

We also identified another kind of pattern that was only present in the combinations with the highest $\mathbf{D_i}$ and the highest $\mathbf{U_i}$ (Fig.36and 37). This case always presented vorticity.

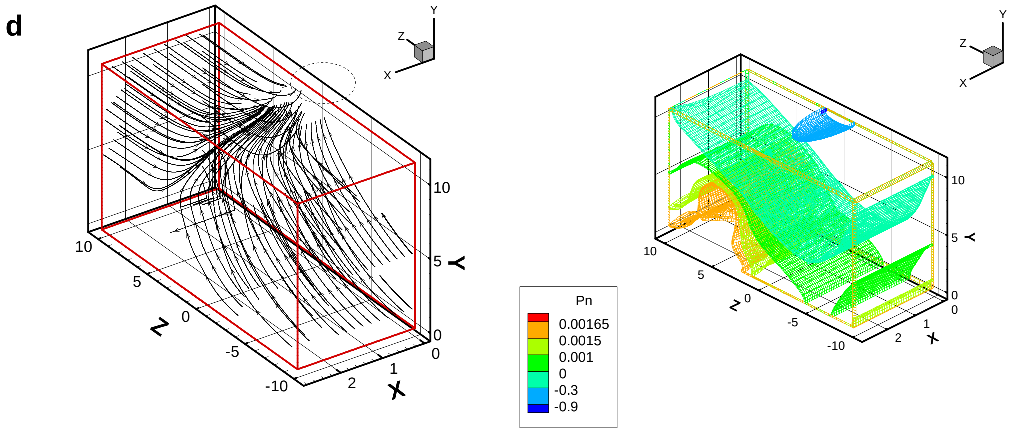

Figure 36. D_i=3,000; h=2,800; U_i=160,000; U_∞=2,200

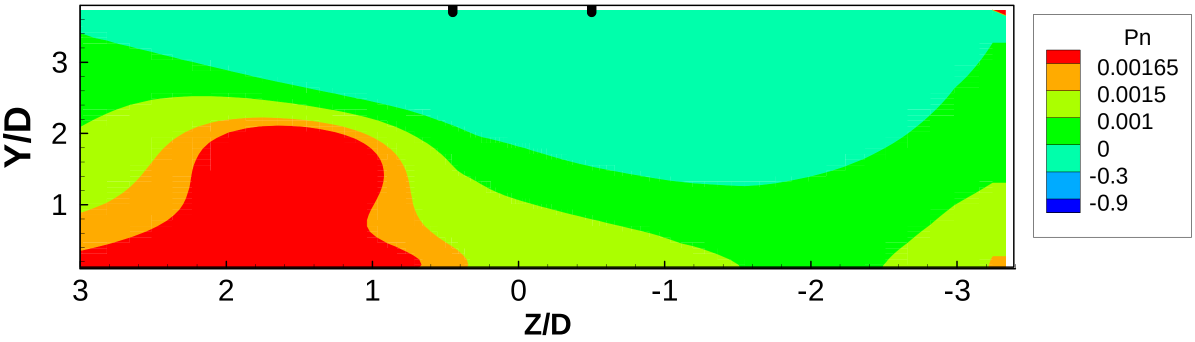

Figure 36. D_i=3,000; h=2,800; U_i=160,000; U_∞=2,200

4 CONCLUSIONS

The present study has shown that is difficult to predict the existence or not of vorticity in the flow be only analyzing the ground pressure.

But it is possible to find some patterns of ground pressure distribution and draw some conclusions.

The first is the presence of small low pressure areas that indicate the presence of a vortex.

When the ground is all a low or high pressure area then vorticity is always present the same happens when there is an area of high near the inlet surrounded by a lower pressure area.

In some cases is possible to determine the presence of by seeing the iso surfaces in 3D graphic.

We can also conclude that when the pressure is low but gradually rises in the direction of the crosswind then no vorticity is verified.

ACKNOWLEDGEMENTS

The authors express their gratitude to FCT for the funding of the research project.

The present work has been performed in the scope of the activities of the Aeronautics and Astronautics Research Center – AeroG of the University of Beira Interior, Covilhã, Portugal.

REFERENCES

[1] Hünecke, K. “Jet Engines: Fundamental of theory, design and operation”, Airlife publishing, UK, 1997.
[2] Mattingly, J.D., Heiser, W.H., Daley, D.H. “Aircraft Engine Design”, AIAA Education Series, New York, 1987.
[3] 3Mattingly, J.D. “Elements of Gas Turbine Propulsion”, Singapore: McGraw-Hill, 1996.
[4] 4Johns, C. “The Aircraft Engine Inlet Vortex Problem”, AIAA’s Aircraft Technology, Integrations and Operations (ATIO) 2002 Technical, 1-3rd 2002, Los Angles, California, AIAA Paper 2002-5894.
[5] 5Swainston, M. “Vortex Formation Near Intakes to Turbomachinery and Duct Systems”, Heat and Fluid Flow, Vol. 4, No. 2, 1974.
[6] 6Nakayama, A. & Jones, J. “Correlation for Formation of Inlet Formation”, AIAA Journal, Vol. 37, No. 4: Technical Notes, 1998.
[7] Motycka, D. & Walter, W. “An Experimental Investigation of Ground Vortex Formation During Reverse Thrust Operation”, AIAA Paper No. 75/1322, AIAA/SAE 11th Propulsion Conference, 1975

[8] Brix, S., Neuwerth, G. & Jacob, D. “The Inlet-Vortex System of Jet Engines Operating Near the Ground”, AIAA Paper 2000-3998, 2000

[9] De Siervi, F., Viguier, H., Greitzer, E. & Tan, C. “Mechanisms of Inlet Vortex Formation”, J. Fluid Mech., Vol. 124, pp. 173-207, 1982

[10] Nakayama, A. & Jones, J. “Correlation for Formation of Inlet Formation”, AIAA Journal, Vol. 37, No. 4: Technical Notes, 1998.

[11] Barata, J. M. M., Maneta, A.M., Silva, A.R.R. “ Numerical Study of Single Impinging Jets Through a Crossflow”, AIAA Paper no. 2009-4801, 45th AIAA/ASME/SAE/ASEE Joint propulsion Conference & Exhibit, Denver, CO, 2-5 Aug., 2009.

[12] Barata, J. M. M., Manquinho, P.A., Silva, A.R.R. “A Comparison of Different Gas Turbine Engines Ground Vortex Flows”, AIAA Paper no. 2010-7116, 46th AIAA/ASME/SAE/ASEE Joint propulsion Conference & Exhibit, Nashville, TN, 25-28 July, 2010.

[13] Barata, J. M. M., Manquinho, P.A., Silva, A.R.R. “Identification of Gas Turbine Ground Vortex Formation Regimes”, AIAA Paper no. 2012-0600, 50th AIAA Aerospace Sciences Meeting, Nashville, TN, 09-12 Jan., 2012.

AIAA Science and Technology Forum and Exposition (SciTech 2015)
Kissimmee, Florida 5 - 9 Jan 2015
AIAA 2015-1668

Pressure Based Comparison of Different Gas Turbine Ground Vortex Flows

Jorge M. M. Barata[1], Pedro Manquinho[2] and André R. R. Silva[3]
Universidade da Beira Interior, Covilhã, 6201-1, Portugal

Abstract

The present paper has the previous work of Barata et al in mind and has the purpose of analyzing the behavior of ground vortex flows through several values of height of the engine axis above the ground, diameter of engine intake and inlet airflow velocity using pressure on the ground and in a 3D scale for that.

Nomenclature

A_i = intake area
A_∞ = frequency of oscillation of the ground vortex
D_i = inner diameter of the intake
r = inner radius of the engine
h = height of the engine axis above the ground
$\boldsymbol{k}$ = turbulent kinetic energy
L_q = intake stream tube length
$\dot{m}$ = mass flow
U_i = intake throat velocity
U_∞ = free stream velocity
V_∞ = tangential velocity
Γ = Vortex circulation
ζ = Vorticity
ρ = Density
μ = dynamic viscosity
ν = kinematic viscosity
ν_T = turbulent kinematic viscosity
ϕ = any dependent variable

Introduction

The inlet is designed to give the appropriate amount of airflow required with minimal pressure loss by the engine. If the pressure losses and the flow distortions are very low, the performance of the engine is optimal. This airflow condition is necessary in all flight configurations including when the aircraft is maneuvering on the ground. The performance of the intake depends on the mass-flow delivered to the compressor. The internal mass-flow stays constant and assuming that the flow is incompressible due to low speed velocities, it will be given by $A_i U_i = A_\infty U_\infty$. Since the mass-flow is constant and the area ratio is related to the stream tube contraction ratio, the area ratio can be expressed as $\frac{A_\infty}{A_i} = \left(\frac{L_q}{D_i}\right)^2$. The capture ratio A_∞ / A_i is controlled by the engine, the engine mass-flow, the inlet diameter and the free-stream velocity. The area called the intake captured area is defined by the boundary between the air that enters in the engine and the air that does not. The flow ratio and the stream-tube shape vary with the operation conditions of the aircraft engine. In near static configuration, the engine must accelerate the air using maximum thrust since the ambient air is at rest. The extreme local acceleration of the flow at the inlet lip can cause airflow separation in this region[2,3]. The shape of the stream tube is modified near the lip in cross-wind

---

[1] Full Professor, Aerospace Sciences Department, Associate Fellow of AIAA.
[2] PhDEng Student, Aerospace Sciences Department, Rua Marques Avila e Bolama.
[3] Assistant Professor, Aerospace Sciences Department, AIAA Member.

configuration,. The cross-flow causes an increase in the flow velocity near the lip depending on the strength of the cross-flow, high velocity origins in flow separation leading to a total pressure loss at the engine fan.

The formation of ground vortices depends on engine power, wind velocity and engine inlet height and size. Previous published work show that the phenomenon can only occur with the presence of a stagnation streamline between the ground and the intake which is dependent on the velocity ratio U_i / U_∞ and the non-dimensional height of the engine axis above the ground, h/D_i (Fig. 1). In static conditions, the inlet airflow demand increases, and the inlet capture surface increases in diameter and starts including the ground to bring the necessary airflow to the fan[4,5]. The typical formation of ground vortices is defined by low h/D_i and high U_i / U_∞ and that is the same has saying the engine is operating close to the ground at a high inlet mass flow[6]. Hence, the mechanism of intake formation is strongly dependent of the height of the engine axis above the ground, the velocity ratio and the presence of an upstream velocity.

Four different types of conditions leading to the formation of inlet ground vortices have been identified. A vortex can be generated without ambient wind and with a low ratio h/D_i (typically less than one). Due to the ground proximity, high levels of suction beneath the engine inlet leads into a strong flow underneath the inlet upstream towards the intake lip[7]. In these conditions, it is possible to visualize at the engine intake and at the ground two upward spiraling vortices. Under no-wind condition, it appears that the two vortices are counter-rotating, and the vorticity is induced by the boundary layer. Is a head-wind flow, when the air is sucked into the engine inlet, the flow field underneath the intake starts to roll up into two upright counter-rotating vortices and a fast flow into the opposite direction of the wind appears between them[8,9]. For high velocity ratios (>20) the sense of rotation of the two vortices switches to the same as in the no-wind mechanism. With a 90° cross-wind two different kinds of vortices appear around the intake: an inlet vortex and a trailing vortex (Fig.2). When the engine intake is oriented at a 90° yaw angle and with the presence of cross-wind with far upstream vertical vorticity, there is the formation of a single vortex inside the intake. In this case the sense of rotation of the vortex is opposite to the ambient vorticity. Other mechanisms of formation also exist and can be considered as combinations of the previous ones that lead to a large number of possible combinations that are responsible for the need of more studies in order to understand all the physics involved.

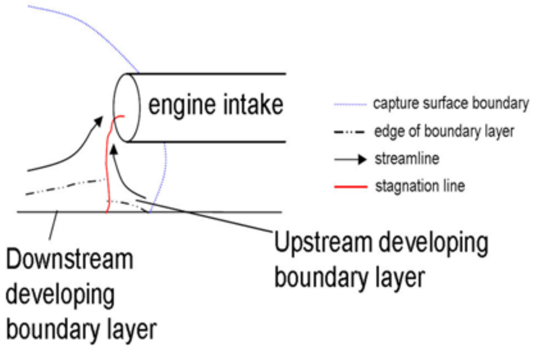

Figure 1. Ground vortex formation.

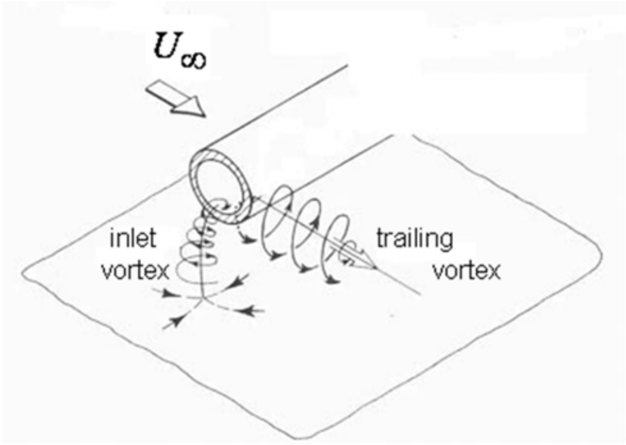

Figure 2. Sense of rotation of the inlet vortex and the trailing vortex (sketch adapted from Ref. 9).

CFD tools have been applied recently to the understanding of the ground vortex with relative success. Nakayama & Jones[10] used panel methods to simulate the inlet and ground interaction, noting that the wind speed needed to blow the vortex away was lower than the measured experimentally. Barata et al.[11] report Navier-Stokes calculations and predicted successfully the ground vortex phenomena using real operational conditions for the case of the engine Trent 9 and GE nx-1B64. The ground vortex formation in irrotational crosswind flow is analyzed in detail for this configuration, and the formation of the trailing vortex was associated to a very complex flow. In the present paper the work of Barata et al.[11, 12, 13] is extended to 572 simulations for different values of inlet diameter, height of the engine axis above the ground and inlet velocity (Table 1). The ground vortex flows produced by the different engine-velocity ratio-clearance distance combination are compared and discussed using pressure has base of comparison. The results have shown that is very difficult to analyze in most cases ground vortex flows using only pressure so we used two-dimensional velocity vectors in the vertical and horizontal planes to determine the existence of vorticity and then draw our conclusions for the pressure. In some cases it was easy to determine the existence of vorticity (Fig. 3).

Table 1. Values tested.

r (m)	D_i (m)	h (m)	U_i (m/s)	U_∞ (m/s)
1,5000	3,0000	2,8000	160,0000	2,2000
1,4000	2,8000	2,6000	140,0000	
1,3000	2,6000	2,4000	120,0000	
1,2000	2,4000	2,3000	100,0000	
1,1000	2,2000	2,2000	80,0000	
1,0000	2,0000	2,1000	60,0000	
0,9000	1,8000	2,0000	40,0000	
0,8000	1,6000	1,9000	20,0000	
0,7500	1,5000			

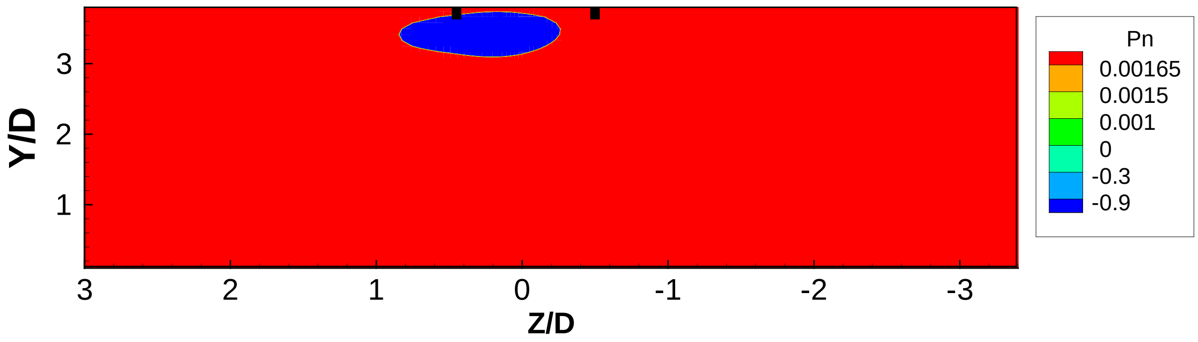

Figure 3. Two-dimensional pressure contours in the horizontal plane parallel to the ground. (D_i=2,800; h=1,900; U_i=160,000; U_∞=2,200)

Mathematical Model

The mathematical model used in the present study is described in detail in Ref. 11 and only the main features will be summarized here. The time averaged partial differential equations governing the steady, uniform-density isothermal three-dimensional flow

$$\rho\overline{U}_j\frac{\partial\overline{U}_i}{\partial X_j}=-\frac{\partial\overline{P}}{\partial X_i}+\frac{\partial}{\partial X_j}\left(\mu\frac{\partial\overline{U}_i}{\partial X_j}-\rho\overline{u'_i u'_j}\right) \quad (1)$$

and the continuity equation,

$$\rho\overline{U}_j\frac{\partial\overline{U}_i}{\partial X_i}=0 \quad (2)$$

where solved together with the equations of transport of the turbulent kinetic energy and dissipation rate of the two-equation "*k*-ε" model[10]

$$\overline{U}_j\frac{\partial k}{\partial X_j}=\frac{\partial}{\partial X_j}\left(\frac{\upsilon_T}{\sigma_k}\frac{\partial k}{\partial X_j}\right)-\overline{u'_i u'_j}\frac{\partial\overline{U}_i}{\partial X_j}-\varepsilon \quad (5)$$

$$\overline{U}_j\frac{\partial\varepsilon}{\partial X_j}=\frac{\partial}{\partial X_j}\left(\frac{\upsilon_T}{\sigma_\varepsilon}\frac{\partial\varepsilon}{\partial X_j}\right)-C_1\frac{\varepsilon}{k}\overline{u'_i u'_j}\frac{\partial\overline{U}_i}{\partial X_j}-C_2\frac{\varepsilon^2}{k} \quad (6)$$

where C_1 and C_2 are additional dimensionless model constants, and σ_k and σ_ε are the turbulent Prandtl numbers for kinetic energy and turbulent dissipation.

The Reynolds stresses are expressed as

$$\overline{u'_i u'_j}=-\upsilon_T\left(\frac{\partial\overline{U}_i}{\partial X_j}+\frac{\partial\overline{U}_j}{\partial X_i}\right)+\frac{2}{3}k\delta_{ij} \quad (3)$$

where υ_T is the turbulence kinematic viscosity, which is derived from the turbulence model and expressed by $C_\mu k^2/\varepsilon$.

The solution of the governing equations was obtained using a quadratic finite-difference method that used discretized algebraic equations deduced from the exact differential equations that they represent.

The solution procedure is based on the SIMPLE algorithm widely used and reported in the literature. It uses the staggered grid arrangement and a guess and correct procedure field such that the solution of the momentum equations satisfies continuity.

The computational domain has six boundaries where dependent values are specified: a free stream plane, a symmetry plane, and a solid wall. On the symmetry plane, the normal velocity vanishes, and the normal derivates of the other variables are zero. At the solid surface, the wall function method is used to prescribe the boundary conditions for the velocity and turbulence quantities, assuming that the turbulence is in state of local equilibrium. The free stream plane is located at *Z*=0 and corresponds to the crossflow conditions. The engine intake boundary is represented by a right angled polygon and the mass flow rates and the momentum are matched to the experimental values.

The intake represents a 1/1th scale model with a diameter that corresponds to each particular engine. The axis of the engine is located at a distance above the ground (h), which corresponds to the specific clearance distance.

All the tests were performed for the case of irrotational crosswind, and the other conditions are shown in Table 1. The domain of solution, their dimensions and the system of axes are represented in Fig.4

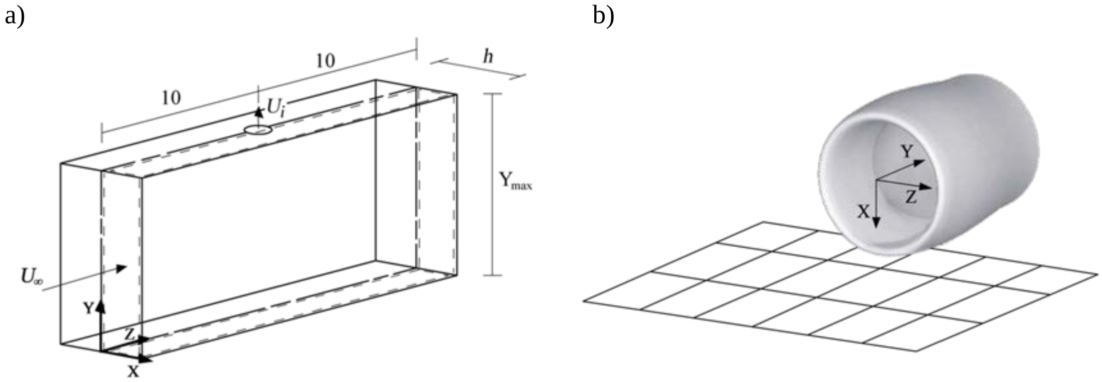

Figure 4. Domain of the solution a). Representation of the intake with referential at the center b).

Results

The ground vortex formation in irrotational crosswind flow is the only mode analyzed in the present paper. In this configuration the ground vortex or inlet vortex that forms near the ground and is sucked by engine is accompanied by an additional feature which is the formation of the trailing vortex (see Fig. 2).
In this section we analyze the various types of pressure distribution for the different velocity ratio-clearance distance combination.

We have types of pressure distribution that always have vorticity for all the cases analyzed others that do not have any or almost any vorticity and cases where the existence of vorticity varies in different combinations.

When the floor is all a low pressure area there is always vorticity present in the flow (Fig. 4 and Fig 55).

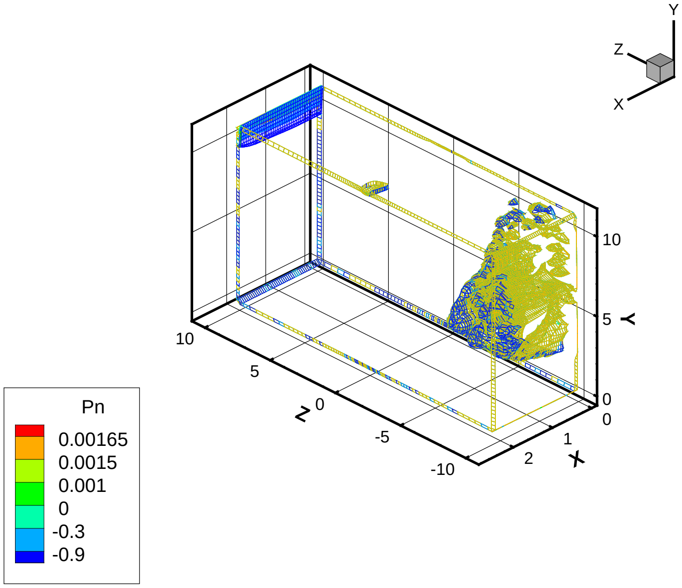

Figure 4. D_i=2,800; h=2,100; U_i=160,000; U_∞=2,200

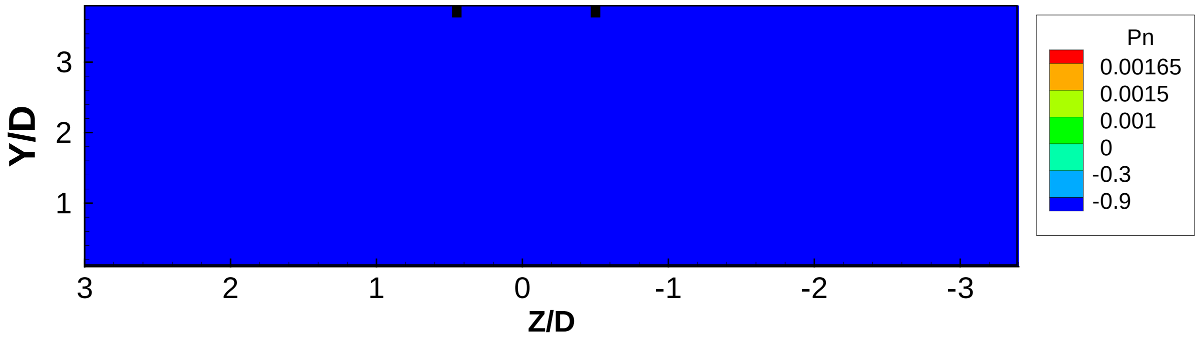

Figure 5. D_i=2,800; h=2,100; U_i=160,000; U_∞=2,200

It is perfectly visible in Fig. 4 an area of vorticity in the flow. All the cases equal or must alike figures 4 and 5 may have vorticity be visible in 3D grafic or not. An exemple of that is Fig. 6 and 7 where nothing is visible but there is vorticity present.

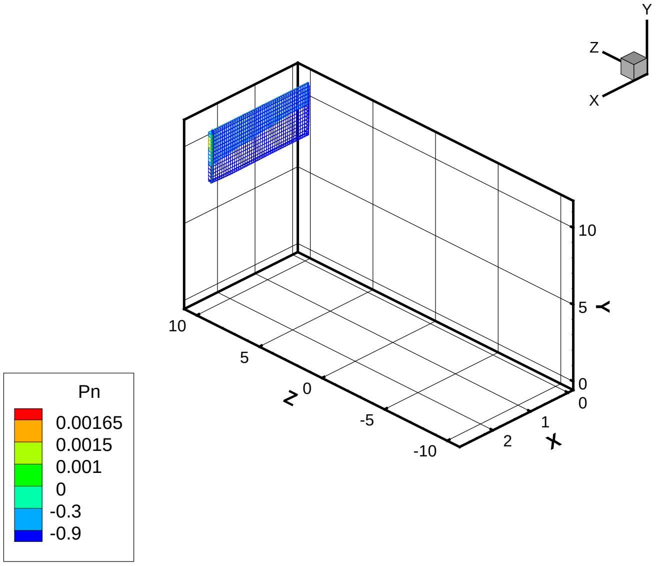

Figure 6. D_i=2,600; h=2,600; U_i=160,000; U_∞=2,200

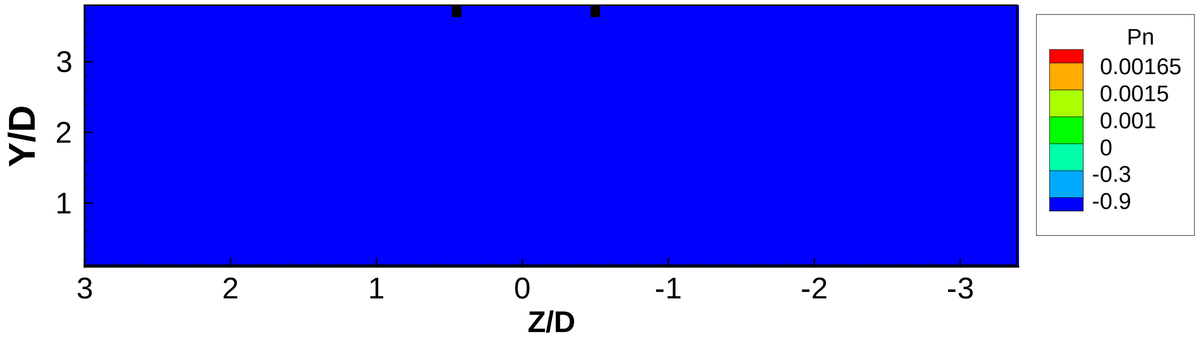

Figure 7. D_i=2,600; h=2,600; U_i=160,000; U_∞=2,200

Still in the same group that always have vorticity we find a case that has two different areas of pressure one high and very low separated be a plane almost perpendicular to the plane of the inlet (Fig. 8 and Fig. 9)

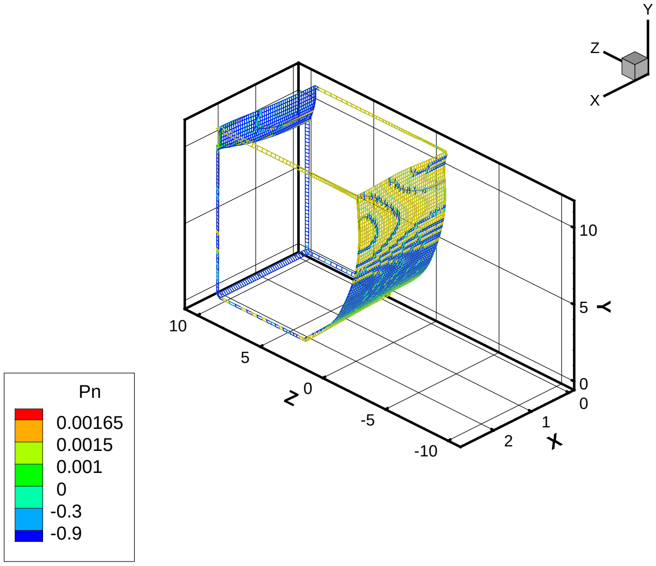

Figure 8. D_i=1,800; h=2,400; U_i=100,000; U_∞=2,200

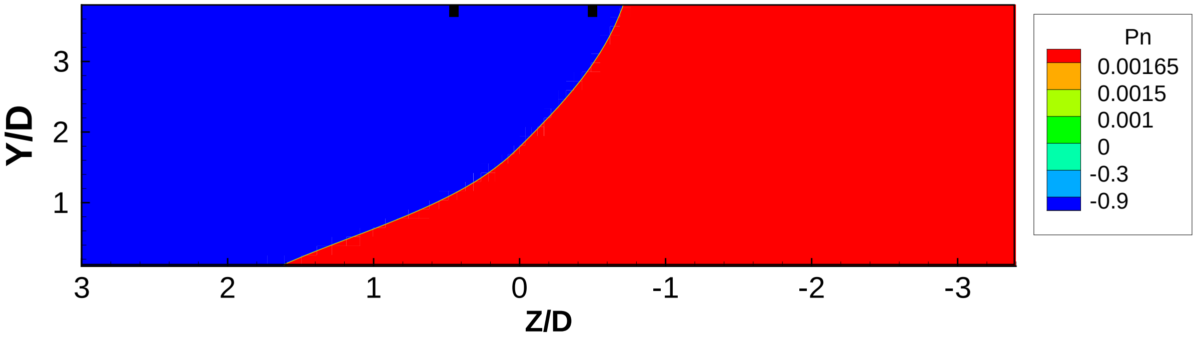

Figure 9. D_i=1,800; h=2,400; U_i=100,000; U_∞=2,200

In next cases there is a high pressure area near the inlet and a low pressure area surrounding it (Fig. 10, 11, 12 and 13).

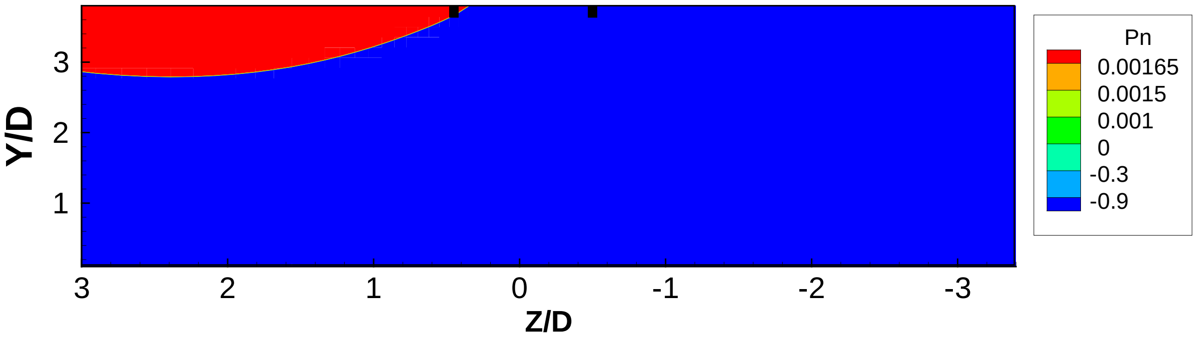

Figure 10. D_i=1,600; h=2,300; U_i=120,000; U_∞=2,200

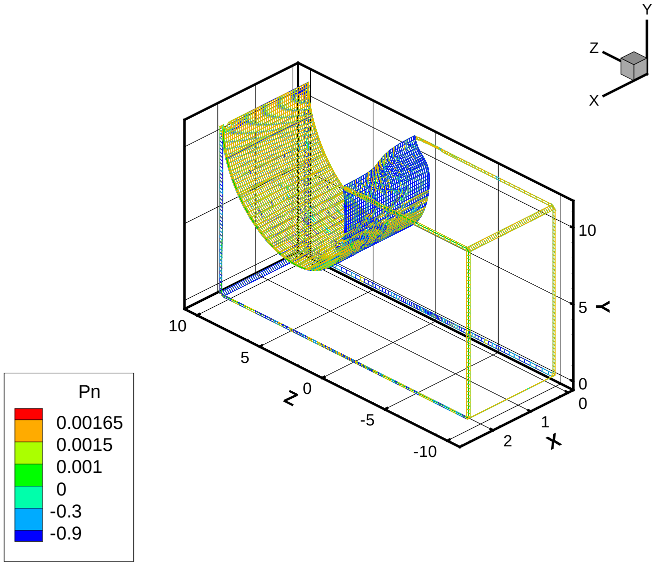

Figure 11. $D_i=1{,}600$; $h=2{,}300$; $U_i=120{,}000$; $U_\infty=2{,}200$

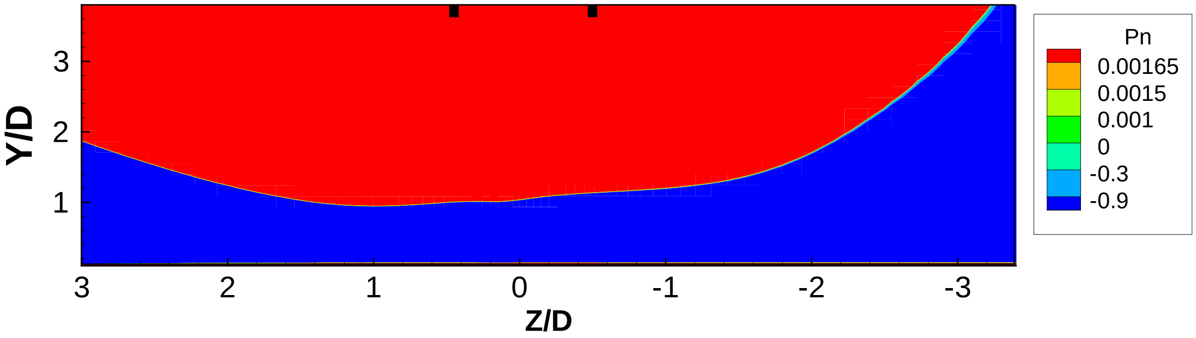

Figure 12. $D_i=1{,}600$; $h=2{,}400$; $U_i=80{,}000$; $U_\infty=2{,}200$

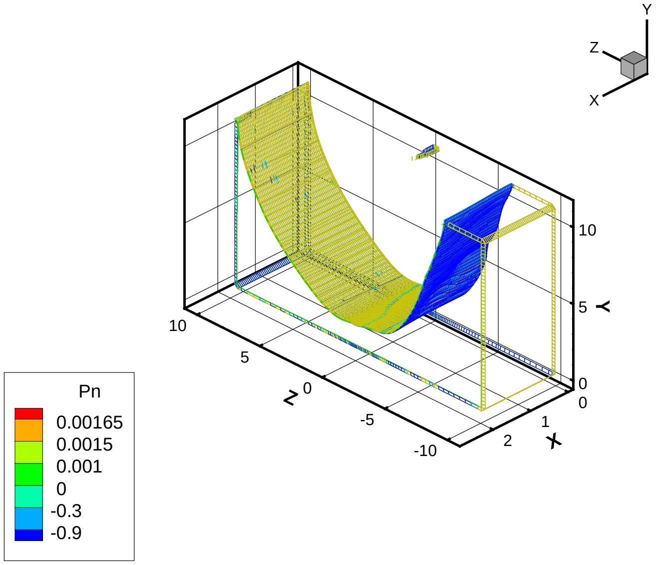

Figure 13. $D_i=1{,}600$; $h=2{,}400$; $U_i=80{,}000$; $U_\infty=2{,}200$

In figure 14 and 15 it can be seen that the fact of the pressure being lower does not change the behavior of flow the same has seen before (Fig.6 and 7).

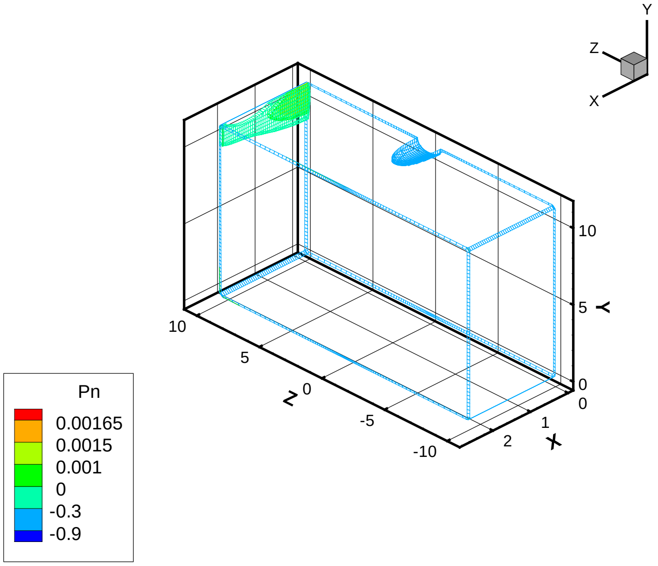

Figure 14. D_i=1,600; h=2,300; U_i=80,000; U_∞=2,200

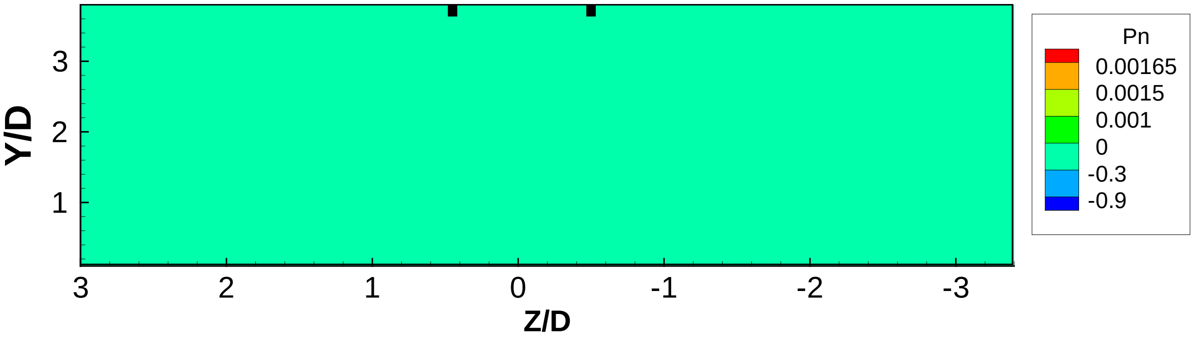

Figure 15. D_i=1,600; h=2,300; U_i=80,000; U_∞=2,200

The next combination has a similar behavior to that showed in figures 8 and 9 but the areas of high and low pressure have changed position (Fig. 16 and 17).

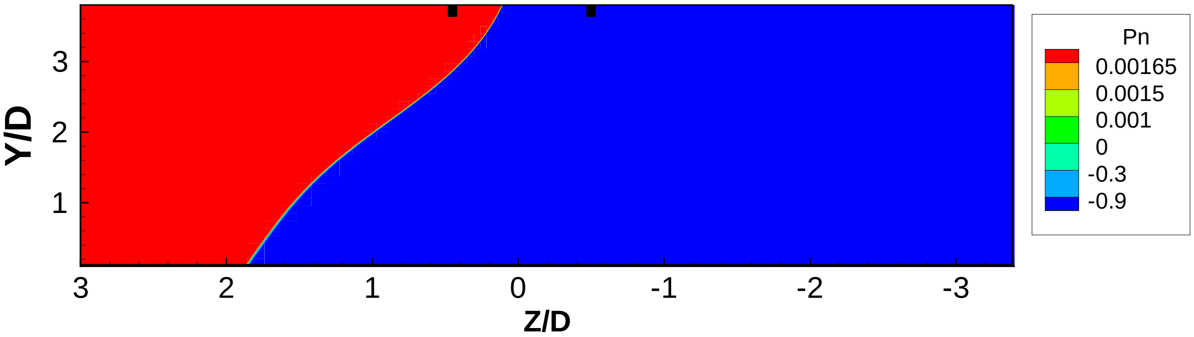

Figure 16. D_i=2,200; h=2,400; U_i=80,000; U_∞=2,200

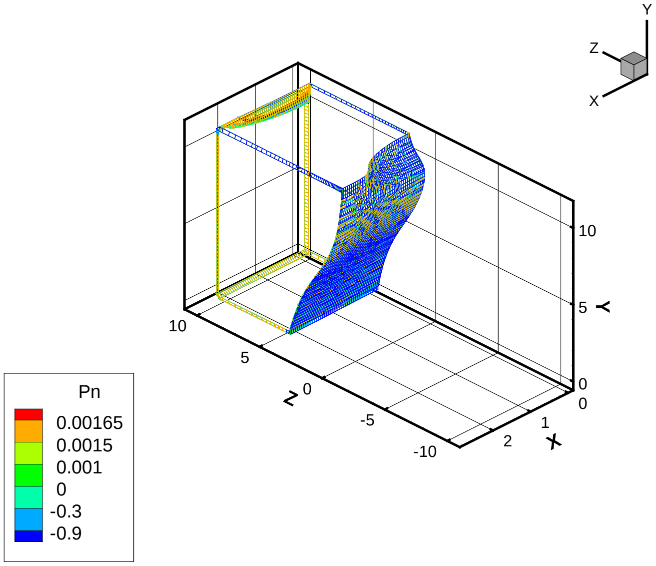

Figure 17. D_i=2,200; h=2,400; U_i=80,000; U_∞=2,200

In figures 18 and 19 we can see the two areas of pressure and the vorticity is present.

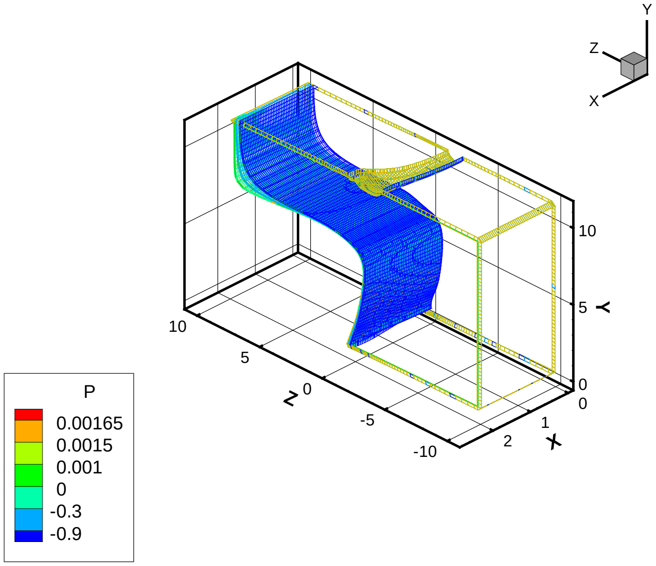

Figure 18. D_i=2,200; h=2,000; U_i=160,000; U_∞=2,200

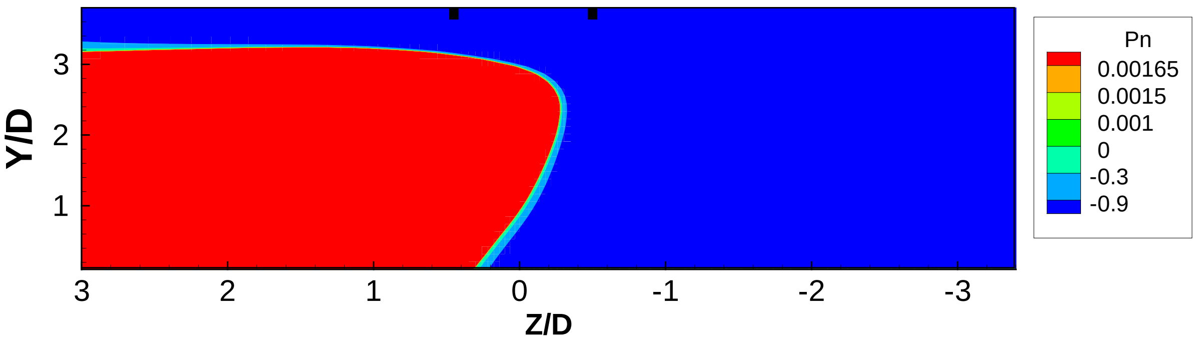

Figure 19. D_i=2,200; h=2,000; U_i=160,000; U_∞=2,200

The next example has the same behavior has the figures 6 and 7 with the obvious difference that the floor is now an high pressure area (Fig. 20 and 21).

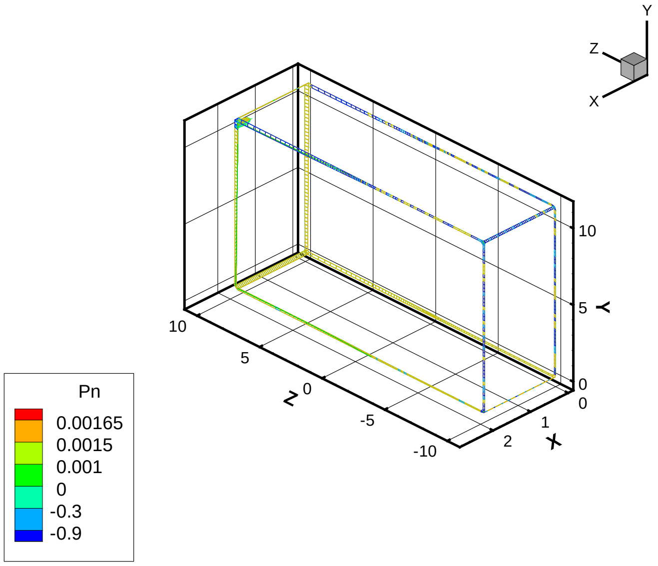

Figure 20. D_i=1,800; h=1,900; U_i=40,000; U_∞=2,200

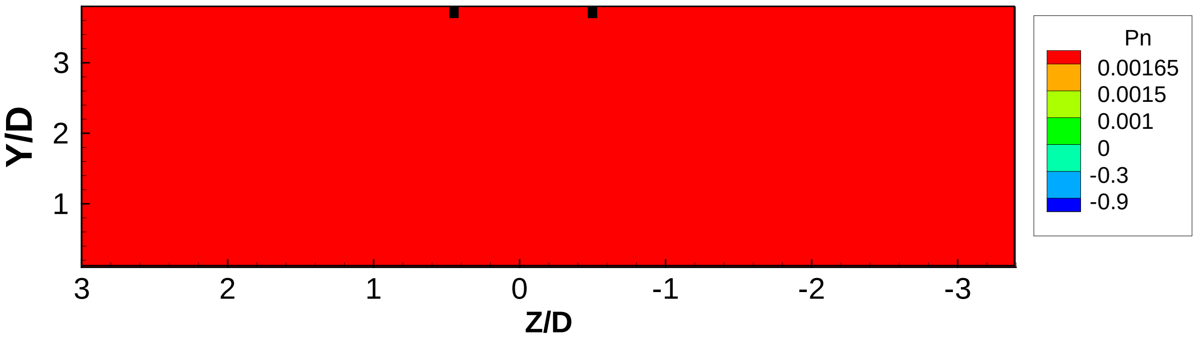

Figure 21. D_i=1,800; h=1,900; U_i=40,000; U_∞=2,200

on the following figures (Fig. 22, 23, 24 and 25) we see that the flow has no pattern and in such a case we have always vorticity present non the flow.

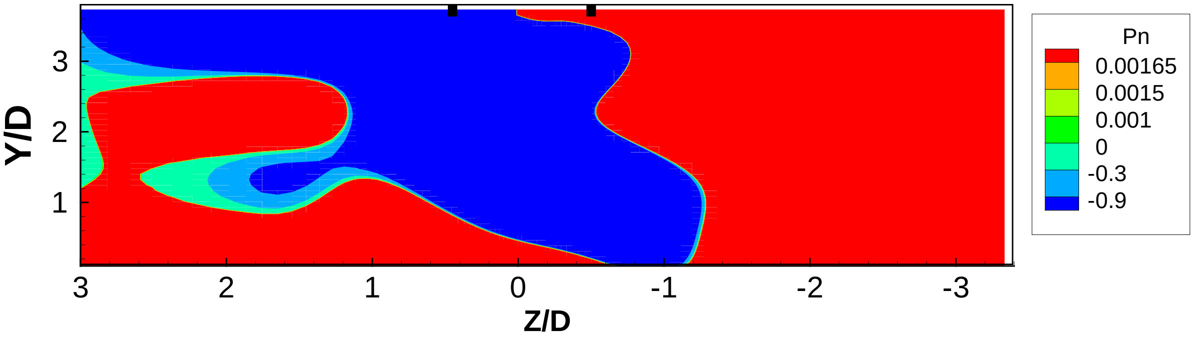

Figure 22. D_i=3,000; h=2,100; U_i=100,000; U_∞=2,200

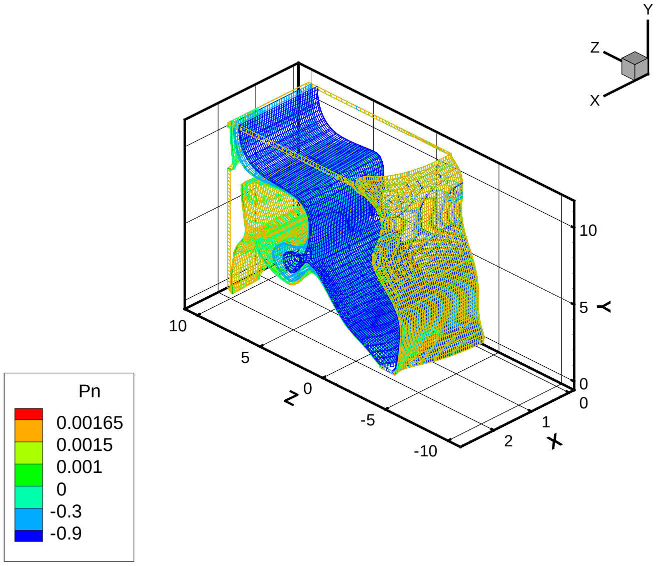

Figure 23. D_i=3,000; h=2,100; U_i=100,000; U_∞=2,200

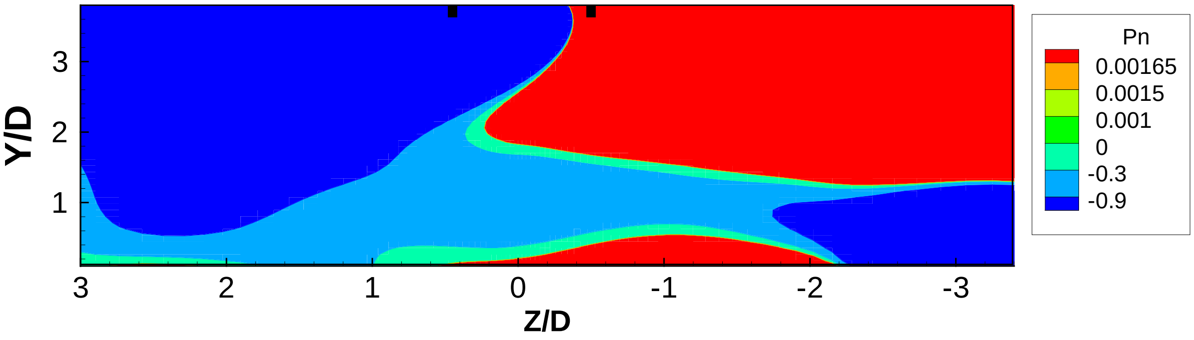

Figure 24. D_i=2,600; h=1,900; U_i=100,000; U_∞=2,200

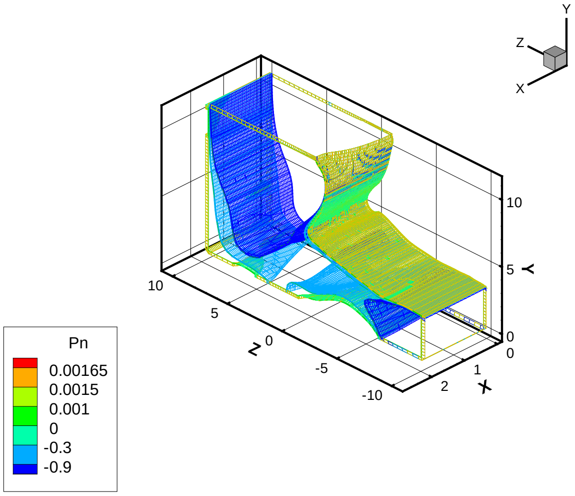

Figure 25. D_i=2,600; h=1,900; U_i=100,000; U_∞=2,200

For the next example we encounter a situation where for basically the same type of pressure pattern there are combinations with vorticity and others with no vorticity.

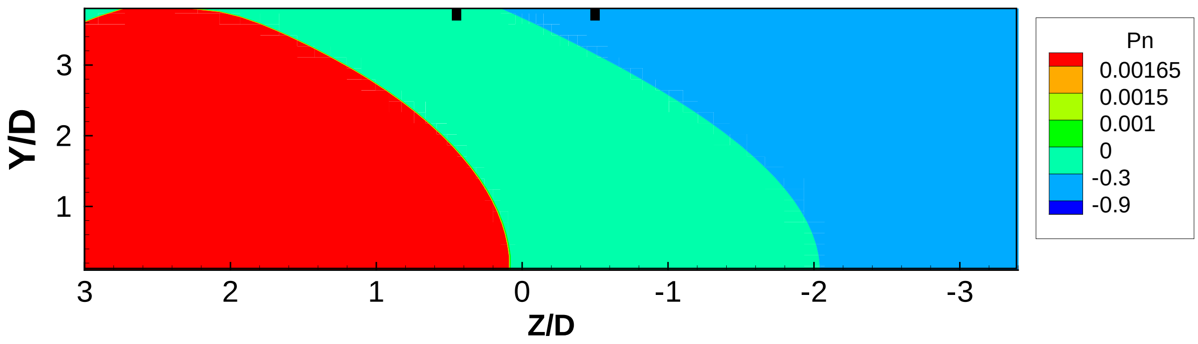

Figure 26. D_i=1,500; h=2,400; U_i=60,000; U_∞=2,200

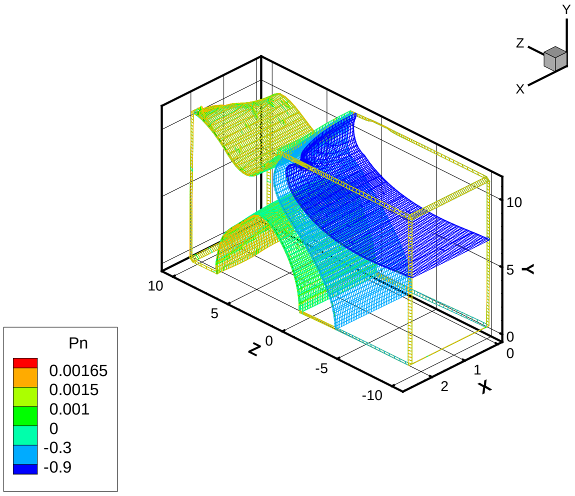

Figure 27. D_i=1,500; h=2,400; U_i=60,000; U_∞=2,200

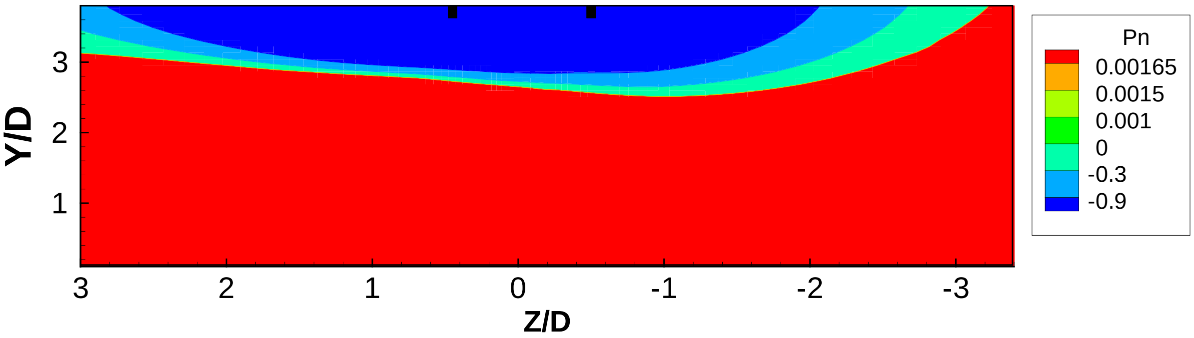

Figure 28. D_i=2,600; h=2,600; U_i=80,000; U_∞=2,200

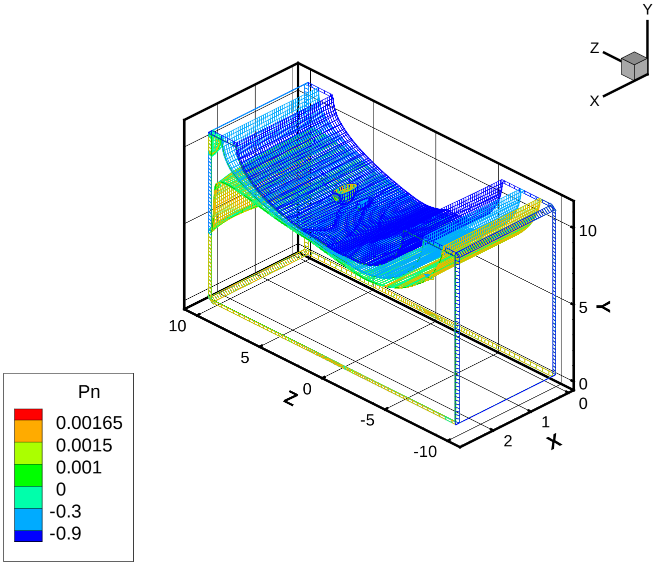

Figure 29. D_i=2,600; h=2,600; U_i=80,000; U_∞=2,200

Now we will show the situations where there is very low vorticity or no vorticity. For our first situation we have figures 30 and 31 where despite the fact of the ground being all a low pressure area there is no vorticity present.

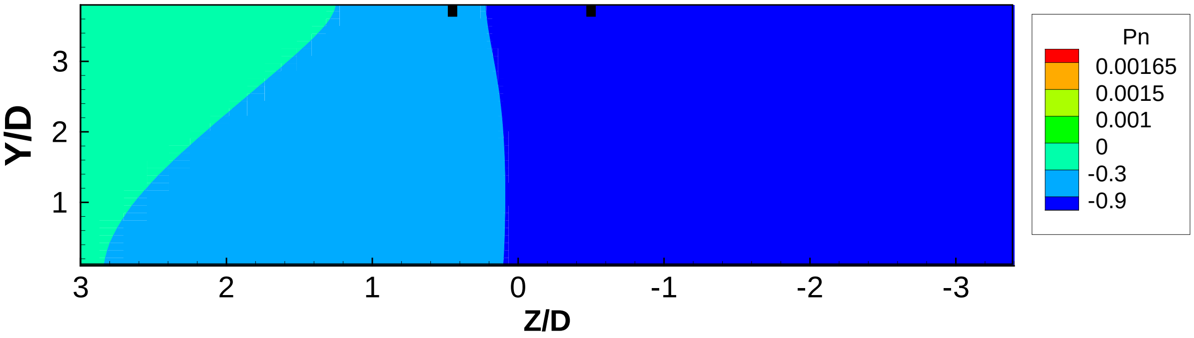

Figure 30. D_i=2,200; h=2,800; U_i=20,000; U_∞=2,200

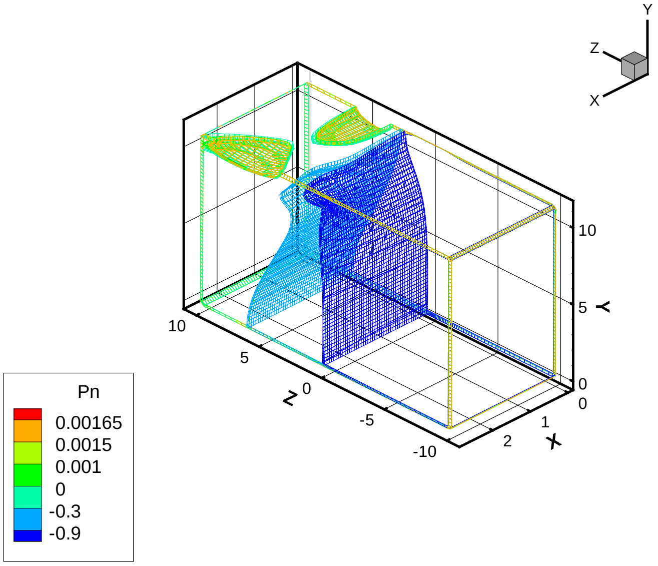

Figure 31. D_i=2,200; h=2,800; U_i=20,000; U_∞=2,200

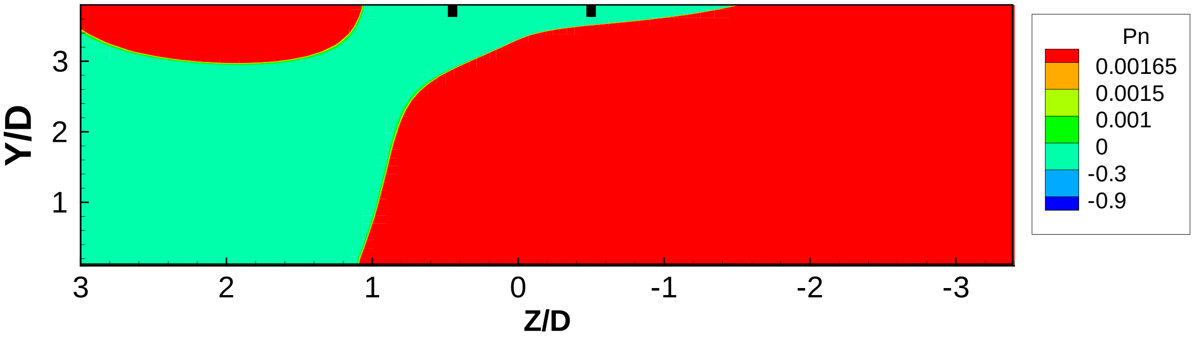

Figure 32. D_i=2,000; h=1,900; U_i=20,000; U_∞=2,200

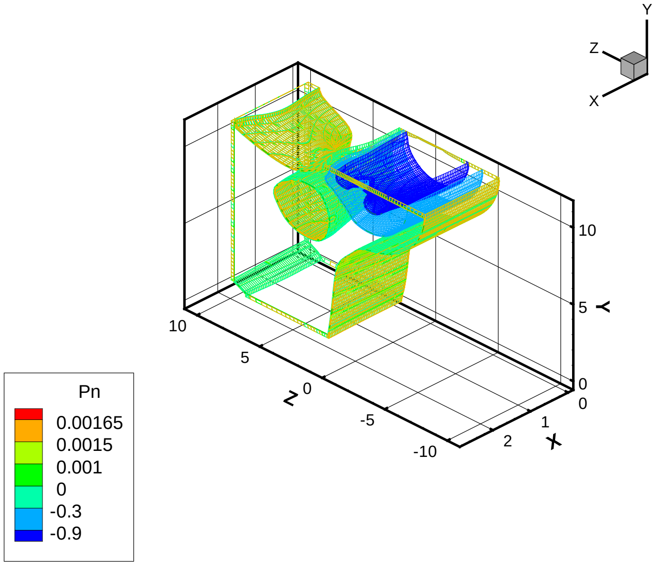

Figure 33. D_i=2,000; h=1,900; U_i=20,000; U_∞=2,200

Regarding the two previous figures (Fig. 32 and 33) in the presence of this type of pattern we never encounter the existence of vorticity on the flow.

The other pattern that we encounter that reveal no existence of vorticity is shown in the figures 34 and 35

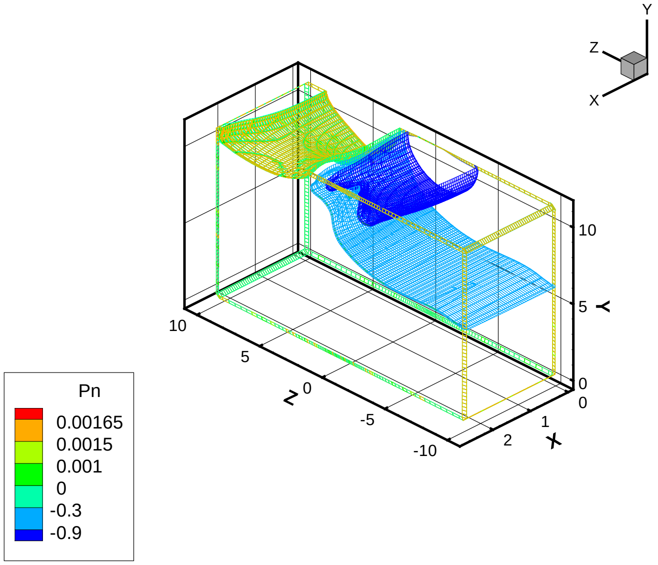

Figure 34. **D_i=2,000; h=1,900; U_i=160,000; U_∞=2,200**

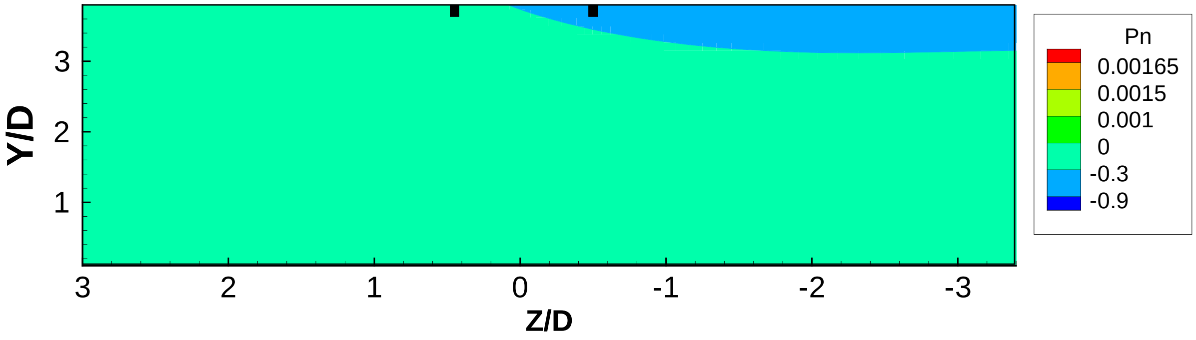

Figure 35. **D_i=2,000; h=1,900; U_i=160,000; U_∞=2,200**

We also identified another kind of pattern that was only present in the combinations with the highest **D_i** and the highest **U_i** (Fig.36and 37). This case always presented vorticity.

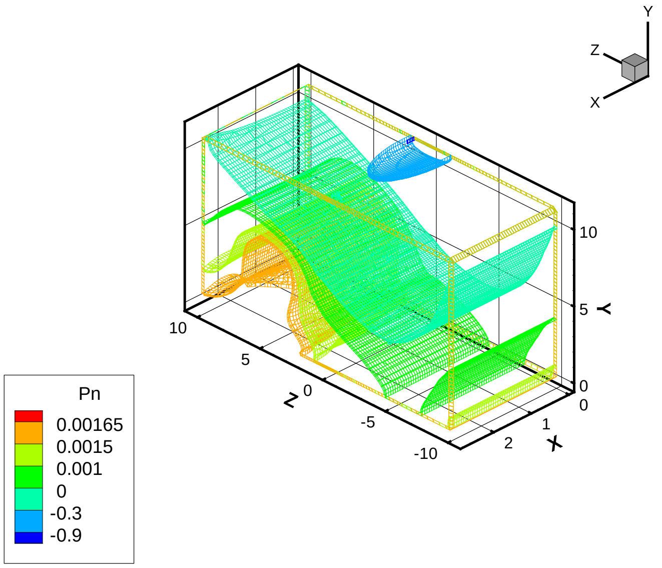

Figure 36. D_i=3,000; h=2,800; U_i=160,000; U_∞=2,200

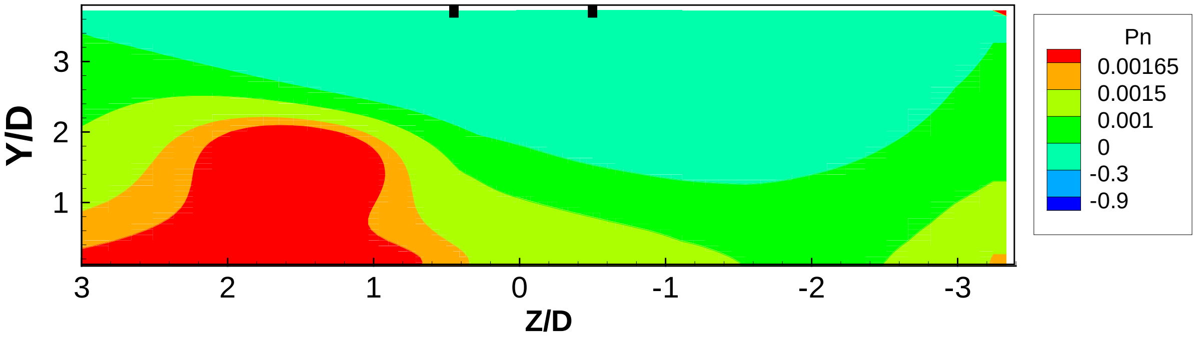

Figure 36. D_i=3,000; h=2,800; U_i=160,000; U_∞=2,200

Conclusions

The present study has shown that is difficult to predict the existence or not of vorticity in the flow be only analyzing the ground pressure.

But it is possible to find some patterns of ground pressure distribution and draw some conclusions.

The first is the presence of small low pressure areas that indicate the presence of a vortex.

When the ground is all a low or high pressure area then vorticity is always present the same happens when there is an area of high near the inlet surrounded by a lower pressure area.

In some cases is possible to determine the presence of by seeing the iso surfaces in 3D graphic.

We can also conclude that when the pressure is low but gradually rises in the direction of the crosswind then no vorticity is verified.

.

References

[1] Hünecke, K. “Jet Engines: Fundamental of theory, design and operation”, Airlife publishing, UK, 1997.

[2] Mattingly, J.D., Heiser, W.H., Daley, D.H. “Aircraft Engine Design”, AIAA Education Series, New York, 1987.

[3] Mattingly, J.D. “Elements of Gas Turbine Propulsion”, Singapore: McGraw-Hill, 1996.

[4] Johns, C. “The Aircraft Engine Inlet Vortex Problem”, AIAA’s Aircraft Technology, Integrations and Operations (ATIO) 2002 Technical, 1-3rd 2002, Los Angles, California, AIAA Paper 2002-5894.

[5] Swainston, M. “Vortex Formation Near Intakes to Turbomachinery and Duct Systems”, Heat and Fluid Flow, Vol. 4, No. 2, 1974.

[6] Nakayama, A. & Jones, J. “Correlation for Formation of Inlet Formation”, AIAA Journal, Vol. 37, No. 4: Technical Notes, 1998.

[7] Motycka, D. & Walter, W. “An Experimental Investigation of Ground Vortex Formation During Reverse Thrust Operation”, AIAA Paper No. 75/1322, AIAA/SAE 11th Propulsion Conference, 1975

[8] Brix, S., Neuwerth, G. & Jacob, D. “The Inlet-Vortex System of Jet Engines Operating Near the Ground”, AIAA Paper 2000-3998, 2000

[9] De Siervi, F., Viguier, H., Greitzer, E. & Tan, C. “Mechanisms of Inlet Vortex Formation”, J. Fluid Mech., Vol. 124, pp. 173-207, 1982

[10] Nakayama, A. & Jones, J. “Correlation for Formation of Inlet Formation”, AIAA Journal, Vol. 37, No. 4: Technical Notes, 1998.

[11] Barata, J. M. M., Maneta, A.M., Silva, A.R.R. “ Numerical Study of Single Impinging Jets Through a Crossflow”, AIAA Paper no. 2009-4801, 45th AIAA/ASME/SAE/ASEE Joint propulsion Conference & Exhibit, Denver, CO, 2-5 Aug., 2009.

[12] Barata, J. M. M., Manquinho, P.A., Silva, A.R.R. “A Comparison of Different Gas Turbine Engines Ground Vortex Flows”, AIAA Paper no. 2010-7116, 46th AIAA/ASME/SAE/ASEE Joint propulsion Conference & Exhibit, Nashville, TN, 25-28 July, 2010.

[13] Barata, J. M. M., Manquinho, P.A., Silva, A.R.R. “Identification of Gas Turbine Ground Vortex Formation Regimes”, AIAA Paper no. 2012-0600, 50th AIAA Aerospace Sciences Meeting, Nashville, TN, 09-12 Jan., 2012.

CEM 2016 – Mechanical Engineering Conference
Porto, Portugal, 1-3 June 2016
LAETA - Associated Laboratory for Energy, Transports and Aeronautics

PARAMETRIC STUDY OF INTAKE GROUND VORTEX FORMATION UNDER CROSSWIND CONDITIONS

Manquinho, Pedro[1]; Barata, Jorge[2]; Silva, André[3]

[1] Univ. of Beira Interior, Aerospace Sciences Department, Portugal, pedro.manquinho@gmail.com
[2] University of Beira Interior, Department of Aerospace Science, Portugal, jbarata@ubi.pt
[3] University of Beira Interior, Department of Aerospace Science, Portugal, andre@ubi.pt

KEYWORDS: *Inlet ground vortex, gas turbine*

ABSTRACT: When an aircraft turbofan engine is operating on the ground or during the take-off run, an inlet ground vortex can occur which can cause the ingestion of foreign objects and could adversely affect the engine. It is a complex flow for which there is currently very little appropriate quantitative preliminary design information. Previous published work show that the phenomenon can only occur with the presence of a stagnation streamline between the ground and the intake which is dependent on the velocity ratio and the non-dimensional height of the engine axis above the ground, h/D_i. The typical formation of ground vortices is defined by low h/D_i and high intake-to-crosswind velocity ratio (U_i/U_∞). CFD tools have been applied recently to the understanding of the ground vortex with relative success. Ref. 2 reports Navier-Stokes calculations and predicted successfully the ground vortex phenomena using real operational conditions for the case of the engine Trent 9 and GE nx-1B64. The ground vortex formation in irrotational crosswind flow is analysed in detail for this configuration, and the formation of the trailing vortex was associated to a very complex flow.

In the present paper the work of [2] is extended to different values of inlet diameter, height of the engine axis above the ground and inlet velocity. The intake ground vortex flows produced by the different engine-velocity and ratio-clearance distance combinations are compared and discussed using D_i, h, U_i/U_∞ and h/D_i. The results have shown that more than one mode can occur for a particular engine-velocity ratio-clearance distance combination with 1, 2, 3 or 4 vortexes that may merge before entering the inlet engine.

Nomenclature

A_i = intake area
A_∞ = frequency of oscillation of the ground vortex
D_i = inner diameter of the intake
r = inner radius of the engine
h = height of the engine axis above the ground
$\boldsymbol{k}$ = turbulent kinetic energy
L_q = intake stream tube length
$\dot{m}$ = mass flow

U_i = intake throat velocity
U_∞ = free stream velocity
V_∞ = tangential velocity
Γ = Vortex circulation
ζ = Vorticity
ρ = Density
μ = dynamic viscosity
ν = kinematic viscosity
ν_T = turbulent kinematic viscosity
ϕ = any dependent variable

1 INTRODUCTION

Ground vortex is a complex flow for which there is currently very little appropriate quantitative preliminary design information [1].

When an aircraft turbofan engine is operating on the ground or during the take-off run, an inlet ground vortex can occur which can cause the ingestion of foreign objects and could adversely affect the engine (Fig. 1).

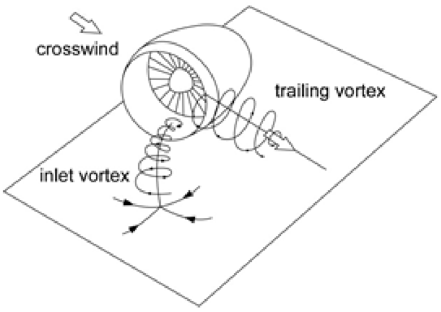

Figure 1. Inlet and trailing vortex.

If the pressure losses and the flow distortions are very low, the performance of the engine is optimal. This airflow condition is necessary in all flight configurations including when the aircraft is maneuvering on the ground. The performance of the intake depends on the mass-flow delivered to the compressor.

The typical formation of ground vortices is defined by low h/Di and high and that is the same has saying the engine is operating close to the ground at a high inlet mass flow.

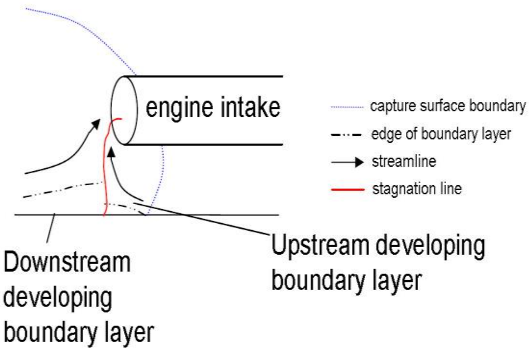

Figure 2. Ground vortex formation**.**

Hence, the mechanism of intake formation is strongly dependent of the height of the engine axis above the ground, the velocity ratio and the presence of an upstream velocity.

Previous published work show that the phenomenon can only occur with the presence of a stagnation streamline between the ground and the intake which is dependent on the velocity ratio and the non-dimensional height of the engine axis above the ground, h/Di (Fig. 2).

Current design rules for the avoidance of ground vortex formation relies on the vortex/no vortex map in which a number of previous researchers have correlated combinations of for both when vortices are observed and when no vortex activity is identified.

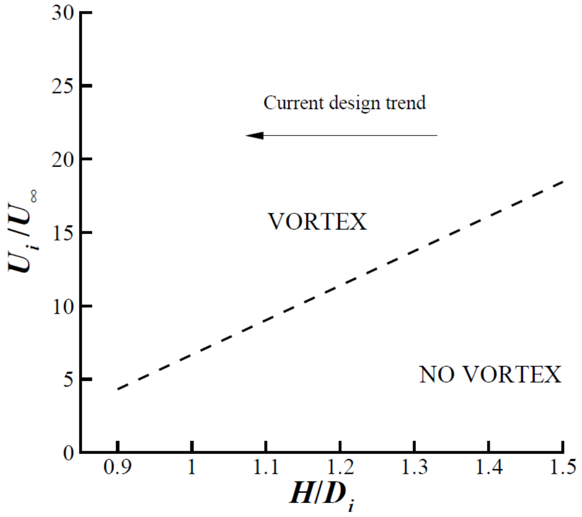

Figure 3. Ui/U∞ against h/Di

However, this graphic gives no indication of what happens to the quantitative vortex characteristics as the engine operates in different regions of the vortex formation zone.

So CFD tools have been applied recently to the understanding of the ground vortex with relative success. Ref. 2 reports Navier-Stokes calculations and predicted successfully the ground vortex phenomena using real operational conditions for the case of the engine Trent 9 and GE nx-1B64.

The ground vortex formation in irrotational

crosswind flow is analysed in detail for this configuration, and the formation of the trailing vortex was associated to a very complex flow.
In the present paper the work of [2] is extended to different values of inlet diameter, height of the engine axis above the ground and inlet velocity

1.1 In Crossflow Conditions

In previous published work were identified two types vortex formations under crosswind conditions [3].
One is the formation with one inlet vortex and a trailing vortex (Fig. 4) and the second with no inlet vortex but with two trailing vortex (Fig. 5).

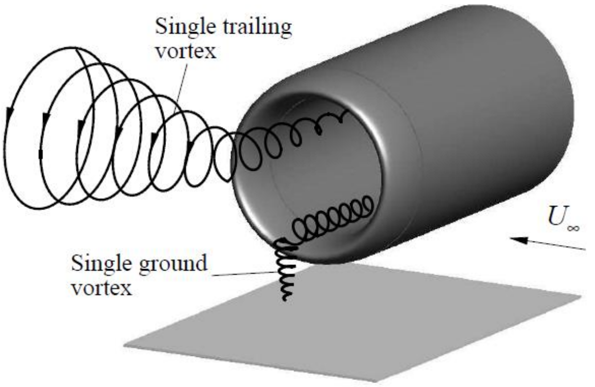

Figure 3. Low h/Di or high Ui/U∞

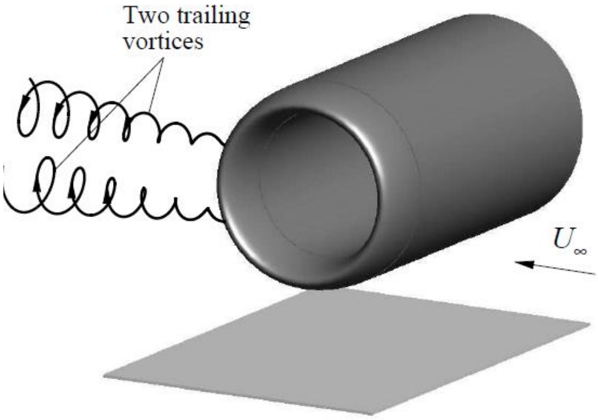

Figure 4. Low Ui/U∞ or high h/Di

In Ref. 2 were identified new formations where one, two and even three inlet vortex are present.

So a wider study was needed.

2 MATHEMATICAL MODEL

The mathematical model used in the present study is described in detail in Ref. 4 and only the main features will be summarized here. The time averaged partial differential equations governing the steady, uniform-density isothermal three-dimensional flow.

$$\rho\overline{U}_j \frac{\partial \overline{U}_i}{\partial X_j} = -\frac{\partial \overline{P}}{\partial X_i} + \frac{\partial}{\partial X_j}\left(\mu \frac{\partial \overline{U}_i}{\partial X_j} - \rho\overline{u'_i\, u'_j}\right) \tag{1}$$

and the continuity equation,

$$\rho\overline{U}_j \frac{\partial \overline{U}_i}{\partial X_i} = 0 \tag{2}$$

where solved together with the equations of transport of the turbulent kinetic energy and dissipation rate of the two-equation *"k-ε"* model

$$\overline{U}_j \frac{\partial k}{\partial X_j} = \frac{\partial}{\partial X_j}\left(\frac{\upsilon_T}{\sigma_k}\frac{\partial k}{\partial X_j}\right) - \overline{u'_i\, u'_j}\frac{\partial \overline{U}_i}{\partial X_j} - \varepsilon \tag{3}$$

$$\overline{U}_j \frac{\partial \varepsilon}{\partial X_j} = \frac{\partial}{\partial X_j}\left(\frac{\upsilon_T}{\sigma_\varepsilon}\frac{\partial \varepsilon}{\partial X_j}\right) - C_1\frac{\varepsilon}{k}\overline{u'_i\, u'_j}\frac{\partial \overline{U}_i}{\partial X_j} - C_2\frac{\varepsilon^2}{k} \tag{4}$$

where C_1 and C_2 are additional dimensionless model constants, and σ_k and σ_ε are the turbulent Prandtl numbers for kinetic energy and turbulent dissipation.
The Reynolds stresses are expressed as

$$\overline{u'_i\, u'_j} = -\upsilon_T\left(\frac{\partial \overline{U}_i}{\partial X_j} + \frac{\partial \overline{U}_j}{\partial X_i}\right) + \frac{2}{3}k\delta_{ij} \tag{5}$$

3 CONDITIONS OF SIMULATION

The computational domain has six boundaries where dependent values are specified: a free stream plane, a symmetry plane, and a solid wall. On the symmetry plane, the normal velocity vanishes, and the normal derivates of the other variables are zero. At the solid surface, the wall function method is used to prescribe the boundary conditions for the velocity and turbulence quantities, assuming that the turbulence is in state of local equilibrium. The free stream plane is located at *Z*=0 and corresponds to the crossflow conditions. The engine intake boundary is represented by a right angled polygon and the mass flow rates and the momentum are matched to the experimental values.

The intake represents a 1/1th scale model with a diameter that corresponds to each particular engine. The axis of the engine is located at a distance above the ground (h), which corresponds to the specific clearance distance.

All the tests were performed for the case of irrotational crosswind, and the other conditions are shown in Table 1. The domain of solution, their dimensions and the system of axes are represented in Fig.5 and Fig. 6.

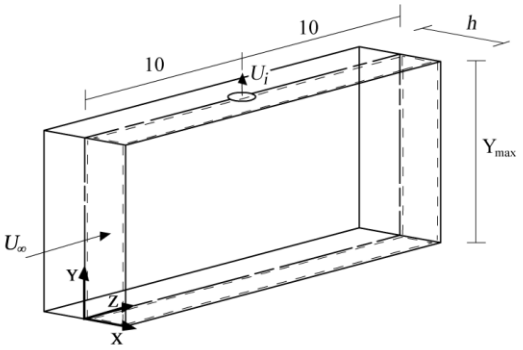

Figure 5. Domain of the solution.

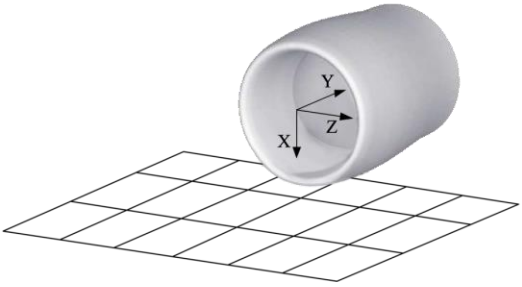

Figure 6. Representation of the intake with referential at the center.

r (m)	D_i (m)	h (m)	U_i (m/s)	U_∞ (m/s)
1,5000	**3,0000**	**2,8000**	**160,0000**	**2,2000**
1,4000	**2,8000**	**2,6000**	**140,0000**	
1,3000	**2,6000**	**2,4000**	**120,0000**	
1,2000	**2,4000**	**2,3000**	**100,0000**	
1,1000	**2,2000**	**2,2000**	**80,0000**	
1,0000	**2,0000**	**2,1000**	**60,0000**	
0,9000	**1,8000**	**2,0000**	**40,0000**	
0,8000	**1,6000**	**1,9000**	**20,0000**	
0,7500	**1,5000**			

Table 1. Values tested.

4 RESULTS

We are going to analyse the results of ours 576 simulations using for that D_i, h, U_i, U_i/U_∞ and h/D_i.

The results are divided in nine values of D_i and using the max of number of vortex found to characterize each run (Fig. 7. to Fig.15.).

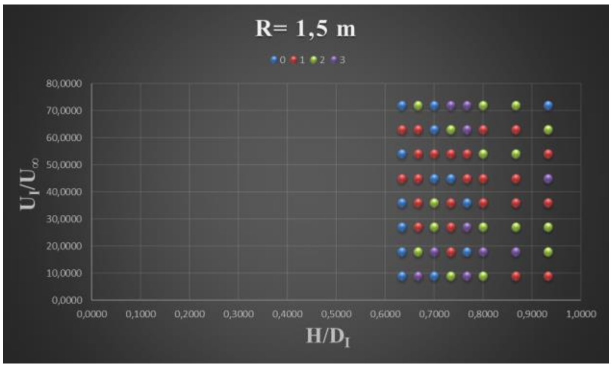

Figure 7.

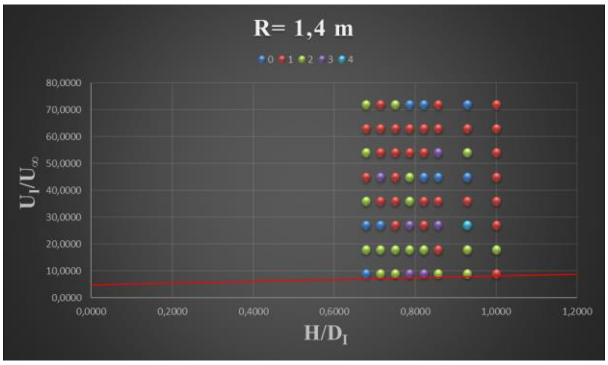

Figure 8.

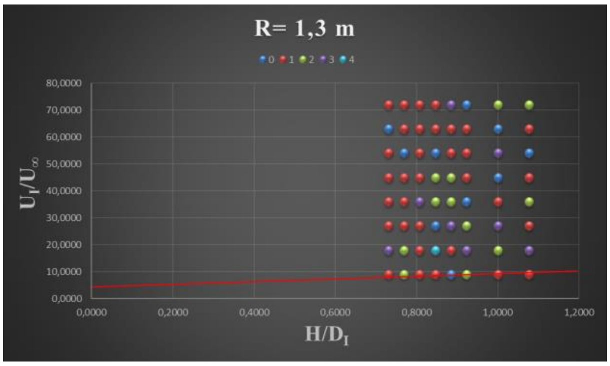

Figure 9.

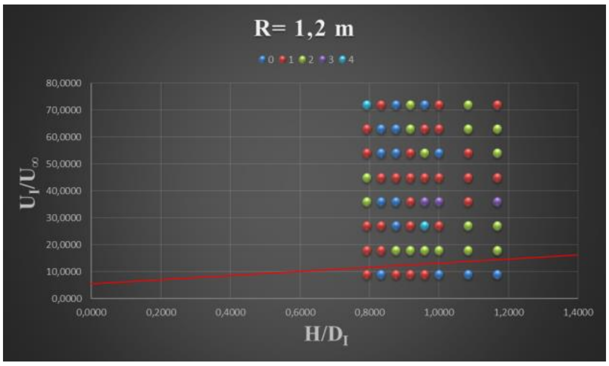

Figure 10.

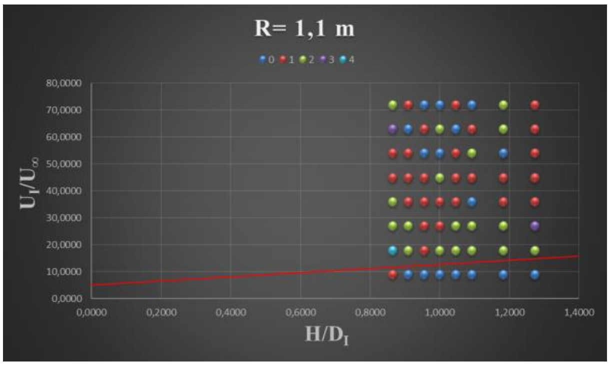

Figure 11.

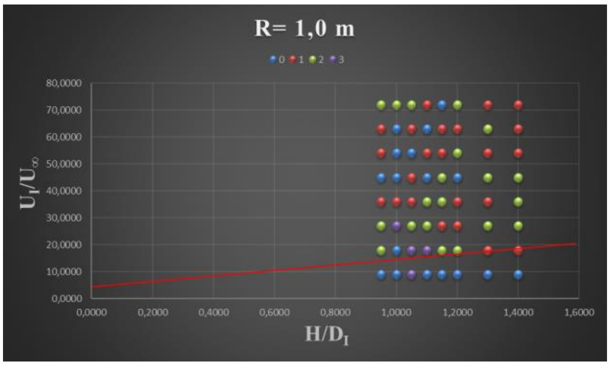

Figure 12.

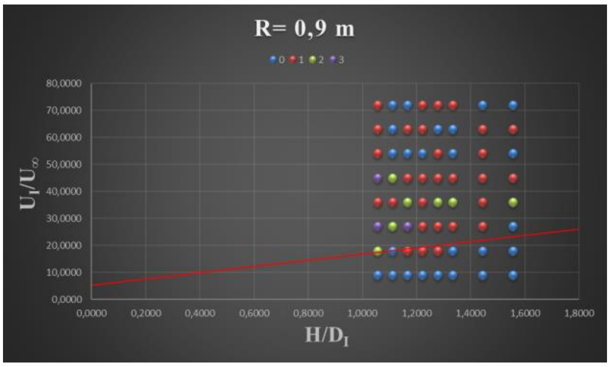

Figure 13.

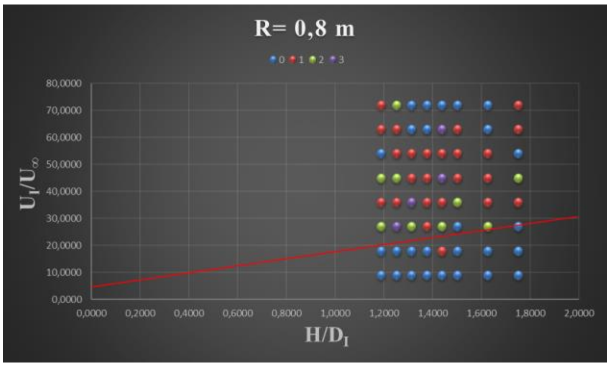

Figure 14.

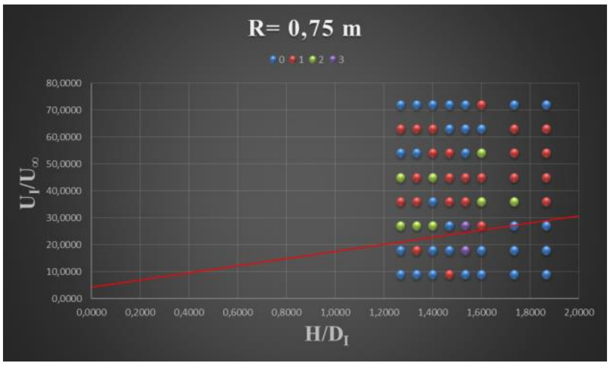

Figure 15.

How we can see from just observing the figures above we can came to the conclusion that our results agrees with the conclusions of previous authors in the no vortex area (below the red line).

But for the other area ours results have some differences.

We have identified several combinations of D_i, h, U_i that have 2, 3 and even 4 vortex present.

Combinations with 4 vortex

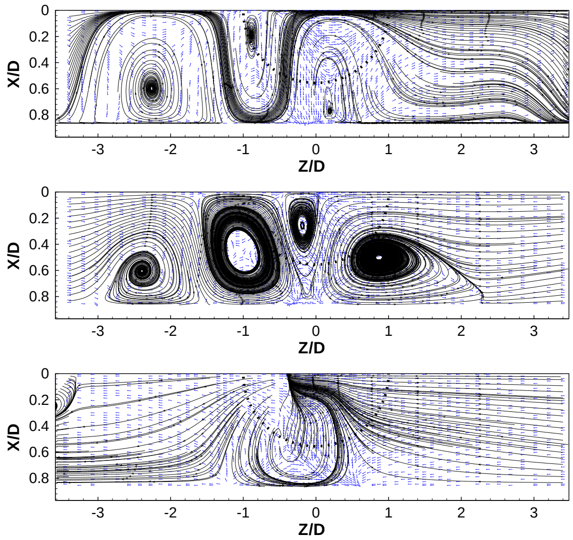

Figure 16. Di=2,200; h=1,900; Ui=40,000; U_∞=2,200

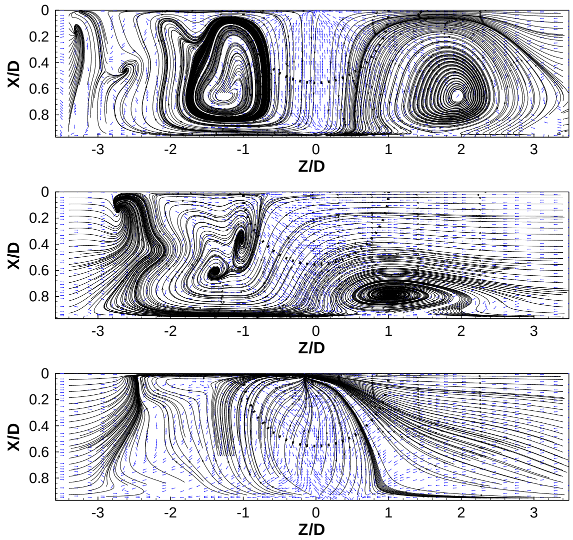

Figure 17. Di=2,400; h=2,300; Ui=60,000; U_∞=2,200

Examples of combinations with three vortex

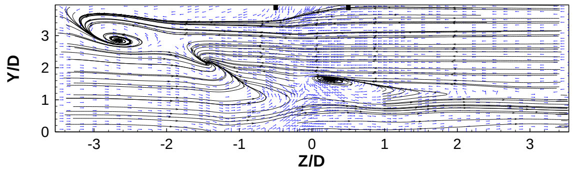

Figure 18. Di=2,800; h=2,000; Ui=100,000; U_∞=2,200

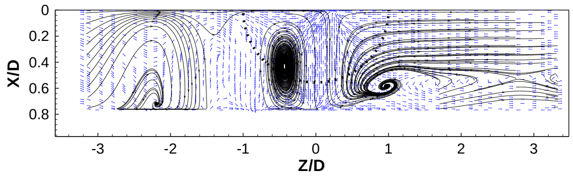

Figure 19. Di=3,000; h=2,300; Ui=160,000; U_∞=2,200

In Fig. 8,9,10,11 and 12 we can see that in the point h/D_i=1,000 and seeing the same for all the cited Fig. it is evident that for the same combination of h/Di and U_i/U_∞ ratio the flow does not have the same behavior.

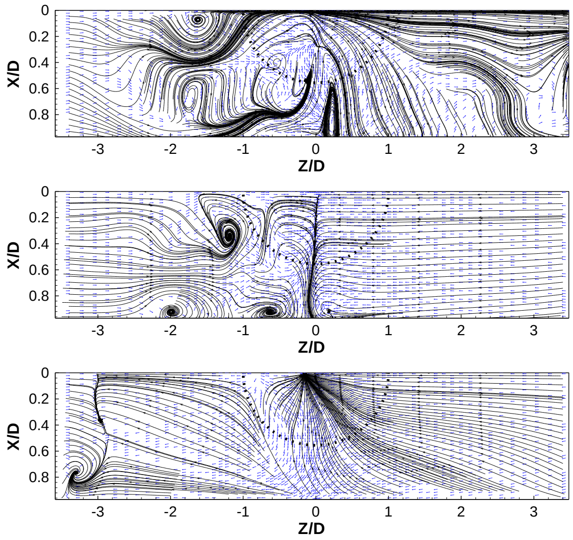

Figure 20. h/D_i=1,000; U_i/U_∞=54,000

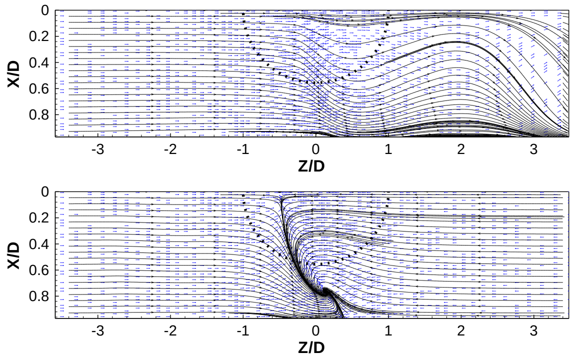

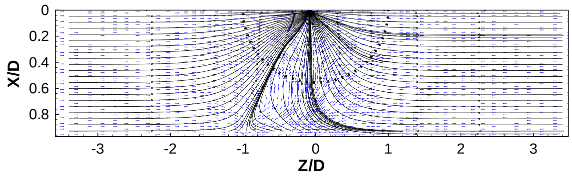

Figure 21. h/D_i=1,000; U_i/U_∞=54,000

There is a combination with one inlet vortex an no trailing vortex

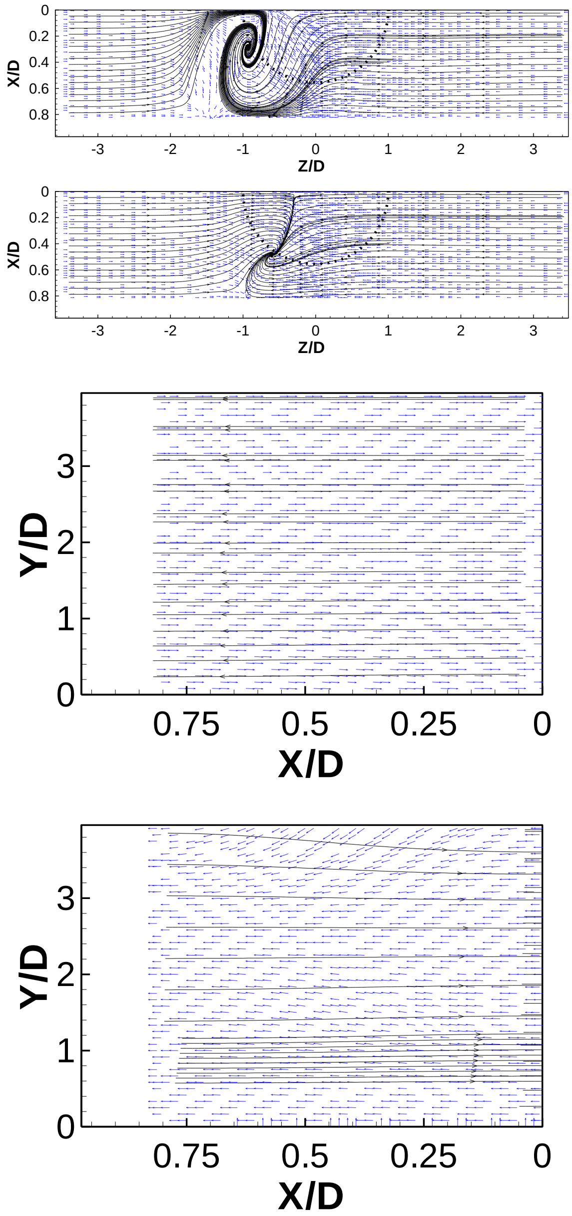

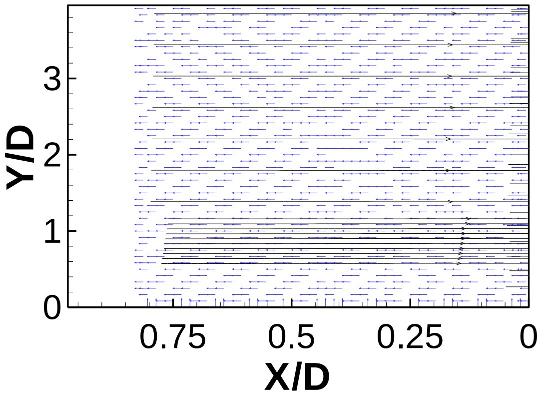

Figure 22. =2,800; =2,300; Ui=140,000; U∞=2,200

4 CONCLUSIONS

We can say that the ground vortex formation it is a very complex process.

That the current approach is very simplified and can only explain with some degree of accuracy part of the ground vortex formation. We found all the same combinations of vortex as the other authors but found some new ones like 1 inlet vortex with no trailing vortex, 2 vortex on the vertical plane close to the inlet, 3 vortex in the ground plane and the vertical plane and a totally new 4 vortex structurer far from the inlet and it will merge before the inlet.

We can say that the influence of Di, h, U_i/U_∞ it is not so linear as we thought because for the same h/D_i and U_i/U_∞ ratios but with different values D_i and h we have completely different behaviour.

5 REFERENCES

[1] Murphy, J.P., and MacManaus, D.G. Intake Ground Vortex Prediction Methods. Journal of Aircraft. 2011; 48(1): 23-33.

[2] Barata, J. M. M., Manquinho, P.A., Silva, A.R.R. “Identification of Gas Turbine Ground Vortex Formation Regimes”, AIAA Paper no. 2012-0600, 50th AIAA Aerospace Sciences Meeting, Nashville, TN, 09-12 Jan., 2012.

[3] de Siervi, F., Viguier, H. C., Greitzer, E. M. and Tan, C. S. “Mechanisms of inlet vortex

formation" Journal of Fluid Mechanics, 124:173–207, 1982.
[4] Barata, J. M. M., Maneta, A.M., Silva, A.R.R. " Numerical Study of Single Impinging Jets Through a Crossflow", AIAA Paper no. 2009-4801, 45th AIAA/ASME/SAE/ASEE Joint propulsion Conference & Exhibit, Denver, CO, 2-5 Aug., 2009